

**A Thesis Submitted for the Degree of PhD at the University of Warwick**

**Permanent WRAP URL:**

<http://wrap.warwick.ac.uk/149923>

**Copyright and reuse:**

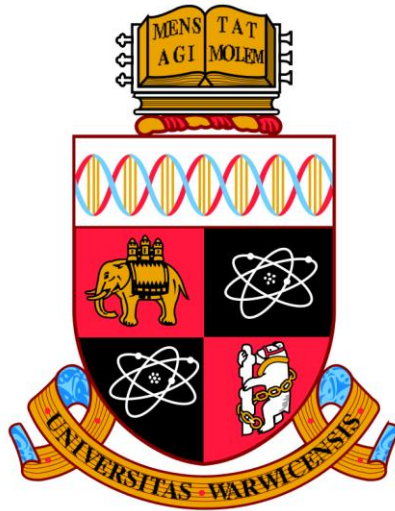
This thesis is made available online and is protected by original copyright.

Please scroll down to view the document itself.

Please refer to the repository record for this item for information to help you to cite it.

Our policy information is available from the repository home page.

For more information, please contact the WRAP Team at: [wrap@warwick.ac.uk](mailto:wrap@warwick.ac.uk)



Phonon transport simulations in hierarchical and  
highly disordered nanostructures

by

Dhritiman Chakraborty

Thesis

Submitted to the School of Engineering, University of Warwick,  
in fulfilment of the requirements for the degree of  
Doctor of Philosophy

May 2020

*Dedicated to my loving family*

‘মাঝে মাঝে তব দেখা পাই  
চিরদিন কেন পাইনা’...

# Table of Contents

<b>List of Figures.....</b>	<b>I</b>
<b>Acknowledgements.....</b>	<b>X</b>
<b>Declaration.....</b>	<b>XI</b>
<b>Abstract .....</b>	<b>XII</b>
<b>Abbreviations.....</b>	<b>XIII</b>
<b>1. Introduction.....</b>	<b>1</b>
1.1 Background.....	1
1.2 Motivation.....	7
1.3 Thesis outline .....	9
<b>2. Phonon theory.....</b>	<b>12</b>
2.1 Phonons and their properties.....	12
2.2 Phonons in silicon .....	24
2.3 Lattice thermal energy and phonon scattering .....	26
2.4 Thermoelectricity and nanostructured thermoelectric materials .....	28
2.5 Summary .....	30
<b>3. Phonon transport theory .....</b>	<b>31</b>
3.1 Approaches to phonon transport simulations .....	31
3.1.1 Molecular Dynamics (MD) methods .....	33
3.1.2 Non-Equilibrium Green's Functions (NEGF).....	35
3.1.3 Boltzmann Transport Equation (BTE) .....	37
3.2 Monte Carlo method .....	38
3.2.1 Incident flux (or single-particle) simulation process.....	40
3.2.2 Phonon scattering treatment.....	42
3.2.3 Thermal gradient and thermal properties .....	44
3.2.4 Validation of thermal conductivity simulations for bulk Si case .....	49
3.2.5 Treatment of nanocrystalline structures .....	50
3.2.6 Treatment of nanoporous structures.....	52
3.3 Summary .....	54

<b>4.</b>	<b>Phonon transport in hierarchically disordered silicon nanostructures.....</b>	<b>55</b>
4.1	Introduction: hierarchically nanostructured materials.....	55
4.2	Effects of grain size and roughness in nanocrystalline case .....	58
4.3	Effects of nanoporous and hierarchical nanostructuring.....	60
4.3.1	Influence of porosity and pore roughness .....	60
4.3.2	Influence of <i>randomized</i> pore positions and diameters.....	62
4.3.3	Hierarchical disordered nanostructures.....	64
4.4	Analytical models developed .....	65
4.4.1	Nanocrystalline case .....	66
4.4.2	Nanoporous case .....	68
4.4.3	Random nanoporous case.....	70
4.5	Verifying Matthiessen's rule.....	77
4.6	Conclusions.....	80
<b>5.</b>	<b>Enhanced phonon boundary scattering in hierarchical nanostructures.....</b>	<b>82</b>
5.1	Introduction: hierarchical nanomaterials at high temperatures .....	82
5.2	Approach: high temperature (HT) systems .....	83
5.3	Results: effects of high temperature.....	85
5.3.1	Pristine structures .....	85
5.3.2	Nanocrystalline case .....	87
5.3.3	Hierarchical case .....	88
5.4	Conclusions.....	92
<b>6.</b>	<b>Thermal rectification in nanoporous silicon material.....</b>	<b>93</b>
6.1	Introduction: thermal rectification in porous nanostructures .....	93
6.2	Approach: determining rectification ( $R$ ) in nanostructures.....	93
6.3	Results: $R$ for different geometry arrangements .....	95
6.3.1	Rectification in asymmetric porous arrangements .....	95
6.3.2	Modelling thermal rectification.....	97
6.3.3	Rectangular porous geometries .....	99
6.3.4	Influence of pore positions and density .....	102

6.3.5	Effect of surface area and grading .....	103
6.3.6	Triangular arrangements and hierarchical nanopores .....	105
6.4	Conclusions.....	107
<b>7.</b>	<b>Wave vs particle phonon nature in thermal transport in nanostructures ...</b>	<b>108</b>
7.1	Introduction: wave and particle phonon treatment.....	108
7.2	Approach: theoretical background and methods.....	110
7.2.1	Non-Equilibrium Green's Function method (NEGF) .....	113
7.2.2	Monte Carlo ray-tracing method (MC) .....	115
7.3	Results: wave vs particle phonon behaviour.....	117
7.3.1	MC transmissions versus geometry .....	118
7.3.2	Influence of neck size $n$ and $n/D$ ratio .....	119
7.3.3	Comparing NEGF and MC variations.....	120
7.4	Discussion: limits of MC and NEGF .....	122
7.5	Multi-pore cases.....	124
7.6	Conclusions.....	126
<b>8.</b>	<b>Effects of conductive nanoinclusions in resistive matrix .....</b>	<b>127</b>
8.1	Introduction: conductive nanoinclusions (NI) in resistive matrix.....	127
8.2	Approach: simulations of systems with NIs.....	128
8.3	Results: effect of conductive NIs .....	129
8.3.1	Influence of NI density (%NI fraction) .....	129
8.3.2	Influence of NI Diameter ( $D$ ).....	131
8.3.3	Comparison to experiments.....	134
8.4	Conclusions.....	135
<b>9.</b>	<b>Conclusions and future work .....</b>	<b>136</b>
9.1	Conclusions.....	136
9.2	Future work.....	138
<b>Appendix A .....</b>		<b>139</b>
<b>Appendix B .....</b>		<b>148</b>
<b>References .....</b>		<b>156</b>

# List of Figures

Figure	Page
<a href="#">1.1</a> Rejected energy as waste heat during primary power generation processes. Pie charts created based on estimated US energy consumption from primary sources of energy in all sectors including industrial, residential and transport sectors. Recreated based on updated data released in March 2020 [3].	1
<a href="#">1.2</a> Thermoelectric efficiency of TE materials, including some recent nanomaterials. (a) ZT measurements for thermoelectric materials from 1940 [19]. (b) Recent novel thermoelectric materials and their active working temperatures [29].	3
<a href="#">1.3</a> Carnot efficiencies vs ZT measurements. $ZT = 2$ was the minimum target to approach the 40% Carnot efficiency [19]. Cold junction is kept at room temperature (300 K).	4
<a href="#">1.4</a> Schematic of hierarchically nanostructured material with pores (blue bordered circles), inclusions (red filled circles) and nanocrystalline grain boundaries (black lines). The temperature gradient from hot ( $T_H$ ) to cold ( $T_C$ ) sides is indicated by gradient coloring (orange to green, respectively). Phonons at higher temperatures have shorter wavelengths, $\lambda$ (or higher frequencies, $\omega$ ) [32].	5
<a href="#">1.5</a> Hierarchically nanostructured material with hierarchical inclusions at the atomic scale, the nanoscale, and the mesoscale in the PbTe–SrTe system [5].	6
<a href="#">1.6</a> Nanostructured Si-based material with porous nanomesh thin film. (a) SEM image with nanometric pore sizes indicated. (b) AFM image of the same material gives its topography. (c) KPM image gives the surface potential for the same material. Uniform contrast indicates homogeneity in the surface potential of the film [33]. This experimental result is given by Taborda <i>et al.</i> in their work [33].	6
<a href="#">2.1</a> Longitudinal and transverse waves in crystals. (a) Schematic of a monoatomic chain with point masses of mass = $M$ representing atoms in the chain and “springs” with force constant ‘ $C$ ’ representing the bonding potential between atoms. (b) Longitudinal wave in monoatomic chain with atoms moving in the direction of wave propagation (black-solid arrows). Each atom (solid red circle) is displaced in the positive $x$ -direction (transparent red circle). (c) Transverse wave with atoms moving from their equilibrium positions (solid red circles) perpendicularly along the $y$ -axis (transparent circles) respectively. (d) Transverse waves in crystal planes (blue-dashed lines). Displacement of atoms for respective planes ( $s-1$ , $s$ , $s+1$ ) perpendicular to the direction of wave propagation are indicated by black-solid lines ( $u_{s-1}$ , $u_s$ , $u_{s+1}$ ), respectively. (e) Longitudinal wave in crystal planes with atoms moving in the direction of propagation (black-solid arrows). Each atom (solid red circle) is displaced in the positive $x$ -direction (transparent red circle) leading to the displacement of the planes (blue-dashed lines). The distance (spacing) between the planes is indicated by ‘ $a$ ’. The positive $x$ and $y$ directions are indicated. Figures recreated from Ref. [63].	13

<a href="#">2.2</a>	Comparing monoatomic and diatomic crystals. (a) Schematic of a one-dimensional monoatomic chain with point masses of mass $M$ representing the atoms in the chain. There is one atom per unit cell (solid red circle) displaced in the positive $x$ -direction by displacement $u_s$ (transparent red circle). (b) Schematic of a diatomic chain with point masses $M_1$ (red) and $M_2$ (blue) representing the two atoms per unit cell. Each atom (solid circle) is displaced in the positive $x$ -direction (transparent circle) by displacement $u_s$ and $v_s$ for masses $M_1$ (red) and $M_2$ (blue) respectively.	15
<a href="#">2.3</a>	Dispersion relation $\omega(q)$ in the first Brillouin zone. At the center of the first Brillouin zone Eq. 2.13 gives $\omega(q) = \omega(0) = 0$ .	17
<a href="#">2.4</a>	Dispersion relation $\omega(q)$ experimentally obtained for silicon [67] for longitudinal acoustic (LA), longitudinal optical (LO), transverse acoustic (TA) and transverse optical (TO) modes.	21
<a href="#">2.5</a>	The fit for the dispersion relation $\omega$ obtained as in Ref. [85] for longitudinal acoustic (LA, blue lines) and transverse acoustic waves (TA, red lines).	25
<a href="#">2.6</a>	The group velocity $v_g$ obtained as in Ref. [85] for longitudinal acoustic (LA, blue lines) and transverse acoustic waves (TA, red lines).	25
<a href="#">2.7</a>	Normal and Umklapp scattering processes. Solid arrows indicate the phonon momenta before scattering (green arrows) and after scattering (red arrows).	28
<a href="#">3.1</a>	Approaches to phonon transport simulations [101-105]. These include Molecular Dynamics or MD methods, NEGF (Non-Equilibrium Green's Functions) and the Boltzmann transport Equation (BTE). The Monte Carlo approach is a method to solve the BTE and is used extensively in this Thesis. This is described in detail in Section 3.2.	32
<a href="#">3.2</a>	Features of Monte Carlo simulations in a domain of length $L_x = 1000$ nm and width $L_y = 500$ nm. Domain coloring indicates local device temperature (in K), corresponding to the temperature color map. Possible phonon trajectories are given by blue and red lines. Blue-solid lines indicate incident phonon trajectories. These can be initialized from either the left (hot) or right (cold) boundary. Blue-dashed lines indicate possible phonon trajectory angles, $\theta$ . Red lines indicate trajectories of scattered phonons after interaction with porous (blue circles) or nanocrystalline (black lines) geometries. Red-solid lines indicate specular scattering, where incident angle ( $\theta_i$ ) = reflected angle ( $\theta_r$ ). Red-dashed lines indicate diffuse scattering, where $\theta_r$ is randomized.	39
<a href="#">3.3</a>	Top view of the studied simulation domain. (a) Coloring indicates established thermal gradients when the left and right contacts are set to $T_H = 310$ K (yellow) and $T_C = 290$ K (green). Dashed-lines indicate the phonon path traced through the simulation domain (pristine silicon channel). Direction of net phonon flux $\Phi$ is indicated above. The domain size is fixed to length $L_x = 1000$ nm and width $L_y = 500$ nm. (b) The temperature gradient established for 5 million phonons (1 point for every 1 nm in $L_x$ ).	46
<a href="#">3.4</a>	Validation of the single-phonon Monte Carlo simulator (blue line) for thermal conductivity ( $\kappa$ ) versus temperature for bulk Si. Simulation works (green lines) [16, 83, 89, 106, 116, 181, 182] and experimental works (red lines) [88, 96, 181, 183] are shown. The inset shows a close up of the temperature range between 250 K and 350 K. The simulated results are in close agreement to other literature results. Adopted from Chakraborty <i>et al.</i> [60].	49



<a href="#">3.5</a>	Phonon scattering in nanocrystalline structures. (a) Nanocrystalline (NC) materials with changing grain dimension ( $\langle d \rangle$ ) and length $L_x$ in the transport direction. (b) Schematic for grain scattering indicating the initial angle of the phonon, $\theta_{GB}$ , from the normal (dashed line), grain boundaries (black lines), initial path of the phonon (blue line) and probable paths of the phonon after scattering (red-dashed lines and green-dashed transmitted line). Specular reflection (red-solid lines) and diffusive reflection (red-dashed lines) are also indicated. Transmission is dependent on grain boundary roughness as well as phonon wavevector $q$ . Transmission probability is given by Eq. 3.13.	50
<a href="#">3.6</a>	Validation of the Monte Carlo phonon transport simulator for nanocrystalline materials through comparisons with various simulation results (green lines) [65, 96, 97, 184, 185], and experimental results (red lines) [96, 98, 116, 185-187] for silicon available in the literature, are shown. Our simulation results showing the thermal conductivity for silicon as the grain size is varied from a grain dimension $\langle d \rangle$ of 1000 nm to 50 nm are shown by the blue line. Error bars represent standard deviations for results over 50 simulations Adopted from Chakraborty <i>et al.</i> [59].	51
<a href="#">3.7</a>	Phonon scattering in nanoporous structures. (a) Ordered nanopores within the pristine channel material in a rectangular arrangement. (b) Random nanopores within the pristine channel material (c) Schematic of scattering mechanism for pore scattering, indicating the pore boundary, the initial angle of the phonon $\theta_{in}$ , and potential new angle of propagation $\theta_{ref}$ depending on specular parameter $p$ . Probable paths of the phonon after scattering for both diffusive (red-dashed lines) and specular (red-solid line) are depicted.	52
<a href="#">3.8</a>	Validation of the simulator for nanoporous Si materials. Various simulation results are shown (green lines) [86, 89, 152, 188, 189], and compared against experimental results (red lines) [41, 96, 190, 191]. Our simulation results for the thermal conductivity of silicon as the percentage porosity ( $\phi$ ) is varied up to 50%. Simulations of ordered porous structures are indicated by the blue-solid line, and of disordered porous structures the blue-dashed line. Adopted from Chakraborty <i>et al.</i> [59].	53
<a href="#">4.1</a>	Examples of the nanostructured geometries considered. The coloring indicates the established thermal gradients when the left and right contacts are set to $T_H = 310$ K (yellow) and $T_C = 290$ K (green). (a) Pristine silicon channel. (b) Nanocrystalline (NC) channel. (c) Ordered nanopores (NP) within the channel material of ~20% porosity in a rectangular arrangement. (d) Combined NC and disordered NP material. (e) Schematic of scattering mechanism for pore scattering, indicating the pore boundary, the initial angle of the phonon $\theta_{in}$ , and potential new angle of propagation $\theta_{ref}$ depending on specular parameter $p$ . Probable paths of the phonon after scattering for both diffusive (red-dashed lines) and specular (red-solid line) are depicted. (f) Schematic of the scattering mechanism for grain boundary scattering, indicating the initial angle of the phonon $\theta_{GB}$ from the normal (dashed line), grain boundaries (black lines), initial path of the phonon (blue line) and probable paths of the phonon after scattering (red-dashed lines and green-dashed transmitted line). Adopted from Chakraborty <i>et al.</i> [58].	57

- [4.2](#) The effects of grain size and grain boundary roughness ( $\Delta_{\text{rms}}$ ) on the thermal conductivity of the silicon channel. Grain size is varied from an average grain dimension  $\langle d \rangle$  of 1000 nm down to 50 nm. The structure geometry insets labelled ‘1’ to ‘6’ give typical examples of geometries from  $\langle d \rangle = 50$  nm to 225 nm, respectively. We simulate three different values of grain boundary roughness,  $\Delta_{\text{rms}} = 0.25$  nm (red line), 1 nm (blue line) and 2 nm (black line). Each point is an average of 50 simulations. A sharp drop in thermal conductivity is observed below  $\langle d \rangle \sim 140$  nm (structure sub-figure and point ‘4’). Inset: Some available experimental results [96, 98, 185, 186, 189] are compared to the  $\Delta_{\text{rms}} = 1$  nm (blue line). Adopted from [58]. 59
- [4.3](#) The thermal conductivity versus porosity ( $\phi$ ) for two geometry cases - ordered case (solid lines) and random case (dashed lines). Three different values for boundary specularity are considered:  $p = 1$ , totally specular boundary scattering (blue lines);  $p = 0.5$  (green lines); and  $p = 0.1$ , almost diffusive boundary scattering (red lines). The inset depicts the percentage reduction in thermal conductivity for the  $p = 0.1$  (red line), random porosity case compared to the ordered case. The geometry structures of the simulated geometries for ordered and random arrangement cases for 5%, 10 % and 15 % porosity are shown on top of the figure. In all cases the domain size is fixed to length  $L_x = 1000$  nm and width  $L_y = 500$  nm. Adopted from [58]. 61
- [4.4](#) The thermal conductivity versus porosity ( $\phi$ ) for ordered pore structures, randomized pore structures, and polydispersed geometries with randomized pore positions and diameters. In the first two cases (red and black solid lines), the diameter is fixed at  $D = 50$  nm. In all cases the specularity for all boundaries is fixed at  $p = 0.1$ . Adopted from [58]. 63
- [4.5](#) Monte Carlo simulations showing the combined effects of grain size and porosity ( $\phi$ ) in both the ordered pores case (solid lines) and random pores case (dashed line) versus grain size  $\langle d \rangle$ . The thermal conductivity at for porosities  $\phi = 0\%$ , 5%, 10% and 15% are shown by the blue, magenta, light-blue, and red lines respectively. The effect of combined nanocrystalline and nanoporous material with random pore positions and sizes is depicted by the red-dashed line. Examples of typical geometries simulated for the case of 5% porosity, for both ordered and random pore arrangements, are shown above the figure. Adopted from [58]. 64
- [4.6](#) Monte Carlo simulation results compared to analytical models. (a) Thermal conductivity versus grain size for commonly employed analytical models for nanocrystalline geometries compared to the Monte Carlo results of this work (blue line). The grain size is varied from an average of  $\langle d \rangle = 1000$  nm down to 50 nm with a roughness  $\Delta_{\text{rms}} = 1$  nm. (b) Thermal conductivity versus porosity for the commonly employed analytical porous material models compared to the Monte Carlo results of this work (blue line). The pore boundary specularity is fixed at  $p = 0.1$ . In both cases the domain top/bottom roughness specularity is set to  $p = 0.1$ . Adopted from [58]. 67
- [4.7](#) Extraction of the variation in distances between pores,  $\delta$ , and variation in porosity,  $\phi$ , in the nanoporous materials examined. Geometries for (a) ordered and (b) randomized (disordered) nanoporous geometries with  $\phi = 10\%$  are shown on top. The distribution of distances between pores, averaged 71

every  $l_s = 100$  nm (depicted by the red-dotted lines), is shown in (c) and (d), respectively. The distribution of pore distances is well defined and constant in the ordered case, but deviates in the randomized pore geometry. The distribution of porosity is shown in (e) and (f), respectively. In this case the distribution can be evaluated with higher resolution along the length of the material. In (e) the porosity averages 10 % in every  $l_s = 100$  nm domain. In (f) the porosity deviates from the 10 % average following an inverse trend compared to the distance between the pores shown in (d). The red shaded portions of the distance profile in (d) and the porosity profile in (f) represent the regions of increased thermal resistance. Adopted from [58].

- [4.8](#) Thermal conductivity versus porosity for the analytical models of randomized pore geometries, compared to the Monte Carlo simulation results of this work (blue line). Pore boundary specularity in Monte Carlo is fixed at  $p = 0.1$ . The model of Tarkhanyan *et al.* [204] as described by Eq. 4.8 is shown by the dashed-purple line. Equation 4.11 (black line) incorporates a deviation  $\Delta\delta$  in the average distance. There is good agreement with Monte Carlo results for porosities beyond  $\phi = 20\%$ . To improve the model, Eq. 4.13 (red line) incorporates a weight on the deviation  $\Delta\delta_w$ , increasing the importance of regions of higher porosity. As a reference, Eq. 4.14 (green line), incorporates a further weighted deviation in porosity  $\Delta\phi_w$ , which, however, slightly underestimates the Monte Carlo simulations. Adopted from [58]. 73
- [4.9](#) Thermal conductivity versus porosity for the analytical models of randomized pore geometries compared to the Monte Carlo simulation results in this work (blue line). Pore boundary specularity in Monte Carlo is fixed at  $p = 0.1$ . The model of Gesele *et al.* [188] as described by Eq. 4.6 is shown by the green-dashed line. Equation 4.15 (black line) incorporates a deviation  $\Delta\phi$  in the average porosity. There is good agreement with the Monte Carlo results for porosities beyond  $\phi = 30\%$ . To improve the model, we incorporate a weight on the porosity  $\Delta\phi_w$  (Eq. 4.16) increasing the importance of regions of higher porosity (red line). Adopted from [58]. 75
- [4.10](#) Comparison between the full Monte Carlo (MC) simulated results in structures with grains and pores (blue bars) and: i) MC simulation results of grains alone and pores alone, but combined through Matthiessen's rule (green bars), ii) results given by the porous material model introduced in Eq. 4.13 ( $\Delta\delta_w$  model) combined with the nanocrystalline model of Eq. 4.4 through Matthiessen's rule (purple bars), and iv) results given by model introduced in Eq. 4.16, ( $\Delta\phi_w$  model) combined with the nanocrystalline model of Eq. 4.4 through Matthiessen's rule (red bars). (a) Ordered pore geometries. For the MC simulations, 50 realizations with grain boundaries of  $\langle d \rangle = 225$  nm are averaged, and pores of a fixed diameter  $D = 50$  nm. (b) Randomized pore geometries. The pore diameters vary from 10 nm to 50 nm. The percentage numbers indicate the variation of each method from the full MC results (blue bars). Porosities  $\phi = 5\%$ , 10 % and 15% are shown. Adopted from [58]. 79
- [5.1](#) Examples of the nanostructured geometries considered at high temperatures. 83  
 (a) Nanocrystalline (NC) materials with changing grain dimension ( $\langle d \rangle$ ). Here  $\langle d \rangle = 100$  nm, black lines represent NC grain edges. (b) Nanocomposite material (NC+NP) with given grain dimension ( $\langle d \rangle$ ) and

porosity ( $\phi$ ). Here  $\phi = 5\%$ , for a random polydispersed pore arrangement, with pore diameter of uniformly distributed between 10 nm - 50 nm and random pore position. (c) Schematic for grain scattering indicating the initial angle of the phonon,  $\theta_{GB}$ , from the normal (dashed line), grain boundaries (black lines), initial path of the phonon (blue line) and probable paths of the phonon after scattering (red-dashed lines and green-dashed transmitted line). Transmission is dependent on grain boundary roughness as well as phonon wavevector  $q$ . Transmission probability is given by Eq. 3.13. (d) Schematic for pore scattering indicating the pore boundary, the initial angle of the phonon  $\theta_{in}$ , and new angle of propagation after reflection,  $\theta_{ref}$ , depending on specular parameter  $p$ . Probable paths of the phonon after scattering for both diffusive (red-dashed lines) and specular (red-solid line) are depicted. Transmission ( $t$ ) through pores is always zero. Adopted from [60].

- [5.2](#) High temperature results for nanocrystalline structures. (a) Effect on  $\kappa$  as temperature increases from 300 K to 900 K, for the pristine case (blue line), nanocrystalline (NC) case with  $\langle d \rangle = 100$  nm (green line) and  $\langle d \rangle = 50$  nm (red line). A sharp reduction in  $\kappa$  of over 75% is observed at 300 K for the  $\langle d \rangle = 100$  nm case (green line). This drops further to more than 85% for temperatures over 800 K. The  $\kappa$  drop is greater in the  $\langle d \rangle = 50$  nm case (red line). A typical geometry for  $\langle d \rangle = 100$  nm case is given as an inset in Fig. (a). (b) The data in (a) normalized by the 300 K  $\kappa$  value of the pristine case (blue line). The effect of phonon boundary scattering is removed from all data after this normalization. (c) The data in (a) normalized by the pristine value (blue line) at every temperature. The effect of phonon-phonon scattering from all data is taken away due to this normalization. Adopted from [60]. 86
- [5.3](#) High temperature results for hierarchical structures. (a) Effect of hierarchical nanostructures on  $\kappa$  as temperature increases from 300 K to 900 K, for the pristine case (blue line), combined nanocrystalline and nanoporous (NC+NP) case with  $\langle d \rangle = 100$  nm (green line) with porosity  $\phi = 5\%$ , and  $\langle d \rangle = 50$  nm (red line) with porosity  $\phi = 5\%$ . A reduction in  $\kappa$  of over 80% is observed at 300 K for the  $\langle d \rangle = 100$  nm case (green line) and more than 90% for temperatures over 800 K. The  $\kappa$  drop is greater in the  $\langle d \rangle = 50$  nm case (red line). A typical geometry for  $\langle d \rangle = 50$  nm with  $\phi = 5\%$  is shown in the inset of Fig. 5.3a. (b) The data in (a) normalized by the 300 K  $\kappa$  value of the pristine case (blue line). The effect of phonon boundary scattering is removed from all data after this normalization. Dashed lines are the data of Fig. 5.2(b) as indicated. (c) The data in (a) normalized by the pristine value (blue line) at every temperature. The effect of phonon-phonon scattering from all data is taken away due to this normalization. Again, the dashed lines are the data of Fig. 5.2(c) for the NC cases of  $\langle d \rangle = 100$  nm (green-dashed line);  $\langle d \rangle = 50$  nm (red-dashed line) alone. The legend of Fig. 5.3b applies one-to-one with the lines of Fig. 5.3c as well. At high temperatures there a further reduction in the normalized ratio observed due to pores. Adopted from [60]. 89
- [5.4](#) Separating effect of  $q$  dependence. (a) The effect of  $q$ -independent and  $q$ -dependent scattering at grain boundaries compared to the pristine case. All values are normalized with respect to their value at 300K. The effect of phonon boundary scattering is removed from all data after this normalization. (b) The data in (a) normalized by the pristine value (blue line) at every temperature. The effect of phonon-phonon scattering from all data is taken 91

away due to this normalization. (c) The data in (b) normalized to the  $q$ -independent NC case at all temperatures. This shows the effect of the  $q$ -dependence of the grain boundary scattering as the temperature increases.

- [6.1](#) Schematic of the basis geometry simulated with porous region of length  $L_1$  and pristine region of length  $L_2$ . Individual properties are assigned for each region, including average phonon mean-free-path, (MFP)  $\lambda$  and average distance between pores (inter-pore distance)  $d$ . The total length of simulation domain is  $L_T$ . In all Monte Carlo simulations, we set  $L_T = 1000$  nm. The coloring indicates the established thermal gradients when the left and right contacts are set to  $T_H = 310$  K (yellow) and  $T_C = 290$  K (green), respectively, with the temperature profile given by blue dots (average of 5 million phonons). The green arrow above the schematic depicts “Forward” direction of heat flow from  $T_H$  to  $T_C$ . 94
- [6.2](#) Monte Carlo simulations showing the effect of porosity ( $\phi$ ) in the rectangular, ordered pores configuration on thermal conductivity,  $\kappa$  (left axis), and rectification,  $R$  (right axis). For each value of  $\phi$ , the  $\kappa$  in the ‘Forward’ direction ( $\kappa_F$ ) is given by the red line, while the  $\kappa$  in the ‘Reverse’ direction ( $\kappa_R$ ) is given by the blue line and the rectification data is given by the purple line. The black line gives the results predicted by the model given by Eqs. 6.1, 6.5-6.6. Examples of typical geometries simulated for 6% and 10% porosity are shown above the figure, as well as our definitions for ‘Forward’ and ‘Reverse’ directions. All pore diameters are 50 nm. Error bars represent standard deviations of results. Adopted from [62]. 96
- [6.3](#) Monte Carlo simulations showing the effect of pore position, inter-pore distance compression and pore staggering on rectification ( $R$  on left axis). Four cases are examined, and the geometries simulated are given in the panel above the figure. These are i) the basis (rectangular) arrangement of pores (‘A’) with pore diameter  $D = 50$  nm; ii) compressed arrangement (‘B’) which has the same configuration as ‘A’, but with halved inter-pore separation; iii) staggered arrangement (‘C’) given by shifting pore positions of ‘A’ by 50 nm in the  $y$ -direction; iv) compressed + staggered arrangement of pores (‘D’) by reducing inter-pore distance to 12.5 nm in (iii). Pores are placed at 200 nm from the domain edge in the first (light-blue,  $x = 200$  nm) cases in all four arrangements ‘A’ – ‘D’. They are left-shifted by 100 nm and placed 100 nm from the domain edge in the second (dark-blue,  $x = 100$  nm) cases in all four arrangements. Adopted from [62]. 100
- [6.4](#) Normalized  $\kappa$  observed in the ‘Forward’ (red bars) and the ‘Reverse’ (blue bars) direction for each structures ‘A’–‘D’ of Fig. 3 (left axis). The rectification is shown by the black line in the right axis. (a) The pores are placed at 200 nm from the domain edge ( $x = 200$  nm). (b) The pores are shifted by 100 nm and placed 100 nm from the domain edge ( $x = 100$  nm). In each graph the  $\kappa$  is normalized to  $\kappa_{\text{PRISTINE}}$ . Adopted from [62]. 102
- [6.5](#) The dependence of thermal rectification on the exposed junction surface area and pore grading. Five cases are examined, and the geometries simulated are given above the bar chart. These are: i) the basis (rectangular) arrangement of pores (‘A’) with pore diameter  $D = 50$  nm; ii) oblique arrangement (‘E’) where pores are arranged in a right-triangular fashion to give increased exposed surface area; iii) staggered arrangement (‘C’); iv) triangular 104



arrangement ('F'); v) graded (triangular) arrangement ('G') of pores by uniformly decreasing pore density in the  $x$  direction. Adopted from [62].

[6.6](#) The rectification dependence on the construction of the triangular regions, and the hierarchical incorporation of smaller nanopores ( $D = 10$  nm) in between the bigger ones ( $D = 50$  nm). Four cases are examined, each for both rectangular geometries (dark-blue bars) and triangular geometries (green bars). The geometries simulated are shown in the panel above the figure. These are: i) the basis arrangement of pores ('A') for both rectangular and triangular configurations given by dark-blue bars or green bars, respectively. For all pores  $D = 50$  nm, and inter pore distance  $d = 50$  nm; ii) hierarchical arrangement ('H') by adding smaller pores in-between 'A'; iii) compressed arrangement ('B') with halved inter-pore separation  $d = 25$  nm; iv) compressed + hierarchical arrangement of pores ('I') by reducing halving the original inter-pore distance. The result for arrangement 'C' from Fig. 3 is also included for comparison. All structures are placed  $x = 100$  nm from the edge of the device. Adopted from [62]. 106

[7.1](#) Nanostructures examined with NEGF wave approach. (a) Schematics of typical geometries studied with length of 100 nm, width 10 nm and thickness 1 nm for two pore diameters of  $D = 2$  nm and  $D = 6$  nm. The neck,  $n$ , is measured, as indicated, as the widest distance between the edge of the pore and the nearest geometry boundary. (b) The NEGF transmission  $vs$  the energy,  $\hbar\omega$ . Transmission for the pristine case ( $T_{P,NEGF}$ ) is given by the black line. Transmission for nanostructured porous cases ( $T_{N,NEGF}$ ) are given for  $D = 1$  nm (purple line),  $D = 2$  nm (blue line),  $D = 3$  nm (dark-green line),  $D = 4$  nm (light-green line),  $D = 5$  nm (orange line),  $D = 6$  nm (red dots), respectively. (c) The typical phonon spectrum for a [100] Si nanowire of 10 nm width and 1 nm thickness. The transmission of the pristine channel (black line in Fig. 7.1b) is essentially a count of the number of modes at each energy of Fig. 1c. (d) The contribution of each phonon state to the total ballistic thermal conductance at room temperature calculated using Eq. 7.8 (without Umklapp scattering). Red and blue colors indicate the largest contribution and the smallest contribution, respectively (colormap). Adopted from [61]. 112

[7.2](#) NEGF fractional transmission  $F_{NEGF}$  versus energy  $\hbar\omega$  given by Eq. 7.11, for  $D = 1$  nm (purple dots),  $D = 2$  nm (blue dots),  $D = 3$  nm (dark-green dots),  $D = 4$  nm (light-green dots),  $D = 5$  nm (orange dots),  $D = 6$  nm (red dots), respectively. Monte Carlo fractional transmission  $F_{MC}$  given by Eq. 7.10, for the same structures. The pore diameters ( $D$ ) and the corresponding neck to diameter ( $n/D$ ) ratios are provided on the right axis. Adopted from [61]. 117

[7.3](#) Monte Carlo fractional transmission  $F_{MC}$  given by Eq. 7.10, for  $D = 1$  nm (purple line),  $D = 2$  nm (blue line),  $D = 3$  nm (dark-green line),  $D = 4$  nm (light-green line),  $D = 5$  nm (orange line),  $D = 6$  nm (red line), respectively, versus neck size,  $n$ . Typical geometries simulated are depicted in the panel above (I – IV). The common  $n/D$  values across structures are indicated by dashed lines. Adopted from [61]. 119

[7.4](#) Percentage variation of the  $F_{NEGF}$  from the  $F_{MC}$  values for  $D = 1$  nm (purple dots),  $D = 2$  nm (blue dots),  $D = 3$  nm (dark-green dots),  $D = 4$  nm (light-green dots),  $D = 5$  nm (orange dots),  $D = 6$  nm (red dots), respectively, versus energy  $\hbar\omega$ . Adopted from [61]. 120

- [7.5](#) Comparing wave and particle approaches. (a) Schematic of effective increase in  $D$  and (b) effective decrease in  $D$ . (c) NEGF fractional transmission for structures with  $n/D = 4.5$ ,  $D = 1$  nm (purple dots), and  $n/D = 0.33$ ,  $D = 6$  nm (red dots), respectively, versus energy  $\hbar\omega$ . MC fractional transmission for the same structures are plotted by the solid lines. The dashed lines represent Monte Carlo ray-tracing for structures with a  $\pm 15\%$  variation on their  $n/D$  ratio. Adopted from [61]. 121
- [7.6](#) NEGF results averaged  $\langle T_{\text{NEGF}} \rangle$  over energy in a part of the spectrum up to 5 meV (purple-dashed line), up to 15 meV (green-dashed line) and for the whole spectrum (red-dashed line) vs  $n/D$ . These limits are depicted in the bottom inset with lines of corresponding colors. Error bars give the standard deviation of  $T_{\text{NEGF}}$  data. MC fractional transmission vs  $n/D$  (blue-solid line) is given for comparison. Schematics of some geometries simulated are depicted at the top left corner. Adopted from [61]. 122
- [7.7](#) NEGF fractional transmission for two-pore structure with pore separation  $l = 0$  nm (black circles),  $l = 5$  nm (blue dots),  $l = 25$  nm (red dots) versus energy. MC fractional transmission for the same structures is shown by the solid lines. Schematic of a typical structure simulated with  $D = 5$  nm is given in the panel above. Adopted from [61]. 124
- [7.8](#) NEGF fractional transmission for two-pore structures with vertical separation  $d = 0$  nm (black dots),  $d = 2$  nm (blue dots),  $d = 3$  nm (red dots) versus energy. MC fractional transmissions for the same structures are shown by the solid lines. A schematic of a typical structure simulated with  $D = 2$  nm is given in the panel above. Adopted from [61]. 125
- [8.1](#) Effect of adding high  $\kappa$  nanoinclusions in low  $\kappa$  matrix. (a) Schematic of a nanoinclusion, with diameter,  $D$ . (b) Schematic of the DMM phonon scattering interaction with a nanoinclusion boundary. (c) NI density vs Normalized  $\kappa_n = \kappa_C/\kappa_M$  for NIs with no DMM (blue line) and with DMM (purple line) for the case of an artificial matrix  $\kappa_M = 0.1 \times \kappa_{\text{Si}}$ , and NIs with  $\kappa_{\text{NI}} = \kappa_{\text{Si}}$ , and  $D = 80$  nm. A typical geometry with configuration ‘C’ of NI density is seen as inset, with  $D = 80$  nm (purple NIs). 130
- [8.2](#) NI density vs Normalized  $\kappa_n = \kappa_C/\kappa_M$  for the case of an artificial matrix  $\kappa_M = 0.1 \times \kappa_{\text{Si}}$ , and NIs with  $\kappa_{\text{NI}} = \kappa_{\text{Si}}$ .  $\kappa_n$  for  $D = 30$  nm (red line),  $D = 44$  nm (orange line),  $D = 60$  nm (green line),  $D = 72$  nm (light-blue line) and  $D = 80$  nm (purple line) are given for the DMM case. Typical geometries simulated are seen in the geometry panel above for  $D = 30$  nm (red NIs),  $D = 60$  nm (green NIs),  $D = 80$  nm (purple NIs) cases, respectively. 131
- [8.3](#) NI Area vs NI Boundary length for the case of an artificial matrix  $\kappa_M = 0.1 \times \kappa_{\text{Si}}$ , and NIs with  $\kappa_{\text{NI}} = \kappa_{\text{Si}}$  are given for all NI diameters and configurations. Typical geometries simulated with configurations A - C are seen in the geometry panel above for  $D = 60$  nm (green NIs). Inset gives the value of  $A/b$  ratio for the peak value of  $\kappa$  observed as diameter changes. 133
- [8.4](#) NI density vs Normalized  $\kappa_n = \kappa_C/\kappa_M$  for the case of an artificial matrix  $\kappa_M = 0.1 \times \kappa_{\text{Si}}$ , and NIs with  $\kappa_{\text{NI}} = 0.5 \times \kappa_{\text{Si}}$  are given for the MC with no DMM (blue line) and MC with DMM (red line) cases. Real-world experimental results from the literature are given for similar  $\kappa_{\text{NI}}/\kappa_M$  ratios.  $\kappa_n$  is normalized to real world  $\kappa_M$  in each case, respectively. 134

## Acknowledgements

It would be impossible to express, in words, the depths of my appreciation for those who made all this possible. Here is my paltry attempt to do the same. To begin with, I would like to thank my supervisor Dr. Neophytos Neophytou. From our very first correspondence and the first time we spoke, you have been a constant source of steadfast support. Thank you for the opportunity, to study under your able tutelage, and to help me teach others, under your guidance. I have truly learnt a lot from the breadth of your knowledge and the scope of your insight, not only of academics, but also of life. I am grateful for your faith in me and for the endless encouragement to present my work at diverse public forums, both locally and internationally. I will forever cherish our interactions moving up to, during, and after these events.

My thanks go out to Dr. Teyeb Ould Ely at UCSB for his sustained support, and to all my friends at Nazarbayev for your help in the cold, sub-zero, dark days. My gratitude to all those I have worked with, learnt from and who have helped me stand - Dr. Jacob Cherian, Dr. Richa Krishna, Dr. Sourav Chattopadhyay, Dr. Jagriti Narang and most of all to Dr. O.P Sinha for your direction and the learning experiences.

I will be eternally grateful to Dr. Joyita Deb for her kind, correct and timely advice, Dr. Chaitali Singhal for her incredible work ethic, Dr. Hossein Karamitaheri for his able assistance and to Dr. William Sidhu and his family for their invaluable aid and constant support in this Covid pandemic. I am much obliged to Dr. Marina Cole, Dr. David Lacroix, and Dr. Peter Brommer for their kind comments after the viva.

My sincere thanks to professors, peers, friends, colleagues and collaborators at the University of Warwick, the University of Cambridge and the University of Exeter for your help and support. My best wishes to my students - you taught me more than you know. I would like to especially thank those in our department at Warwick and particularly members of my group for sound, sage advice. Thanks to Damiano Archetti, Sam Foster, Patrizio Graziosi, Chathu Kumarasinghe, Laura de Sousa Oliveira, and Vassilios Vargiamidis, for great insight and useful discussions.

Most of all, I am indebted to my family - without whom none of this would be.

Dhritiman Chakraborty



## Declaration

This thesis is submitted to the University of Warwick, Coventry, UK in support of my application for the degree of Doctor of Philosophy. No part of this thesis has been submitted for a research degree at any other institution.

This thesis represents my own work, carried out under the supervision of Dr. Neophytos Neophytou, Professor at the University of Warwick, except where references to other works are given. The work in Chapter 7 was carried out in collaboration with Dr. Hossein Karamitaheri, and this has been noted in the chapter.

The work presented in this thesis has been published in the following peer-reviewed journal articles:

- D. Chakraborty, S. Foster, and N. Neophytou, Monte Carlo phonon transport simulations in hierarchically disordered silicon nanostructures, *Physical Review B* **98**, 115435 (2018). [Chapter 3 and Chapter 4]
- D. Chakraborty, S. Foster, and N. Neophytou. Monte Carlo simulations for phonon transport in silicon nanomaterials. *Materials Today: Proceedings* **8**, 652 (2019). [Chapter 3]
- D. Chakraborty, L. de Sousa Oliveira, and N. Neophytou. Enhanced Phonon Boundary Scattering at High Temperatures in Hierarchically Disordered Nanostructures. *Journal of Electronic Materials* **48**, 4, 1909-1916, (2019). [Chapter 5]
- D. Chakraborty, J. Brooke, N. C. S. Hulse and N. Neophytou. Thermal rectification optimization in nanoporous Si using Monte Carlo simulations. *Journal of Applied Physics* **126**, 184303 (2019). [Chapter 6]
- D. Chakraborty, H. Karamitaheri, L. de Sousa Oliveira, and N. Neophytou. Effect of wave versus particle phonon nature in thermal transport through nanostructures. *Computational Materials Science* **180**, 109712 (2020). [Chapter 7]
- D. Chakraborty and N. Neophytou. Effects of boundary interfaces on dissimilar materials *in process* (2020). [Chapter 8]

A complete list of all contributions to publications and presentations associated with this thesis is enclosed in the Appendix.

## Abstract

Nanostructuring is considered a very promising direction for high performance thermoelectric materials, which can convert waste heat into useful energy. These materials can reduce dependence on fossil fuels and enhance thermal energy harvesting, with huge environmental and societal benefits. In this work we investigate thermal transport in nanostructures and study methods to reduce the thermal conductivity (which enhances thermoelectric efficiency). Using silicon as an example, we consider the combined presence of nanocrystallinity and nanopores, arranged under both ordered and disordered (randomized) positions and sizes by using a phonon transport simulator constructed as a part of this work. We show that nanocrystalline boundaries degrade the thermal conductivity more drastically when the average grain size becomes smaller than the material average phonon mean-free-path. Introduction of pores in a hierarchical fashion degrades the thermal conductivity even further. Its effect, however, is significantly more severe when the pore sizes and positions are randomized, as randomization results in regions of higher porosity along the phonon transport direction, which introduce significant thermal resistance. We show that this randomization, or disorder, acts as a large increase in the overall *effective* porosity.

Using our simulations, we show that existing compact nanocrystalline and nanoporous theoretical models describe thermal conductivity accurately under uniform nanostructured conditions but overestimate it in disordered geometries. We propose extensions to these models that accurately predict the thermal conductivity of disordered nanoporous materials based solely on a few geometrical features. Additionally, we show that the new compact models introduced can be used within Matthiessen's rule to combine scattering from different geometrical features within  $\sim 10\%$  accuracy. Looking at high temperature regimes, we show that the relative reduction in thermal conductivity is stronger at high temperatures in the presence of nanocrystallinity, a consequence of the wavevector-dependent nature of phonon scattering on the nanocrystalline grain domain boundaries.

We next consider asymmetric nanoporous structures, and investigate the combined effects of porosity, inter-pore distance, and pore position on thermal rectification in nanoporous silicon. We define thermal rectification in terms of system mean-free-paths rather than non-linearity in temperature – as conventionally done. We show that systems: i) with denser, compressed pore arrangements (i.e. with smaller inter-pore distances), ii) with pores positioned closer to the device edge/contact, and iii) with pores in a triangular arrangement, can achieve rectification of over 55%. Introducing hierarchically smaller pores into existing porous geometries increases rectification even further. Importantly, for the structures we simulate, we show that sharp rectifying junctions, separating regions of long from short phonon mean-free-paths are more beneficial than spreading the asymmetry throughout the material along the heat direction in a graded fashion.

Lastly, comparing a full wave-based quantum mechanical Non-Equilibrium Green's Function (NEGF) method, and a particle-based classical ray-tracing approach, we investigate the qualitative differences in the wave and particle-based phonon transport at the vicinity of nanoscale features, indicating when simplified particle based approaches fail, and when not. Insight extracted from this work can be used to provide better and more complete understanding of phonon transport in nanomaterials.

## Abbreviations

AFM	Atomic Force Microscopy
BTE	Boltzmann Transport Equation
DOS	Density Of States
HT	High Temperature ( $> 300$ K)
KPM	Kelvin Probe Microscopy
LA	Longitudinal Acoustic
LO	Longitudinal Optical
MC	Monte Carlo
MD	Molecular Dynamics
MFP	Mean-Free-Path (of phonons, unless stated otherwise)
NC	Nanocrystalline (structures)
NEGF	Non-Equilibrium Green's Function
NP	Nanoporous (structures)
NI	Nanoinclusion (structures)
PF	Power Factor
SEM	Scanning Electron Microscopy
SL	Superlattice (structures)
TA	Transverse Acoustic
TE	Thermoelectric
TO	Transverse Optical

# 1. Introduction

## 1.1 Background

In the currently prevailing context of global warming and dwindling conventional non-renewable energy resources, there is an increased interest in environmentally friendly and renewable energy resources, including ambient heat. An incredibly large amount of heat is available everywhere, either naturally in the environment (e.g. solar or geothermal), or when we burn fossil fuels to generate energy. Around two thirds of all the energy is lost in the process as waste heat [1-5] (as seen in Fig. 1.1 below). Sources put this wasted heat at anywhere between 13 to 15 TWh [5, 6]. Thermoelectric materials can convert this waste heat directly into useful electrical energy, which can vastly contribute to energy sustainability, fighting against energy scarcity and global warming. In addition, heat available in small amounts from our bodies and the surrounding environment can be used to operate smart devices and power the Internet of Things (IoT). Conversely, thermoelectric materials can also be used to convert electricity to heat for localized heating or cooling applications. Hence, understanding thermal transport overall is vital for improvements in energy harvesting, reducing global warming, battery-less operation of smart devices and enhanced heat management systems for novel advanced applications.

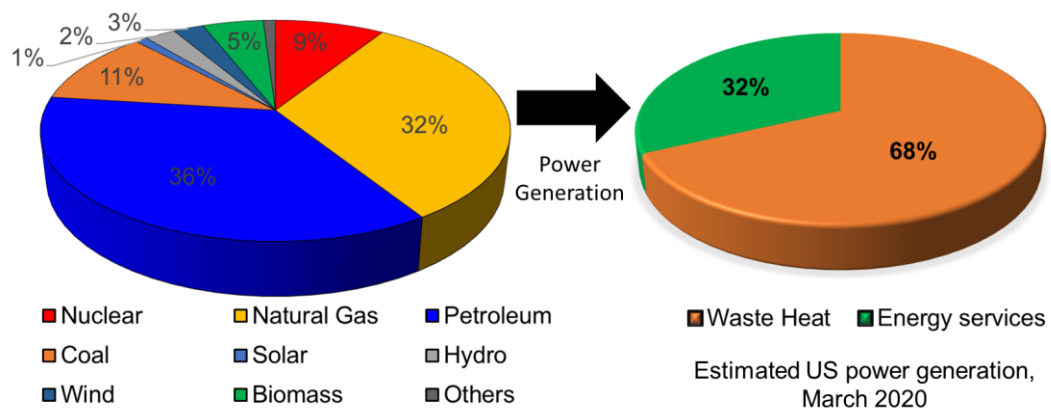


**Figure 1.1:** Rejected energy as waste heat during primary power generation processes. Pie charts created based on estimated US energy consumption from primary sources of energy in all sectors including industrial, residential and transport sectors. Recreated based on updated data released in March 2020 [3].

Clear understanding of thermal transport improves the design of thermoelectric (TE) materials and devices. Novel applications include flexible, foldable TE materials, TE generators, wearable devices, thermal rectifiers, thermal management systems (for both accurate heating and cooling) and TE materials that can be used as paint to recoup energy from irregular surfaces in the environment [7-9]. Miniaturization, coupled with faster processing speeds, results in a very large quantity of heat being generated per unit volume in integrated circuits (i.e. VLSI devices) [10]. Research shows that ‘on-chip power density’ has already exceeded that of a nuclear reactor at  $100 \text{ W/cm}^2$  [11]. Unmitigated localized overheating can lead to extensive damage, as seen in batteries [12, 13], battery powered vehicles, [14] and other devices like smartphones or laptops, catching fire or even exploding [15]. Thermal management and thermoelectric cooling are thus TE device applications actively being researched for targeted cooling of local hotspots inside integrated circuits. With no inherently moving parts they are easy to miniaturize and integrate on chip [10, 16] using nanostructuring. Novel materials are also being examined for applications in thermal rectification, thermal cloaking, phonon waveguides, phonovoltaics and organic TEs.

Still, energy harvesting and thermal management remain the primary applications of TE materials, potentially able to promote energy sustainability and the reduction in the use of fossil fuels, with huge environmental and societal benefits. Unfortunately, conventional bulk TE materials – such as tellurides of antimony, of bismuth and of lead [17] (e.g.  $\text{Sb}_2\text{Te}_3$ ,  $\text{Bi}_2\text{Te}_3$ , and  $\text{PbTe}$  [9]) were unable to match the requirements in the commercial space – mainly due to poor material efficiencies. Primarily discovered in the mid-20<sup>th</sup> century, the conversion efficiency of these bulk materials did not exceed 5% [9, 18, 19]. Thus, research slowed, and their applications have largely been restricted to niche applications like nuclear batteries [20], space exploration (e.g. the Curiosity Rover) and some forays into pacemakers – which were abandoned in the 1980s [9, 21]. In recent years, technology and materials have been rapidly moving towards miniaturization and added functionality. At the forefront of this evolution in technology and complete overhaul in processing power is nanotechnology – the study of materials and processes that exist at a billionth of a meter, leading to vast improvements in materials, sensors and devices across fields [12, 13, 22-27]. Recent studies in nanostructuring and the introduction of nanostructured TE materials have improved efficiencies manifold.

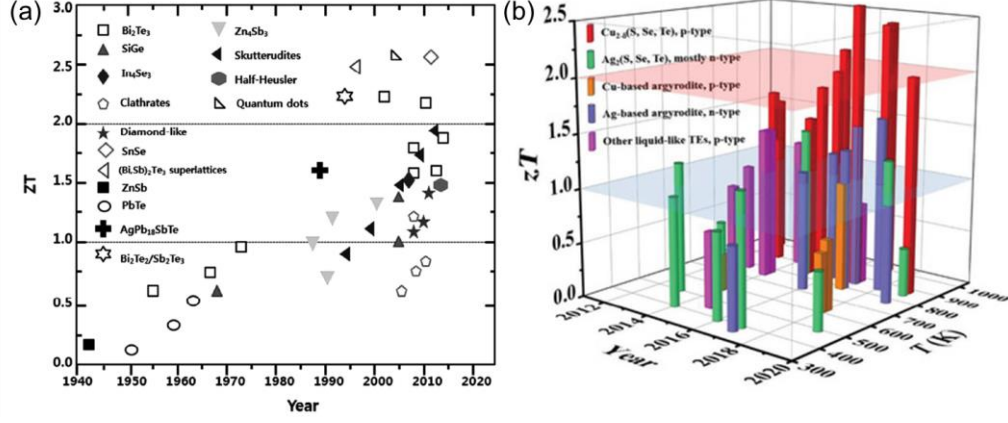


**Figure 1.2:** Thermoelectric efficiency of TE materials, including some recent nanomaterials. (a)  $ZT$  measurements for thermoelectric materials from 1940 [19]. (b) Recent novel thermoelectric materials and their active working temperatures [29].

The efficiency of a thermoelectric material can be determined by its dimensionless thermoelectric figure of merit,  $ZT$ , given as follows:

$$ZT = \frac{\sigma S^2}{\kappa} T \quad (1.1)$$

where  $\sigma$  is the electrical conductivity,  $\kappa$  is the thermal conductivity,  $S$  is the Seebeck coefficient and  $T$  is the temperature. The numerator  $\sigma S^2$  is also collectively known as the power factor,  $PF$ . The mid-20<sup>th</sup> century gave us TE materials such as Lead Telluride (PbTe) and Zinc Antimonide (ZnSb) with  $ZT$  values below 0.5 (see Fig. 1.2a). A  $ZT = 3$  or above is desirable to be competitive (efficiency wise) with conventional sources of energy (which operate at 40% Carnot efficiencies), as seen in Fig. 1.3. (A detailed comparison of efficiency of TE power generation and that of other methods is given in Fig. A1 in **Appendix A**.) As can be seen from the Fig. 1.2 and Fig. 1.3 bulk  $ZT$  values for these thermoelectric materials are much lower than what is required, and thus research stalled. In the later part of the 20<sup>th</sup> century and thereafter, it was shown that nanostructuring can dramatically reduce the  $\kappa$ , or increase the  $PF$  to enhance efficiencies. For nanostructured TEs,  $ZT$ s over 2 in multiple instances, [9, 29] and even up to 5 in one instance [30] have been reported. To properly harness and apply these materials it is necessary to understand heat and heat transport at nanoscale. Thus, this Thesis focuses on methods to reduce the thermal conductivity ( $\kappa$ ) using nanostructuring to improve the efficiency of thermoelectric materials.

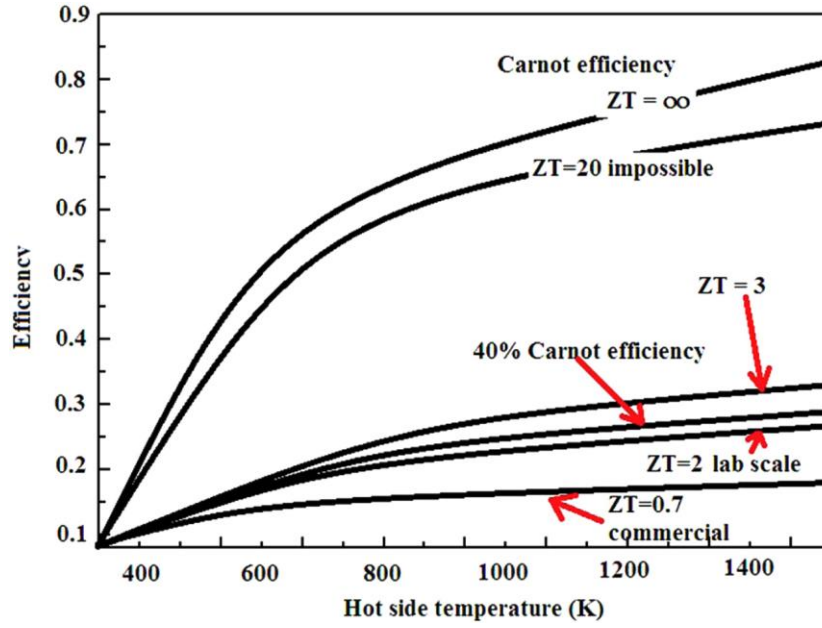


**Figure 1.3:** Carnot efficiencies vs ZT measurements.  $ZT = 2$  was the minimum target to approach the 40% Carnot efficiency [19]. Cold junction is kept at room temperature (300 K).

Phonons are fundamental to the understanding of heat transport at nanoscale. Much like photons for electromagnetic energy, phonons are the fundamental *quasi*-particles for thermal energy. They have characteristic frequencies ( $\omega$ ), wavevectors ( $q$ ) and wavelengths ( $\lambda$ ), which determine the amount of thermal energy (heat) they carry. A phonon can be considered the physical particle representing mechanical vibration, [31] (analogous to the photon representing EM vibration). They are responsible for the transmission of everyday sound and heat. Importantly, phonons dictate the transport of heat and the change of temperature at nanometric length scales. In nanostructures with feature sizes that could vary from a few to up to hundreds of nanometers, heat and phonon transport behaviour is distinctly different than in bulk materials. Phonons carry heat through these materials and interact with other phonons, boundaries, pores, inclusions or other nanostructures (as shown in Fig. 1.4 below) which causes them to scatter and the heat flow is interrupted. As a result, materials with ultra-low thermal conductivities and enhanced thermoelectric performance can be realised.

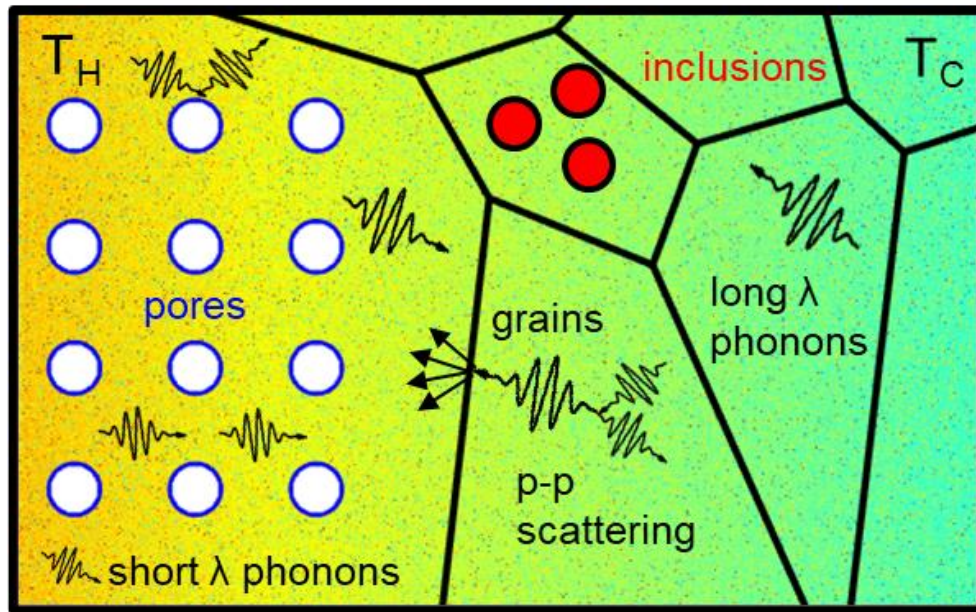


**Figure 1.4:** Schematic of hierarchically nanostructured material with pores (blue bordered circles), inclusions (red filled circles) and nanocrystalline grain boundaries (black lines). The temperature gradient from hot ( $T_H$ ) to cold ( $T_C$ ) sides is indicated by gradient coloring (orange to green, respectively). Phonons at higher temperatures have shorter wavelengths,  $\lambda$  (or higher frequencies,  $\omega$ ) [32]. Phonons with different wavelengths and mean-free-paths are scattered across length-scales in hierarchical nanostructures drastically reducing thermal conductivity [32-34].

Some of the lower thermal conductivities in nanostructured materials have been achieved in materials that include hierarchical nanostructuring [5, 33]. These are materials incorporating multiple types of nanostructures, where boundaries or defects are introduced at the atomic size, the nanoscale, and mesoscale (as shown in Fig. 1.5 below). Hence hierarchical materials scatter phonons of various wavelengths and reduce phonon transport throughout the phonon spectrum [5, 32-34] (as shown in Fig. 1.4 above and Fig. 1.5 below).

The choice of material when developing hierarchical nanocomposites is extremely important. Recent studies show that nanostructured compounds based on Bi, Te and Sb provide some of the most optimal thermoelectric nanomaterials at room temperature [5, 35-38], as in their bulk form. However, expensive raw material, poor processability, high processing cost and heavy metal pollution potentially limits their wide-scale application [38, 39].



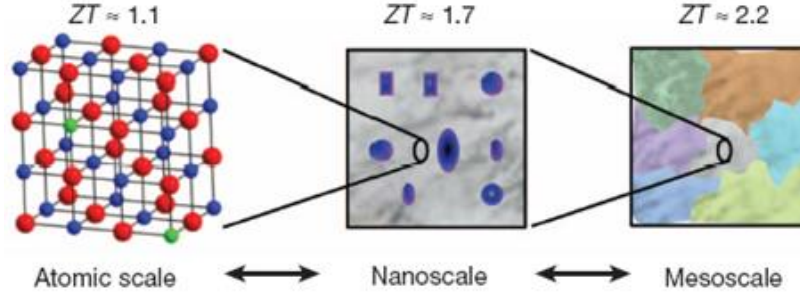


**Figure 1.5:** Hierarchically nanostructured material with hierarchical inclusions at the atomic scale, the nanoscale, and the mesoscale in the PbTe–SrTe system [5]. Phonons scattered across length-scales can enhance ZT [5, 32, 40].

On the other hand, structures based on silicon or SiGe [33, 41-45] are comparatively non-toxic [44] and have easy bulk availability. The industrial infrastructure behind silicon makes their cost of manufacturing much cheaper as compared to other thermoelectric materials. Unfortunately, while silicon has favourable  $PF$  properties, the thermal conductivity of silicon is quite high (at  $\kappa \sim 150 \text{ Wm}^{-1} \text{ K}^{-1}$ ) when compared to other TE materials like  $\text{Bi}_2\text{Te}_3$  ( $\kappa \sim 2 \text{ Wm}^{-1} \text{ K}^{-1}$ ),  $\text{Bi}_2\text{Se}_3$  ( $\sim 1.3 \text{ Wm}^{-1} \text{ K}^{-1}$ ), and so on [38, 46, 47]. The use of nanostructuring can help greatly reduce the thermal conductivity. Specifically, for Si-based materials, silicon nanowires have been reported to exhibit  $\kappa < 2 \text{ Wm}^{-1} \text{ K}^{-1}$ . Similar observations have been reported for SiGe nanowires [48] and silicon thin films of 2 nm to 6 nm in thickness [49, 50]. By introducing grain boundaries (see Fig. 1.4) thermal conductivity in nanostructured silicon can be reduced down to  $0.787 \pm 0.12 \text{ Wm}^{-1} \text{ K}^{-1}$  [51, 52].

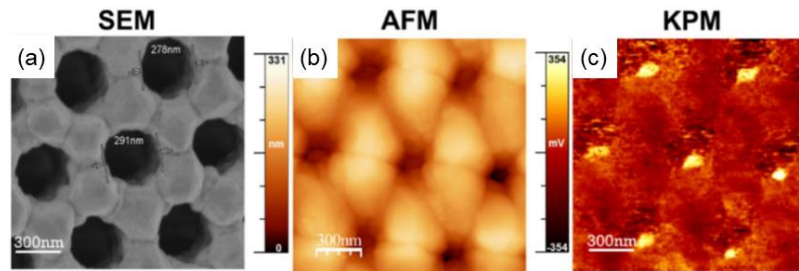


**Figure 1.6:** Nanostructured Si-based material with porous nanomesh thin film. (a) SEM image with nanometric pore sizes indicated. (b) AFM image of the same material gives its topography. (c) KPM image gives the surface potential for the same material. Uniform contrast indicates homogeneity in the surface potential of the film [33]. This experimental result is given by Taborda *et al.* in their work [33].

In novel single-crystalline silicon membranes with nanometric sized pores  $\kappa$  around  $1\text{-}2\text{ Wm}^{-1}\text{ K}^{-1}$  [41, 43, 53], has been reproducibly achieved, while still maintaining sufficient electronic properties. A recent work with hierarchical nanostructuring reported ultra-low  $\kappa$  of  $0.55 \pm 0.10\text{ Wm}^{-1}\text{ K}^{-1}$  for SiGe nanocrystalline nanoporous structures, a value well below that of amorphous silicon structures [33] (see Fig. 1.6 above). Reports also show that hierarchical nanostructures can improve the thermoelectric power factor as well [45, 54-57]. Hence in this work we focus on silicon-based nanomaterials.

Thus, a clear understanding of thermal transport at nanoscale is of paramount importance for energy harvesting, thermal safety management and continued development of novel, miniaturized devices. Various computational methods, such as the wave-based Non-Equilibrium Greens Functions or the particle-based Monte Carlo methods, have been used to study phonon transport and heating management in devices at these length scales. The Monte Carlo method has the added comparative advantage of being able to simulate large-scale geometries (up to several micrometers in size), while still incorporating multiple phonon scattering mechanisms and complex, hierarchical nanostructures. In this work, we describe the development, validation and employment of a Monte Carlo phonon transport simulator to investigate thermal transport in nanostructured materials.

## 1.2 Motivation

As we have discussed in the last section, understanding thermal transport at the nanoscale is of vital importance for sustainable energy harvesting, mitigation of waste heat and the development of improved thermoelectric devices. These materials can reduce dependence on fossil fuels, with huge environmental and societal benefits. An in-depth study of phonons and phonon transport is fundamental to the understanding of thermal transport at nanoscale.

Primarily, we focus on phonon transport in hierarchically nanostructured silicon. Silicon is a well understood, established material. It is comparatively non-toxic, cost effective and with established industry for mass scale device production. However, silicon's comparatively high bulk thermal conductivity ( $\kappa$ ) makes it an

inefficient thermoelectric (TE) material in the bulk form (see Eq. 1.1). Hierarchical nanostructuring (including nanocrystalline and nanoporous structures) drastically reduces  $\kappa$  in TE materials and enhances TE efficiency by scattering across the phonon spectrum (see Fig. 1.4 and Fig. 1.5). We investigate the effects of different types of nanostructuring – individually and combined at different temperature regimes to provide a thorough study of phonon transport for these materials [58-60]. We describe the development and validation of a Monte Carlo phonon transport simulator to model thermal transport (particularly thermal conductivity) in nanostructures [58, 59].

The Monte Carlo (MC) method is a semi-classical particle-based approach, capable of incorporating multiple phonon scattering mechanisms. MC was chosen as it can incorporate complex large-scale geometries at appropriate length scales to understand phonon transport in hierarchical silicon structures. The advantage of MC is that it can be used to simulate complex, hierarchical geometries with channels up to several micrometers in size (scaling linearly with size). Our simulator is validated for both bulk and nanostructured Si-based materials [58, 59]. However, comprehensive understanding of thermal transport in even smaller structures need large scale simulations bridging length scales dictated by different physics related to the wave versus particle nature of phonons. Yet, available computational approaches implicitly treat phonons as either just waves or as particles. Here, we also seek to bridge this gap. Using a full wave-based NEGF method, and a particle-based ray-tracing MC approach, we investigate the qualitative differences in the wave-based and particle-based phonon transport at the vicinity of nanoscale features [61].

Novel applications in heat management and thermoelectric materials have also been explored and thermal rectification is one exciting application in this context. With analogies to electrical diodes and transistors, operational, durable and efficient thermal rectifiers have the capacity to open new chapters in future semiconductor physics. We investigate the thermal rectification in geometrically asymmetric nanoporous silicon structures to give optimized thermal rectifiers [62].

### 1.3 Thesis outline

This PhD thesis investigates phonon transport in nanostructures including hierarchical and highly disordered Si-based nanomaterials. Overall, this project has led to several publications in high impact journals (5 journal publications, including in *Physical Review B*, *Journal of Applied Physics* and one more under preparation, see detailed list in **Appendix B**). The research and the results have been presented at many national and international conferences (over 10 presentations, including the Eurotherm, the International Conference on Thermoelectrics and the European Conference on Thermoelectrics, as listed in **Appendix B**), which have garnered various awards. This work has also contributed to many public engagement activities (including the British Science Festival and the Cheltenham Science Festival). The complete details of these are enclosed as **Appendix B**.

An outline of the thesis is as follows:

**Chapter 2** starts with an overview of phonon theory and thermoelectric theory, with particular emphasis on properties used to understand phonon transport in silicon-based nanomaterials. This chapter heavily draws from the established literature on phonons [34, 63, 64].

**Chapter 3** investigates phonon transport theory and some methods that are used to simulate thermal properties in nanomaterials. We then outline the single-particle ‘incident-flux’ Monte Carlo method and the simulator specifically developed during this PhD to determine thermal transport through nanostructures. We present our initial corroboration to bulk silicon material and validation at nanoscale feature sizes by comparing simulator results to those in the established literature. The results presented in this chapter have been published in *Physical Review B* and *Materials Today: Proceedings* [58, 59].

In **Chapter 4** the MC simulator is used to investigate thermal transport in hierarchically nanostructured silicon. We consider the combined presence of nanocrystallinity and nanopores, arranged under both ordered and and disorderd (randomized) positions and sizes at room temperature. We show that randomization or disorder acts as a large increase in the overall effective porosity. Using our simulations, we show that existing compact nanocrystalline and nanoporous

theoretical models describe thermal conductivity accurately under uniform nanostructured conditions but overestimate it in randomized geometries. We propose extensions to these models that accurately predict the thermal conductivity of randomized nanoporous materials based solely on a few geometrical features. Additionally, we show that the new compact models introduced can be used within Matthiessen’s rule to combine scattering from different geometrical features within ~10% accuracy. The results in this chapter have been published in *Physical Review B* [58, 59].

In **Chapter 5** we extend the work presented in **Chapter 4** to investigate thermal properties at higher temperatures – we investigate phonon transport in silicon-based disordered hierarchically nanostructured materials in the presence of nanocrystallinity and nanopores at the range of 300 K – 900 K. We show that at high temperatures phonon wavelength and spatial frequency dependent surface scattering could account for even a ~40% enhanced reduction in the thermal conductivity of nanocrystalline Si. Introduction of nanopores with randomized positions magnifies this effect, which suggests that hierarchical nanostructuring is actually more effective at high temperatures than previously thought. The results presented in this chapter have been published in the *Journal of Electronic Materials* [60].

**Chapter 6** explores thermal rectification in geometrically asymmetric nanoporous structures, and investigates the combined effects of porosity, inter-pore distance, and pore position relative to the device boundaries. We show that systems: i) with denser, compressed pore arrangements (i.e. with smaller inter-pore distances), ii) with pores positioned closer to the device edge/contact, and iii) with pores in a triangular arrangement, can achieve rectification of over 55%. Introducing hierarchically smaller pores into existing porous geometries increases rectification even further to over 60%. Importantly, for the structures we simulate, we show that sharp rectifying junctions, separating regions of long from short phonon mean-free-paths are more beneficial than spreading the asymmetry throughout the material along the heat direction in a graded fashion. The results presented in this chapter have been published in the *Journal of Applied Physics* [62].

**Chapter 7** compares particle and wave effects in phonon transport in simple systems. In this chapter, using a full wave-based Non-Equilibrium Green's Function

(NEGF) method, and a particle-based ray-tracing Monte Carlo (MC) approach, we investigate the qualitative differences in the wave and the particle-based phonon transport at the vicinity of nanoscale features. Using the simple example of a nanoporous geometry, we show that phonon transmission agrees very well for both methods with an error margin of  $\pm 15\%$ , across phonon wavelengths even for features with sizes down to 3-4 nm. For cases where phonons need to squeeze in smaller regions to propagate, we find that MC underestimates the transmission of long wavelength phonons whereas wave treatment within NEGF indicates that those long wavelength phonons can propagate more easily. We also find that particle-based simulation methods are somewhat more sensitive to structural variations compared to the wave-based NEGF method. The insight extracted from comparing wave and particle methods can be used to provide a better and more complete understanding of phonon transport in nanomaterials. The results presented in this chapter have been published in *Computational Materials Science* [61].

In **Chapter 8** we investigate the influence of adding high thermal conductivity nanoinclusions to thermally resistive media. A way to increase the thermal (or electrical) conductivity of resistive matrix media is to incorporate highly conductive nanoinclusions. This is particularly important in organic electronics and thermoelectrics, where a flexible matrix can prove useful for numerous applications such as wearable electronics and thermoelectric devices. But the power factor of the matrix needs to be improved by incorporating highly electrically conductive nanoinclusions. These, however, inevitably conduct heat more easily as well. In this work we attempt to shed light on thermal transport in a low thermal conductivity medium in the presence of a network of nanoinclusions of higher thermal conductivity. The results presented in this chapter are in preparation for publication.

Finally, in **Chapter 9** we summarize our conclusions and present some possibilities for future work.

## 2. Phonon theory

This chapter presents the theory pertaining to phonons and their properties, including material specific properties for silicon, and the physics of intrinsic phonon-phonon scattering. The role of phonons and thermal conductivity in the thermoelectric efficiency of materials is described. Lastly, improvements in thermoelectric efficiency, achieved by nanostructuring bulk materials, are examined. This chapter draws heavily from the established literature on phonons [34, 63, 64].

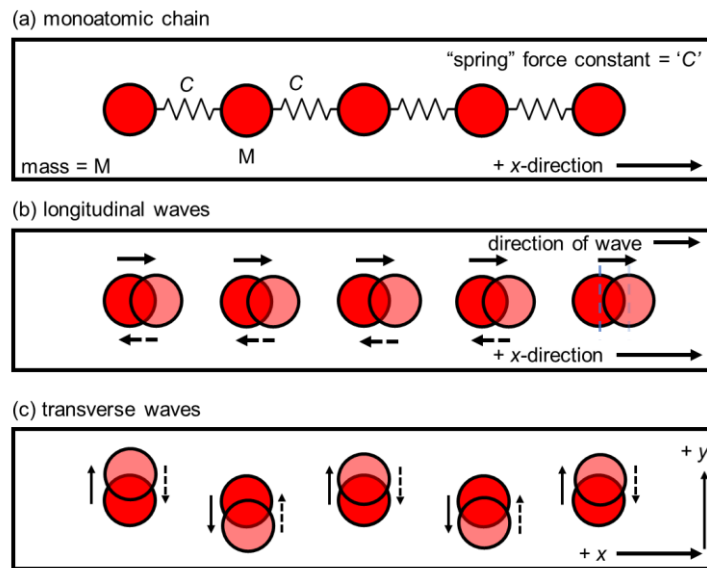
### 2.1 Phonons and their properties

The crystal lattice can be visualized as a three-dimensional, periodic array of identical building blocks or primitive cells. The equilibrium positions of each atom in a solid is defined by the nature of the interatomic forces that bind the atoms. The displacement of atoms from their equilibrium positions creates vibrational waves that propagate through the crystal lattice. The energy of the wave propagating through the lattice is quantized and each quantum is called a phonon – (somewhat) analogously to the photon of the electromagnetic wave. Summarily, the phonon is a *quasi*-particle representing the mechanical vibration. A phonon can, thus, also be interpreted and studied as a mechanical wave of the lattice, with the same energy and momentum as the equivalent *quasi*-particle. These atomic oscillations (phonons) are responsible for the transmission of sound and heat. Understanding and controlling the phononic properties of materials provides opportunities to reduce environmental noise, transform waste heat into electricity (thermoelectricity), power IoT, develop novel device applications and even earthquake protection mechanisms [9, 31, 65].

Phonons can be treated as both particles and waves [63, 65]. Every phonon has different wave-properties that describe it – its frequency [Hz], wavelength,  $\lambda$  [m], time period [s], wavenumber  $q$  (the spatial frequency of the wave,  $2\pi/\lambda$ ) and so on. Phonon propagation direction and magnitude is described by their wavevectors ( $\mathbf{q}$ ). To describe a phonon, we must understand the relationship between these properties. The derivations of these relationships are extensively covered in various works [63, 64, 66]. We re-derive the pertinent parts below for a more complete understanding of phonon properties. If we assume the lattice vibrations to be perfectly elastic [63], each of the individual atoms in the lattice primitive cell can be modeled as a point-mass

where the bonding potential between the atoms is represented by springs, say with a force constant ‘ $C$ ’ with units of N/m. This force constant  $C$  depends on the distance of separation between the masses (say  $u$  [m]) and is responsible for keeping the masses at their equilibrium positions, i.e.  $F \sim Cu$ . Displacement of these masses (atoms) from their equilibrium positions creates the vibrational waves that propagate through the crystal lattice – phonons. For a given phonon, the phonon frequency (number of oscillations per unit time) is given by  $\omega$ . The energy of the phonon is therefore  $E_{\text{phonon}} = \hbar\omega$ , where  $\hbar$  is the reduced Planck's constant.

For a simple description of phonon vibrations let us first assume a one-dimensional picture, say a linear chain of masses (monoatomic chain) where waves travel along the  $x$ -axis (see Fig. 2.1a). Individual atoms are allowed a range of motion determined by the force constant  $C$  that acts as a ‘spring’ moving the atoms back to their equilibrium position. Atoms can move either along the direction of propagation of the wave (longitudinal wave), here defined along the  $x$ -axis (see Fig. 2.1b), or perpendicular to it (transverse wave), here defined in the  $y$ -direction (see Fig. 2.1c). In longitudinal waves, atoms vibrate along the  $x$ -axis when the wave reaches them, but the chain of atoms remains straight with no perpendicular motion. In transverse waves the atoms remain in their equilibrium positions in the  $x$ -axis and move in the  $y$ -direction, perpendicular to the direction of phonon propagation. These two modes of vibration represent the longitudinal and transverse phonon waves modes seen here in the schematics below (Fig. 2.1).





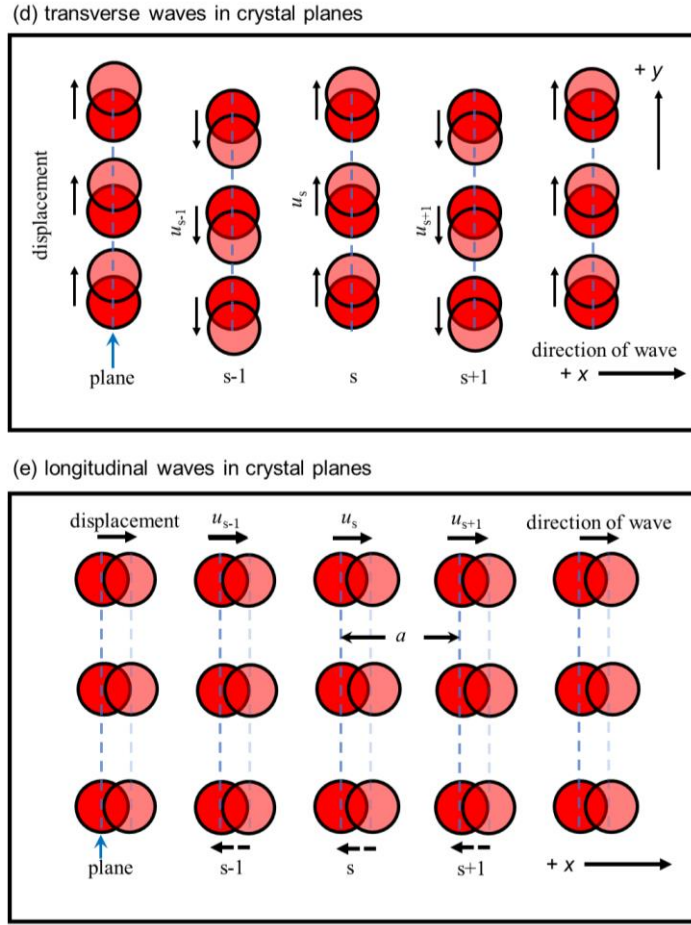


**Figure 2.1.** Longitudinal and transverse waves in crystals. (a) Schematic of a monoatomic chain with point masses of mass =  $M$  representing atoms in the chain and “springs” with force constant ‘ $C$ ’ representing the bonding potential between atoms. (b) Longitudinal wave in monoatomic chain with atoms moving in the direction of wave propagation (black-solid arrows). Each atom (solid red circle) is displaced in the positive  $x$ -direction (transparent red circle). (c) Transverse wave with atoms moving from their equilibrium positions (solid red circles) perpendicularly along the  $y$ -axis (transparent circles) respectively. (d) Transverse waves in crystal planes (blue-dashed lines). Displacement of atoms for respective planes ( $s-1$ ,  $s$ ,  $s+1$ ) perpendicular to the direction of wave propagation are indicated by black-solid lines ( $u_{s-1}$ ,  $u_s$ ,  $u_{s+1}$ ), respectively. (e) Longitudinal wave in crystal planes with atoms moving in the direction of propagation (black-solid arrows). Each atom (solid red circle) is displaced in the positive  $x$ -direction (transparent red circle) leading to the displacement of the planes (blue-dashed lines). The distance (spacing) between the planes is indicated by ‘ $a$ ’. The positive  $x$  and  $y$  directions are indicated. Figures recreated from Ref. [63].

In a realistic three-dimensional crystal, it is simplest to assume a cubic lattice crystal and consider the movement along one of the principal directions ([100], [110] or [111]) [63]. As the wave propagates, entire collections of atoms (planes) move in

phase with displacements, either perpendicular or parallel to the direction of the wave propagation (Fig 2.1d and Fig 2.1e, respectively). The phonon wave can be partially described by the vector form of the wavenumber  $q$  – the wavevector  $\mathbf{q}$ , for a given direction of propagation. For a displacement from the equilibrium position in any direction (solid red circles to transparent red circles in Fig. 2.1), we can describe the displacement as a linear combination of displacements in the  $x$ ,  $y$  and  $z$  directions. Thus, in *each* direction the description of motion is reduced to a one-dimensional problem [63], which we derive below [63, 64, 66]. Every phonon has three modes – one longitudinal (in the direction of phonon propagation, say along the  $x$ -axis) and two transverse (in the other 2 directions, say  $y$  and  $z$ , i.e. perpendicular to the direction of propagation). Any oscillation in three dimensions can be interpreted as a *linear combination* of three waves travelling in three linearly independent directions [66].

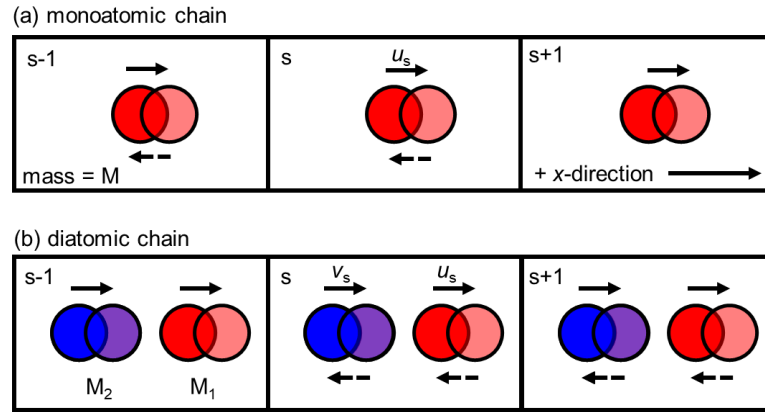


**Figure 2.2.** Comparing monoatomic and diatomic crystals. (a) Schematic of a one-dimensional monoatomic chain with point masses of mass =  $M$  representing the atoms in the chain. There is one atom per unit cell (solid red circle) displaced in the positive  $x$ -direction by displacement  $u_s$  (transparent red circle). (b) Schematic of a diatomic chain with point masses  $M_1$  (red) and  $M_2$  (blue) representing the two atoms per unit cell. Each atom (solid circle) is displaced in the positive  $x$ -direction (transparent circle) by displacement  $u_s$  and  $v_s$  for masses  $M_1$  (red) and  $M_2$  (blue) respectively.

For a simple mathematical description of phonon vibrations let us solve for a one-dimensional picture i.e. a linear chain of equal masses (monoatomic chain) where waves travel along the  $x$ -axis (again, as shown in Fig. 2.1a and Fig. 2.2a). Individual atoms are allowed a range of motion determined by the force constant  $C$  (that is equal for equal masses). For a point mass (representing an atom)  $M$  that is displaced by a distance  $u$  to a position  $s$  along the  $x$ -axis, the force acting on  $M$  is given by the Newton's second law, as follows:

$$F_s = M \frac{d^2 u_s}{dt^2} \quad (2.1)$$

in the direction of motion. As long as there is no permanent deformation in the chain due to this motion (i.e. the displacement is elastic), we can express the force as the product of the displacement  $u$  with the force (spring) constant  $C$  by using Hooke's law. Cubic and higher-order terms may be neglected for sufficiently small elastic deformations [63, 66]. Considering only nearest-neighbor interactions we find that total force  $F_s$  on  $s$  from its nearest neighbors  $s+1$  and  $s-1$  is:

$$F_s = C(u_{s+1} - u_s) + C(u_{s-1} - u_s) \quad (2.2)$$

$C$  is the force constant between two nearest neighbors in the same chain (as Fig. 2.2a).

Phonon dispersion relation – the phonon dispersion relation gives the relation between the phonon frequency  $\omega$  and  $q$ . If the force constant  $C$  is defined for one atom of mass  $M$  of the plane, then the force acting on one atom is given by Eq. 2.1 and Eq. 2.2. Combining these we get the equation of motion of an atom in the plane position  $s$ , given by:

$$M \frac{d^2 u_s}{dt^2} = C(u_{s+1} + u_{s-1} - 2u_s) \quad (2.3)$$

with  $M$  as the mass of the atom. We can describe the motion (change in position  $u_s$ ) of an atom as a wave with time dependence  $e^{-i\omega t}$ . This gives us:

$$u_s = A e^{-i\omega t} \quad (2.4)$$

and differentiating twice with respect to time we have:

$$\frac{d^2 u_s}{dt^2} = -\omega^2 A e^{-i\omega t} = -\omega^2 u_s \quad (2.5)$$

Hence, Eq. 2.3 can be re-written using Eq. 2.5 as:

$$-M\omega^2 u_s = C(u_{s+1} + u_{s-1} - 2u_s) \quad (2.6)$$

To solve Eq. 2.6 we can now look at it as a differential equation in space with a travelling wave solution of the form:

$$u_s = u e^{isqa} \quad (2.7)$$

where,  $a$  is the spacing between the planes (see Fig. 2.1e) and  $u$  is the amplitude of the wave. Putting in the solution form obtained in Eq. 2.7 into Eq. 2.6 we have:

$$-M\omega^2 u e^{(isqa)} = Cu[e^{i(s+1)qa} + e^{i(s-1)qa} - 2e^{isqa}] \quad (2.8)$$

Dividing both sides of Eq. 2.8 by  $u e^{isqa}$  we get:

$$-M_1\omega^2 = C(1 + e^{-iqa}) - 2Cu \quad (2.9)$$

Applying Euler's formula,  $2\cos x = e^{ix} + e^{-ix}$  to Eq. 2.9 we get:

$$M\omega^2 = 2C[1 - \cos(qa)] \quad (2.10)$$

$$\omega^2 = \left(\frac{2C}{M}\right)[1 - \cos(qa)] = \left(\frac{4C}{M}\right)\sin^2\left(\frac{qa}{2}\right) \quad (2.11)$$

From here we easily get the dispersion relation  $\omega(q)$  as:

$$\omega(q) = \sqrt{\left(\frac{4C}{M}\right)} \left| \sin\left(\frac{qa}{2}\right) \right| \quad (2.12)$$

We can plot this dispersion relation for the first unit cell of the reciprocal lattice i.e. the first Brillouin zone. A Brillouin zone is defined as a Wigner-Seitz primitive cell in the reciprocal lattice which gives a geometric interpretation of (x-ray) diffraction conditions observed for a given material [63]. Brillouin zones are used to describe energy bands for phonons (or other elementary excitations, like electrons) [63, 64].

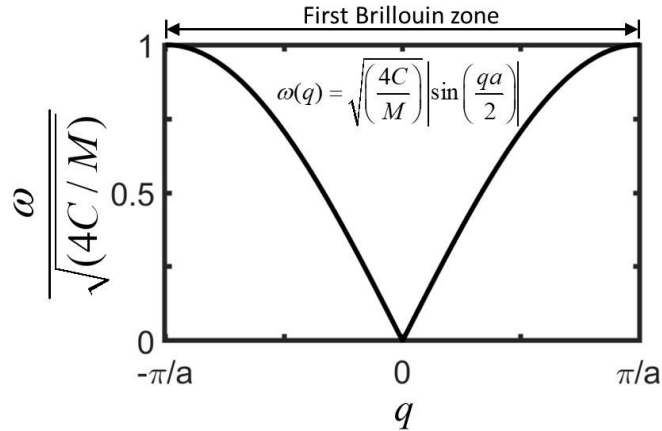


**Figure 2.3.** Dispersion relation  $\omega(q)$  in the first Brillouin zone. At the center of the first Brillouin zone Eq. 2.13 gives  $\omega(q) = \omega(0) = 0$ .

Phonon group velocity – For travelling waves the velocity of some of its characteristics (amplitude maxima/minima) is given by its phase velocity  $v_p$ . However, the velocity at which energy is transported by the travelling wave is generally slower and given by its group velocity,  $v_g$ . The group velocity of a phonon (i.e. energy wave packet) transmission in the direction of phonon propagation is given by:

$$v_g = \frac{d\omega}{dq} \quad (2.13)$$

In the case of our example, the monoatomic chain,  $v_g$  becomes:

$$v_g = \frac{d}{dq} \sqrt{\left(\frac{4C}{M}\right)} \left| \sin\left(\frac{qa}{2}\right) \right| = \sqrt{\left(\frac{4C}{M}\right)} \left(\frac{a}{2}\right) \left| \cos\left(\frac{qa}{2}\right) \right| \quad (2.14)$$

Or, simplifying further:

$$v_g = a \sqrt{\frac{C}{M}} \left| \cos\left(\frac{qa}{2}\right) \right| \quad (2.15)$$

Thus, at the edge of the first Brillouin zone, where  $q = \pi/a$ , the cosine term causes the group velocity to go down to zero – meaning that there is a standing wave with no net phonon propagation at the zone edge.

Two atoms per basis primitive cell – The dispersion relation we derived in Eq. 2.12 is for the case where there is only one atom per unit cell (we use the same mass  $M$  throughout). In more realistic crystalline materials, there is more than one atom per unit cell. With this reconsideration, the derivation for the dispersion relation changes. We now consider a diatomic unit cell with atoms with masses  $M_1$  and  $M_2$  in the unit cell (as in Fig. 2.2b) for a 3D crystal. This leads to interesting new phonon vibrational modes or phonon ‘branches’ which we will see in the derivation below. As an overview we can note that for a primitive cell with two atoms – say NaCl, Si or diamond (C) – 2 ‘branches’ are formed: the acoustic and optical branches. Each branch contains one longitudinal phonon mode (along the direction of phonon propagation) and two transverse phonon modes (perpendicular to the direction of phonon propagation) as before for a total of 6 modes or possible ‘*polarizations*’. They are labeled as one longitudinal acoustic (LA) mode, two transverse acoustic (TA) modes, plus one longitudinal optical (LO) mode and two transverse optical (TO) modes. Their derivations are given below.

To determine the dispersion relation and to see how these branches (optical and acoustic) appear we once again start with the equations of motion. Since we have two atoms per unit cell, with masses  $M_1$  and  $M_2$ , we start with two different amplitudes  $u$  and  $v$  for masses  $M_1$  and  $M_2$  respectively [63]. Again, we assume that each atom plane only interacts with its nearest neighbor (see Fig. 2.2b). We also assume that the

force constant  $C$  is the same between all nearest-neighbor plane pairs. The force  $F_1$  and  $F_2$  are given by:

$$F_1 = M_1 \frac{d^2 u_s}{dt^2} \quad (2.16)$$

$$F_2 = M_2 \frac{d^2 v_s}{dt^2} \quad (2.17)$$

where  $u$  and  $v$  are the amplitudes for mass  $M_1$  and  $M_2$  respectively. Again, for elastic displacements  $u_s$  and  $v_s$ , we can express the force as the product of the displacement and  $C$  using Hooke's law. Cubic and higher-order terms may be neglected for sufficiently small elastic deformations. Considering only nearest-neighbor interactions from its nearest neighbors we have:

$$F_1 = C(v_s + v_{s-1} - 2u_s) \quad (2.18)$$

$$F_2 = C(u_{s+1} + u_s - 2v_s) \quad (2.19)$$

Note that the nearest neighbor to an atom with  $M_1$  is actually an atom with mass  $M_2$  (see Fig. 2.2b). Next, we look at Eq. 2.3 to determine the two equations of motion as:

$$M_1 \frac{d^2 u_s}{dt^2} = C(v_s + v_{s-1} - 2u_s) \quad (2.20)$$

$$M_2 \frac{d^2 v_s}{dt^2} = C(u_{s+1} + u_s - 2v_s) \quad (2.21)$$

with  $M_1$  and  $M_2$  as the masses of the atoms respectively. The displacement of each set of atoms can be described by waves in space and time:

$$u_s = u e^{isqa} e^{-i\omega t} \quad (2.22)$$

$$v_s = v e^{isqa} e^{-i\omega t} \quad (2.23)$$

where,  $a$  is the spacing between the planes (see Fig. 2.1e),  $u$  and  $v$  are the amplitudes of the waves respectively (just as in Eq. 2.7). From Eq. 2.5 we see how we can insert the wave form and differentiate twice with respect to time which gives us:

$$\frac{d^2 u_s}{dt^2} = -\omega^2 u_s \quad (2.24)$$

$$\frac{d^2 v_s}{dt^2} = -\omega^2 v_s \quad (2.25)$$

Comparing Eq. 2.24 to Eq. 2.22 we easily get:

$$\frac{d^2 u_s}{dt^2} = -\omega^2 u_s = -\omega^2 u e^{isqa} e^{-i\omega t} \quad (2.26)$$

Similarly, comparing Eq. 2.25 to Eq. 2.23 we also get:

$$\frac{d^2 v_s}{dt^2} = -\omega^2 v_s = -\omega^2 v e^{isqa} e^{-i\omega t} \quad (2.27)$$

Comparing the left-hand side (LHS) of Eq. 2.20 to Eq. 2.26 we can easily see that:

$$M_1 \frac{d^2 u_s}{dt^2} = -M_1 \omega^2 u e^{isqa} e^{-i\omega t} \quad (2.28)$$

and, comparing the LHS of Eq. 2.21 to Eq. 2.27 we have:

$$M_2 \frac{d^2 v_s}{dt^2} = -M_2 \omega^2 v e^{isqa} e^{-i\omega t} \quad (2.29)$$

For the right-hand side (RHS) of Eq. 2.20 we insert the wave forms of  $u_s$  and  $v_s$  to get:

$$C(v_s + v_{s-1} - 2u_s) = v e^{isqa} e^{-i\omega t} + v e^{i(s-1)qa} e^{-i\omega t} - 2u e^{isqa} e^{-i\omega t} \quad (2.30)$$

Similarly, for the RHS of Eq. 2.21 we again insert the wave forms to get:

$$C(u_{s+1} + u_s - 2v_s) = u e^{i(s+1)qa} e^{-i\omega t} + u e^{isqa} e^{-i\omega t} - 2v e^{isqa} e^{-i\omega t} \quad (2.31)$$

We can cancel out the  $e^{isqa}$  and  $e^{-i\omega t}$  terms in each of the above Eq. 2.28 and Eq. 2.30 as they are common to each term in both sets of coupled equations. Thus, from the LHS of Eq. 2.28 and the RHS of Eq. 2.30 we can rewrite Eq. 2.20 as:

$$-M_1 \omega^2 u = Cv(1 + e^{-iqa}) - 2Cu \quad (2.32)$$

Similarly, from the LHS of Eq. 2.29 and the RHS of Eq. 2.31 we rewrite Eq. 2.21 as:

$$-M_2 \omega^2 v = Cu(e^{iqa} + 1) - 2Cv \quad (2.33)$$

Eq. 2.32 and Eq. 2.33 can be rearranged with all terms on the LHS to give:

$$\begin{cases} u(2C - M_1 \omega^2) - vC[1 + \exp(-iqa)] = 0 \\ -uC[1 + \exp(iqa)] + v(2C - M_2 \omega^2) = 0 \end{cases} \quad (2.34)$$

We can then write Eq. 2.34 as a determinant:

$$\begin{vmatrix} 2C - M_1 \omega^2 & -C[1 + \exp(iqa)] \\ -C[1 + \exp(iqa)] & 2C - M_2 \omega^2 \end{vmatrix} = 0 \quad (2.35)$$

And then solve by subtracting the second diagonal from the first:

$$(2C - \omega^2 M_1)(2C - \omega^2 M_2) - \{[-C(1 + e^{-iqa})][C(1 + e^{iqa})]\} = 0 \quad (2.36)$$

$$4C^2 - 2C\omega^2 M_2 - 2C\omega^2 M_1 + \omega^4 M_1 M_2 - C^2(1 + e^{-iqa})(1 + e^{iqa}) = 0 \quad (2.37)$$

Again, using Euler's formula and simplifying further we get:

$$M_1 M_2 \omega^4 - 2C(M_1 + M_2)\omega^2 + 2C^2[1 - \cos(qa)] = 0 \quad (2.38)$$

From here we solve as a quadratic equation in  $\omega^4$  for the roots in terms of  $\omega^2$ :

$$\omega^2 = \frac{C(M_1 + M_2)}{M_1 M_2} \pm C \sqrt{\frac{(M_1 + M_2)^2}{(M_1 M_2)^2} - \frac{4}{(M_1 M_2)} \sin^2\left(\frac{qa}{2}\right)} \quad (2.39)$$

We can now easily get the dispersion relation by taking the square root of Eq. 2.39:

$$\omega(q) = \sqrt{\frac{C(M_1 + M_2)}{M_1 M_2} \pm C \sqrt{\frac{(M_1 + M_2)^2}{(M_1 M_2)^2} - \frac{4}{(M_1 M_2)} \sin^2\left(\frac{qa}{2}\right)}} \quad (2.40)$$

The outer root with the  $\pm$  leads to the appearance of the two branches of the dispersion relation – an optical and an acoustic branch (for both longitudinal and transverse waves). We can use Eq. 2.40 to plot the dispersion relation (see Fig. A2 **Appendix A**), however, dispersion relations in real materials are more complicated. The full dispersion relation of silicon with all 6 polarizations (LA, LO, and two each of TA and TO) is given in Fig. 2.4 below.

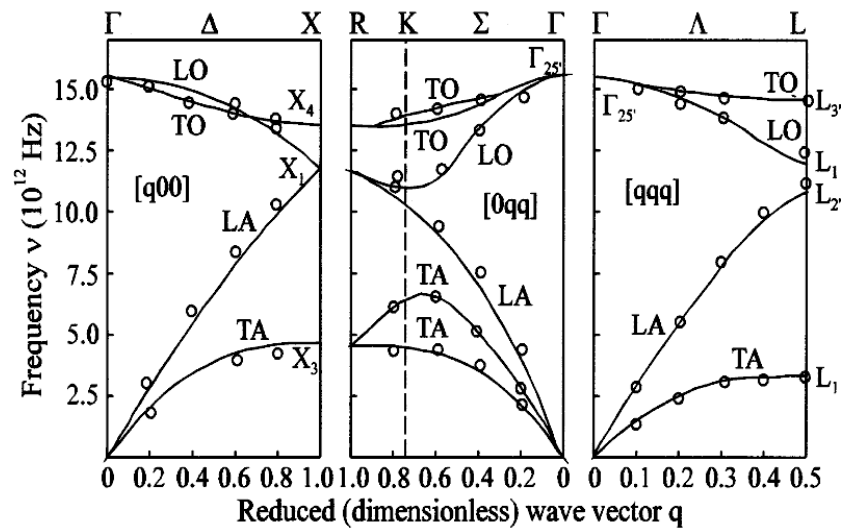


**Figure 2.4.** Dispersion relation  $\omega(q)$  experimentally obtained for silicon [67] for longitudinal acoustic (LA), longitudinal optical (LO), transverse acoustic (TA) and transverse optical (TO) modes.



We must note that the two branches (acoustic and optical) appear due to the presence of two atoms in the unit cell – not just because  $M_1$  and  $M_2$  have different masses. In order to clarify this, we set  $M_1 = M_2 = M$ .

We have,

$$\omega(q) = \sqrt{\frac{C(M_1 + M_2)}{M_1 M_2} \pm C \sqrt{\frac{(M_1 + M_2)^2}{(M_1 M_2)^2} - \frac{4}{(M_1 M_2)} \sin^2\left(\frac{qa}{2}\right)}} \quad (2.40)$$

Setting  $M_1 = M_2 = M$  we have:

$$\omega(q) = \sqrt{\frac{2C(M)}{M^2} \pm C \sqrt{\frac{4M^2}{M^4} - \frac{4}{M^2} \sin^2\left(\frac{qa}{2}\right)}} \quad (2.41)$$

which gives us:

$$\omega(q) = \sqrt{\frac{2C}{M} \pm C \sqrt{\frac{4}{M^2} - \frac{4}{M^2} \sin^2\left(\frac{qa}{2}\right)}} \quad (2.42)$$

which can be further simplified to:

$$\omega(q) = \sqrt{\frac{2C}{M} \left( 1 \pm \sqrt{2 - 2 \sin^2\left(\frac{qa}{2}\right)} \right)} \quad (2.43)$$

From here we can quite clearly see that the two branches – acoustic and optical are a consequence of having two atoms in the unit cell and that the branches remain even if the masses of the two atoms are the same. For a more detailed study of how the dispersion relation changes with the relative values of masses  $M_1$  and  $M_2$ , please see Fig. A3a and Fig. A3b in **Appendix A**. It is interesting to note from Fig. 2.4 that the shape of the acoustic branch in the diatomic case is similar to the dispersion relation determined for the monoatomic case in Fig. 2.3. Intuitively, this represents when the atoms are moving “in-sync” (as if they are one atom) in each unit cell for the diatomic case – hence we see the same shape as if there were one atom. However, when the atoms are moving “out-of-sync” we get the shape of the optical branch, which is very different. We can see why, if we calculate the dispersion relation at the center of the first Brillouin zone.

At the center of the Brillouin zone, for  $\omega(0)$  from Eq. 2.40 we have:

$$\omega(0) = \sqrt{\frac{C(M_1 + M_2)}{M_1 M_2} \pm C \sqrt{\frac{(M_1 + M_2)^2}{(M_1 M_2)^2} - \frac{4}{(M_1 M_2)} \sin^2(0)}} \quad (2.44)$$

$$\omega(0) = \sqrt{\frac{C(M_1 + M_2)}{M_1 M_2} \pm C \sqrt{\frac{(M_1 + M_2)^2}{(M_1 M_2)^2} - 0}} \quad (2.45)$$

Eq. 2.45 has two possible solutions (one for each branch):

$$\omega(0) = \sqrt{\frac{2C(M_1 + M_2)}{M_1 M_2}} \quad (2.46)$$

or,

$$\omega(0) = 0 \quad (2.47)$$

Clearly, the frequency of the acoustic branch is hence zero in this limit, i.e. the center of the first Brillouin zone, as we have seen in Fig. 2.4. The frequency of the optical branch, on the other hand, depends only on the two masses  $M_1$  and  $M_2$  and the spring constant ‘ $C$ ’. Furthermore, if we consider a reduced mass  $\mu$ , such that:

$$\mu = \frac{M_1 M_2}{M_1 + M_2} \quad (2.48)$$

We see that the solution for the optical branch is:

$$\omega(0) = \sqrt{\frac{2C}{\mu}} \quad (2.49)$$

Now, it is important to note that the reduced mass is always going to be smaller than the two component masses [63, 64, 66]. Hence,  $\omega(0)$  gives the maxima for the optical branches.

Thus, in this section we have seen how phonons can be described as vibrations or waves with longitudinal and transverse phonon modes. For materials with more than one atom in their unit cell – like diamond or silicon, the phonon modes further break up into branches – the optical and acoustic branches, for each of the longitudinal and transverse phonon modes. In silicon, for instance, this gives us an overall 6 phonon modes or polarizations – a longitudinal acoustic (LA), a longitudinal optical (LO), two transverse acoustic (TA) and two transverse optical (TO). These branches exist as a

consequence of having two atoms in the unit cell, even if the atoms have equal masses. From the next section onwards, we focus on the particular case of silicon materials and nanostructures for all cases, where not otherwise specified.

## 2.2 Phonons in silicon

Since the innovative work done by Atalla *et al.* in the late 1950s on silicon surface passivation and the invention of the silicon based MOSFET [68, 69] the next half-century has been referred to as the silicon age [69-71]. Silicon has become the dominant go-to material for semiconductor applications [69, 72]. It is a widely available, well understood material, relatively non-toxic and low cost, with a large, established manufacturing industry [44, 73]. This makes it an excellent candidate for research on thermal properties, heat management, nanostructured devices, phonons and phonon transport [73-78].

The dispersion relation of phonons in silicon has been discussed in Section 2.1. It has been well documented that in silicon optical phonons (phonons of the optical branch) do not contribute significantly to thermal transport [63, 64, 79-81]. Lacroix *et al.* mention in their works on thermal transport that they do not consider optical phonons because of their low group velocity which means that they do not contribute significantly to the heat transfer [16, 82]. However, they add, optical modes can contribute indirectly through the interaction with other (acoustic) modes by potentially modifying their relaxation times. This could influence the overall thermal conductivity of the material [16]. Nevertheless, in these works, optical phonons are not considered. Hence, for the purposes of our work we can simplify the full dispersion relation seen in Fig. 2.4 to a quadratic fit, which is widely used in the literature. For simplicity, and since most of the heat is transferred by acoustic phonons (at least in Si [16, 80-84]), the dispersion for the acoustic branches of Si is described by [85]:

$$\omega(q) = v_s q + cq^2 \quad (2.50)$$

Above,  $v_s$  is the sound velocity, and three acoustic modes are typically employed, one longitudinal, and two transverse modes. Fitting parameters to match bulk Si in the [100] direction is used and isotropy is assumed [16, 81, 84]. The transverse modes are degenerate, but lie on top of each other, as seen in Fig. 2.4. Each branch is described

by its own set of fitting parameters as indicated in Table 2.1 and plotted in Fig. 2.5 [85, 86].

Parameter	Longitudinal acoustic (LA) branch	Transverse acoustic (TA) branch
$v_s$ [ $\text{ms}^{-1}$ ]	$9.01 \times 10^3$	$5.23 \times 10^3$
$c$ [ $\text{m}^2\text{s}^{-1}$ ]	$-2 \times 10^{-7}$	$-2.26 \times 10^{-7}$

**Table 2.1.** Parameters used to produce the Si acoustic phonon branches [85].

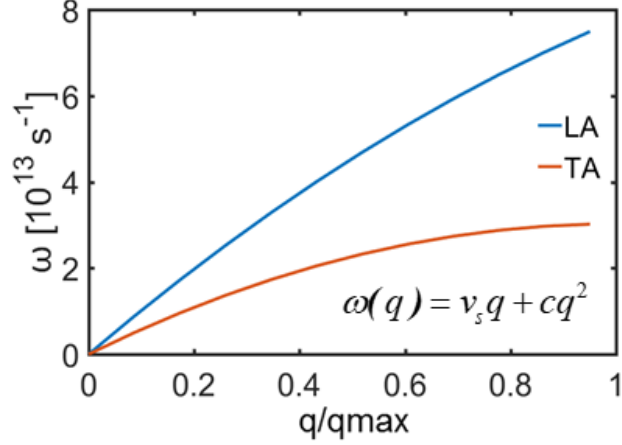


**Figure 2.5.** The fit for the dispersion relation  $\omega$  obtained as in Ref. [85] for longitudinal acoustic (LA, blue lines) and transverse acoustic waves (TA, red lines).

The phonon group velocity, can then be easily found as the as given by the slope of the dispersion relation, is extracted as Eq. 2.13.

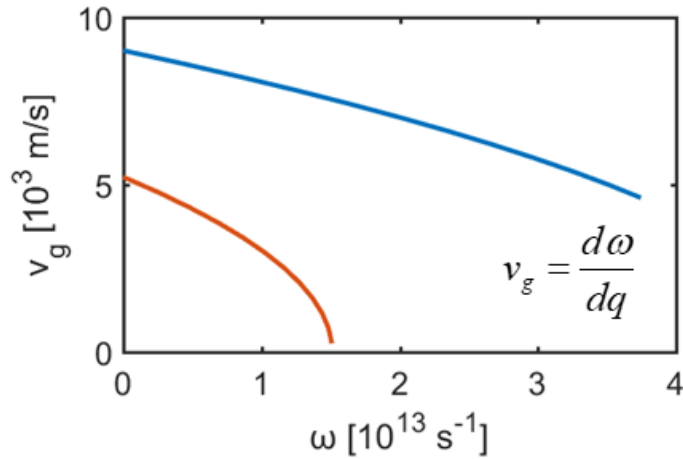


**Figure 2.6.** The group velocity  $v_g$  obtained as in Ref. [85] for longitudinal acoustic (LA, blue lines) and transverse acoustic waves (TA, red lines).

### 2.3 Lattice thermal energy and phonon scattering

Phonon thermal energy – Phonons, like photons, are quantized. Thus, for an angular frequency  $\omega$ , the energy  $E$  of a phonon is given by  $\hbar\omega$ , where  $\hbar$  is the reduced Planck's constant. For phonons, like in the case of photons, we consider the equivalence to a quantum harmonic oscillator for determining energy eigenvalues  $E_n$ .

$$E_n = \left(n + \frac{1}{2}\right) \hbar\omega \quad (2.51)$$

where, the quantum number  $n$  determines the excitation, and  $\frac{1}{2} \hbar\omega$  is the zero-point energy of the mode given by  $\omega$ . At thermal equilibrium, for a certain temperature  $T$ , the occupation number  $\langle n \rangle$  for a given  $\omega$  is determined by the Bose-Einstein distribution:

$$\langle n \rangle = \frac{1}{\exp\left(\frac{\hbar\omega}{k_B T}\right) - 1} \quad (2.52)$$

where  $k_B$  is the Boltzmann constant. To determine the total phonon energy – or thermal energy  $E_T$  (for a given temperature  $T$ ) we sum  $E_n$  determined by Eq. 2.51 for all available phonons given by Eq. 2.52, and for all wavevectors and polarizations ( $pol$ ). Thus, thermal energy of the lattice in a material of volume  $V$  is:

$$E_T \cdot V = \sum_{pol} \sum_q \left( \langle n \rangle + \frac{1}{2} \right) \hbar\omega \quad (2.53)$$

The summations in Eq. 2.53 are performed over all polarizations and wavevectors summed over the first Brillouin zone [81]. The phonon is a travelling wave, and its ability to transmit its energy is dependent on its group velocity  $v_g$ . The phonon group velocity is given by the slope of the dispersion relation – as seen in Eq. 2.13 – which is much smaller in optical modes in silicon than acoustic modes – as seen in Fig. 2.4. Hence, optical phonons do not contribute significantly to thermal conductivity in a direct manner [16, 63, 64, 80, 81, 87] and are ignored in the summation henceforth. Assuming a large bulk 3D crystal lattice (i.e. with a dense wavevector space) the wavevector space can be considered continuous. This allows us to replace the wavevector summation with an integral over the Brillouin zone, as follows:

$$E \cdot V = \sum_{pol} \int_q \left( \langle n \rangle + \frac{1}{2} \right) \hbar \omega \frac{dq}{8\pi^3 / V} \quad (2.54)$$

Now, using the dispersion relation we can transform the integral over the wavevector space into an integral over the frequency space assuming that the Brillouin zone is isotropic. Considering that the number of phonon vibrational states available in the frequency range  $\omega$  to  $\omega + d\omega$  is given by the phonon density of states, we can calculate the energy from Eq. 2.54 as [81]:

$$E_T = \sum_{pol} \int_{\omega} \left( \langle n \rangle + \frac{1}{2} \right) \hbar \omega D(\omega) d\omega \quad (2.55)$$

where the density of states is given by [64]:

$$D(\omega) = \frac{q^2}{2\pi^2} \frac{dq}{d\omega} \quad (2.56)$$

Intrinsic phonon scattering – Phonons travelling in a crystal will often encounter boundaries, inclusions and imperfections and scatter, which will cause them to change their energy and/or momentum. Scattering processes can also take place in a pristine crystal through phonon-phonon scattering. These phonon-phonon processes can be inelastic and preserve neither the number of phonons nor their frequency in the collision process [16, 81]. These anharmonic interactions usually involve three phonons (two phonons annihilate to give birth to a third one) and while quartic interactions exist (four phonons – two phonon annihilate to give birth to two others), they usually contribute less to restore thermal equilibrium [16].

There are two kinds of three-phonon processes: normal processes which preserve momentum and Umklapp processes which do not preserve momentum but satisfy it by means of a reciprocal lattice vector (see Fig. 2.7 below). Hence Umklapp processes directly provide resistance to energy transport, while normal processes do not. Normal processes only indirectly effect the phonon energy or heat flow through the material by changing the frequency distribution of the phonons existing in the material [81]. Under normal scattering, the phonons involved do not change direction and the momentum and energy are conserved [16, 88, 89]. For both processes energy is always conserved. At higher temperatures (higher than the Debye temperature), Umklapp processes become significantly more important and directly affect heat propagation due to their resistance to energy transport.

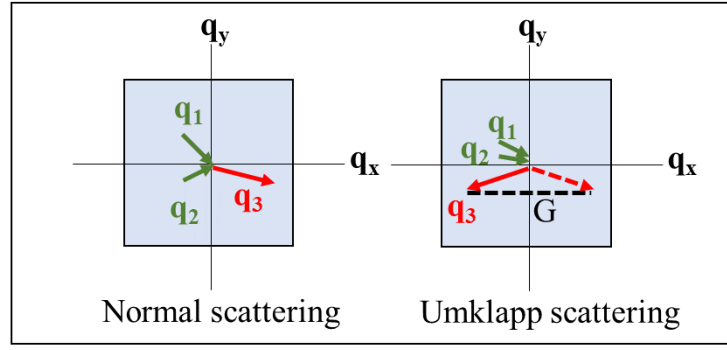


**Figure 2.7.** Normal and Umklapp scattering processes. Solid arrows indicate the phonon momenta before scattering (green arrows) and after scattering (red arrows).

Three-phonon Umklapp processes involve three phonons, typically of higher energies, and are dissipative in nature [34]. When two phonons interact, if their added momentum is larger than the length of the Brillouin zone  $G$ , then a third phonon is created, with total momentum  $p_1 + p_2 - G$  and backscattered (see Fig. 2.7). The energy lost is dissipated in the crystal lattice, changing (increasing) the lattice temperature. This dissipation of temperature due to scattering causes the establishment of a temperature gradient in the material and is primarily responsible for the thermal conductivity ( $\kappa$ ). On the other hand, normal scattering processes are less important and only affect heat transfer by modifying the frequency distribution of the phonons. Together, these mechanisms determine the thermal properties of the material.

## 2.4 Thermoelectricity and nanostructured thermoelectric materials

Thermoelectricity is the phenomenon of interconverting between temperature difference and electricity. First discovered in 1786 by Alessandro Volta [90] it was independently rediscovered by Johann Seebeck by 1822 [91]. When thermoelectric elements (dissimilar materials) are connected electrically and heat is applied at one end, charge carriers (say, electrons in n-type semiconductors) diffuse towards the other cold end (with p-type semiconductors). This creates a charge build up or voltage proportional to temperature difference which can be used to drive a current through an external load [2, 11, 33, 43, 44, 54]. Thermoelectricity can be explored as a collection of thermoelectric effects including the Seebeck effect – the conversion of a temperature difference to current; and the Peltier effect – the conversion of electric

current to a temperature difference. All conducting materials exhibit some thermoelectric effect, but in most cases the observable effect is very small [9].

In the past, the application of commonly used thermoelectric materials such as bismuth telluride ( $\text{Bi}_2\text{Te}_3$ ) or lead telluride ( $\text{PbTe}$ ) was limited due to the material's limited availability, toxicity, high cost and low efficiencies. Recently, increased research in the area of nanostructured thermoelectric materials and devices has led to significant breakthroughs. At the same time, dwindling conventional non-renewable energy resources, and climate change concerns have increased research in environmentally friendly and renewable energy resources. Many of the problems stated above may be simply solved by the introduction of highly efficient thermoelectric materials. This would decrease the requirement for conventional non-renewable, environmentally harmful sources of energy, re-use waste heat to generate further energy and mitigate damage in devices at nanoscale.

Various studies have been carried out on nanostructuring TE materials in order to modify  $\sigma$ ,  $\kappa$  or  $S$  of a given material in order to improve the  $ZT$  to a figure of 2 or more at room temperature (as discussed previously in **Chapter 1**). This can be done by either increasing the power factor or by decreasing the thermal conductivity. This work focuses on ways to do the latter – to use nanostructuring to reduce the thermal conductivity,  $\kappa$ . Focusing on Si-based materials, Si nanowires have been reported to exhibit thermal conductivities close to, or even below the amorphous limit ( $\kappa < 2 \text{ Wm}^{-1} \text{ K}^{-1}$ ), which allowed a 50-fold increase in  $ZT$  to  $ZT \sim 0.5$  by surface roughness engineering [92, 93, 94]. (The experimentally determined  $\kappa$  of amorphous silicon thin films is in the range of  $1 - 2 \text{ Wm}^{-1} \text{ K}^{-1}$  at room temperature [95]). Similar observations have been reported for SiGe nanowires [48] and silicon thin films of 2 nm to 6 nm in thickness [49, 50]. Drastic reductions in thermal conductivity were also reported in nanocrystalline materials. Wang *et al.* [96] showed that the room temperature silicon thermal conductivity decreases from  $81 \text{ Wm}^{-1} \text{ K}^{-1}$  to  $24 \text{ Wm}^{-1} \text{ K}^{-1}$  as the average grain size decreases from 550 nm to 76 nm, whereas  $\kappa$  below  $5 \text{ Wm}^{-1} \text{ K}^{-1}$  has been reported for average grain sizes of about 10 nm [97]. For grain sizes of 3 nm Nakamura *et al.* reported  $\kappa = 0.787 \pm 0.12 \text{ Wm}^{-1} \text{ K}^{-1}$  [51, 52]. Additionally novel silicon membranes with nanoscopic pores have shown reproducibly low  $\kappa$  around  $1\text{-}2 \text{ Wm}^{-1} \text{ K}^{-1}$  [41, 53, 43], with little detriment to the electronic properties.



Nanostructures that combine the effects of alloying, nanocrystallinity, and porosity have started to appear as well, as a means to achieve an even lower  $\kappa$ . A recent Si-based work reported  $\kappa$  of  $20.8 \pm 3.7 \text{ Wm}^{-1} \text{ K}^{-1}$  for an average pore size of  $\sim 30 \text{ nm}$  and grain sizes between  $50 \text{ nm}$  to  $80 \text{ nm}$  [98]. By reducing both pore and grain sizes, however, Basu *et al.* reported  $\kappa = 1.2 \text{ Wm}^{-1} \text{ K}^{-1}$  at 40% porosity in p-type silicon [99]. A recent work in SiGe nanomeshes, reported ultra-low  $\kappa$  of  $0.55 \pm 0.10 \text{ Wm}^{-1} \text{ K}^{-1}$  for SiGe nanocrystalline nanoporous structures, a value well below the amorphous limit [33]. More recently, by considering hierarchical nanostructuring for p-type  $\text{Pb}_{0.98}\text{Na}_{0.02}\text{Te-SrTe}$ , Tan *et al.* reported an even lower lattice thermal conductivity ( $\kappa$ ) of  $0.5 \text{ W K}^{-1}\text{m}^{-1}$  and a higher  $ZT$  of 2.5 at 923K [100].

## 2.5 Summary

This chapter explored the properties of phonons, the material specific dispersion relation of silicon and intrinsic phonon-phonon scattering that leads to thermal conductivity. In the first section we described phonons as waves with longitudinal and transverse phonon modes where additional branches occur for materials with more than one atom in their unit cell – like diamond or silicon. In silicon, this gives us an overall 6 phonon modes or polarizations – one longitudinal acoustic (LA), one longitudinal optical (LO), two transverse acoustic (TA) and two transverse optical (TO). These branches exist as a consequence of having two atoms in the unit cell, even if the atoms have equal masses. Focusing on silicon, we used a simplified approximation of its dispersion relation to examine further phonon properties. The next section explored the contribution of phonons to thermal energy and other thermal properties of silicon. Intrinsic phonon scattering and its role in the thermal conductivity of silicon structures was examined. Lastly, we briefly touched upon how thermoelectric elements function, and examined thermoelectric material properties. We delved into improvements in thermoelectric efficiency offered by nanostructuring the existing thermoelectric materials and explored new novel nanomaterials for thermoelectric applications. In the next chapter we look at methods to simulate and model phonon transport in nanoscale structures.

### 3. Phonon transport theory

This chapter describes different approaches used to perform phonon transport simulations, including an introduction to Boltzmann transport theory, and then focuses on the Monte Carlo method, which is implemented in a simulator – especially developed for this study and used extensively for the results in this Thesis. The Monte Carlo simulator specifics are discussed. Treatment of phonon interactions for various scattering mechanisms, including phonon-phonon scattering, phonon-grain boundaries and phonon-pores scattering are described. Initial validation of the simulator results for the pristine bulk Si, for nanocrystalline silicon and for nanoporous cases are then carried out by comparing the obtained simulation results against available measured data for the thermal conductivity of silicon nanomaterials.

#### 3.1 Approaches to phonon transport simulations

The problems outlined in the previous **Chapters 1 and 2**, such as device overheating leading to thermal breakdown, waste of two-third of all energy generated, improving thermoelectric efficiency, could be addressed by improving our fundamental understanding of how phonons propagate through materials and devices – which at the moment is far from complete. In this context, theoretical simulations can help with both, predicting the thermal properties of a material and clarifying the physics of phonon transport. In **Chapter 2** we have seen that nanostructuring materials has demonstratively improved the thermoelectric efficiency of several materials. The pertinent length scales and properties of the nanostructured materials that we primarily study make simulations a crucial tool to clarify the physics of phonon transport in these materials, and to be able to study them in a viable, repeatable and methodical manner.

A significant number of simulation approaches are available in the literature which can be used to explain the experimental observations of reduced thermal conductivity and enhanced  $ZT$  in nanostructures. Understanding the qualitative and quantitative effects of such structures on the thermal conductivity would allow for the design of more efficient thermoelectric materials and heat management systems in general. Some of these methods are discussed further in this section.

Theoretical simulations can predict the thermal conductivity of a nanostructured material through a comprehensive and rigorous analysis of the molecular level structure and the interatomic interactions [101]. Some methods are based in ‘momentum space’ (phonon spectrum) which assume periodic systems, while other methods use ‘real space’ techniques which directly consider the nanostructuring. In this work we focus on the latter. A hierarchical chart giving an overview of these methods is given in Fig. 3.1 below.

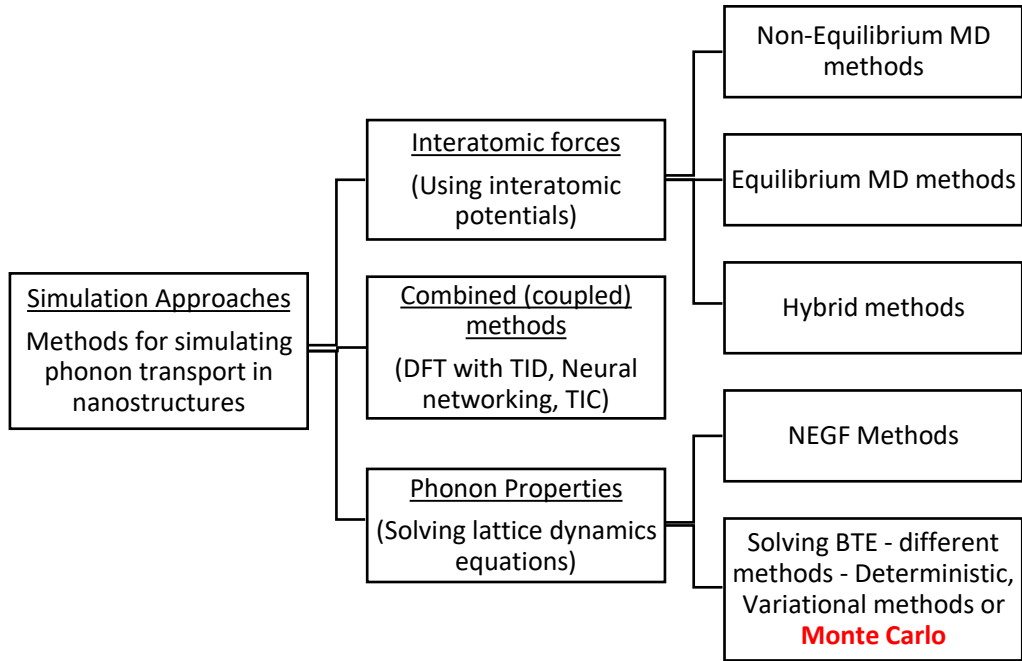


**Figure 3.1:** Approaches to phonon transport simulations [101-105]. These include Molecular Dynamics or MD methods, coupled methods, NEGF (Non-Equilibrium Green’s Functions) and the Boltzmann transport Equation (BTE). The Monte Carlo approach is a method to solve the BTE and is used extensively in this Thesis. This is described in detail in Section 3.2.

Simulation methods commonly used for studying thermal transport from an atomistic perspective, which we touch upon here, include Molecular Dynamics, Non-Equilibrium Green’s Functions and solving the Boltzmann Transport Equation. Classical molecular dynamics (MD), Non-equilibrium molecular dynamics (NEMD) and hybrid methods use interatomic forces and thermodynamic interactions to describe thermal transport and determine thermal conductivity. Combined (coupled) approaches combine facets from multiple approaches to determine thermal properties. Alternatively, the Boltzmann Transport Equation (BTE) describes the transport of an

ensemble of particles. Using phonon properties (dispersion relation, scattering rates, etc.) the phonon transport behaviour and thermal conductivity can be determined for a given material [16, 81, 89]. The Monte Carlo method is one approach to solve the BTE. Lastly, Non-Equilibrium Green's Functions (NEGF) use harmonic approximations of phonon properties (phonon dispersion relations) directly to determine thermal properties and thermal conductivity [105]. Both MD and NEGF methods are briefly outlined below, before focusing on the Boltzmann Transport Equation (BTE) and the Monte Carlo method which is used extensively in this Thesis.

### 3.1.1 Molecular Dynamics (MD) methods

The solution to Newton's laws (i.e., the classical equations of motion) at the atomic scale gives us the molecular dynamics (MD) approach. In MD, atomic interactions (i.e., how the atoms move with respect to each other) are determined by *interatomic potentials* [106, 107]. Interatomic potentials are functions that relate the potential energy of a system to its atomic positions. Thus, MD can capture coherence effects and anharmonicity through the choice of potentials [108]. Finite difference algorithms are used to solve the system at each time step, usually less than a femtosecond [103]. Thus, there is a trade-off computationally between the size of the system and the time for the simulation. The main methods of calculating thermal conductivity using MD include equilibrium [109-111] and non-equilibrium [112-115] approaches.

Non-equilibrium MD (NEMD) approaches are direct and analogous to simple experiments [101, 108]. Simply put, in NEMD approaches (e.g., [113]), one region of the simulation cell is heated and a second region some distance away is cooled. The temperature profile between the hot and cold regions is determined, from which the temperature gradient can be calculated. If the amount of energy needed to maintain the elevated temperature in the hot region and reduced temperature in the cool region is known, then the heat current can be computed, from which the thermal conductivity can be calculated using Fourier's law. The direct method usually involves large ( $10^9$  K/m) [108] temperature gradients and system sizes dictate the ability to accommodate long wavelength phonons and large phonon mean-free-paths.

In the equilibrium molecular dynamics (EMD) approach periodic boundary conditions are commonly utilized and hence some phonon mean-free-paths (MFPs) that are larger than the size of the systems domains can be simulated. However, one of the major drawbacks of this approach is that while EMD allows for shorter system sizes, it also requires a longer simulation time. A widely used and well established EMD approach is the Green–Kubo method [101, 108-110]. The Green–Kubo method is based on linear response theory and the assumption that local fluctuations in the heat flux of a system in equilibrium are due to the same mechanisms which govern the overall thermal properties of the material. The thermal properties of the material are computed using the Green-Kubo expression which relates the thermal conductivity of the system to the heat current autocorrelation function  $\mathbf{J}$  vector [101, 102, 108]. The thermal conductivity can be derived as:

$$\kappa_{ij} = \frac{1}{3k_B VT^2} \int_0^\infty \langle \mathbf{J}_i(0) \mathbf{J}_j(t) \rangle \quad (3.1)$$

Here,  $k_B$  is the Boltzmann constant,  $V$  is the volume  $T$  is the temperature  $i, j$  denote the cartesian coordinates for the thermal conductivity tensor and the angular brackets ( $\langle \rangle$ ) here denote an average over time [108].

A significant advantage of the Green–Kubo method is the relatively small simulation cell size required – which is much smaller than the simulation cell sizes required for NEMD calculations. The disadvantages of the Green–Kubo method include poor convergence and the intrinsic difficulty in defining the heat current for complicated many-body interatomic potentials [101, 107, 108, 115]. Additionally, both of the classes of MD methods also continue to suffer from system size effects, that is, the longest wavelength of a phonon is limited by the system size [115, 116].

There are also hybrid MD methods for analyzing thermal transport in hybrid nanomaterials. One method [108, 117] simulates the interaction of wave packets with nanomaterials, i.e., the interaction of a group or a packet of phonons with the nanostructure. This has been carried out in various nanoscale defects and structures, such as for grain boundaries [118], point defects [119] as well as carbon nanotube junctions [120]. The system of interest is initialized with an initial state, structure and localized wave packet of phonons from a single branch and with a narrow range of wavevector values. The wave packet is then allowed to propagate and its interaction

with the nanostructured features is then studied to provide information about phonon transport through the system. An alternate approach calculates the relaxation time (RTA) of the individual phonons from equilibrium molecular dynamics (RTA-ED) [121, 122]. The RTA is then used to calculate the thermal conductivity, but the approach is applicable only above the Debye temperature. This method, however, does have the computational advantage that it requires shorter MD runs than the Green–Kubo method, and smaller system sizes than direct methods [121, 122].

### 3.1.2 Non-Equilibrium Green’s Functions (NEGF)

NEGF is a well-established, fully quantum mechanical method which takes into account the exact geometry without any underlying assumptions [123, 124]. NEGF was originally used for electronic systems but has also started to be used for phonon transport, recently [125]. The NEGF method has been used widely for thermal transport in low dimensional materials [126-133]. For computational reasons it cannot scale to large bulk systems. It provides the phonon transport through a given material including all phonon wave effects.

Unlike MD, in which the phonon properties are implicit in (and can be extracted from) the choice of interatomic potentials, the NEGF is one approach that begins with harmonic approximations of phonon properties. This method was primarily developed to study quantum transport in the nanostructures [134, 135]. Unlike other methods, the NEGF method does not require thermal equilibrium to be established in the system of interest. Hence, some consider NEGF the only method that is strictly valid for very small nanostructures, since the notion of the thermodynamic equilibrium for a handful of atoms is ill defined [126, 135]. However, similar to MD methods, practical applications of the NEGF approach require limiting the simulation system domain size to reduce the computational cost of modelling.

The NEGF method easily captures coherence effects and the exact geometry is included [126, 136]. Similar to the case of electrical conductivity through molecular junctions, for phonon calculations, nanostructures are considered to be connected by two contacts, both of which are semi-infinite and coupled to a heat bath at some lead temperature. Phonon populations are established in the contacts corresponding to the lead temperature. Heat current through the system might be expressed through the

Landauer formula, analogous to the electrical conductivity [128]. The thermal conductivity can be computed by solving the Green's function  $G(E)$  in the non-equilibrium case, which involves the dynamical matrix of the nanostructure and gives a thermal conductivity which appears to be quantized, as experimentally observed [137]. The Green's function is given by [134]:

$$G(E) = \left[ (\hbar\omega)^2 I - D - \Sigma_1 - \Sigma_2 \right]^{-1} \quad (3.2a)$$

where,  $D$  is the Dynamical matrix,  $\Sigma_1, \Sigma_2$  are the self-energy matrices for the device contacts. These matrices and the NEGF method is described in greater detail in **Chapter 7**.

There are various applications of NEGF with corresponding modifications. An efficient way of computing the transmission coefficient ( $Tr(\omega)$ ) is through the Caroli formula:  $Tr(\omega) = Tr(G(E)\Gamma_L(E)G(E)\Gamma_R(E))$  [134, 118], where  $\Gamma_L$  and  $\Gamma_R$  describe the interaction between the contacts and the central region. Caroli *et al.* first obtained a formula for the electronic transport using a more restricted case [138]. The thermal conductance can then be obtained using the Landauer formula:

$$G_k = \frac{1}{2\pi A} \int_0^\infty Tr(\omega) \hbar\omega \left( \frac{\partial n(\omega)}{\partial T} \right) D(\omega) d\omega \quad (3.2b)$$

where  $n(\omega)$  is the Bose-Einstein distribution and  $T$  is the temperature,  $A$  is the cross-sectional area perpendicular to the heat flow direction,  $D(\omega)$  is the phonon density of states for given frequency. Given a system with length  $L$ , the thermal conductivity,  $\kappa = G_k L/A$ . For thermal transport, the NEGF has been derived, modified and applied across various systems [126, 136, 139-144].

In short, the NEGF method has not only been used primarily for electronic transport [134], but also for phonon transport in low-dimensional materials [126-132], yielding results in agreement with experimental measurements [126, 129]. We discuss NEGF at greater depth in **Chapter 7**, which deals with wave transport through nanostructures. Typically, the NEGF method describes transport in the ballistic limit but the formalism can also be applied to diffusive cases [132]. This is also expanded upon in **Chapter 7**.

### 3.1.3 Boltzmann Transport Equation (BTE)

Heat conduction is classically described by the Fourier law and the heat conduction equation – which is essentially a diffusion equation [16].

$$\frac{\partial T}{\partial t} = \alpha \Delta T \quad (3.3)$$

where the LHS determines the temperature variation,  $\partial T$ , per change in unit time given by  $\partial t$ ,  $\alpha$  is the medium diffusivity and  $\Delta T$  is the change in temperature. Eq. 3.3 is also commonly known as the heat equation. This kind of equation can be interpreted as describing a random walk of particles [16, 145]. When looking at heat transport, we are actually dealing with energy carriers: electrons are the dominant carriers in metals, while phonons are the dominant carriers in semiconducting and insulating materials. When these carriers undergo a large number of collisions and their behavior is diffusive in nature, Fourier's law can suitably yield predictive results. However, Fourier's law ignores changes to nanoscale structuring and quantum features. Hence for nanoscale structures where there are a lower number of collisions, Fourier's law fails. This is the case in a ballistic regime, which often occurs in low-dimensional or nanostructured materials. In such regimes, a different approach is needed. A convenient method is to consider the evolution of a distribution function which describes the number of particles (phonons) in a certain elementary region around a point, i.e.,  $\tilde{f} = \tilde{f}(t, \mathbf{r}, \mathbf{q})$ , where  $\tilde{f}$  is the distribution function (a number between one and zero describing the average distribution of carriers),  $\mathbf{r}$  is the particle position,  $\mathbf{q}$  is its wavevector, and  $t$  is time. This equation varies in space and time under the influence of external forces and collisions and is called the Boltzmann Transport Equation [146]. The Boltzmann Transport Equation (BTE) is a transport equation describing the transport of an ensemble of particles and can be used to model the phonon behavior in a crystal lattice [16, 81, 85, 86, 89]. In the absence of external forces, (such as external lattice stress/strain), the BTE is given by:

$$\frac{\partial \tilde{f}}{\partial t} + \mathbf{v} \cdot \nabla \tilde{f} = \left. \frac{\partial \tilde{f}}{\partial t} \right|_{scatt} \quad (3.4)$$

Where  $\mathbf{v}$  is the velocity of the particles. Here the left side of the Eq. 3.4 represents the advection component (ballistic component) which causes deviations from the equilibrium. The right side of the equation represents the scattering component which restores the equilibrium by means of scattering events – phonon-phonon or phonon-



geometry scattering, etc. The distribution function typically has multiple variables – time, space variables, and wavevector variables and the scattering rate – which is usually a nonlinear function of  $\mathbf{q}$  [16, 81, 89]. These complexities and large number of independent variables render the BTE extremely difficult to solve by deterministic means [81]. An alternative method to solve the BTE is the Monte Carlo method. Understanding and modelling the collision term is of key importance in the resolution of the BTE, which can be done in a straight-forward way with Monte Carlo [16]. The collision term is given by:

$$\left. \frac{\partial \tilde{f}}{\partial t} \right|_{scatt} = \sum_{\mathbf{q}'} [\Phi(\mathbf{q}, \mathbf{q}') \tilde{f}(\mathbf{q}') - \Phi(\mathbf{q}', \mathbf{q}) \tilde{f}(\mathbf{q})] \quad (3.5)$$

where  $\Phi(\mathbf{q}, \mathbf{q}')$  is the scattering rate from  $\mathbf{q}'$  to  $\mathbf{q}$ . This scattering term is due to three phonon scattering and is a non-linear function which is difficult to treat. However, we know that the scattering term restores the equilibrium and thus we can take the relaxation time approximation (RTA) for the three phonon processes such that, for a time  $\tau$  the function  $\tilde{f} = \tilde{f}(t, \mathbf{r}, \mathbf{q})$  reduces to  $\tilde{f} = \tilde{f}(0, \mathbf{r}, \mathbf{q})$  at rate  $1/\tau$ . Thus, the scattering term in the Eq. 3.5 reduces to [34]:

$$\left. \frac{\partial \tilde{f}}{\partial t} \right|_{scatt} = - \frac{\tilde{f} - \tilde{f}^0}{\tau} \quad (3.6)$$

We can hence now use the Monte Carlo method to solve the BTE to study phonon transport through a material and determine its thermal properties. Note that this approach is not relevant to treat the wave aspects of the problem such as interference or tunnelling.

### 3.2 Monte Carlo method

The Monte Carlo method is an alternative, effective way to solve the BTE in a statistical manner capable of dealing with larger and more complex devices and geometries. Understanding the qualitative and quantitative effects of such geometries on the phonon transport and thermal conductivity would allow the design of more efficient thermoelectrics and heat management systems in general.

Monte Carlo methods strike a compromise between the comprehensive (but sometimes prohibitive) detail of molecular dynamics and the simple (and sometimes

inaccurate) application of Fourier's law at the nanoscale [147]. Herein, a large number of random events (scattering events) and trajectories are simulated for a given number of particles. Multiple geometries, including pores, nanocrystalline grains, both diffusive and specular boundaries can all be considered and incorporated simultaneously. Some of these can be seen in Fig. 3.2 below.

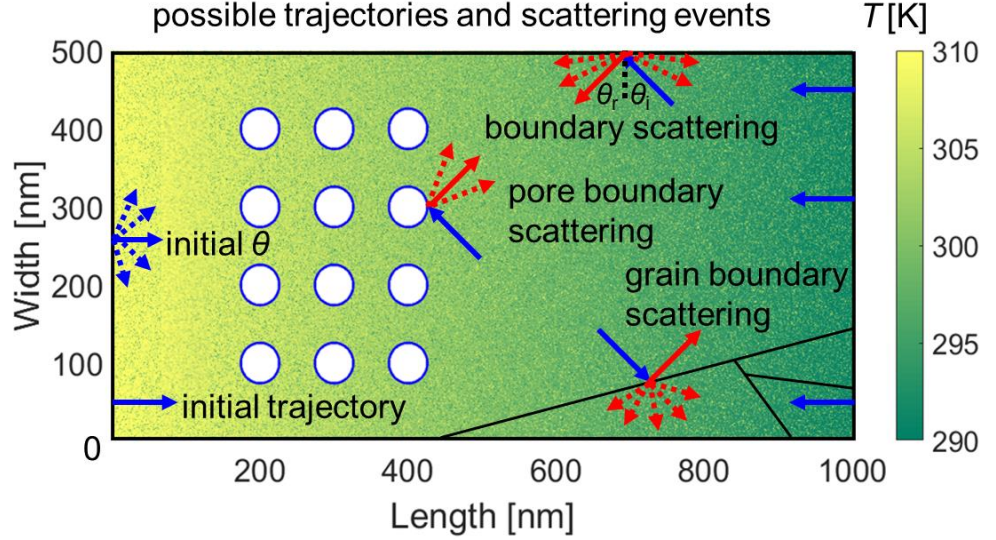


**Figure 3.2:** Features of Monte Carlo simulations in a domain of length  $L_x = 1000$  nm and width  $L_y = 500$  nm. The domain coloring indicates the local device temperature (in K), corresponding to the temperature color map. Possible phonon trajectories are given by blue and red lines. Blue-solid lines indicate initial or incident phonon trajectories. These can be initialized from either the left (hot) or right (cold) boundary. Blue-dashed lines indicate possible phonon trajectory angles,  $\theta$ . Red lines indicate trajectories of scattered phonons after interaction with porous (blue circles) or nanocrystalline (black lines) geometries. Red-solid lines indicate specular scattering, where incident angle ( $\theta_i$ ) = reflected angle ( $\theta_r$ ). Red-dashed lines indicate diffuse scattering, where  $\theta_r$  is randomized.

One of the earliest works where Monte Carlo was implemented in phonon transport is by Mazumder *et al.* in 2001 [81]. Since then transport schemes of greater complexities and with various different focuses have been attempted, such as the work by Lacroix *et al.* [16] which features simulations on silicon and germanium thin films where bulk thermal conductivities of silicon and germanium were numerically retrieved with a maximal error lower than 8%. In their work, Aksamija *et al.* dealt with rough boundaries in both the specular and the diffusive case with an attempt to improve upon the final random angle in the phonon-phonon scattering as given by the relaxation-time approximation, by attempting to conserve the ('quasi') momentum as

determined by the full phonon dispersion [10, 148]. More complex nanostructures have since been examined using MC, such as nanowires [82, 149], thin films [150, 151], nanoporous materials [89, 152-155], polycrystalline materials [95, 97, 156-158], nanocomposites [87, 159], and corrugated structures [160-163]. In devices specific work, Vasileska *et al.* have successfully simulated self-heating effects in Silicon-on-Insulator devices [164]. They show that at very high porosities, the strong increase in boundary scattering due to the decrease in nanowire and nanocrystal size, together with the confinement effects involved, results in reduced carrier diffusion and a quenching of phonon drag, with consequent reduction in the total TE efficiency [164].

This section describes the basis MC simulator developed and employed to solve the Boltzmann Transport Equation for phonons in Si nanostructures using the Monte Carlo method. We outline the theory behind this method as it applies to pristine, nanocrystalline and nanoporous geometries and describe the approach and specific implementation used throughout this Thesis.

### **3.2.1 Incident flux (or single-particle) simulation process**

The Monte Carlo (MC) approach has been adopted for a semi-classical particle-based description of phonon transport. For computational efficiency we consider a 2D simulation domain of length  $L_x = 1000$  nm and width  $L_y = 500$  nm. This choice of domain size has been verified in previous work as being large enough to give good agreement with other experimental and theoretical results for real nanomaterials, while being small enough to be computationally efficient [58, 59, 60, 86, 89], as shown in validation sections 3.2.4 to 3.2.6. It is also much longer than the average MFP of the system ( $\sim 130$  nm), which ensures diffusive transport.

The MC simulation method is described adequately in the literature, but because our method differs in some details, below we describe our numerical scheme. We use the incident flux or ‘single-phonon MC’ approach which differs from the multi-phonon MC approach described in various works in the literature [11, 16, 34, 80, 81, 85] in terms of phonon attributes book-keeping.

In a multi-phonon approach, many phonons are initialized simultaneously. This is the ‘many particle’ or the ‘ensemble Monte Carlo’ method and it is the most common method used in electronic devices [34]. Phonon paths, energy and

temperature of all cells are traced simultaneously at every time step, and often periodic boundary conditions are employed to remove the effect of the limited simulation domain. In the single phonon approach one phonon is simulated at a time from the domain edge and propagates through the simulation domain until it exits at either edge. Once the phonon exits, the next phonon is then initialized. This is similar to the Ab Initio Monte Carlo method developed by Davies *et al.*, but in a 2D domain [166].

The simulation procedure is then as follows: Phonons enter from either direction of the simulation domain and alternate between free flight and scattering events. The time it spends in the simulation domain until it exits again, is recorded as its Time-Of-Flight (TOF). The regions at the left/right of the simulation domain are given ‘Hot’ and ‘Cold’ temperatures,  $T_H$  and  $T_C$ , respectively. The rest of the domain is initially set at the average temperature of  $T_H$  and  $T_C$  – we label that as  $T_{BODY}$ . At room temperature, a  $\Delta T = 20$  K is adequate to gather the necessary statistics for simulation convergence, and low enough to ensure the simulation is still within the linear response regime [58, 86, 89].

Phonons are initialized in the contacts only, based on polarization, frequency, velocity, and energy. Phonon probabilities are drawn from a dispersion relation  $\omega(q)$ , modified by the Bose Einstein distribution at the given temperature. We use the dispersion relation  $\omega(q)$  and corresponding group velocities  $v_g(q)$  as described in **Chapter 2** by Eq. 2.50 and Eq. 2.13 below [85]:

$$\omega(q) = v_s q + c q^2 \quad (2.50)$$

$$v_g = \frac{d\omega}{dq} \quad (2.13)$$

where  $v_s$  and  $c$  are fitting parameters to match the thermal conductivity of bulk Si in the [100] direction. The dispersion coefficients we use are  $v_s = 9.01 \times 10^3 \text{ ms}^{-1}$  and  $c = -2 \times 10^{-7} \text{ m}^2 \text{ s}^{-1}$  for the longitudinal acoustic (LA) branch, and  $v_s = 5.23 \times 10^3 \text{ ms}^{-1}$  and  $c = -2.26 \times 10^{-7} \text{ m}^2 \text{ s}^{-1}$  for the transverse acoustic (TA) branches [86]. Following common practice, the contribution of optical phonons is neglected as they have low group velocities and do not contribute significantly to phonon transport [16, 80, 81, 84] (although they indirectly could influence the interaction between optical and acoustic phonons and alter the effective relaxation rates of the acoustic phonons [16, 165]).

### 3.2.2 Phonon scattering treatment

Phonons in the simulation domain either scatter, or are in free flight. During free flight, the position  $\mathbf{r}$  at time  $t$  of the phonon is given by the equation:

$$\mathbf{r}(t_i) = \mathbf{r}(t_{i-1}) + \mathbf{v}_g \Delta t \quad (3.7)$$

Scattering of phonons is caused either by interaction with geometrical features, or by three-phonon internal scattering (Umklapp processes). The three-phonon scattering, which is responsible for the change in the temperature of the domain, is computed in the relaxation time approximation and is a function of temperature and frequency, as [16, 80, 81, 85, 89, 88]:

$$\tau_{\text{LA}}^{-1} = B_{\text{NU}}^{\text{LA}} \omega^2 T^3 \quad (3.8a)$$

$$\tau_{\text{TA, N}}^{-1} = B_{\text{N}}^{\text{TA}} \omega T^4 \quad (3.8b)$$

for normal scattering processes in the LA and TA branches respectively, and:

$$\tau_{\text{TA, U}}^{-1} = \begin{cases} 0 & \text{for } \omega < \omega_{1/2} \\ \frac{B_{\text{U}}^{\text{TA}} \omega^2}{\sinh\left(\frac{h\omega}{2\pi k_{\text{B}} T}\right)} & \text{for } \omega > \omega_{1/2} \end{cases} \quad (3.8c)$$

for Umklapp processes in the TA branch, where  $\omega$  is the frequency,  $T$  is the temperature and  $\omega_{1/2}$  is the frequency corresponding to  $q = q_{\text{max}}/2$ . The parameters  $B$  used in the case of Si are:  $B_{\text{NU}}^{\text{LA}} = 2.0 \times 10^{-24} \text{ s}$ ,  $B_{\text{N}}^{\text{TA}} = 9.3 \times 10^{-13} \text{ s}$ ,  $B_{\text{U}}^{\text{TA}} = 5.5 \times 10^{-18} \text{ s}$  [86, 88, 89]. In the works of Holland *et al.* a simpler Debye approximation is used with impurity scattering implemented. Yet, these equations used here are commonly used to describe relaxation time in phonon Monte Carlo simulations for Si [11, 16, 80, 81, 82, 85, 89, 86], even with more advanced approximations and including in works that ignore the impurity scattering [86, 89]. However, in these works a small temperature difference ( $\Delta T \sim 5\%$ ) between the device contacts is required to accurately capture the low temperature peak [86, 89, 116] and this was used in our work. Using the Matthiessen's rule, the total relaxation time  $\tau^{-1} = \tau_{\text{LA}}^{-1} + \tau_{\text{TA, N}}^{-1} + \tau_{\text{TA, U}}^{-1}$  is determined. When a phonon has spent this time  $\tau$  in the simulation domain, travelling with its state velocity, it undergoes the next scattering event, after which the  $\tau$  is reset.

Physically, under the normal scattering condition, pair-systems of two phonons do not change their direction and their pair momentum and energy are conserved [16, 88, 89]. There is just momentum transfer between the two phonons of the pair-system, but this does not affect the thermal conductivity directly. However, indirectly it can affect the momentum causing phonons which undergo dissipative processes to interact differently with boundaries than the original system [34]. In phonon MC simulations, however, we alter the frequency (and consequently energy and momentum) and magnitude of the velocity of the phonon, and only leave its direction unchanged. This is further described below. Three-phonon Umklapp processes involve three phonons, typically of higher energies, and are dissipative. Two-phonons interact, and if their added momentum is larger than the length of the Brillouin zone  $\mathbf{G}$ , then a third phonon is created, with total momentum  $\mathbf{p}_1 + \mathbf{p}_2 - \mathbf{G}$  and backscattered. (However, when simulating these processes there are cases where it is more convenient in simulations to randomize the direction rather than just backscattering [34].) The energy lost is dissipated in the lattice, raising its temperature. This dissipative mechanism causes the establishment of a temperature gradient in the channel material and is responsible for the thermal conductivity [34, 81].

The scattering process is as follows: If the phonon is in the TA branch its frequency determines the scattering process used. If the frequency of the phonon is high ( $\omega > \omega_{1/2}$ ) Umklapp scattering is carried out, whereas for a low frequency phonon ( $\omega < \omega_{1/2}$ ) normal processes are carried out. This means that for normal process a new frequency, wavevector/momentum and velocity amplitude is chosen in the same way as is done during the initialization procedure, using the temperature of the simulation cell, but the direction remains unchanged. The relaxation time estimation [16, 167] states that  $\omega_{1/2}$  corresponds to the  $q_{\max}/2$  for the TA branch. For phonons in the LA branch we set that half phonons have the probability to undergo a normal scattering process, where there is no change in direction and half scatter according to Umklapp processes [16]. This means that we draw a random number from a uniform distribution, and check if it is below (normal) or above (Umklapp) 0.5. During the Umklapp processes we reset the phonon direction, and reset its energy using the temperature of the simulation cell where the Umklapp event happened [34, 58]. During normal processes, all the participating phonons must be collinear to achieve scattering.

Thus, TA mode phonon interactions would only give another TA phonon, whereas LA phonon interaction would only result in a LA phonon [81, 168].

Momentum conservation is more difficult to maintain within our simulation framework where particle-phonons travel independently. Lacroix *et al.* suggest an approach, by which the normal processes “approximately” preserve momentum [16]. Considering that Umklapp processes contribute to the thermal resistance directly (unlike normal processes), when the phonons scatter through an Umklapp process their direction after scattering is randomized as in the initialization procedure (rather than backscattered). Therefore, these phonons randomly scatter and contribute to the diffusion of heat. For normal processes, it is then assumed that when scattering, phonons do not change their propagation direction, only their frequency, the magnitude of their wavevector and velocity. By this treatment, the normal processes “approximately” preserves momentum. For a plane-parallel geometry, it seems possible to guarantee the momentum conservation in a single direction [16, 34]. One must note that according to Holland [88] only normal processes exist for the LA branch. However, as pointed out by Lacroix *et al.* [16] applying this assumption means momentum has to be conserved for each scattering event involving an LA phonon, which leads to thermal conductivity values higher than the theoretical ones for temperatures between 100 K and 250 K in Si. Thus, in order to ensure a more realistic momentum conservation only half of the LA phonons are scattered using normal processes and this has been validated by various works [16, 58, 59, 82, 89, 86].

### **3.2.3 Thermal gradient and thermal properties**

Three-phonon scattering causes a change in the energy, and thus the temperature ( $T$ ) of the simulation domain ‘cell’ where scattering took place (we use a 1 nm domain discretization). If a phonon undergoes a three-phonon scattering as it propagates in the channel material, its frequency and energy will be re-initialized according to the temperature of the simulation ‘cell’ where it scatters. The total energy of the phonons in a simulation lattice ‘cell’ and the temperature is connected through the relation [89]:

$$E = \frac{V}{W} \sum_{pol} \sum_i \left( \frac{\hbar \omega_i}{\exp\left(\frac{\hbar \omega_i}{k_B T}\right) - 1} \right) g_p DOS \Delta \omega \quad (3.9)$$

where,  $\omega$  is the frequency,  $T$  the temperature,  $DOS$  the density of states and  $g_p$  the polarization branch degeneracy. A scaling factor  $W$  is also introduced to scale the number of phonons simulated to the real population (i.e. in Si at 300 K the phonon population is  $\sim 10^5$  per  $10 \text{ nm}^{-3}$  [89, 169]).

Every time a phonon with energy  $E_{ph}$  undergoes a three-phonon scattering event in a ‘cell’ whose temperature  $T_{cell}$  corresponds to energy  $E_{cell}$ , a new phonon frequency, wavevector and energy is re-initialized according to  $T_{cell}$ , in the same way that is done for the initialization in the contacts to begin with, i.e. according to the phonon  $DOS$  weighted by the Bose Einstein distribution function at that  $T_{cell}$ . The energy difference between this new phonon energy and the old phonon energy  $\Delta E$  is dissipated in the cell. Thus, new  $E_{cell}(\text{new}) = E_{cell}(\text{old}) + \Delta E$ . This energy dissipation corresponds to a change in the ‘cell’s’ temperature – the temperature can both, rise or fall, to account for the energy dissipated or extracted from the lattice. The energy difference  $\Delta E$  corresponds to a temperature change  $\Delta T$  as well, obtained from back-solving Eq. 3.9 equation for  $T$ . Thus, for each ‘cell’ in the domain we keep and update its energy  $E_{cell}$  and temperature  $T_{cell}$ .

Repeated iterations and scattering events that lead to exchange of energy with the lattice give a steady state thermal gradient between the two contacts that are placed at different temperatures  $T_H$  and  $T_C$ . If a phonon originates from a region of higher temperature (higher energy phonons), and enters a region of lower temperature, it is more probable that after a three-phonon scattering event a phonon with a lower energy will be created (initialized) since the temperature in the new ‘cell’ is lower and the rest of the energy will be dissipated in the lattice, raising the lattice temperature.

On the other hand, if a phonon enters a hotter region, coming from a colder region (lower energy phonon), it is more probable that after a three-phonon scattering event a phonon of higher energy will be created, absorbing energy from the lattice, and lowering its temperature. Thus, a temperature gradient is established for a continuous flow of phonons (shown in Fig. 3.3 with the yellow to green color scheme).



Initially, phonons are injected from both ends of the domain at their respective junction temperatures to establish a temperature gradient across the device as seen by the coloring in Fig. 3.3. An average of 2.5 million phonons are simulated for this, injected from each side.

Once the thermal gradient has converged, another 2.5 million phonons are then injected into the domain from each side. They can make it to the other side, or backscatter to where they originated from. The total energy entering and leaving the simulation domain is calculated by the net sum of the corresponding phonon energies that enter/exit at the hot and cold junctions as calculated by Eq. 3.9. We label the total incident energy from the hot junction as  $E_{\text{in}}^{\text{H}}$  and the total energy of phonons leaving the simulation domain from the hot junction as  $E_{\text{out}}^{\text{H}}$ . Similarly,  $E_{\text{in}}^{\text{C}}$  and  $E_{\text{out}}^{\text{C}}$  are the in-coming and out-going energies at the cold junction. We then determine the average phonon energy flux in the system as:

$$\Phi = \frac{(E_{\text{in}}^{\text{H}} - E_{\text{out}}^{\text{H}}) - (E_{\text{in}}^{\text{C}} - E_{\text{out}}^{\text{C}})}{n \langle \text{TOF} \rangle} \quad (3.10)$$

where  $n$  is the total number of phonons simulated and  $\langle \text{TOF} \rangle$  is their average time-of-flight. In-depth study on variations of  $\langle \text{TOF} \rangle$  is given as Fig. A4 in **Appendix A**. The simulated thermal conductivity is then extracted as:

$$\kappa_s = \Phi \frac{L_x}{A_c \Delta T} \quad (3.11)$$

where is the effective (scaled) cross section area of the simulation domain, which together with the scaling factor  $W$  above, are used to convert the simulated energy flux to thermal conductivity with the proper units [W/mK], as well as calibrate our 2D simulation result to the pristine Si bulk thermal conductivity value. Here  $A_c = L_y \times \text{effective thickness of } 0.1 \text{ nm}$  (details to follow).

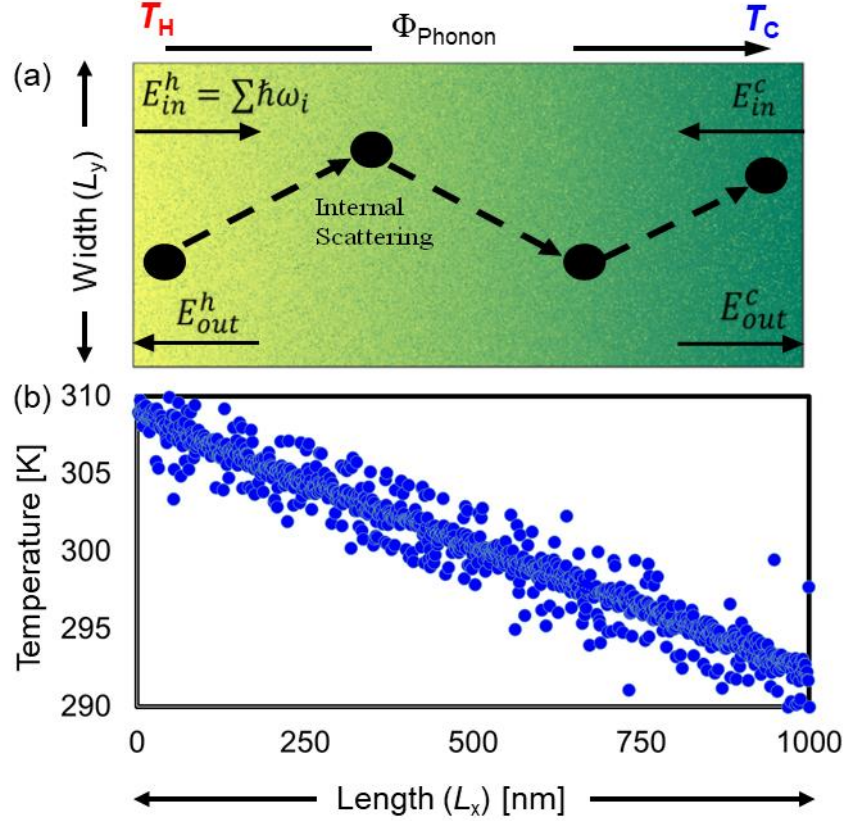


**Figure 3.3:** This is a top view of the studied simulation domain. (a) The coloring indicates the established thermal gradients when the left and right contacts are set to  $T_H = 310$  K (yellow) and  $T_C = 290$  K (green). Dashed-lines indicate the phonon path traced through the simulation domain (pristine silicon channel). Direction of net phonon flux  $\Phi$  is indicated above. The domain size is fixed to length  $L_x = 1000$  nm and width  $L_y = 500$  nm. (b) The *linear* temperature gradient established for 5 million phonons (1 point for every 1 nm in  $L_x$ ).

Next, to account for the fact that the length of the simulated domain ( $L_x$ ) is smaller than some phonon wavelengths, especially at lower temperatures, a scaling of the simulated thermal conductivity ( $\kappa_s$ ) is needed to compute the final thermal conductivity  $\kappa$  as [83]:

$$\kappa = \kappa_s \frac{(L_x + \lambda_{pp})}{(L_x)} \quad (3.12)$$

where  $\lambda_{pp}$  is the average phonon mean-free-path (MFP) of Si. Values for the average bulk MFP of phonons in Si at room temperature vary in the literature. In experimental studies, values from 100 nm [115] to 300 nm [170, 171] are mentioned (the latter is a study on Si films). In theoretical works an even greater variation – from 43 nm [172], 100 nm [173], 135 nm [83, 88], to 200-300 nm [11] have been reported. A simple

gray-body approximation based analytical estimate using kinetic theory gives a value of 43 nm [174, 175], however, this fails to address the phonon size effects observed in nanoporous silicon materials [175, 176]. More recent calculations estimate longer MFPs [177, 178]. Here we chose to use  $\lambda_{pp} = 135$  nm from Jeong *et al*, because in that work the MFP is reported over a variety of temperatures, and we could then validate our scaling method over the entire temperature range.

In this way, the finite size of the simulation domain is overcome using the average mean-free-path to scale the simulated thermal conductivity to the actual thermal conductivity of an infinite channel length. This scaling is important for the pristine bulk case of silicon where a large number of phonons have mean-free-paths larger than the simulation domain size, and replaces the need for periodic boundary conditions [89]. It is particularly important in the low temperature range where the low temperature  $\kappa$  peak of silicon is observed only after this scaling (see Fig. 3.4 below). It allows us to simulate shorter channels (in the micrometer range), which simplifies the simulation considerably. Thus, with the width of our simulation domain fixed at 500 nm and a scaling factor of  $W = 4 \times 10^5$  as specified above [179], which accounts for the reduction of the number of simulated phonons per unit volume, when using the thickness of 0.1 nm which corresponds to a single atomic layer [180] (to compute the volume  $V$  of the ‘cells’ above), our simulated thermal conductivity is  $\kappa_s = 130 \text{ Wm}^{-1}\text{K}^{-1}$  at 300 K.

After using Eq. 3.12 to account for the finite simulation domain we obtain the pristine bulk silicon  $\kappa \sim 148 \text{ Wm}^{-1}\text{K}^{-1}$ , which is the value for pristine bulk Si at room temperature [151, 86]. Note that in the case of nanocrystalline and nanoporous structures (the focus of this work), where the scattering length is determined by the grain sizes and pore distances, this scaling is less important. Indeed, the difference between the calculated thermal conductivity if the MFP scaling is performed using  $\lambda_{pp} = 135$  nm, vs  $\lambda_{pp} = 300$  nm is at most 15% in the pristine material case, drops to ~6% in the case pores are introduced, and becomes insignificant when nanocrystallinity is introduced as well. This is also reinforced by the fact that we have fully diffusive transport in our disordered systems, verified by simulations of channels with different lengths and extraction of the average phonon paths. (See Fig. A5, **Appendix A** for

validation of this method and the above statement for different  $\lambda_{pp}$  considerations, as well as demonstration of diffusive transport in the channels we simulate).

Thus, scaling by an ‘effective’ thickness we can calibrate the pristine material to Si bulk values, and by scaling with the mean-free-path in Eq. 3.12 we make it possible to simulate shorter channels and avoid periodic boundary conditions (see Fig. A6, **Appendix A** for validation this statement in channels with different lengths). Also, the use of the ‘single-phonon’ method is computationally simpler since we do not keep track of all phonon positions at the same time. All these simplify the computation significantly. In addition, although Monte Carlo can be efficient for complex geometries in 3D [16, 80, 81, 84, 86, 89, 151], here we effectively simulate a 2D material, i.e. corresponding to ribbons. We executed over 1000 simulations (just for validations and results in **Chapter 4**), each simulation taking approximately 8-10 hrs, which is an order of magnitude less computationally expensive compared to 3D simulations. Our results have been validated by comparing with experimental results, and other (2D and 3D) simulators in the next section.

### 3.2.4 Validation of thermal conductivity simulations for bulk Si case

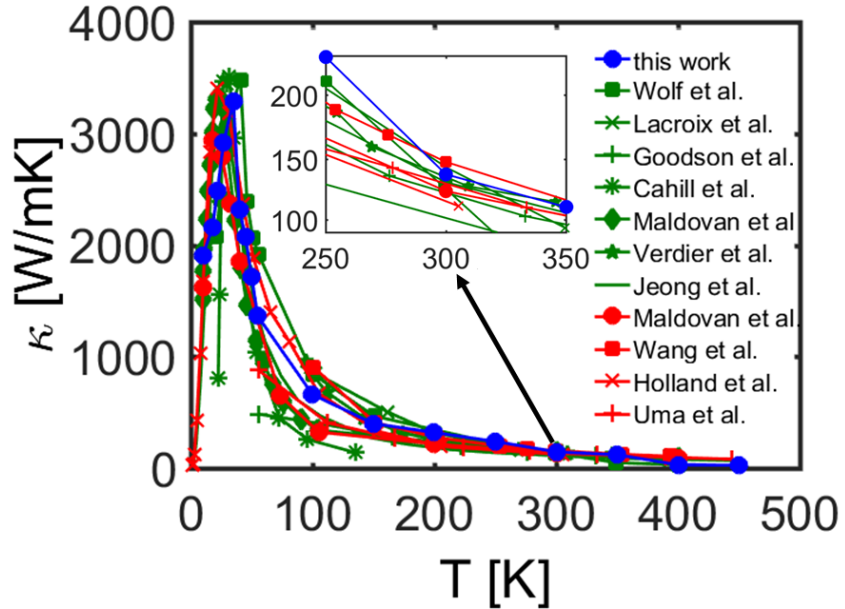


**Figure 3.4:** Validation of the single-phonon Monte Carlo simulator (blue line) for thermal conductivity ( $\kappa$ ) versus temperature for bulk Si. Simulation works (green lines) [16, 83, 89, 106, 116, 181, 182] and experimental works (red lines) [88, 96, 181, 183] are shown. The inset shows a close up of the temperature range between 250 K and 350 K. The simulated results are in close agreement to other literature results. Adopted from Chakraborty *et al.* [60].

Initially simulations were carried out to compare and validate the simulator for bulk values of silicon thermal conductivity. The figure above (Fig. 3.4) compares the single-phonon Monte Carlo thermal conductivity simulation results (blue line) for Si versus temperature to other (multi-phonon) Monte Carlo methods (in green lines) and experimental measured data (in red lines). Excellent agreement is found [59, 60].

### 3.2.5 Treatment of nanocrystalline structures

We consider transport in different nanostructured geometries. In the first case we consider nanocrystalline geometries as shown in Fig. 3.5a, with the average grain size in the simulation domain defined as  $\langle d \rangle = L_x / \langle N_G \rangle$ , where  $L_x$  is the length of the domain in the transport direction and  $\langle N_G \rangle$  is the average number of grains encountered in that length.

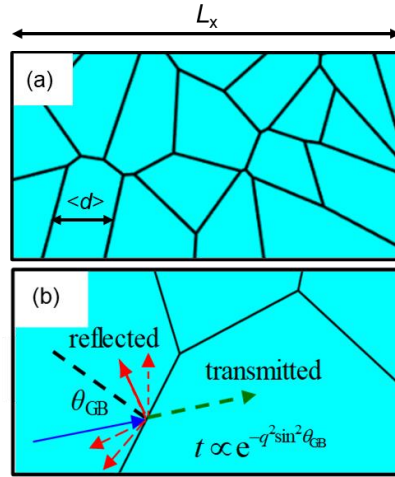


**Figure 3.5:** Phonon scattering in nanocrystalline structures. (a) Nanocrystalline (NC) materials with changing grain dimension ( $\langle d \rangle$ ) and length  $L_x$  in the transport direction. (b) Schematic for grain scattering indicating the initial angle of the phonon,  $\theta_{GB}$ , from the normal (black-dashed line), grain boundaries (black lines), initial path of the phonon (blue line) and probable paths of the phonon after scattering (red-dashed lines and green-dashed transmitted line). Examples of specular reflection (red-solid lines) and diffusive reflection (red-dashed lines) are also indicated. Transmission is dependent on grain boundary roughness as well as phonon wavevector  $q$ . Transmission probability is given by Eq. 3.13.

Grains in the nanocrystalline case are generated using Voronoi tessellations, where grain boundaries are created by considering input values for the number of

“seeding points” and the dimensions of the domain [156]. In these structures  $\kappa$  is impeded in two ways – the scattering of phonons due to the grain boundaries and internal three-phonon Umklapp scattering inside the grains. If a phonon reaches a boundary, then a decision is made whether the phonon will transmit to the other side, or reflect. This decision is made upon a probability distribution, which depends on the phonon wavevector, the roughness of the boundary  $\Delta_{\text{rms}}$  and the angle of incidence between the phonon path and the normal to the grain boundary  $\theta_{\text{GB}}$  (see Fig. 3.5b), and is given by the commonly employed relation [156]:

$$t_{\text{scatter}} = \exp\left(-4q^2 \Delta_{\text{rms}}^2 \sin^2 \theta_{\text{GB}}\right) \quad (3.13)$$

If the phonon makes it to the other side of the boundary, it continues its path intact. If it is reflected, then another random number, that depends on the specularly parameter  $p$  (roughness strength), dictates whether it will scatter specularly, or diffusively [81]. We do not assume that the phonon changes its energy at the interface as is common practice, but only its direction.

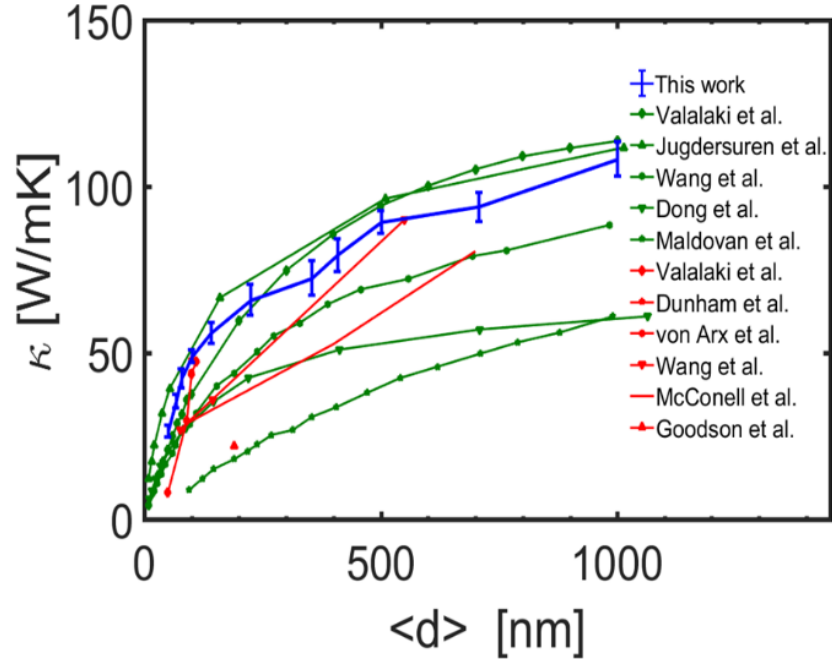


**Figure 3.6:** Validation of the Monte Carlo phonon transport simulator for nanocrystalline materials through comparisons with various simulation results (green lines) [65, 96, 97, 184, 185], and experimental results (red lines) [96, 98, 116, 185-187] for silicon available in the literature, are shown. Our simulation results showing the thermal conductivity for silicon as the grain size is varied from a grain dimension  $\langle d \rangle$  of 1000 nm to 50 nm are shown by the blue line. Error bars represent standard deviations for results over 50 simulations. Adopted from Chakraborty *et al.* [59].

Simulations were carried out from a grain dimension  $\langle d \rangle$  of 1000 nm to 50 nm as shown by the blue line in Fig. 3.6 above. Comparing with existing theoretical literature values (in green lines) and experimental data (in red lines) we see good agreement [59].

### 3.2.6 Treatment of nanoporous structures

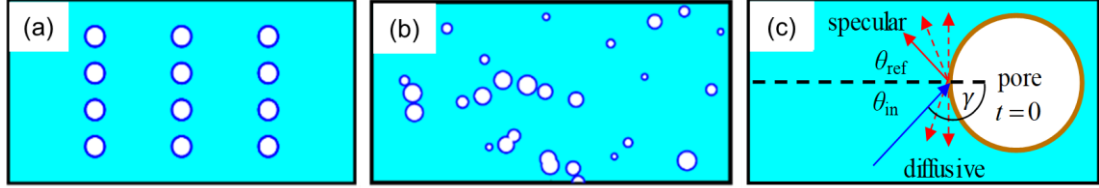


**Figure 3.7:** Phonon scattering in nanoporous structures. (a) Ordered nanopores within the pristine channel material in a rectangular arrangement. (b) Random nanopores within the pristine channel material (c) Schematic of scattering mechanism for pore scattering, indicating the pore boundary, the initial angle of the phonon  $\theta_{in}$ , and potential new angle of propagation  $\theta_{ref}$  depending on specularity parameter  $p$ . Probable paths of the phonon after scattering for both diffusive (red-dashed lines) and specular (red-solid line) are depicted.

We next look at the treatment of porous structures as we see in Fig. 3.7a and Fig. 3.7b above. If a phonon interacts with a pore boundary, it is reflected either specularly or diffusively. When it is reflected, then a random number, that depends on the specularity parameter  $p$  (roughness strength), dictates whether it will scatter specularly, or diffusively [81]. We do not assume that the phonon changes its energy at the interface as is common practice, but only its direction.  $p$  takes values from 0 to 1, with  $p = 0$  indicating diffusive, randomized reflection angle and  $p = 1$  specular reflection where the angle of incidence is the same as the angle of reflection (see Fig. 3.7c). In the case of specular pore boundary scattering, the angle the phonon will be reflected into, is defined based on geometrical considerations (the angle of incidence is the same as the angle of reflection) as:

$$\theta_{ref} = 2\gamma - \theta_{inc} \quad (3.14)$$

where  $\theta_{inc}$  is the angle of propagation of the phonon relative to the  $x$ -axis, and  $\gamma$  is the angle formed by the line perpendicular to the pore at the point of interaction and the  $x$ -axis, as explained in Fig. 3.7c. Using this formalism, we carry out simulations for the nanoporous structures – changing the number of pores in the pristine channel in

both the ordered and random nanoporous cases, seen in Fig. 3.7a and Fig. 3.7b respectively. We vary the percentage porosity (area of pores as a percentage of total area of domain) from 0% (an empty, pristine channel) up to 50%. Results vary depending on if the pore arrangements are ordered (blue-solid lines) or random i.e. disordered (blue-dashed line), however, again qualitatively and quantitatively our results are within other literature data. This is seen in Fig. 3.8 below.

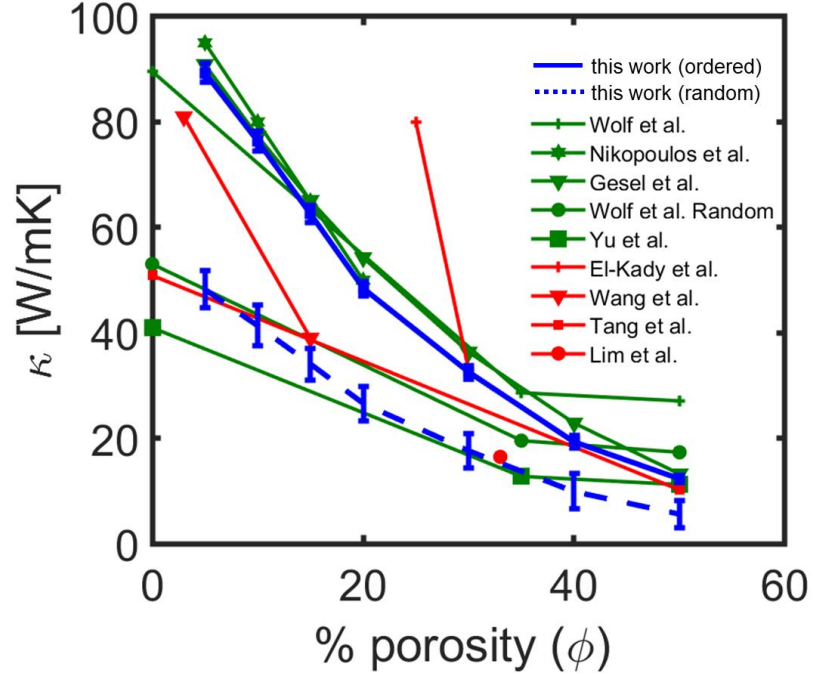


**Figure 3.8:** Validation of the simulator for nanoporous Si materials. Various simulation results are shown (green lines) [86, 89, 152, 188, 189], and compared against experimental results (red lines) [41, 96, 190, 191]. Our simulation results for the thermal conductivity of silicon as the percentage porosity ( $\phi$ ) (area of pores as a percentage of total area of domain) is varied up to 50%. Simulations of ordered porous structures are indicated by the blue-solid line, and of disordered porous structures the blue-dashed line. Adopted from Chakraborty *et al.* [59].

Note that instead of a constant specularity  $p$ , in Monte Carlo it is also possible to determine the actual specularity for each phonon using the expression:

$$p(q) = \exp(-4q^2 \Delta_{\text{rms}}^2 \cos^2 \theta) \quad (3.15)$$

where  $\Delta_{\text{rms}}$  is the roughness of the pore boundary surface and  $\theta$  is the angle of phonon incidence [192]. This formalism would also allow wavevector ( $q$ ) dependence of reflections. In that case, what is constant is the surface roughness ( $\Delta_{\text{rms}}$ ). Here we use a constant  $p$ , and the rationale behind studies which use constant  $\Delta_{\text{rms}}$  versus constant  $p$  [86, 89, 172, 193-196], is that the microscopic details of phonon scattering at



interfaces are poorly understood anyway [195]. However, either way gives very similar results without any qualitative or quantitative differences in disordered structures. For example, one can map a specific  $\Delta_{\text{rms}}$  to a specific speculariry; the  $p = 0.1$  case in our results below corresponds to  $\Delta_{\text{rms}} \sim 0.3$  nm (see Fig. A7, **Appendix A**), which corresponds well to rough silicon surfaces [197, 198].

### 3.3 Summary

In summary, in this chapter we explored different methods to simulate phonon transport in nanostructured materials. We developed a large-scale ‘single-phonon’ Monte Carlo phonon transport simulator to solve the Boltzmann Transport Equation for phonons in Si nanostructures. We established the treatment of nanocrystalline and nanoporous geometries in silicon nanomaterials. The simulator was thoroughly validated for the bulk pristine, nanocrystalline and nanoporous cases, against both experimental and theoretical values in the literature. The MC method and the phonon transport simulator described in this chapter form a part of our published works [58-62]. For these results simulations were carried out using up to 10 million phonons at a time (and up to 50 iterations per geometry) with appropriate supercomputing clusters, when necessary. The phonon transport simulator was also repackaged, written entirely in Matlab, as a more user friendly app using in-built Matlab GUI. The app was used and validated against existing literature [41, 86, 89, 96, 152, 189, 190, 191]. Feedback was used to improve the app and further details regarding its most updated version are available in **Appendix A**, in the section A12.

Using the methods discussed in this chapter we now investigate the phonon transport in hierarchical nanostructures, highly disordered geometries at different temperature regimes and novel nanostructured material designs in the following chapters.

## 4. Phonon transport in hierarchically disordered silicon nanostructures

### 4.1 Introduction: hierarchically nanostructured materials

As discussed in **Chapter 1**, hierarchical and highly disordered nanostructures are one of the most promising ways to achieve very high thermoelectric (TE) efficiencies and, thus, engineering such materials has recently attracted significant attention. Strong disorder, and more specifically disorder on hierarchical length scales, originating from various types of defects, can scatter phonons of different wavelengths throughout the spectrum and drastically reduce thermal conductivity. This approach substantially improves thermoelectric efficiency and it is currently being employed in a variety of new generation thermoelectric materials. For example, using hierarchical inclusions at the atomic scale, the nanoscale, and the mesoscale in the PbTe–SrTe system, Biswas *et al.* reported a  $\kappa$  of  $0.9 \text{ W m}^{-1} \text{ K}^{-1}$  at 915 K and a  $ZT$  of 2.2 [5]. More recently, using this method for the p-type  $\text{Pb}_{0.98}\text{Na}_{0.02}\text{Te}$ –SrTe system, Tan *et al.* reported an even lower lattice thermal conductivity ( $\kappa$ ) of  $0.5 \text{ W K}^{-1} \text{ m}^{-1}$  and a higher  $ZT$  of 2.5 at 923K [100]. Reports also show that hierarchical nanostructures can improve the thermoelectric power factor as well [45, 54-58].

Drastic reductions in thermal conductivity have been reported in nanocrystalline silicon materials. Wang *et al.* [96] showed that the room temperature silicon thermal conductivity decreases from  $81 \text{ W m}^{-1} \text{ K}^{-1}$  to  $24 \text{ W m}^{-1} \text{ K}^{-1}$  as the average grain size decreases from 550 nm to 76 nm, whereas  $\kappa$  below  $5 \text{ W m}^{-1} \text{ K}^{-1}$  has been reported for average grain sizes of about 10 nm [97]. For grain sizes of 3 nm Nakamura *et al.* reported  $\kappa = 0.787 \pm 0.12 \text{ W m}^{-1} \text{ K}^{-1}$  [51, 52]. Nanoporous ‘holey’ structures have been shown to exhibit reproducibly low  $\kappa$  around  $1\text{-}2 \text{ W m}^{-1} \text{ K}^{-1}$  [41, 53, 43], while still maintaining sufficient electronic properties. Nanostructures that combine these achieve even lower  $\kappa$ . A recent silicon-based work reported  $\kappa$  of  $20.8 \pm 3.7 \text{ W m}^{-1} \text{ K}^{-1}$  for an average pore size of  $\sim 30$  nm and grain sizes between 50 nm to 80 nm [98]. By reducing both pore and grain sizes, however, Basu *et al.* reported  $\kappa = 1.2 \text{ W m}^{-1} \text{ K}^{-1}$  at 40% porosity in p-type silicon [99]. A recent work in SiGe nanomeshes, reported ultra-low  $\kappa$  of  $0.55 \pm 0.10 \text{ W m}^{-1} \text{ K}^{-1}$  for SiGe nanocrystalline nanoporous structures, a value well below the amorphous limit [33].

A significant amount of work can be found in the literature attempting to clarify these experimental observations. However, theoretical investigations of thermal conductivity in highly/hierarchically disordered nanostructures (which include not only crystalline boundaries, but also pores of random sizes placed at random positions) are very limited. Understanding the qualitative and quantitative details of such geometries on the thermal conductivity would allow the design of more efficient thermoelectrics and heat management materials in general. In this chapter, we solve the Boltzmann Transport Equation for phonons in disordered Si nanostructures using the Monte Carlo (MC) method and the simulator described in **Chapter 3**. Monte Carlo, which can capture the details of geometry with relevant accuracy, is widely employed to understand phonon transport in various nanostructures such as nanowires [16, 82, 149], thin films [150, 151], nanoporous materials [89, 152-155], polycrystalline materials [95, 97, 156-158], nanocomposites [87, 159], corrugated structures [160-163], Silicon-on-Insulator devices [164], etc.

In this chapter, we consider geometries that include grain boundaries, surfaces, and pores as in realistic nanocomposite materials, which all contribute to reducing thermal conductivity. We show that the influence of randomization in the disorder has a crucial effect in determining thermal conductivity, despite being usually overlooked. After examining the influence of nanocrystallinity and porosity individually and combined, we validate the simplified compact models commonly employed in the literature. We then propose more accurate models based on simple geometrical configurations that describe the randomization of disorder. These improved models could serve as a valuable tool for materials design and for experimentalists to more accurately evaluate a first order interpretation of their results, without the need of large-scale simulations.

This chapter is organized as follows: In Section 4.2 we investigate the effects of nanocrystallinity, grain size and grain roughness in nanocrystalline case. In Section 4.3 we present our results on the effects of nanoporous structures, randomized disordered pores and hierarchical nanostructuring on thermal conductivity  $\kappa$ . In Section 4.4 we validate existing analytical models for such geometries and develop our more accurate compact models for highly disordered cases. In Section 4.5 we

verify the applicability of Matthiessen's rule for the hierarchical nanostructures considered in previous sections. Finally, in Section 4.6 we present our conclusions.

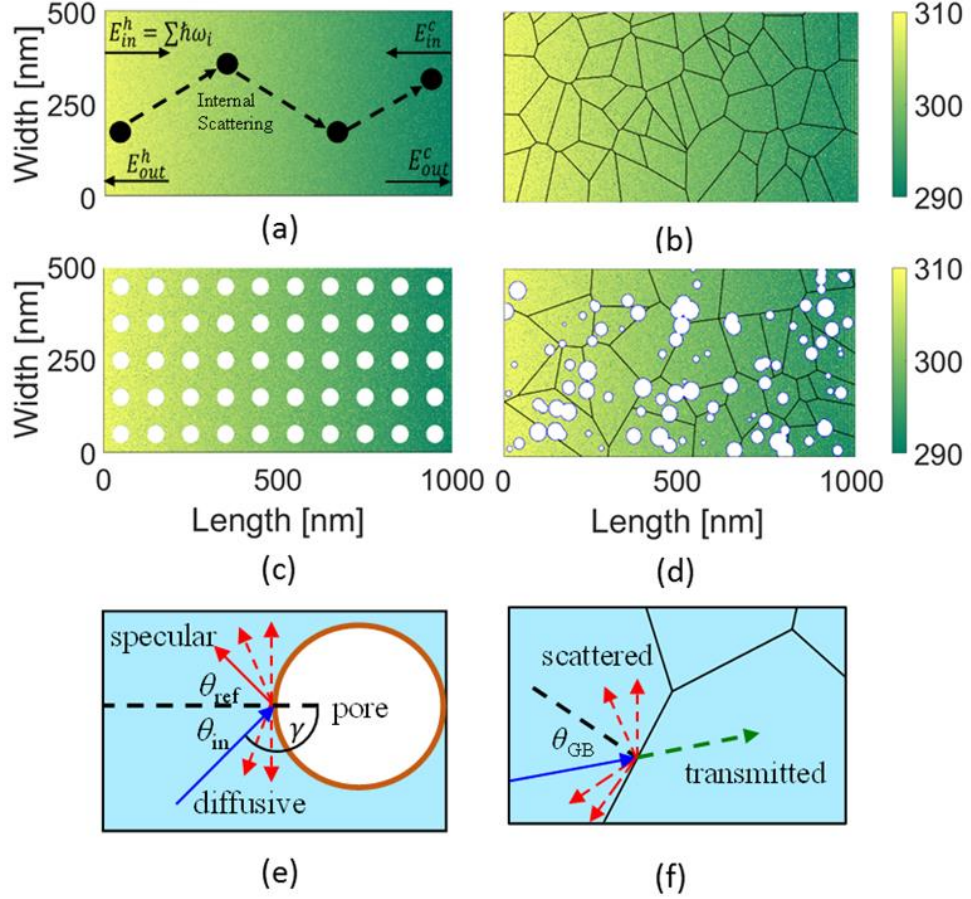


**Figure 4.1:** Examples of the nanostructured geometries considered. The coloring indicates the established thermal gradients when the left and right contacts are set to  $T_H = 310$  K (yellow) and  $T_C = 290$  K (green). (a) Pristine silicon channel. (b) Nanocrystalline (NC) channel. (c) Ordered nanopores (NP) within the channel material of  $\sim 20\%$  porosity in a rectangular arrangement. (d) Combined NC and disordered NP material. (e) Schematic of scattering mechanism for pore scattering, indicating the pore boundary, the initial angle of the phonon  $\theta_{in}$ , and potential new angle of propagation  $\theta_{ref}$  depending on specularly parameter  $p$ . Probable paths of the phonon after scattering for both diffusive (red-dashed lines) and specular (red-solid line) are depicted. (f) Schematic of the scattering mechanism for grain boundary scattering, indicating the initial angle of the phonon  $\theta_{GB}$  from the normal (dashed line), grain boundaries (black lines), initial path of the phonon (blue line) and probable paths of the phonon after scattering (red-dashed lines and green-dashed, transmitted line). Reproduced from [D. Chakraborty *et al.*, Phys. Rev. B 98, 115435 (2018)], Copyright 2018, American Physical Society.

## 4.2 Effects of grain size and roughness in nanocrystalline case

The Monte Carlo (MC) approach has been adopted for a semi-classical particle-based description of phonon transport. The MC simulation method is described adequately in the literature, but because our method differs in some details, we have described our numerical scheme thoroughly in **Chapter 3**. We use the ‘single-phonon MC’ approach which differs from the multi-phonon MC approach described in various works in the literature [11, 16, 80, 81, 85] in terms of phonon attributes book-keeping. The domain is populated with nanostructured features as shown in Fig. 4.1 above. Here, we look at the structures depicted in Fig. 4.1 above at 300 K only. Initially simulations were carried out to compare and validate the simulator for bulk values of silicon thermal conductivity as seen in **Chapter 3**. Good agreement is found between our simulated results and literature values of silicon thermal conductivity across a large temperature range with several works in the literature. After bulk-Si validation, we proceeded with the analysis of nanostructuring on the thermal conductivity.

The treatment and validation of nanocrystalline structures is outlined in **Chapter 3** (Section 3.3.5). We begin our investigation with the effects of the grain size  $\langle d \rangle$  and boundary roughness ( $\Delta_{\text{rms}}$ ) on the thermal conductivity. The probability of phonon transmission across a grain boundary is given by:

$$t_{\text{scatter}} = \exp\left(-4q^2 \Delta_{\text{rms}}^2 \sin^2 \theta_{\text{GB}}\right) \quad (3.13)$$

The results are shown in Fig. 4.2 where  $\kappa$  is plotted as a function of average grain size  $\langle d \rangle$ . Each point is an average of 50 simulations of different geometry realizations.

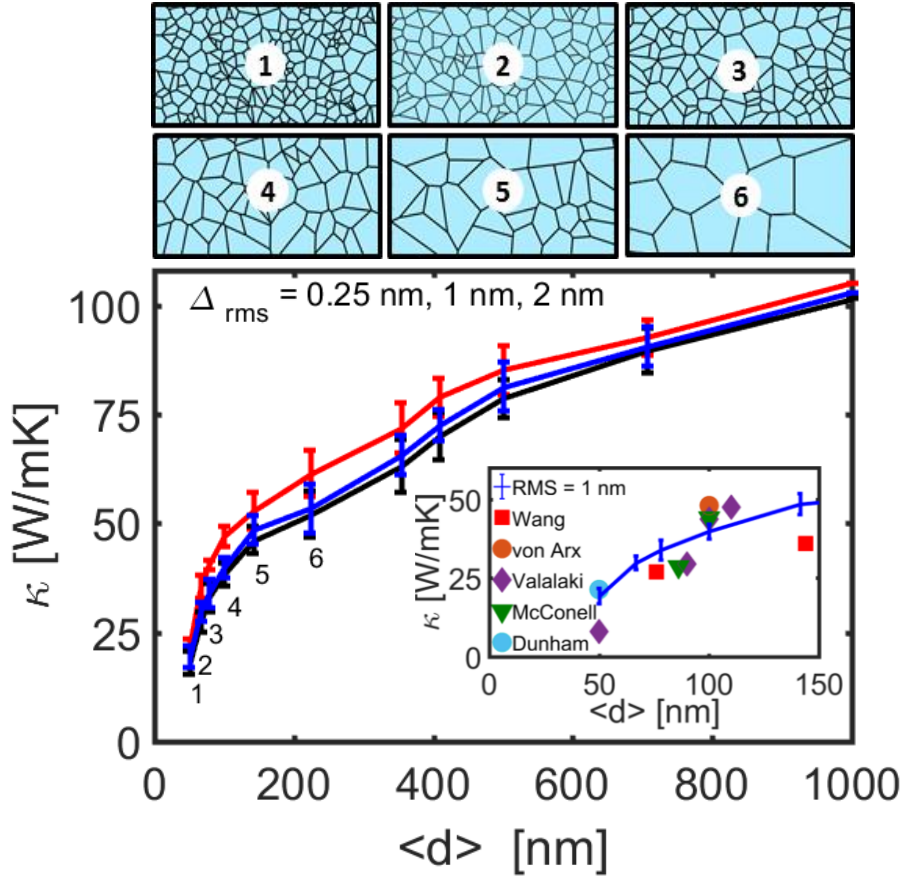


**Figure 4.2:** The effects of grain size and grain boundary roughness ( $\Delta_{rms}$ ) on the thermal conductivity of the silicon channel. Grain size is varied from an average grain dimension  $\langle d \rangle$  of 1000 nm down to 50 nm. The structure geometry insets labelled ‘1’ to ‘6’ give typical examples of geometries from  $\langle d \rangle = 50$  nm to 225 nm, respectively. We simulate three different values of grain boundary roughness,  $\Delta_{rms} = 0.25$  nm (red line), 1 nm (blue line) and 2 nm (black line). Each point is an average of 50 simulations. A sharp drop in thermal conductivity is observed below  $\langle d \rangle \sim 140$  nm (structure sub-figure and point ‘4’). Inset: Some available experimental results [96, 98, 185, 186, 189] are compared to the  $\Delta_{rms} = 1$  nm (blue line). Reproduced from [D. Chakraborty *et al.*, Phys. Rev. B 98, 115435 (2018)], Copyright 2018, American Physical Society.

We consider average grain size from  $\langle d \rangle = 1000$  nm down to  $\langle d \rangle = 50$  nm as indicated by the geometry sub-figures above the graph in Fig. 4.2 (from sub-figure 1 where  $\langle d \rangle = 50$  nm to sub-figure 6 where  $\langle d \rangle = 225$  nm). Three different values of  $\Delta_{rms} = 0.25$  nm, 1 nm, and 2 nm were simulated, shown in Fig. 4.2 by the red, blue, and black lines, respectively. Decreasing grain size causes a reduction in  $\kappa$ , from  $97.8 \text{ Wm}^{-1}\text{K}^{-1}$  to  $19.9 \text{ Wm}^{-1}\text{K}^{-1}$ . This is consistent with other available theoretical [65, 95-97, 116, 183-187, 199] and experimental results [96, 98, 185, 186, 189], as shown in the inset in Fig. 4.2. Note that our large grain thermal conductivity does not reach the bulk value ( $\kappa \sim 140 \text{ Wm}^{-1}\text{K}^{-1}$ ) because we consider boundary scattering on the

surfaces of the simulation domain. An important observation is that a rapid drop in  $\kappa$  is observed for structures in which the average grain size is below the average phonon mean-free-path ( $\lambda_{pp} = 135$  nm). For these structures, grain boundary scattering has a more dominant role than intrinsic three-phonon scattering. This observation is consistent for the different values of grain boundary roughness. On the other hand, changes in the values of grain boundary roughness ( $\Delta_{rms}$ ) seem to play a comparatively smaller role in decreasing  $\kappa$  (comparing the red, blue, and black lines respectively, in Fig. 4.2). Phonon paths are already randomized by the numerous grains and intrinsic scattering, and thus the additional randomness from grain boundary roughness plays a minimal role. Similarly, it is also noticeable that as the grain size decreases the variability in the results (the average of the 50 simulations for each point), as indicated by the error bars, also decreases, especially for grain sizes smaller than the MFP.

### 4.3 Effects of nanoporous and hierarchical nanostructuring

This section explores the effects of nanoscale porous structures, highly random disordered porous structures and combined hierarchical nanostructuring on the thermal conductivity. The effects of porosity (percentage of porous region compared to total area), pore boundary roughness (in terms of specularity) are initially investigated. The effects of randomness or disorder at the nanoscale is then examined using only nanoporous structures. Finally, nanocrystalline and nanoporous structures are combined to form hierarchical composite nanostructures. Thermal behaviour in hierarchically nanostructured material, in both ordered and disordered cases, is then further investigated.

#### 4.3.1 Influence of porosity and pore roughness

Figure 4.3 summarizes the effects of porosity ( $\phi$ ) and pore boundary roughness on the thermal conductivity of nanoporous silicon. Treatment of nanoporous structures is outlined in **Chapter 3** (Section 3.3.6). Examples of the typical geometries considered, with porosities of 5%, 10% and 15%, for both ordered and disordered configurations, are shown as sub-figures above Fig. 4.3. In all sub-figures the channel dimensions are length  $L_x = 1000$  nm and width  $L_y = 500$  nm.

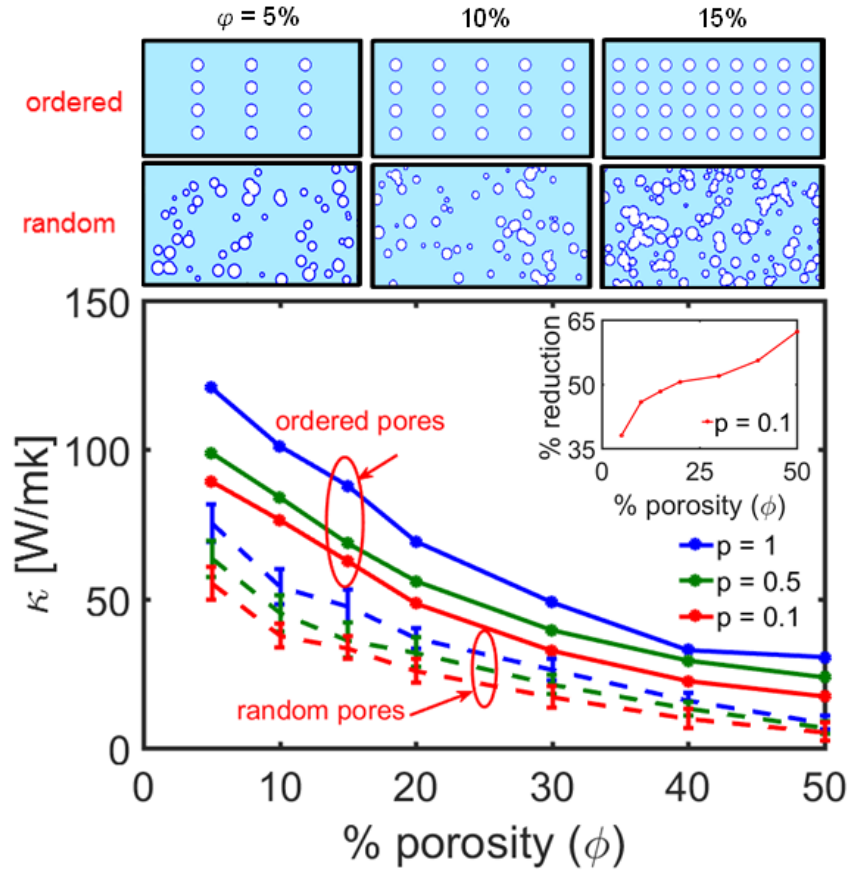


**Figure 4.3:** The thermal conductivity ( $\kappa$ ) versus porosity ( $\phi$ ) for two geometry cases – ordered case (solid lines) and random case (dashed lines). Three different values for boundary specularities are considered:  $p = 1$ , totally specular boundary scattering (blue lines);  $p = 0.5$  (green lines); and  $p = 0.1$ , almost diffusive boundary scattering (red lines). The inset depicts the percentage reduction in thermal conductivity for the  $p = 0.1$  (red line), random porosity case compared to the ordered case. The geometry structures of the simulated geometries for ordered and random arrangement cases for 5%, 10 % and 15 % porosity are shown on top of the figure. In all cases the domain size is fixed to length  $L_x = 1000$  nm and width  $L_y = 500$  nm. Reproduced from [D. Chakraborty *et al.*, Phys. Rev. B 98, 115435 (2018)], Copyright 2018, American Physical Society.

In the ordered geometry cases the pore diameter is fixed at  $D = 50$  nm. In the random cases the pores are arranged in random positions and their diameters vary from 10 nm to 50 nm using a uniform distribution. Here,  $\kappa$  is plotted as a function of porosity  $\phi$  ( $x$ -axis), and results for structures with boundary specularities parameters  $p = 1$  (fully specular case, blue line),  $p = 0.5$  (green line), and  $p = 0.1$  (almost fully diffusive case, red line) are shown. The ordered pore cases are shown in solid and the randomized pore cases in dashed lines. Again, each point is the average of 50 different configurations with the variation bar denoted. Note that for the  $p = 1$  case (blue-solid



line), where boundaries everywhere are completely specular, and for zero porosity, the value of  $\kappa$  approaches the bulk  $148 \text{ Wm}^{-1} \text{ K}^{-1}$ .

Phonons back-scatter on the pores since the pores are large and transmission is not allowed, unlike in the case of grain boundary scattering where transmission of phonons through the grain boundary is statistically allowed. Firstly, we observe that reducing specularity causes a reduction in  $\kappa$ . However, an order of magnitude decrease in  $p$  from  $p = 1$  (blue line) to  $p = 0.1$  (red line) causes only a  $\sim 33\%$  drop in  $\kappa$  at most, and only at low porosities where phonon trajectories might still not be completely randomized [86]. Increasing porosity, on the other hand, causes a significant decrease in  $\kappa$  as also observed in previous theoretical [86, 89, 152, 173, 188, 200] and experimental results [41, 43, 53, 201]. In fact, the effect of porosity has a much greater impact than pore roughness. An order of magnitude reduction in specularity causes roughly the same effect as 15 % porosity in the ordered case (blue-solid line), an observation consistent with previous works [86, 89]. We note here that Monte Carlo does not account for coherent phonon effects which could affect the phonon spectrum and thermal conductivity, but there is increasing evidence that such effects are important only at low temperatures and weak roughness conditions [196, 202], whereas here we deal with room temperature and mostly diffusive boundaries.

#### **4.3.2 Influence of randomized pore positions and diameters**

We next consider the effects of random diameter and pore positions at different porosities as shown in the ‘random’ sub-figures in Fig. 4.3. A further decrease in thermal conductivity is observed as a consequence of disorder, irrespective of pore boundary specularity. For the diffusive pore case the reduction can vary from  $\sim 35\%$  (low porosity) to  $\sim 65\%$  (high porosity), which is quite significant, as shown in the inset of Fig. 4.3. We discuss the reasons behind this in detail in Section 4.4 below when we construct an analytical model to account for this reduction. On the other hand, the influence of specularity in the randomized pore cases is again comparatively minimal and diminishes as porosity increases (blue, green and red-dashed lines in Fig. 4.3). It is illustrative to separate the two effects that constitute the randomization in the polydispersed nanoporous geometries, i.e. the randomization in pore position and randomization in pore diameter. Figure 4.4 shows the thermal conductivity if

structures with ordered pores and polydispersed pores (solid and dashed red lines – same as the  $p = 0.1$  cases in Fig. 4.3), and the corresponding thermal conductivity of the structures in which only the pore positions are randomized. Typical geometries are depicted in the schematics of Fig. 4.4.

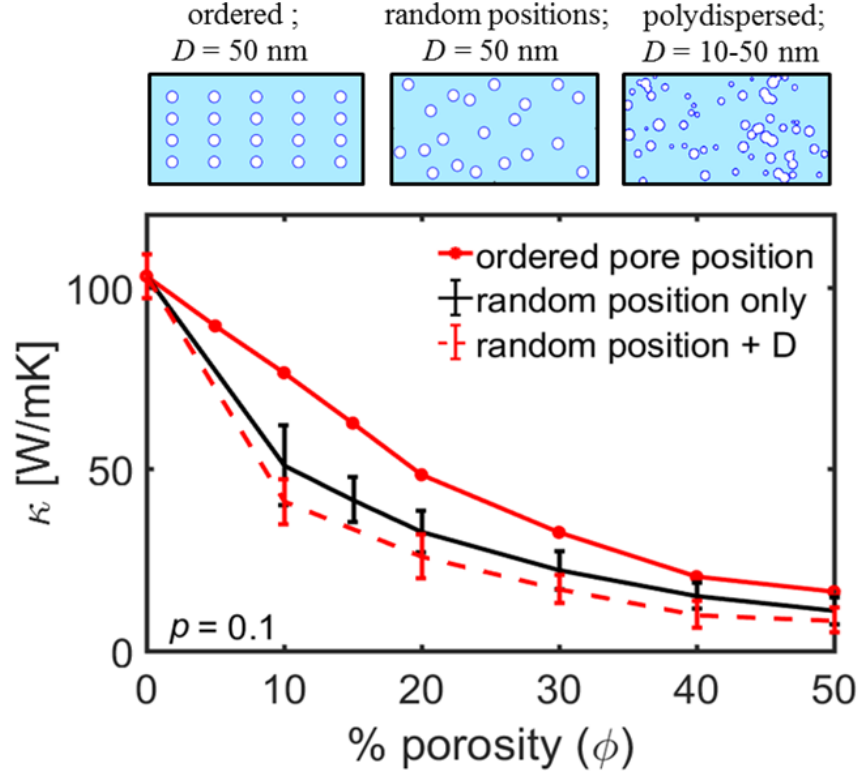


**Figure 4.4:** The thermal conductivity versus porosity ( $\phi$ ) for ordered pore structures, randomized pore structures, and polydispersed geometries with randomized pore positions and diameters. In the first two cases (red and black solid lines), the diameter is fixed at  $D = 50$  nm (see sub-figure schematics for 10% porosity). In all cases the specularity for all boundaries is fixed at  $p = 0.1$ . Reproduced from [D. Chakraborty *et al.*, Phys. Rev. B 98, 115435 (2018)], Copyright 2018, American Physical Society.

Clearly, the randomization of the positions alone has a significant effect in lowering the thermal conductivity. It seems that for lower porosities it is the dominant factor for the deviation between the ordered and the polydispersed geometries. For higher porosities both randomized location and randomized diameters have similar influence in further reducing the thermal conductivity from the ordered pore case. The effect of pore scattering surface area on thermal conductivity is also further explored in Section 4.4.3 and in the Appendix (see Section A8 and Fig. A8 in **Appendix A**).

### 4.3.3 Hierarchical disordered nanostructures

We next combine the effects of nanocrystallinity and porosity, as in realistic nanocomposite materials. Again, ordered and randomized pores are considered as shown in Fig. 4.5a and Fig. 4.5b, respectively, shown here for 5% porosity.

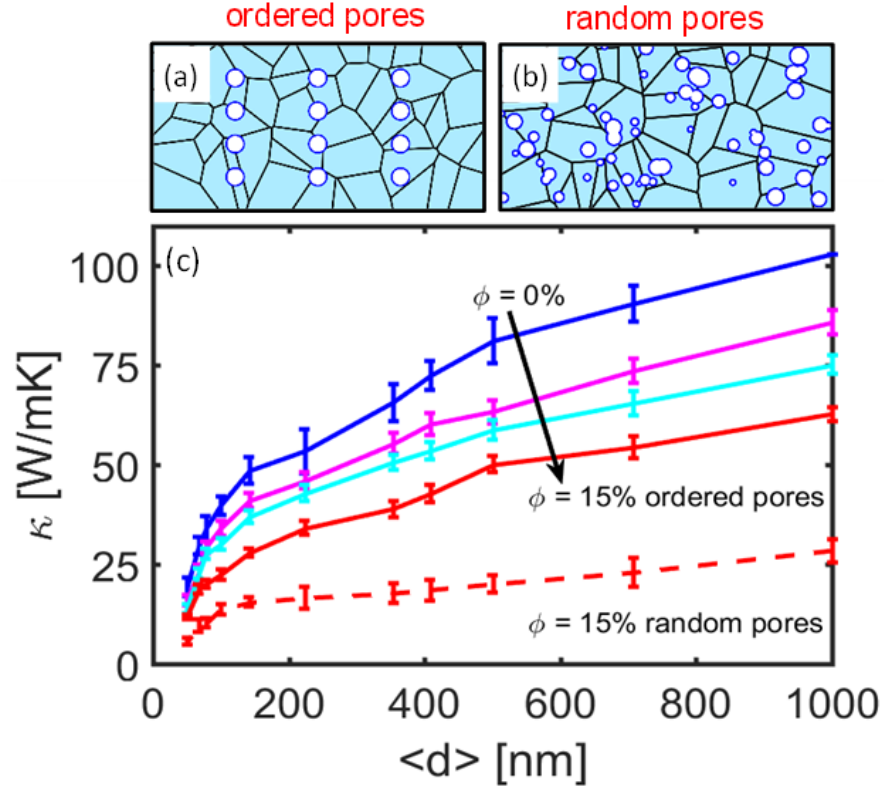


**Figure 4.5:** Monte Carlo simulations showing the combined effects of grain size and porosity ( $\phi$ ) in both the ordered pores case (solid lines) and random pores case (dashed line) versus grain size  $\langle d \rangle$ . The thermal conductivity at for porosities  $\phi = 0\%$ ,  $5\%$ ,  $10\%$  and  $15\%$  are shown by the blue, magenta, light-blue, and red lines respectively. The effect of combined nanocrystalline and nanoporous material with random pore positions and sizes (uniformly distributed between 10 nm to 50 nm) is depicted by the red-dashed line. Examples of typical geometries simulated for the case of 5% porosity, for both ordered and random pore arrangements, are shown above the figure. Reproduced from [D. Chakraborty *et al.*, Phys. Rev. B 98, 115435 (2018)], Copyright 2018, American Physical Society.

Figure 4.5c plots the thermal conductivity versus the average grain size ( $\langle d \rangle$ ) for structures with different porosity values ( $\phi$ ). The roughness on the transmittable grain boundaries is fixed to  $\Delta_{\text{rms}} = 1$  nm, while for the outer top/bottom boundaries of the simulation domain and the pore boundaries we use a specularity parameter of  $p =$

0.1. Both conditions correspond to rough, almost fully diffusive cases. Again, each point shown in Fig. 4.5c is an average of 50 simulations. The top blue line depicts the zero porosity case, the same as the initial results for  $\Delta_{\text{rms}} = 1$  nm shown in Fig. 4.2 (blue line). Adding pores in an ordered fashion further reduces  $\kappa$ . This can be seen for 5% (magenta line), 10% (light-blue line) and 15% (red line) ordered porosity. The thermal conductivity decreases as either porosity increases, or the average grain size  $\langle d \rangle$  decreases, with large porosity dominating at large grain sizes, whereas boundary scattering dominates at small grain sizes. With regards to the variation bars, as porosity increases and/or grain size decreases, scattering becomes more and more randomized, and variations in the thermal conductivity are reduced, as also observed above.

The red-dashed line in Fig. 4.5c shows the thermal conductivity versus average grain size in the case of a  $\phi = 15\%$  randomized porous structure. The pores are randomized in terms of diameter and position as indicated in Fig. 4.5b. The pore sizes are again varied from  $D = 10$  nm to 50 nm in a random fashion using a uniform distribution. As in the case of only porous geometries earlier, randomization in the pore features reduces  $\kappa$  significantly. In this case, at  $\langle d \rangle = 1000$  nm at the right side of Fig. 4.5c, there is an initial 50% drop in  $\kappa$  in the randomized case compared to the ordered (red lines), followed by a slow rate of decrease in  $\kappa$  as the grain size decreases. This suggests that a high degree of randomization and small average pore size, makes phonon scattering on pores much more dominant than the intrinsic three phonon scattering and grain boundary scattering. When the grain size becomes very small (below  $\lambda_{\text{pp}}$ ), then it starts to play an important role again. In these structures, around 20 scattering events is not uncommon across the domain (see Fig. A6b, **Appendix A**).

#### 4.4 Analytical models developed

There are many analytical models available in the literature that describe the effects of material geometry on  $\kappa$ , either in the presence of grain boundaries [184, 199, 200, 203], or pores [182, 188, 204, 205]. These are based on simple geometrical considerations, and assume uniformity of the corresponding features, but in the case of non-uniformities, or in the presence of two or more types of nanosized features, their accuracy fades. Here we compare our full simulation results to some of these

widely employed analytical models found in the literature. We aim to quantify their validity and further develop more accurate models that can capture the effects of non-uniformity (disorder) in nanostructuring, based on simple geometrical considerations.

#### 4.4.1 Nanocrystalline case

The analytical models widely employed for nanocrystalline materials, are based on the simple logic that: i) phonons in a nanostructured material undergo additional scattering events at a rate at which they meet the boundaries as they propagate in the material, ii) an additional interface resistance (Kapitza resistance) is introduced due to disruptions in the phonon flow. Based on these principles, a few examples of the form that these models take are given in the works of Nan *et al.* [200], Yang *et al.* [203] and Dong *et al.* [184], given by Eqs. 4.1, 4.2, and 4.3, respectively:

$$\kappa = \frac{\kappa_0}{\left[1 + \frac{2R_K\kappa_0}{d}\right]} \quad (4.1)$$

$$\kappa = \frac{\kappa_0}{\left[1 + \frac{R_K\kappa_0}{d}\right]} \quad (4.2)$$

$$\kappa = \frac{\frac{\kappa_0}{1 + \frac{\lambda_{pp}}{d^\alpha}}}{\left[1 + \frac{R_K\kappa_0}{\left(1 + \frac{\lambda_{pp}}{d^\alpha}\right)}\right]} \quad (4.3)$$

Above,  $\kappa_0$  is the bulk thermal conductivity of silicon and  $\lambda_{pp}$  is the average phonon-phonon mean-free-path (here  $\lambda_{pp} = 135$  nm),  $R_K$  is the Kapitza resistance, and  $d$  the average grain size ( $\langle d \rangle$  in Monte Carlo). Here we use  $R_K = 1.06 \times 10^9 \text{ Km}^2\text{W}^{-1}$  [206]. Literature values for  $R_K$  vary slightly in the range of  $1 - 1.16 \times 10^9 \text{ Km}^2\text{W}^{-1}$  [118, 184, 206 - 210], a variation that makes only very little qualitative difference to the results we show below (at most 2 to 3%, see Fig. A9, **Appendix A**). In another simplified intuitive picture,  $\kappa$  is scaled by how many more scattering events a phonon undergoes due to the crystalline boundaries within the length of its pristine material MFP as:

$$\kappa = \frac{\kappa_0}{\left(1 + \frac{\lambda_{pp}}{d}\right)} = \kappa_0 \left[ \frac{d}{d + \lambda_{pp}} \right] \quad (4.4)$$

Note that  $\Delta_{rms}$  or the boundary specularity does not appear in any of these models, which are assumed valid under diffusive phonon scattering conditions.

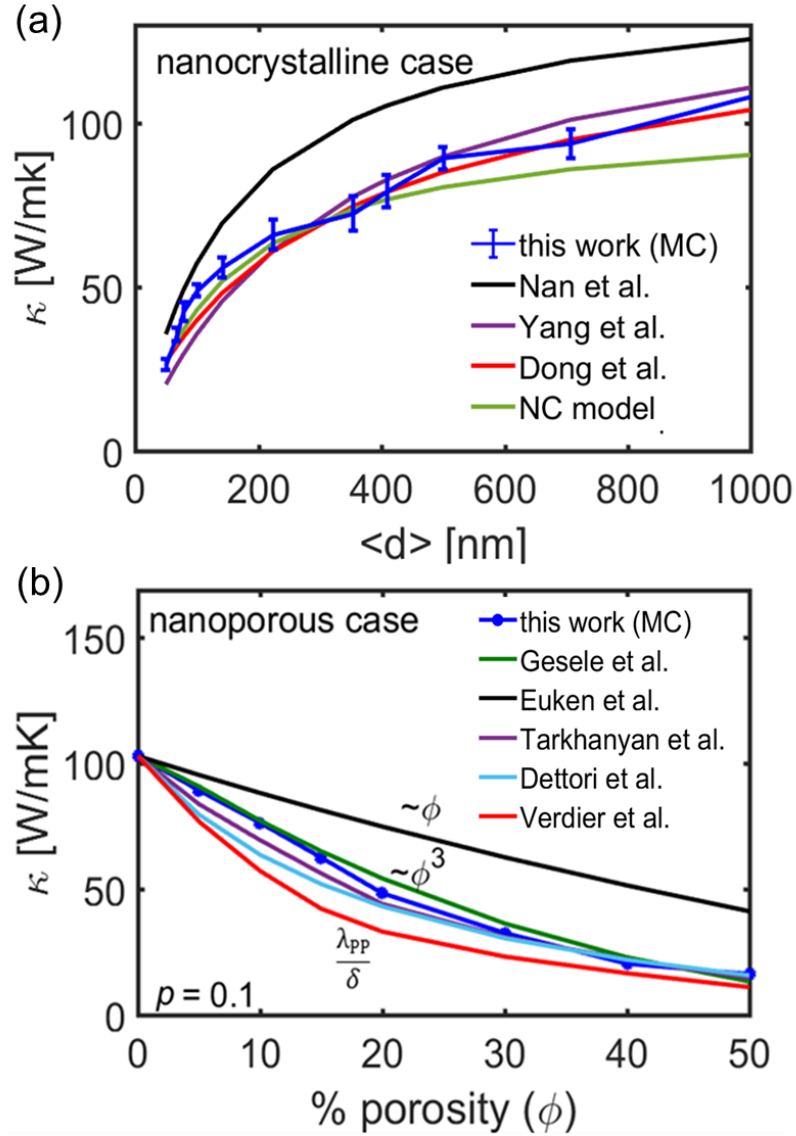


**Figure 4.6:** Monte Carlo simulation results compared to analytical models. (a) Thermal conductivity versus grain size for commonly employed analytical models for nanocrystalline geometries compared to the Monte Carlo results (blue line). The grain size is varied from an average of  $\langle d \rangle = 1000$  nm down to 50 nm with a roughness  $\Delta_{rms} = 1$  nm. (b) Thermal conductivity versus porosity for the commonly employed analytical porous material models compared to the Monte Carlo results (blue line). The pore boundary specularity is fixed at  $p = 0.1$ . In both cases the domain top/bottom roughness specularity is set to  $p = 0.1$ . Updated, adopted from Chakraborty *et al.* [58].

Figure 4.6a compares our Monte Carlo simulation results to those of the various nanocrystalline material models. We keep the temperature fixed at  $T = 300$  K and almost diffusive grain boundary scattering with  $p = 0.1$ . With the exception of the model described by Eq. 4.1 which overestimates the thermal conductivity, and the model by Eq. 4.4 (‘NC model’) which underestimates it slightly at larger grain sizes, the models based on the simple reasoning of increased scattering rates and Kapitza resistance are in very good qualitative and quantitative agreement with the full Monte Carlo simulation results (blue line).

#### 4.4.2 Nanoporous case

In the case of porous materials, the various analytical models are based on the simple logic that the thermal conductivity is reduced due to: i) the material volume reduction reflecting the reduction in the material heat capacity, and ii) the larger number of scattering events on the pore boundaries within the intrinsic phonon-phonon scattering mean-free-path length, similar to the nanocrystalline material case. A few commonly employed models in the literature for the thermal conductivity of nanoporous materials are given in the works of Eucken *et al.* [205], Gesele *et al.* [188], Dettori *et al.* [173], Tarkhanyan *et al.* [204], and Verdier *et al.* [182], given by Eqs. 4.5 [205], 4.6 [188], 4.7 [173], 4.8 [204] and 4.9 [182], respectively:

$$\kappa = \kappa_0 \frac{(1-\phi)}{(1+\phi/2)} \quad (4.5)$$

$$\kappa = \kappa_0 (1-\phi) g_0^2 = \kappa_0 (1-\phi)^3 \quad (4.6)$$

$$\kappa = \kappa_0 \frac{(1-\phi)}{1 + \frac{\phi}{2} + \frac{3\lambda_{pp}}{2D}} \quad (4.7)$$

$$\kappa = \kappa_0 \frac{(1-\phi)}{1 + \left( \frac{\lambda_{pp}}{\delta} \right)} \quad (4.8)$$

$$\kappa = \frac{\kappa_0}{1 + \frac{4}{3} \frac{\lambda_{pp}}{\delta}} \quad (4.9)$$

where  $\delta$  is the average distance between adjacent pores and  $D$  is the pore diameter. In Eq. 4.6,  $g_0$  is related to percolation transport, approximated by the Looyenga effective medium model to be  $(1-\phi)^2$  [211]. To extract the distance  $\delta$ , we determine the number of collision (scattering) events,  $N_{\text{coll}}$ , per unit length (along the length of the material towards the transport direction). The way that the number of collisions encountered is extracted, is simply by multiplying the size of the pores (area) by the number density of the pores ( $\rho$ ) in domain in units of number/area, as [173]:

$$N_{\text{coll}} = \frac{\pi D^2}{4} \rho \quad (4.10)$$

The inverse of the number of interface scattering events per unit length provides the effective scattering distance  $\delta$  between the pores ( $\delta = 1/N_{\text{coll}}$ ). We adopted this from the works of Dettori *et al.* [173] and Lorenzi *et al.* [212]. For instance, in the case of 10% porosity in the geometries we consider, the pores are spaced every 150 nm. The diameter is 50 nm, which from the above equation one can extract  $\delta \sim 100$  nm, which is similar to an effective distance between the pore perimeters. In the case of 30% order porosity, for example this number changes to 39 nm.

Figure 4.6b shows a comparison of our diffusive boundary Monte Carlo simulations for the ordered porous structures of Fig. 4.3 ‘ordered cases’, with the analytical models as described by Eqs. 4.5-4.9. The model of Gesele *et al.* (green line) [188] and Tarkhanyan *et al.* (purple line) [204] given by Eq. 4.6 and Eq. 4.8, respectively, show excellent agreement. The model by Dettori *et al.* (light-blue line) [173] given by Eq. 4.7 initially slightly underestimates the Monte Carlo results, but shows good agreement after  $\phi = 20\%$ . The model of Eucken *et al.* given by Eq. 4.5, which only accounts for the reduction in the material volume ( $\phi$ ) in the first order, significantly overestimates the Monte Carlo results. Alternately, the model given by Eq. 4.8 [182] (red line) accounts only for the mean-free-path reduction, but underestimates the reduction in  $\kappa$  in the Monte Carlo results.

Overall, there is good match for the ordered porous cases (especially using Eq. 4.6 and Eq. 4.8), but not for the polydispersed cases – where the thermal conductivity results are much lower. This signals that, disordered pores these models fail, and more accurate models are needed. In fact, the models described by Eq. 4.5 and Eq. 4.6 do



not consider specific information regarding the details of the pore distribution in the material (positioning, diameters, shapes, interfaces, etc.), but only the volume reduction value. The models given by Eq. 4.7, Eq. 4.8, and Eq. 4.9 further consider an effective distance where scattering events are introduced, but still nothing about the distribution of those geometrical features in the material. We now expand on these models to include details of the random disordered pore distribution.

#### 4.4.3 Random nanoporous case

To construct an effective analytical model for the thermal conductivity in the case of structures with randomized pore geometries, we consider the following logic: In the case of pores with randomized diameters and positioning, there are regions in the simulation domain that have a higher porosity than the average porosity of the overall material. These regions have an increased thermal resistance compared to the average resistance of the other segments of the material, something referred to as reduced ‘line-of-sight’ [213-215]. It is not clear though, how rearrangement of the thermal resistance along the length of the material in low and high resistance regions can affect the thermal conductivity and at what degree. Previous work shows that there is indeed a correlation between such rearrangements and lowering thermal conductivity [89, 213]. On the other hand, by introducing a larger number of small diameter pores, as in this work, the effect of resistance variation along the path is magnified, since a reduced average diameter of pores provides greater surface area for phonon scattering [154, 196]. The effect of pore surface area on thermal conductivity is explored in further depth in Section A8, **Appendix A**.

To construct an analytical model that can take this thermal resistance variation into account, we proceed as follows: We start by dividing the simulation domain into subdomains perpendicular to the transport direction, whose length  $l_s$  is determined from scattering mean-free-path considerations using Eq. 4.10, i.e.  $l_s = \delta$ , as shown in Fig. 4.7a and 4.7b (for ordered and randomized geometries, respectively).

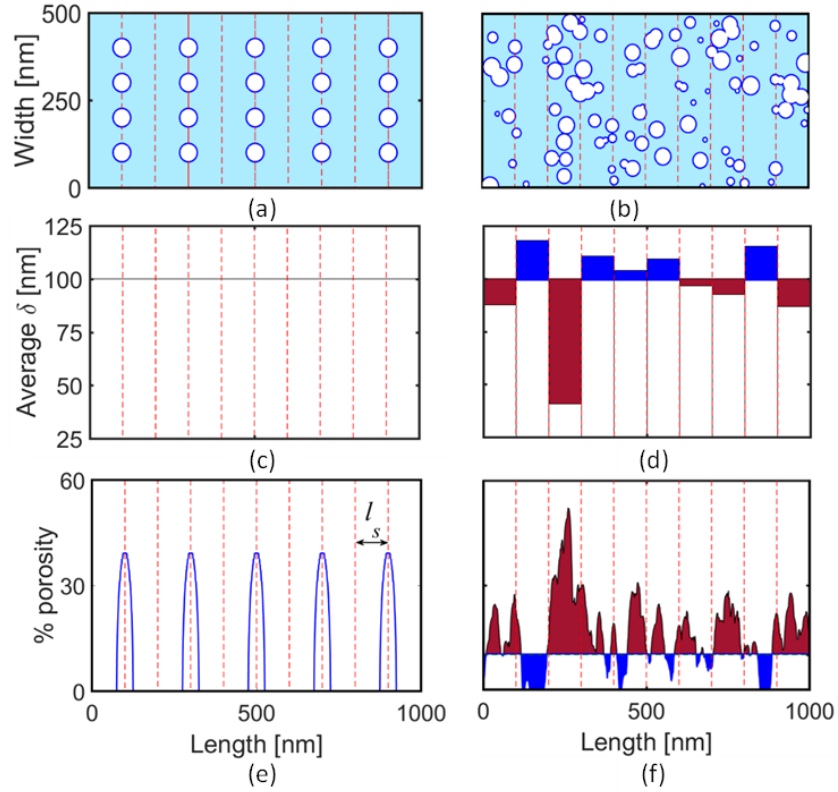


**Figure 4.7:** Extraction of the variation in distances between pores,  $\delta$ , and variation in porosity,  $\phi$ , in the nanoporous materials examined. Geometries for (a) ordered and (b) randomized (disordered) nanoporous geometries with  $\phi = 10\%$  are shown on top. The distribution of distances between pores, averaged every  $l_s = 100$  nm (depicted by the red-dotted lines), is shown in (c) and (d), respectively. The distribution of pore distances is well defined and constant in the ordered case, but deviates in the randomized pore geometry. The distribution of porosity is shown in (e) and (f), respectively. In this case the distribution can be evaluated with higher resolution along the length of the material. In (e) the porosity averages to  $\phi = 10\%$  in every  $l_s = 100$  nm domain. In (f) the porosity deviates from the 10% average following an inverse trend compared to the distance between the pores shown in (d). The red shaded portions of the distance profile in (d) and the porosity profile in (f) represent the regions of increased thermal resistance. Reproduced from [D. Chakraborty *et al.*, Phys. Rev. B 98, 115435 (2018)], Copyright 2018, American Physical Society.

Here, in the case of 10% porosity the  $l_s \sim 100$  nm. We then compute the effective distance to adjoining pores  $\delta_s$  separately for each subdomain of length  $l_s$  again using Eq. 4.10. This is done over the total length of the simulation domain as shown in Fig. 4.7c and 4.7d, respectively. In the ordered case this remains at  $l_s = \delta = 100$  nm (horizontal line in Fig. 4.7c). In the randomized pore geometry, however,  $\delta_s$  deviates from  $l_s$ , as seen in Fig. 4.7d, especially in the regions of large deviation in local porosity. The local porosity profiles are also shown in Fig. 4.7e and Fig. 4.7f,

respectively. In the ordered case the porosity averages to the global porosity (10%) every  $l_s$ , whereas in the disordered case the porosity deviates substantially, following the inverse trend of the distance deviation of Fig. 4.7d. For porosity we can construct higher resolution profiles as we have access to the porosity along the channel length limited by our domain discretization resolution. The red shaded regions in Fig. 4.7d and 4.7f depict the areas of distance/porosity smaller/greater than the average distance/porosity, which will introduce additional thermal resistance. We need to stress here that the choice of  $l_s$ , as the calculation of  $\delta$  are extracted in a logical way, based completely on the underlying geometries. These change only when the porosity and randomness changes in the geometry, and are not parameters that we use arbitrarily to map the models to Monte Carlo data. Although the choice of  $\delta$  as the distance between scattering events is intuitive, the choice of  $l_s$  can also be justified by the fact that the important things that affect transport happen within the scattering lengths (see Fig. A10, **Appendix A** for sensitivity of the results in variations in  $l_s$ ).

We then evaluate the standard deviation of the average scattering distance values along the length  $\delta_s$ , and label this as  $\Delta\delta$ . In the case of ordered pore arrangements this deviation would be zero. In the case of randomized pore geometries, however, it can be significant. To extract a more accurate value for  $\Delta\delta$  we run 50 simulations of different randomized geometries for each porosity value and average the extracted 50  $\Delta\delta$ . We then alter the distance  $\delta$  in the models for random porosities as  $\delta_r = \delta - \Delta\delta$  to account for an average smaller scattering mean-free-path. For example, in the case of 10% porosity with  $\delta = 100$  nm,  $\Delta\delta \sim 10$  nm, indicating an effective increase in boundary scattering. In a similar way, the average deviation in porosity  $\Delta\phi$  can be determined by using the porosity profiles along the length of the channel. We refer to these models from here on as the  $\Delta\delta$  and the  $\Delta\phi$  models. As a first attempt to model thermal conductivity in randomized pore geometries we consider altering  $\delta$  in the model by Tarkhanyan *et al.* [204] given by Eq. 4.8, which provides the best match to ordered porous simulations in Fig. 4.6b (purple line). The model now becomes:

$$\kappa = \kappa_0 \frac{(1-\phi)}{1 + \left( \frac{\lambda_{pp}}{\delta - \Delta\delta} \right)} \quad (4.11)$$

In the simulated geometries, again the pore sizes are varied from  $D = 10$  nm to 50 nm in a random fashion using a uniform distribution. The thermal conductivity predictions are plotted by the black line in Fig. 4.8, which compares this model with the full Monte Carlo results (blue line). For reference, we plot by the purple-dashed line the result of the same model in the ordered case as in Fig. 4.6b, which significantly overestimates the thermal conductivity. As we can see, the improved model has very good agreement with the MC results for high porosities, but for low porosities still some mismatch is observed.

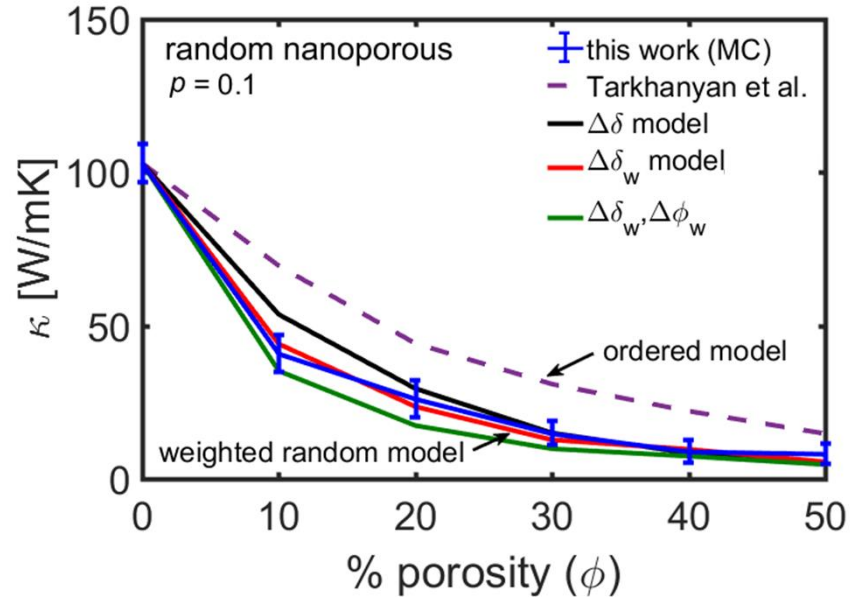


**Figure 4.8:** Thermal conductivity versus porosity for the analytical models of randomized pore geometries, compared to the Monte Carlo simulation results (blue line). Pore boundary specularity in Monte Carlo is fixed at  $p = 0.1$ . The model of Tarkhanyan *et al.* [204] as described by Eq. 4.8 is shown by the purple- dashed line. Equation 4.11 (black line) incorporates a deviation  $\Delta\delta$  in the average distance. There is good agreement with Monte Carlo results for porosities beyond  $\phi = 20\%$ . To improve the model, Eq. 4.13 (red line) incorporates a weight on the deviation  $\Delta\delta_w$ , increasing the importance of regions of higher porosity. As a reference, Eq. 4.14 (green line), incorporates a further weighted deviation in porosity  $\Delta\phi_w$ , which, however, slightly underestimates the Monte Carlo simulations. Reproduced from [D. Chakraborty *et al.*, Phys. Rev. B 98, 115435 (2018)], Copyright 2018, American Physical Society.

In order to improve the  $\Delta\delta$  model (Eq. 4.11) for low porosities, we consider further the effect of local resistance imposed by the geometrical arrangement. Clearly, a large number of pores would give a very small local  $\delta_s$ , i.e. high local porosity and

will impose a significant degradation of thermal conductance. Thus, the model is extended to include the possibility that some subdomains can have a porosity much higher than the average porosity, i.e. regions of high thermal resistance contributing to a more substantial drop in  $\kappa$ . For this, we simply consider the deviation in the scattering distances in each subdomain as before, but we now weigh more the regions where the local  $\delta_s$  is less than that of the uniform case. Similarly, we can also weigh more those regions as the porosity there exceeds the average porosity. In this way, we increase the dominance of regions with higher local porosity in determining thermal resistance. Thus, the deviation in the scattering lengths/porosity, decreases/increases even further as:

$$\Delta\delta_w = \Delta\delta \frac{L_x}{L_x - L_H} \quad (4.12)$$

where  $L_H$  is the proportion of these high porosity regions compared to the overall length of the domain  $L_x$ . For example, for porosities  $\phi = 10\%, 20\%, 30\%$ ,  $\Delta\delta_w \sim 19$  nm, 10 nm, and 8 nm, respectively, an increase compared to the corresponding non-weighted  $\Delta\delta \sim 10$  nm, 8 nm, and 8 nm. Thus, an improved model (we will refer to it as ‘ $\Delta\delta_w$  model’) is now given by:

$$\kappa = \kappa_0 \frac{(1-\phi)}{1 + \left( \frac{\lambda_{pp}}{\delta - \Delta\delta_w} \right)} \quad (4.13)$$

As can be seen in Fig. 4.8, this model (red line) has very close agreement with the full Monte Carlo results (blue line) for the random porosity case. We note that considering both the weighted deviation in distance and porosity as:

$$\kappa = \kappa_0 \frac{(1 - (\phi + \Delta\phi_w))}{1 + \left( \frac{\lambda_{pp}}{\delta - \Delta\delta_w} \right)} \quad (4.14)$$

seems to underestimate the thermal conductivity predictions compared to Monte Carlo (green line in Fig. 4.8), possibly because of double counting the scattering events. We note that the choice of the regions  $L_H$  that have in absolute terms smaller  $\delta_s$  (or higher porosity) than the average  $\delta$ , is arbitrary. One can consider  $L_H$  as regions which have

$\delta_s$  smaller than a fraction of  $\delta$ , which might be more relevant when the variations are very small. In our case, however, the variation is substantial and the reference we used ( $\delta$ ) provided a good match with the Monte Carlo simulation results (where  $L_H \sim 500$  nm, 200 nm, and 0 nm, for porosities  $\phi = 10\%$ , 20%, 30%, respectively). Next, as a second example, we test the same methodology by increasing the effective porosity in the model by Gesele *et al.* [188] in Eq. 4.6. We increase the porosity by the overall deviation  $\Delta\phi$ , and by the weighted deviation  $\Delta\phi_w$  (referring to them as the ‘ $\Delta\phi$ ’ and ‘ $\Delta\phi_w$ ’ models). Here we only modify the transport component in the model, i.e.:

$$\kappa = \kappa_0 (1 - \phi) (1 - (\phi + \Delta\phi))^2 \quad (4.15)$$

$$\kappa = \kappa_0 (1 - \phi) (1 - (\phi + \Delta\phi_w))^2 \quad (4.16)$$

Figure 4.9 shows the comparison of these models to our Monte Carlo results (blue line) versus porosity.

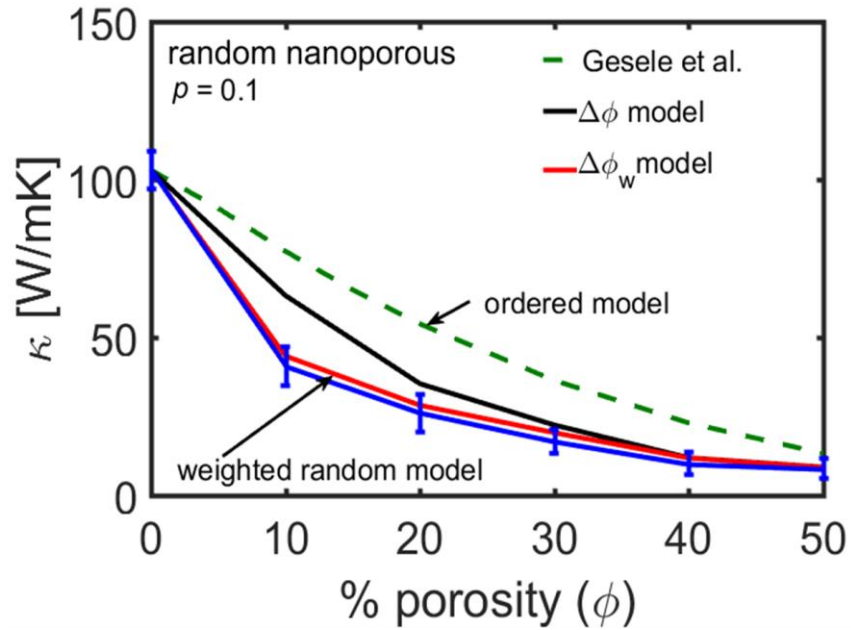


**Figure 4.9:** Thermal conductivity versus porosity for the analytical models of randomized pore geometries compared to the Monte Carlo (MC) simulation results in this work (blue line). Pore boundary specularity in MC is fixed at  $p = 0.1$ . The model of Gesele *et al.* [188] as described by Eq. 4.6 is shown by the green-dashed line. Equation 4.15 (black line) incorporates a deviation  $\Delta\phi$  in the average porosity. There is good agreement with the MC results for porosities beyond  $\phi = 30\%$ . To improve the model, we incorporate a weight on the porosity  $\Delta\phi_w$  (Eq. 4.16) increasing the importance of regions of higher porosity (red line). Reproduced from [D. Chakraborty *et al.*, Phys. Rev. B 98, 115435 (2018)], Copyright 2018, American Physical Society.

Since we simulated 50 different channels for each porosity value, in the model we use the average  $\Delta\phi_w$  value for all 50 of these geometries. In the case of 10% porosity, for example (shown in Fig. 4.7a),  $\Delta\phi$  increases the effective porosity by another 7.5% to the total 17.5% porosity. The model predictions using  $\Delta\phi$ , given by Eq. 4.15, are shown by the black line in Fig. 4.9.

While this model works well for higher porosity values above  $\phi = 20\%$ , it again overestimates the thermal conductivity for porosities below  $\phi = 20\%$ . This is again due to the possibility of regions of porosities above the average value in the simulation domain, which dominate thermal resistance. At higher porosities the pores make the different regions look more uniform. However, this is significant improvement compared to the starting model of Gesele *et al.* Eq. 4.6, which as shown by the green-dashed line, it significantly overestimates the thermal conductivity. Note that in the uniform porosity cases  $\Delta\phi$  is effectively zero.

In the case where we include the weighted porosity  $\Delta\phi_w$  (the ‘ $\Delta\phi_w$  model’ given by Eq. 4.16), the model is significantly improved as indicated by the red line in Fig. 4.9, which essentially overlaps the Monte Carlo results (blue line). Here, for the 10% porosity case,  $\Delta\phi_w$  is computed to be 18% after we average it over 50 different channels. This is a  $\sim 10\%$  increase in the overall porosity over the non-scaled  $\Delta\phi$  above. This makes the effective porosity of this disordered channel to increase by almost a factor of three to  $\phi + \Delta\phi_w = 28\%$ . In summary, it turns out that for  $\phi = 10\%$ , 20%, and 30%,  $\Delta\phi_w = 18\%$ , 21%, and 16%. As porosity increases the deviation in porosity, in general, decreases. However, these numbers stress the importance of nanostructured geometry variability in thermal conductivity, an effect that is usually overlooked, but increases the effective porosity significantly, with its effect being more dominant even than boundary roughness.

Thus, the new models ( $\Delta\delta_w$  and  $\Delta\phi_w$ ) described by Eq. 4.13 and Eq. 4.16 are shown to be accurate and can be used to extract first order thermal conductivity estimations for structures with random pore positions and diameters, using knowledge of basic geometrical specifics of the nanostructure. In an experimental setting, these

models can not only be used to understand thermal conductivity measurements if the geometrical features are known, but also conversely, to estimate the degree of disorder in nanostructures, once average porosity and thermal measurement data is available. Details on the degree of randomization might be hard to extract in the entire domain of the material, but these models provide a possible way of estimating this. Finally, we note that recent theoretical studies about the effect of variations for electronic transport (where the mean-free-path is much shorter), is not as noticeable [57, 216]. Thus, variability can be used as means to achieve lower thermal conductivity without affecting the electronic system, which is advantageous for thermoelectric applications.

#### 4.5 Verifying Matthiessen's rule

When different scattering events are considered independently, it is usual practice to combine the different scattering rates, or resistivities using Matthiessen's rule. Matthiessen's rule dictates that if each scattering process can be characterized by a relaxation time  $\tau$ , then all such processes combined contribute to a combined relaxation time  $\tau_{\text{TOTAL}}$ , such that:

$$\frac{1}{\tau_{\text{TOTAL}}} = \frac{1}{\tau_1} + \frac{1}{\tau_2} + \frac{1}{\tau_3} + \dots \quad (4.17)$$

where,  $\tau_1$ ,  $\tau_2$ , etc. are relaxation times for different scattering mechanisms (nanostructures, etc). It is important to examine if the combination of nanocrystallinity and nanoporosity can be combined using Matthiessen's rule, which will provide an indication of the degree of independence of the two scattering mechanisms. Here, we examine this using the Monte Carlo simulation results for each mechanism independently and together. We also examine the eligibility of the analytical models we have constructed in being used within the Matthiessen's rule. In this case we consider scattering due to: i) three phonon processes leading to a  $\kappa_{\text{PH}}$ , ii) scattering due to nanocrystalline geometries leading to a  $\kappa_{\text{NC}}$ , and iii) scattering due to nanopores leading to a  $\kappa_{\text{NP}}$ . Thus, the total conductivity is given by:

$$\frac{1}{\kappa_{\text{TOTAL}}} = \frac{1}{\kappa_{\text{PH}}} + \frac{1}{\kappa_{\text{NC}}} + \frac{1}{\kappa_{\text{NP}}} \quad (4.18)$$



We proceed with our verifications as follows: i) We simulated structures including nanocrystallinity with  $\langle d \rangle = 225$  nm and nanoporosities 5%, 10%, and 15%. In the ordered pore case we use  $D = 50$  nm and in the random pore case  $D$  varies from  $D = 10$  nm to 50 nm in a random fashion using a uniform distribution. ii) We simulated the nanocrystalline geometry structures and the nanoporous structures separately, for the same  $\langle d \rangle$  and  $\phi$  as in (i). iii) We computed the combined thermal conductivity of the two simulations in (ii) using Matthiessen's rule and compared that to the combined Monte Carlo simulation of (i). iv) We combined the results of the analytical models for nanocrystallinity (the 'NC model' given by Eq. 4.4) and porosity ( $\Delta\delta_w$  and  $\Delta\phi_w$  models given by Eq. 4.13 and Eq. 4.16 respectively) and compared those to the Monte Carlo simulation results of (i). For the structures with porosities  $\phi = 5\%$ ,  $10\%$ ,  $15\%$ , we extracted  $\Delta\delta_w = 27$  nm, 19 nm, 13 nm, and  $\Delta\phi_w = 20\%$ , 18%, 16%, respectively.

The summary of these comparisons is shown in Fig. 4.10a and 4.10b for the ordered and randomized porous materials, respectively. The blue bars show the full MC simulations which include nanocrystallinity and porosity. The error bars indicate the spread of the 50 simulations performed to extract the average value of the thermal conductivity. The green bars indicate MC simulations for each scattering environment separately (nanocrystallinity and porosity), coupled together using Matthiessen's rule to extract the overall thermal conductivity. The purple bars indicate the thermal conductivity predicted by the  $\Delta\delta_w$  analytical model (Eq. 4.13) combined with the nanocrystalline model by Eq. 4.4 using Matthiessen's rule. Finally, the red bars indicate the thermal conductivity predicted by the combination of the  $\Delta\phi_w$  model (Eq. 4.16) and Eq. 4.4 using Matthiessen's rule. The percentage difference of the three latter situations compared to the full MC results is indicated on top of the respective bars.

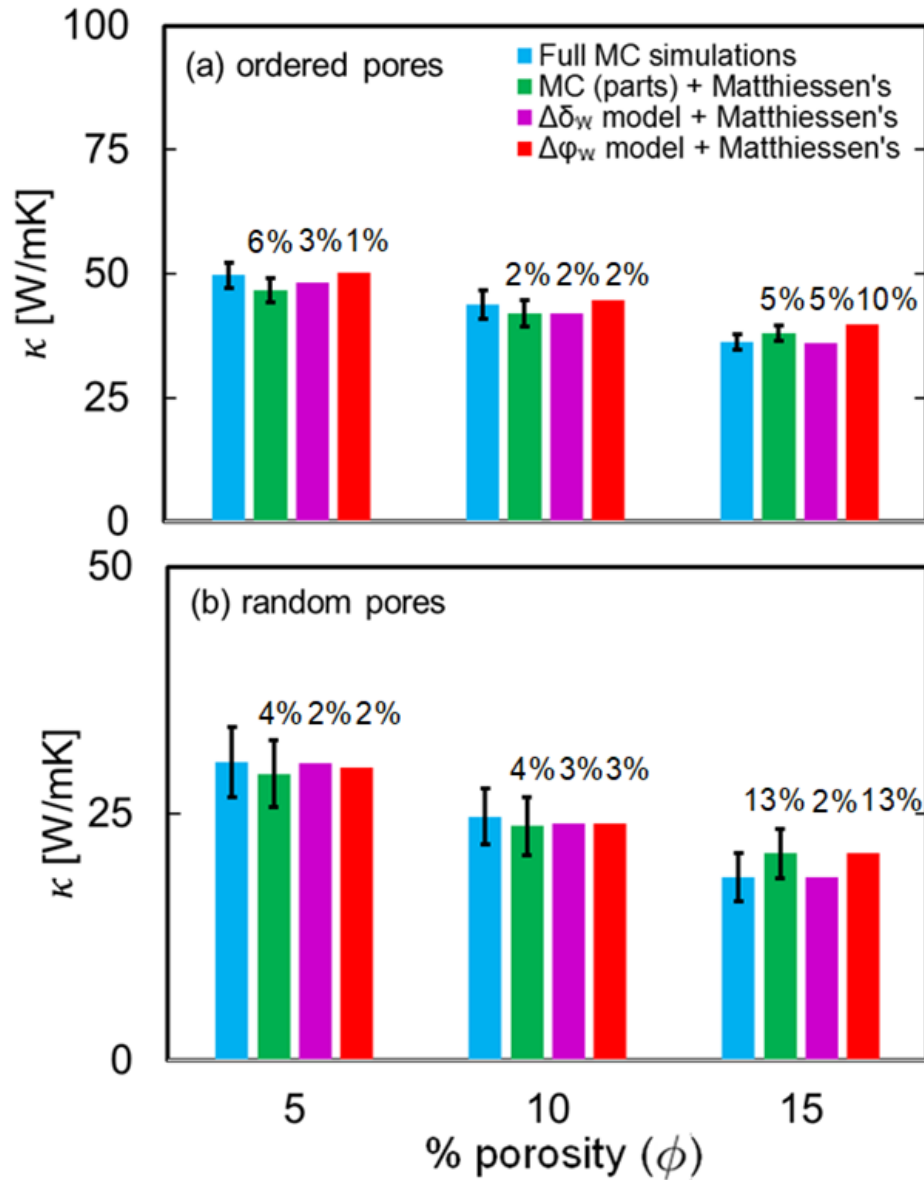


**Figure 4.10:** Comparison between the full Monte Carlo (MC) simulated results in structures with grains and pores (blue bars) and: i) MC simulation results of grains alone and pores alone, but combined through Matthiessen's rule (green bars), ii) results given by the porous material model introduced in Eq. 4.13 ( $\Delta\delta_w$  model) combined with the nanocrystalline model of Eq. 4.4 through Matthiessen's rule (purple bars), and iv) results given by model introduced in Eq. 4.16, ( $\Delta\phi_w$  model) combined with the nanocrystalline model of Eq. 4.4 through Matthiessen's rule (red bars). (a) Ordered pore geometries. For the MC simulations, 50 realizations with grain boundaries of  $\langle d \rangle = 225$  nm are averaged, and pores of a fixed diameter  $D = 50$  nm. (b) Randomized pore geometries. The pore diameters vary from 10 nm to 50 nm. The percentage numbers indicate the variation of each method from the full MC results (blue bars). Porosities  $\phi = 5\%$ ,  $10\%$  and  $15\%$  are shown. Reproduced from [D. Chakraborty *et al.*, Phys. Rev. B 98, 115435 (2018)], Copyright 2018, American Physical Society.

Clearly, a very good agreement between the full MC results, the partial MC results, and the analytical models is observed. In the ordered pore case shown in Fig. 4.10a the error introduced by the analytical models is at most 10%, observed for the 15% porosity material. In the case of random pores results shown in Fig. 4.10b, a slightly larger variation is observed for the larger porosities, but it is still at most 13 % (for both partial MC results and the analytical models).

The good agreement between all results, indicates that Matthiessen's rule is still valid to a large degree and the nanocrystallinity and nanoporosity can be treated as independent mechanisms. It also indicates that well-validated analytical models are at first order accurate for estimating phonon transport in complex nanostructured materials, at least for silicon at room temperature. Quantifying the validity of Matthiessen's rule is especially important for experimentalists seeking a fast verification of measured data, but we should note that our conclusions could be only confidently valid for the structures and geometries we considered. Deviations from Matthiessen's rule have been observed in various cases for phononic, but also electronic systems [217, 218]. In particular, we only considered nanopores larger than 10 nm in diameter to stay within the validity of the particle nature of phonons as treated by Monte Carlo. Other works, however, have considered smaller pores ( $D$  less than 10 nm), which also drastically reduce  $\kappa$ , but indicate larger violations of Matthiessen's rule [173, 212, 219-222].

## 4.6 Conclusions

In conclusion, here in this chapter we have employed a 'single-phonon' Monte Carlo phonon transport simulator to solve the Boltzmann Transport Equation for phonons in hierarchical and highly disordered Si nanostructures. We investigated the presence of nanocrystalline and nanoporous features separately and combined, in ordered and disordered realizations. In nanocrystalline geometries the effect of grain size on  $\kappa$  is more pronounced at grain sizes  $\langle d \rangle$  smaller than the average phonon mean free path of the system ( $\lambda_{pp}$ ). In that case, boundary scattering dominates over internal three-phonon scattering. We further show that the effect of changing porosity ( $\phi$ ) on thermal conductivity is much larger than boundary roughness and specularity ( $p$ ) in

reducing  $\kappa$ . An important result of this work is that it demonstrates that randomization in disorder, which is often overlooked, can play an important effect, further reducing thermal conduction by even up to 60% compared to the ordered pore geometry. Thus, non-uniformity can be as important, if not more important in reducing  $\kappa$  compared to boundary roughness and specularity ( $p$ ) and needs to be considered at a similar level when interpreting experimental data.

Based on simple geometrical rules and previous analytical models for ordered structures, we constructed accurate analytical models for randomized porous structures with excellent agreement with the full-scale Monte Carlo simulations. We believe our results and the models presented will provide guidance in developing better understanding of thermal transport in nanostructured materials and aid the design of better thermoelectric and heat management materials. The results presented in this chapter form a part of our published work Chakraborty *et al.* [58].

## 5. Enhanced phonon boundary scattering in hierarchical nanostructures

### 5.1 Introduction: hierarchical nanomaterials at high temperatures

There is significant work available in the literature explaining thermal conductivity trends in nanostructured materials using a variety of theoretical and simulation methods [11, 16, 58-62, 80-86, 223-226]. In the previous **Chapter 4** we provide a complete room temperature analysis of thermal conductivity trends in Si-based nanomaterials in the presence of multiple defects, such as nanocrystalline boundaries and nanopores, also in the presence of disorder, however, exclusively at room temperature 300 K. Here, we extend these Si-based studies [58, 59] to higher temperatures, and focus specifically on answering the following question: Are there any quantitative differences in the thermal conductivity trends in hierarchically nanostructured and highly disordered materials between what is observed at room temperature versus what can be observed at higher temperatures? In other words, are nanostructured features more effective, or less effective in reducing the thermal conductivity at higher, rather than lower temperatures?

The main motivation for this study emanates from the following: i) The average mean-free-path for phonon-phonon scattering at room temperature in Si is indicated in several reports to reside somewhere between 100 nm – 300 nm [83, 88, 170-173]. At elevated temperatures, the mean-free-path is reduced as the phonon-phonon scattering increases, increasing the importance of phonon-phonon scattering compared to phonon boundary scattering. ii) On the other hand, as the temperature is raised, phonons of different frequencies and wavevectors (usually larger wavevectors) participate in transport, which react differently to scattering off the various nanofeatures, and specifically for this study, off nanocrystalline boundaries (usually increasing scattering probabilities) [60, 156]. Therefore, in this chapter we focus on understanding how these two seemingly counter-acting features affect the thermal conductivity of disordered hierarchically nanostructured materials at higher temperatures. This study can enhance the understanding of silicon based thermoelectric (TE) devices operating at high temperatures, and could help the design

of better TE materials with ultra-low thermal conductivities. The insight provided by this chapter could be generalized for other materials, beyond Si, as well. The rest of this chapter is organized as follows. Section 5.2 presents the approach to high temperature systems, Section 5.3 presents the main results and analysis, and Section 5.4 gives the conclusions.

## 5.2 Approach: high temperature (HT) systems

For calculating the thermal conductivity we solve the phonon Boltzmann Transport Equation (BTE) using the Monte Carlo method, with all details and validation described in previous **Chapters (3 and 4)** and published works [58, 59, 60], therefore, we provide below the method details that are important in this study alone. The geometries we consider are shown in Fig. 5.1 below.

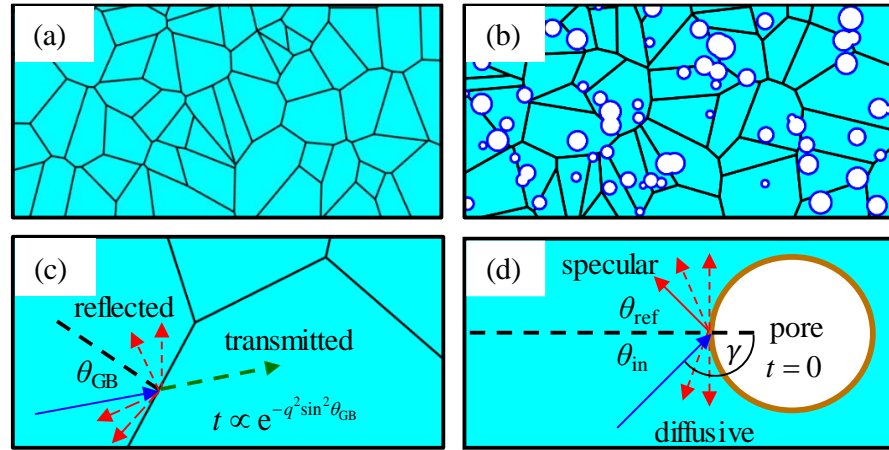


**Figure 5.1:** Examples of the nanostructured geometries considered at high temperatures. (a) Nanocrystalline (NC) materials with changing grain dimension ( $\langle d \rangle$ ). Here  $\langle d \rangle = 100$  nm, black lines represent NC grain edges. (b) Nanocomposite material (NC+NP) with given grain dimension ( $\langle d \rangle$ ) and porosity ( $\phi$ ). Here  $\phi = 5\%$ , for a random polydispersed pore arrangement, with pore diameter of uniformly distributed between 10 nm - 50 nm and random pore position. (c) Schematic for grain scattering indicating the initial angle of the phonon,  $\theta_{GB}$ , from the normal (dashed line), grain boundaries (black lines), initial path of the phonon (blue line) and probable paths of the phonon after scattering (red-dashed lines and green-dashed transmitted line). Transmission is dependent on grain boundary roughness as well as phonon wavevector  $q$ . Transmission probability is given by Eq. 3.13. (d) Schematic for pore scattering indicating the pore boundary, the initial angle of the phonon  $\theta_{in}$ , and new angle of propagation after reflection,  $\theta_{ref}$ , depending on specularity parameter  $p$ . Probable paths of the phonon after scattering for both diffusive (red-dashed lines) and specular (red-solid line) are depicted. Transmission ( $t$ ) through pores is always zero. Adopted from Chakraborty *et al.* [60].

Fig. 5.1a shows a typical nanocrystalline geometry in the simulation domain of length  $L_x = 1000$  nm and width  $L_y = 500$  nm whereas Fig. 5.1b shows a typical hierarchically nanostructured disordered geometry, where nanopores of random position and diameter through a normal distribution are inserted.

In the nanocrystalline geometry cases, the average grain size in the simulation domain is defined as  $\langle d \rangle$  (as shown in **Chapter 3**, Section 3.2.5). Following the commonly employed boundary scattering picture, the scattering probability at grain boundaries depends on the phonon wavevector,  $q$ , the roughness of the boundary,  $\Delta_{\text{rms}}$ , and the angle of incidence between the phonon path and the normal to the grain boundary,  $\theta_{\text{GB}}$ , as indicated in Fig. 5.1c. This determines whether an incident phonon will be transmitted to the other side or will be reflected, and is given by the commonly employed relation [156] as given by Eq. 3.13 in **Chapter 3**:

$$t_{\text{scatter}} = \exp\left(-4q^2 \Delta_{\text{rms}}^2 \sin^2 \theta_{\text{GB}}\right) \quad (3.13)$$

If the phonon is reflected, another parameter which depends again on the roughness and the phonon wavevector, the specularity,  $p$ , determines the angle of phonon reflection [81].  $p$  takes values from 0 to 1, with  $p = 0$  indicating a diffusive, randomized reflection angle and  $p = 1$  specular reflection where the angle of incidence is the same as the angle of reflection. This is specularity parameter is also applied to the boundaries of pores in the nanoporous cases (see Fig. 5.1b). Its treatment is also given in Section 3.26 and highlighted here in Fig. 5.1d. In the case of the pores, however, we do not *explicitly* consider the  $q$ -dependence, but we consider specular or diffusive boundary scattering just by assigning the specularity parameter  $p$ .

The main investigation we undertake in this work concerns the influence of boundary scattering at high temperatures, and more specifically the role that different wavevector ( $q$ ) and MFP phonons play in grain boundary scattering. Therefore, it is useful to have an indication of the participation of larger  $q$  phonons in thermal conductivity as the temperature is raised. The  $\Delta T$  taken for these calculations is 5% of the temperature considered.

In our published work, Chakraborty *et al.* [60], we show that high frequency phonon scattering has a greater overall contribution (up to 20% for  $T = 600$  K) to

thermal transport at higher temperatures. This includes the increase in Umklapp scattering, which are competing processes in increasing/reducing the participation of high  $q$ -states. It seems from the simple analysis that the statistics have more influence in increasing participation. This makes boundary scattering more dominant in reducing the thermal conductivity at higher temperatures as we show below in the Monte Carlo simulations.

### 5.3 Results: Effects of high temperature

In this section we study the effects of temperature on thermal transport in nanostructured material. Particularly, we focus on the *enhanced* reduction of thermal conductivity due to nanocrystalline structures. This is done by *removing* the effects of high temperature (above 300 K) in pristine structures, and the effect of nanocrystalline structures at room temperature (300 K) from the overall effect of nanocrystalline structures at high temperatures (above 300 K) by successive normalizations. We first normalize the thermal conductivity to the 300 K value for all given systems (i.e. at 300 K all geometries begin from the same reference), therefore, essentially *removing* the effect of the average MFP reduction due to the grain boundary scattering. By further normalizing  $\kappa$  again for the NC geometries by the pristine  $\kappa$  value at each temperature we can further *eliminate* the effect of the temperature-dependent phonon-phonon scattering reduction which is common for all cases. This leaves us just the effect of the  $q$ -dependent boundary scattering which we want to examine. We also explore disordered hierarchical nanostructures in this way, by introducing disordered nanoporous structures into the existing nanocrystalline geometries.

#### 5.3.1 Pristine structures

In Fig. 5.2a below, with the blue line we show the thermal conductivity  $\kappa$  for the bulk pristine system (without nanocrystallinity) as a function of temperature from 300 K to 900 K, which has the typical reduction trend due to the increase in the phonon-phonon scattering rates. At 900 K, for example, there is a decrease in  $\kappa$  by more than 60%. The  $\Delta T$  used for these simulations and calculations is 5% of the temperature considered.



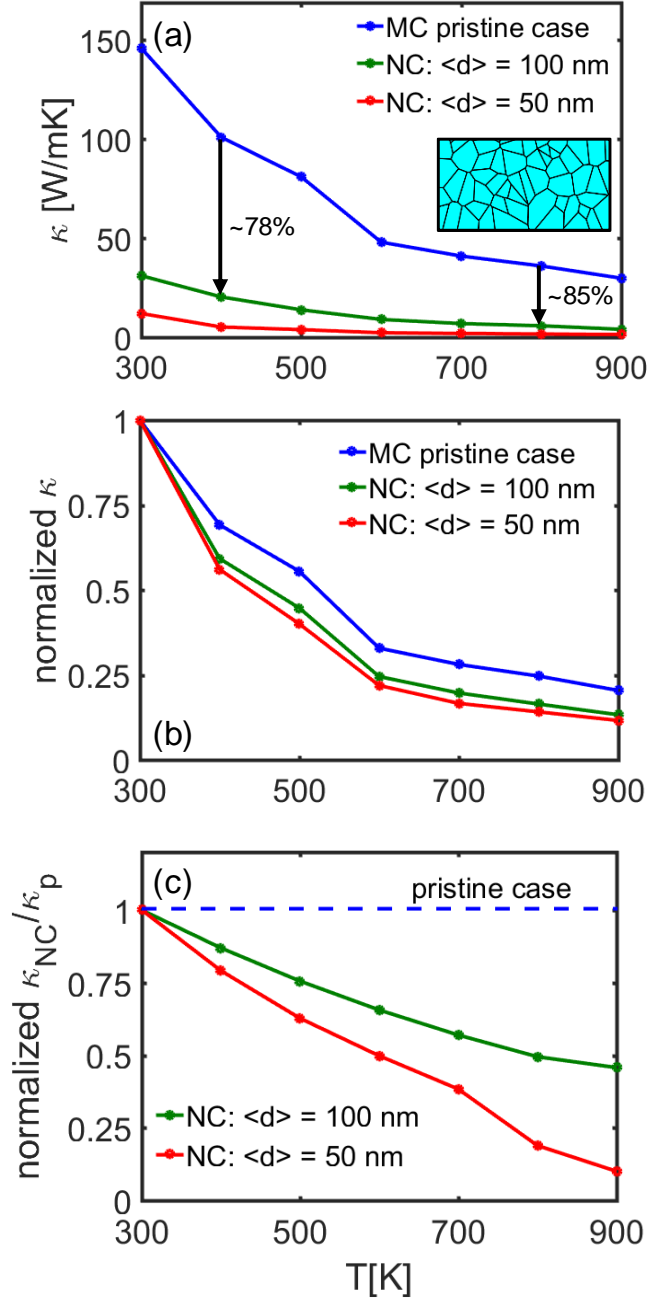


**Figure 5.2:** High temperature results for nanocrystalline structures. The  $\Delta T$  taken for these calculations is 5% of the temperature considered. (a) Effect on thermal conductivity ( $\kappa$ ) as temperature increases from 300 K to 900 K, for the pristine case (blue line), nanocrystalline (NC) case with  $\langle d \rangle = 100$  nm (green line) and  $\langle d \rangle = 50$  nm (red line). A sharp reduction in  $\kappa$  of over 75% is observed at 300 K for the  $\langle d \rangle = 100$  nm case (green line). This drops further to more than 85% for temperatures over 800 K. The  $\kappa$  drop is greater in the  $\langle d \rangle = 50$  nm case (red line). A typical geometry for  $\langle d \rangle = 100$  nm case is given as an inset in Fig. (a). (b) The data in (a) normalized by the 300 K  $\kappa$  value of the pristine case (blue line). The effect of phonon boundary scattering is removed from all data after this normalization. (c) The data in (a) normalized by the pristine value (blue line) at every temperature. The effect of phonon-phonon scattering from all data is taken away due to this normalization. Adopted from Chakraborty *et al.* [60].

### 5.3.2 Nanocrystalline case

We begin our investigation on the effects of nanocrystallinity on the thermal conductivity of Si as the temperature is raised. The introduction of nanograin boundaries into the material (as shown in the inset of Fig. 5.2a) causes an additional reduction in  $\kappa$  as expected. We further show in Fig. 5.2a the effect on  $\kappa$ , as temperature increases from 300 K to 900 K for nanocrystalline (NC) geometries with  $\langle d \rangle = 100$  nm (Fig. 5.2a, green line) and  $\langle d \rangle = 50$  nm (Fig. 5.2a, red line). A sharp reduction in  $\kappa$  of over 75% is observed at 300 K for the  $\langle d \rangle = 100$  nm case (green line) from the bulk value (blue line) at 300 K. The  $\kappa$  drop is greater in the  $\langle d \rangle = 50$  nm case (red line) indicating as expected that a smaller grain size causes greater  $\kappa$  reduction.

Noticeably, however, at elevated temperatures, the reduction in  $\kappa$  for the  $\langle d \rangle = 100$  nm NC structure (Fig. 5.2a, green line) drops by a larger amount (85% at 800K). This *enhanced* reduction of  $\kappa$  observed at high temperatures cannot be explained based on phonon-phonon scattering and/or the reduction in average MFP due to grain boundaries alone, but as we show further below, it is a consequence of the  $q$ -dependent boundary scattering, which increases as the average phonon  $q$ -value increases. This overall enhanced  $\kappa$  reduction of  $\sim 7\%$  of the pristine value (from 78% to 85% due to the  $q$ -dependent scattering processes) might seem small compared to just the pristine case values, however, in absolute terms that number is large if compared to the  $\kappa$  of the NC case, which stands at just 16% of the pristine material at 300 K for  $\langle d \rangle = 100$  nm. Essentially, this 7% reduction is almost half of the remaining  $\kappa$  after the introduction of NC.

To clarify this magnitude, in Fig. 5.2b, we normalize the thermal conductivity to the 300 K value for both the single crystal and NC systems (i.e. at 300 K all geometries begin from the same reference), therefore, essentially *removing* the effect of the average MFP reduction due to the grain boundary scattering. The difference in the blue line (pristine) versus the green/red lines (NC structures), is now the difference in the phonon-phonon scattering, and the  $q$ -dependent boundary scattering. By further normalizing  $\kappa$  for the NC geometries by the pristine  $\kappa$  value at all temperatures in Fig. 5.2c, i.e. by computing the  $\kappa_{\text{NC}}/\kappa_{\text{pristine}}$  ratio at each temperature (where  $\kappa_{\text{pristine}}$  is the

blue line in Fig. 5.2b), we can further *eliminate* the effect of the temperature-dependent phonon-phonon scattering reduction which is common for all cases.

Thus, the differences in the lines of Fig. 5.2c from the pristine blue-dashed line show the influence of the  $q$ -dependent boundary processes for the NC cases of  $\langle d \rangle = 100$  nm (green line) and  $\langle d \rangle = 50$  nm (red line). The  $q$ -dependent processes are responsible for doubling the reduction in  $\kappa$  for the  $\langle d \rangle = 100$  nm (green line) and amplifying the reduction in  $\langle d \rangle = 50$  nm (red line) by a factor of four at 900 K. Note that this  $q$ -dependent scattering at the grain boundaries corresponds to a small decrease in  $\kappa$  (compared to the pristine material). In the presence of crystalline boundaries where  $\kappa$  is already reduced this is a large component. As a result, the  $ZT$  value of a thermoelectric material will benefit significantly due to this. Note that this effect is built in the boundary scattering, it is not something that can be easily used as a design strategy directly, but separating its effect from the geometrical features alone helps the understanding of phonon transport in nanostructures.

### 5.3.3 Hierarchical case

Next, we perform the same investigation for disordered hierarchically nanostructured Si-based materials, in which case we incorporate nanopores into the nanocrystalline structures (as in Fig. 5.1b). A typical simulated geometry for  $\phi = 5$  % porosity with randomly sized and randomly distributed pores is also shown in the inset of Fig. 5.3a. Here we chose the pore diameter randomly from  $D = 10$  nm to  $D = 50$  nm using a uniform distribution. Again, we consider operating temperatures from  $T = 300$  K to 900 K. In Fig. 5.3a (blue line) we show the thermal conductivity versus temperature as in Fig. 5.2a, but for the new geometry (the blue line for the pristine material is the same in Fig. 5.2a). The green and red lines show the behavior of the hierarchical nanostructures (combined nanocrystalline and nanoporous (NC+NP) case) with  $\langle d \rangle = 100$  nm (green line) and  $\langle d \rangle = 50$  nm (red line). A reduction in  $\kappa$  of over 80% is observed at 300 K for the  $\langle d \rangle = 100$  nm case (green line), which is more than the NC only case.  $\kappa$  drops further by more than 90% for temperatures at 800 K. The drop in  $\kappa$  is even larger in the  $\langle d \rangle = 50$  nm case (red line) at  $\sim 95\%$ .

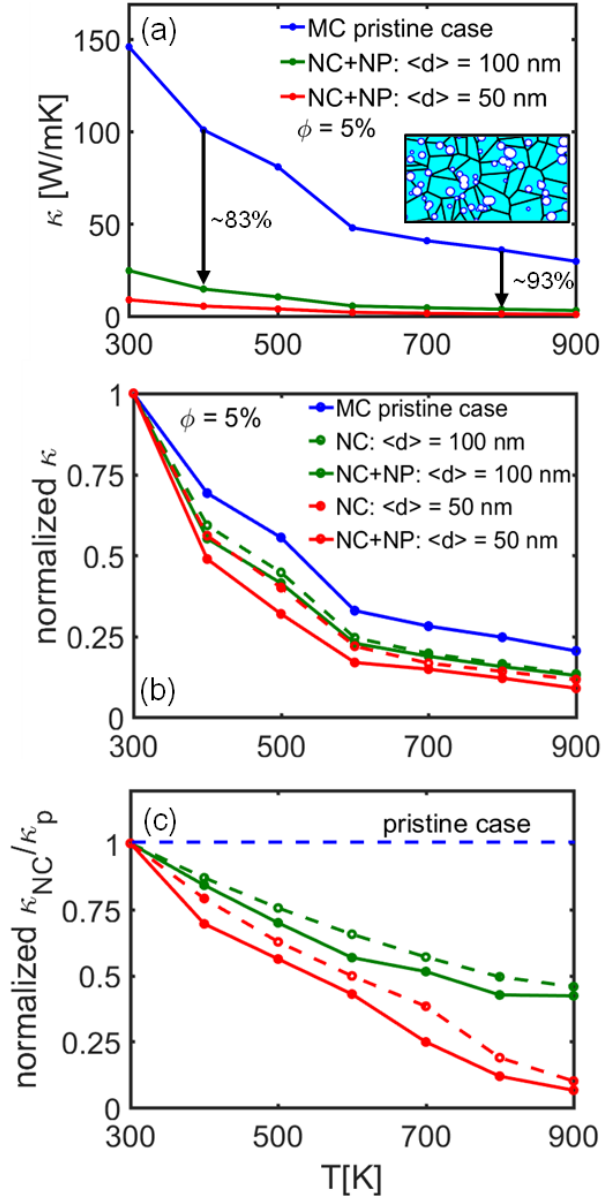


**Figure 5.3:** High temperature results for hierarchical structures. (a) Effect of hierarchical nanostructures on  $\kappa$  as temperature increases from 300 K to 900 K, for the pristine case (blue line), combined nanocrystalline and nanoporous (NC+NP) case with  $\phi = 5\%$  for  $\langle d \rangle = 100$  nm (green line)  $\langle d \rangle = 50$  nm (red line). A reduction in  $\kappa$  of over 80% is observed at 300 K for the  $\langle d \rangle = 100$  nm case (green line) and more than 90% for temperatures over 800 K. The  $\kappa$  drop is greater in the  $\langle d \rangle = 50$  nm case (red line). A typical geometry for  $\langle d \rangle = 50$  nm with  $\phi = 5\%$  is shown in the inset of Fig. 5.3a. (b) The data in (a) normalized by the 300 K  $\kappa$  value of the pristine case (blue line). The effect of phonon boundary scattering is removed from all data after this normalization. (c) The data in (a) normalized by the pristine value (blue line) at every temperature. The effect of phonon-phonon scattering from all data is taken away due to this normalization. Again, the dashed lines are the data of Fig. 5.2(c) for the NC cases of  $\langle d \rangle = 100$  nm (green-dashed line);  $\langle d \rangle = 50$  nm (red-dashed line) alone. The legend of Fig. 5.3b applies one-to-one with the lines of Fig. 5.3c as well. At high temperatures there a further reduction in the normalized ratio observed due to pores. Adopted from Chakraborty *et al.* [60].

In Fig. 5.3b, as earlier in Fig. 5.2b, we normalize the thermal conductivity of the three structures to their value at  $T = 300$  K. Thus, we *remove* in this figure the effect of geometry and the MFP of boundary scattering due to the nanostructured features that the phonons encounter. What remains is then the effect of different phonon-phonon MFP (which we do not expect to have much difference) and the  $q$ -dependence of the boundary scattering. It is clear from this figure that as the temperature increases, the reduction in the thermal conductivity is larger in the nanocomposite structure, as also observed earlier. In dashed lines we also show the NC lines of Fig. 5.2b, indicating that the reduction is slightly larger in the hierarchically nanostructured materials.

This is more clearly shown in Fig. 5.3c, in which we normalize the data lines of Fig. 5.3b to the pristine blue line of Fig. 5.3b. This removes the influence of the phonon-phonon scattering, and what is left is just the influence that the  $q$ -dependence has on the boundary scattering as in Fig. 5.2c. Again, the  $q$ -dependence of the boundary scattering has a severe effect, even larger by  $\sim 15\%$  in the case of the hierarchical disordered geometries (solid lines) compared to the nanocrystalline geometries (dashed lines). This is again expected to have a proportional contribution to  $ZT$ . We remark that while pores themselves do not have any  $q$ -dependent transmission properties (we treat pore scattering as  $q$ -independent), their presence introduces more disorder, increases the number of scattering events in the system and the times phonons pass through the grain boundaries, thus enhancing the overall effect of  $T$ -dependent surface scattering. Effectively, pores force phonons to pass through grain boundaries back and forth more times, which increases the importance of the  $q$ -dependent processes across the boundaries.

In order to directly compare and contrast  $q$ -dependent and  $q$ -independent scattering at grain boundaries, we turn off the  $q$ -dependence and re-run the simulations. In this case we consider only specular scattering at grain boundary and transmission without change in phonon angle. In Figs. 5.4a–5.4c the effect of  $q$ -independent grain boundary scattering, for the nanocrystalline (NC) case with  $\langle d \rangle = 50$  nm (purple-dashed line) is compared to the  $q$ -dependent case (red line).

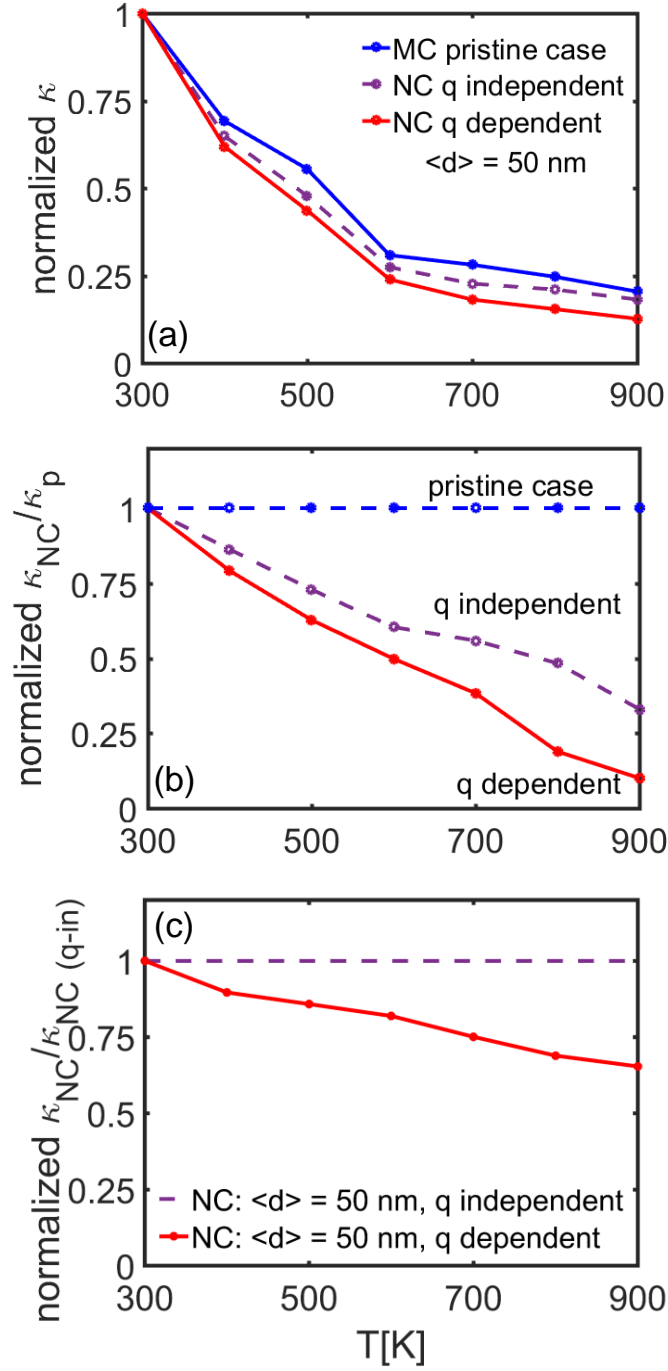


**Figure 5.4:** Separating effect of  $q$  dependence. (a) The effect of  $q$ -independent and  $q$ -dependent scattering at grain boundaries compared to the pristine case. All values are normalized with respect to their value at 300K. The effect of phonon boundary scattering is removed from all data after this normalization. (b) The data in (a) normalized by the pristine value (blue line) at every temperature. The effect of phonon-phonon scattering from all data is taken away due to this normalization. (c) The data in (b) normalized to the  $q$ -independent NC case at all temperatures. This shows the effect of the  $q$ -dependence of the grain boundary scattering as the temperature increases. Adopted from Chakraborty *et al.* [60].

Figure 5.4a corresponds to same calculations shown in Figs. 5.2b and 5.3b, now also including the  $q$ -independent  $\langle d \rangle = 50$  nm (purple line) calculation. Clearly, the  $q$ -independent simulation result resides between the pristine and  $q$ -dependent result through the entire temperature range. Figure 5.4b is equivalent to Fig. 5.2c and Fig. 5.3c and shows the result of removing phonon-phonon scattering effects, indicating the difference between  $q$ -dependent and  $q$ -independent boundary scattering. This is shown more clearly in Fig. 5.4c, where we normalize the  $q$ -dependent system to the  $q$ -independent case (purple dashed line) at 300 K. In the nanocrystalline (NC) case that is  $q$ -dependent, there is a steady decrease in  $\kappa$  as temperature increases, approaching a  $\sim 40\%$  further reduction in comparison with the  $q$ -independent case.

## 5.4 Conclusions

In this chapter we employed the Monte Carlo transport simulator to solve the BTE for phonons in nanocrystalline Si-based materials and nanocrystalline materials with pores. We investigated the influence of wavevector  $q$ -dependent scattering on the nanocrystalline boundaries, and how this affects the thermal conductivity. We show that at higher temperatures, because the average phonon wavevector ( $q$ ) increases, scattering through boundaries becomes stronger, and the thermal conductivity reduction is enhanced with temperature, compared to  $q$ -independent boundary scattering. We show that even up to  $\sim 40\%$  further reduction in thermal conductivity at high temperatures (800 K) is attributed to the  $q$ -dependence of boundary scattering, compared to if the boundary scattering was  $q$ -independent. The introduction of random nanopores in addition to nanocrystallinity, i.e. hierarchical disorder, magnifies this effect by an additional  $\sim 15\%$  at 800 K. This suggests that nanostructuring at high temperatures can actually be more effective than previously thought, and a simple constant MFP due to boundary scattering overestimates the thermal conductivity. This approach could be used to predict the behavior of materials depicting  $q$ -dependent boundary scattering at high temperatures, as well as providing insight into the design of low thermal conductivity, high  $ZT$  hierarchically disordered nanostructured materials for high temperature applications. The results presented in this chapter can be seen in our published work, Chakraborty *et al.* [60].

## 6. Thermal rectification in nanoporous silicon material

### 6.1 Introduction: thermal rectification in porous nanostructures

This chapter explores thermal rectification in geometrically asymmetric nanoporous structures. Significant research has been done on understanding and controlling thermal transport in nanostructures for novel materials and applications [212, 227-233]. Thermal rectification refers to the application where the thermal conductivity of the device material changes with material orientation [230-236]. This is analogous to current or charge transport through a diode and we define it as Eq. 6.1 below [230, 231, 233]. Since initial findings of thermal rectification between Cu and Cu<sub>2</sub>O [234] interfaces in the 1930s, various experimental [230, 235-237] and theoretical studies [155, 238-245] have investigated thermal rectification in different materials. Rectification values of up to 350% were theoretically predicted in graphene nanoribbons [233], while experiments showed that graphene junctions could provide even higher values of up to 800% rectification [237]. In case of the more technologically and commercially placed silicon, theoretical studies suggest that geometrically asymmetric structures can enhance thermal rectification effects [36, 239-245], as verified by some experimental works as well [243, 247]. Rectification is achieved when the structure is separated into regions in which the mean-free-path (MFP) is controlled by two mechanisms – the temperature-dependent Umklapp scattering, and a mechanism much less temperature dependent such as boundary scattering. To-date, however, the specifics that determine rectification, as well as the design details which would allow further optimization, are not well understood.

Our simulation method is outlined in Section 6.2. In Section 6.3 we present and discuss our results before drawing our conclusions in Section 6.4.

### 6.2 Approach: determining rectification ( $R$ ) in nanostructures

Here, using Monte Carlo (MC) phonon transport simulations, we intend to provide the details and important points that control thermal rectification in nanostructured materials. We use nanoporous Si as an example, and place the pores in



various geometrical configurations to identify the parameters that determine rectification. The basis geometry we begin with is shown in Fig. 6.1.

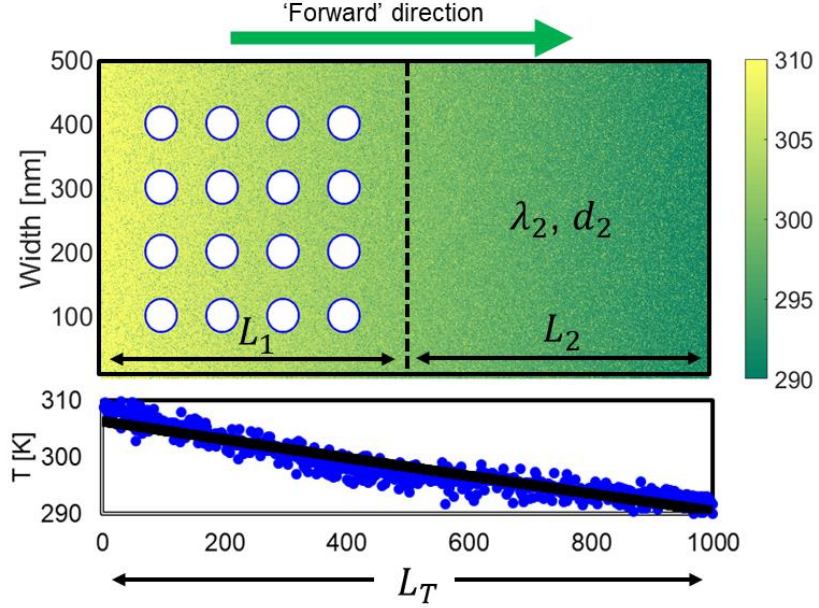


**Figure 6.1:** Schematic of the basis geometry simulated with porous region of length  $L_1$  and pristine region of length  $L_2$ . Individual properties are assigned for each region, including average phonon mean-free-path, (MFP)  $\lambda$  and average distance between pores (inter-pore distance)  $d$ . The total length of simulation domain is  $L_T$ . In all Monte Carlo simulations, we set  $L_T = 1000$  nm. The coloring indicates the established thermal gradients when the left and right contacts are set to  $T_H = 310$  K (yellow) and  $T_C = 290$  K (green), respectively, with the temperature profile given by blue dots (average of 5 million phonons). The green arrow above the schematic depicts “Forward” direction of heat flow from  $T_H$  to  $T_C$ . Updated and adopted from Chakraborty *et al.* [62].

We consider a simulation domain of length  $L_x = 1000$  nm in the  $x$ -direction and width  $L_y = 500$  nm in the  $y$ -direction. The asymmetry is created by placing the pores only in one part (porous region) of the material. We investigate the influence of porosity, pore density (as a function of inter-pore distance,  $d$ ) and pore position relative to the device left/right boundary. We compute the thermal conductivity in the materials by using the MC phonon transport simulator described in **Chapter 3**. The MC approach offers great flexibility of geometrical configurations and parametric control over the scattering mechanisms that the phonons undergo, while still allowing very good accuracy [58, 59] and large micrometer size simulation domains.

In the structures we consider, the domain is populated with circular pores of different arrangements. Each pore has a diameter of 50 nm. All phonons reflect on the

pores in a specular fashion [58, 59]. While systems with asymmetric roughness do have a thermal rectification effect [248], in this work we leave the effect of roughness aside, and focus on the geometrical configurations of the pores. The basis simulation domain with 8% porosity is shown in Fig. 6.1. The coloring indicates the thermal gradient between the hot side with temperature  $T_H = 310$  K (yellow) and the cold side with  $T_C = 290$  K (green). The green arrow on top of the schematic indicates the ‘Forward’ direction of heat flow ( $\kappa_F$ ), which we define when the pores are placed near the left, ‘hot’ contact, while keeping the ‘cold’ side empty of pores, thus creating an asymmetry in the transport direction. Next, the structure is ‘flipped’ by rotating it 180 degrees such that the pores are now on ‘cold’ side while keeping the ‘hot’ side empty of pores. The thermal conductivity in this ‘Reverse’ direction is denoted as  $\kappa_R$ . The rectification,  $R$ , is defined here as:

$$R = \frac{\kappa_F}{\kappa_R} - 1 \quad (6.1)$$

It should be noted, that unlike in other works where large  $\Delta T$  have been used to determine thermal rectification ( $T_H \sim 2 T_C$  or more are commonly used [238, 245])  $\Delta T$  is very small in our case. This is reflected here in the temperature profile obtained in Fig. 6.1 (blue dots) where there is very little deviation from a linear thermal gradient observed. This was also the case for all the devices/structures investigated here on.

### 6.3 Results: $R$ for different geometry arrangements

In this section we investigate the effects of porosity, pore density and pore position relative to the device boundaries on  $R$ . Different geometrical arrangements of pores and hierarchical inclusion of smaller sized pores are explored to improve  $R$ .

#### 6.3.1 Rectification in asymmetric porous arrangements

We begin our investigation by considering rectangular arrangements of pores as in Fig. 6.1 and the schematics in Fig. 6.2 below. Figure 6.2 summarizes the effect of asymmetry on the thermal rectification ( $R$ ) of this type of geometrical configuration. To change the asymmetry, we begin with placing pores on the left of the

domain/material, and then gradually add more and more layers separated by an inter-pore distance  $d$ , until the material becomes fully porous symmetric. We denote this asymmetry as the increasing average porosity ( $\phi$ ) of the material with the addition of porous layers. Examples of the typical geometries considered, with porosities of 6% and 10% for both ‘Forward’ and ‘Reverse’ configurations, are shown in the geometry panels above Fig. 6.2. As explained above, the temperature profiles for these systems deviated very little from a linear thermal gradient due to small  $\Delta T$  used and have thus been omitted in the figure below. In Fig. 6.2 we plot the thermal conductivity  $\kappa$  as a function of porosity  $\phi$  on the left y-axis. The ‘Forward’ direction thermal conductivity ( $\kappa_F$ ) is plotted by the red line, whereas ‘Reverse’  $\kappa_R$  is by the blue line. The rectification  $R$ , is given by the purple line and indicated on the right y-axis.

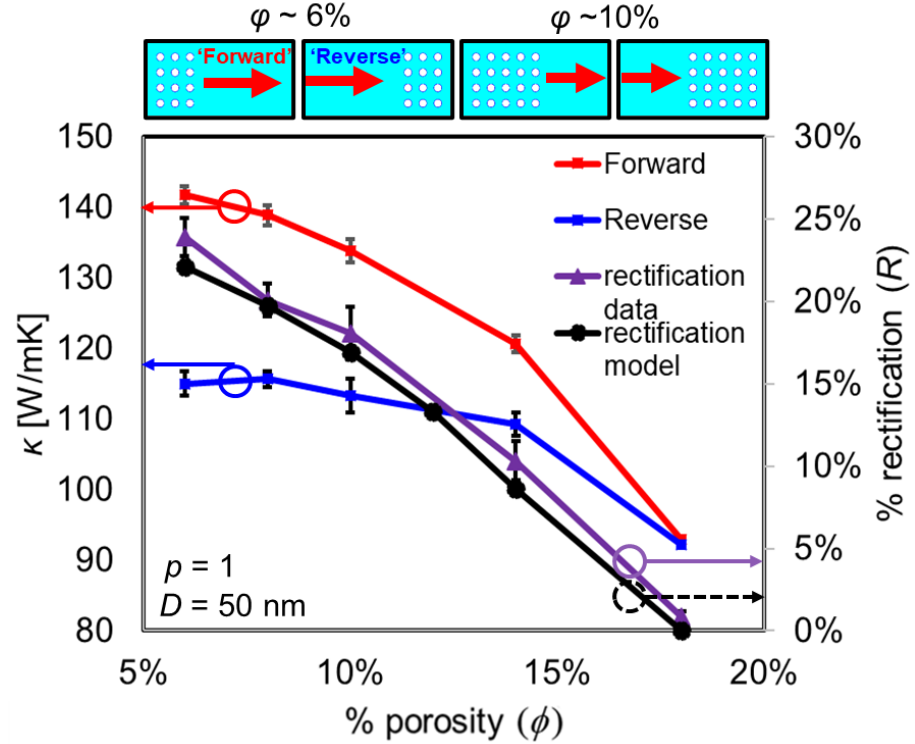


**Figure 6.2:** Monte Carlo simulations showing the effect of porosity in the rectangular, ordered pores configuration on thermal conductivity,  $\kappa$  (left axis), and rectification,  $R$  (right axis). For each value of  $\phi$ , the  $\kappa$  in the ‘Forward’ direction ( $\kappa_F$ ) is given by the red line, while the  $\kappa$  in the ‘Reverse’ direction ( $\kappa_R$ ) is given by the blue line and the rectification data is given by the purple line. The black line gives the results predicted by the model given by Eqs. 6.1, 6.5-6.6. Examples of typical geometries simulated for 6% and 10% porosity are shown above the figure, as well as our definitions for ‘Forward’ and ‘Reverse’ directions. The direction of heat flow (from  $T_H$  to  $T_C$ ) is given by the red arrows in the schematics above the graph. All pore diameters are 50 nm. Error bars give standard deviations of results. Adopted from Chakraborty *et al.* [62].

First, we observe that the largest difference between  $\kappa_F$  and  $\kappa_R$  is observed for the lower porosity case, where the pores are placed all the way to the edge of one side. For that case ( $\phi = 6\%$ ) a difference of  $\sim 30 \text{ Wm}^{-1} \text{ K}^{-1}$  between  $\kappa_F$  and  $\kappa_R$  is observed. This gives the highest rectification value of 25% for the geometries in Fig. 6.2. As more porous columns are added and the overall porosity increases, the structure becomes more symmetric, the thermal conductivity decreases, but the difference in  $\kappa_F$  and  $\kappa_R$  also decreases, which reduces rectification. At  $\phi = 18\%$  the pores are uniformly distributed throughout the simulation domain and no rectification is observed. Thus, structural asymmetry in the transport direction ( $x$ -direction) gives rise to thermal rectification as also observed in previous theoretical [36, 155, 245] and experimental works [249, 250]. In Fig. 6.2, we can clearly observe that the  $\kappa_F$  is larger compared to  $\kappa_R$ , which means that the hot phonons with shorter MFPs encountering the pores suffer less. In the  $\kappa_R$  situation (when the structure is ‘flipped’), the phonons that propagate from the pristine left (hot) to the porous right (cold), however, suffer more as by the time they reach the cold right side they develop longer MFPs. This behaviour can be understood through a simple application of Matthiessen’s rule.

### 6.3.2 Modelling thermal rectification

Under the assumption of Matthiessen’s rule, we consider the fact that  $R$  is actually determined by the change in transport properties of phonons as they encounter the pores while at high temperature regions (shorter MFPs), or while at lower temperature regions (longer MFPs). A simple model that can predict this behaviour is obtained by splitting the material system into two regions of length  $L_i$ , that determine the total thermal resistance when added together as:

$$\frac{L_T}{\kappa_T} = \frac{L_{\text{PRISTINE}}}{\kappa_{\text{PRISTINE}}} + \frac{L_{\text{POROUS}}}{\kappa_{\text{POROUS}}} \quad (6.2)$$

Equivalently, the thermal conductivities in each region are proportional to the MFPs of phonons in each region as:

$$\frac{L_T}{\kappa_T} \sim \frac{L_{\text{PRISTINE}}}{\lambda_{\text{PRISTINE}}} + \frac{L_{\text{POROUS}}}{\lambda_{\text{POROUS}}} \quad (6.3)$$

Where  $\lambda_{\text{PRISTINE}}$  is the temperature dependent Umklapp three-phonon scattering MFP for Si ( $\lambda_{\text{PRISTINE}} = \lambda_{\text{pp}} = 135$  nm at  $T = 300$  K) and  $\lambda_{\text{POROUS}}$  is the MFP in the porous region, which is given by the combination of two different scattering mechanisms, the Umklapp scattering MFP  $\lambda_{\text{pp}}$  and the pore scattering MFP, which we take as  $d$ , the average distance between the pores. Thus, the MFP in the porous region is given by:

$$\frac{1}{\lambda_{\text{POROUS}}} = \frac{1}{\lambda_{\text{pp}}} + \frac{1}{d} \quad (6.4)$$

Considering the thermal conductivity in the Forward direction ( $\kappa_F$ ), when pores are placed closer to the hot junction as in Fig. 6.1, we then have:

$$\kappa_F \sim \left( \frac{1}{\frac{1}{\lambda_H} + \frac{1}{d}} \right) \frac{L_H}{L_T} + \lambda_C \frac{L_C}{L_T} \quad (6.5)$$

where  $\lambda_H < \lambda_{\text{pp}} < \lambda_C$  since the two regions are on the hotter/colder sides of the average temperature. Similarly, in the reverse direction we have:

$$\kappa_R \sim \lambda_H \frac{L_H}{L_T} + \left( \frac{1}{\frac{1}{\lambda_C} + \frac{1}{d}} \right) \frac{L_C}{L_T} \quad (6.6)$$

Inserting Eq. 6.5 and Eq. 6.6 in Eq. 6.1 we can estimate the rectification  $R$ . The black line in Fig. 6.2 shows the rectification  $R$  calculated using Eq. 6.1 with  $\lambda_H = 120$  nm for the hot side ( $T_H = 310$  K) as and  $\lambda_C = 150$  nm for the cold side ( $T_C = 290$  K), taken from Jeong *et al.* [83] and verified by our simulator. Note that the model only provides the rectification  $R$ , and not thermal conductivity values, as we only have proportionalities to the MFPs in Eq. 6.5 and Eq. 6.6. This model may be improved by including effects of boundary roughness and resistance [238, 239], pore shape [155] or by including multiple materials in the same device [239, 270]. However, for a first order approximation of porous silicon material this model gives satisfactory results. Using Eq. 6.1 and the lengths of the different porous regions,  $R$  values for all porosities are calculated, and a very surprising match to the Monte Carlo results is observed (black versus purple lines in Fig. 6.2) using the values of  $\lambda_H$  and  $\lambda_C$  above.

Thus, based on this reasoning, what is important for rectification is the formation of the regions which force phonons from the hot side in the ‘Forward’ direction to interact as differently as possible with phonons reaching there from the cold side during the ‘Reverse’ direction. The closer the porous region is to the contacts, the larger the differences between the  $\lambda_H$  and  $\lambda_C$ , which in our simulations varies almost linearly between the two contacts [65, 83], and the larger the rectification is (purple line in Fig. 6.2). Note that studies also suggest that a non-linear temperature gradient can lead to rectification [238, 245], in our case, however, it is the *variation* of the phonon MFPs that does so. Another important observation is the monotonic decrease in rectification as the pore columns pile up across the transport direction, in which case the structure becomes more and more ‘symmetric’. From Eqs. 6.5 and 6.6, one would expect that the lengths of the porous versus non-porous regions would also play a role, with the longer  $L_{\text{POROUS}}$  to increase rectification. The longer the porous region, however, the smaller the difference between  $\lambda_H$  and  $\lambda_C$ , which is the primary reason behind rectification.

### 6.3.3 Rectangular porous geometries

To better understand the geometric details that influence rectification further, we perform a series of simulations by altering the position, inter-pore spacing, and porous regions’ effective resistance (the latter is achieved by changing from an aligned to a staggered pore configuration) [59, 62]. In Fig. 6.3 we show the rectification achieved by the porous geometries illustrated in the depicted schematics. The first series of simulations begin with the rectangular arrangement of pores located at the left side at a distance of 200 nm ( $\sim 2$  MFPs) from the left contact ( $x = 200$  nm). The pores are located at distances  $d = 50$  nm with respect to each other (light-blue, upper-left most schematic). We then investigate geometrical features on the rectifications as follows: i) by changing inter-pore distance,  $d$ , and making the structures more ‘compressed’, thus increasing thermal resistance; (still keeping the number of pores the same), ii) by staggering the overall geometry, thus reducing the line-of-side [213-215], also increasing the pore region resistance. iii) by combining effects (i) and (ii) i.e. reducing the inter-pore distance and staggering the pores.

First, we look at the rectification results shown by the light-blue bars ( $x = 200$  nm) in Fig. 6.3. We start from the basis (rectangular) arrangement of pores (labelled arrangement ‘A’ on the figure) with a porosity of 8% and pore diameter  $D = 50$  nm which provides 11% rectification. Reducing the inter-pore distance (arrangement ‘B’) increases rectification to 20%, then by staggering every alternate line of pores i.e. by moving the pores by 50 nm in the y-axis (arrangement ‘C’), an additional small rectification is added to reach 24%. The combination of the two further increases rectification to 31% (arrangement ‘D’) This indicates that the *larger the resistance* of the rectifying region/junction, the *larger the rectification* that can be achieved.

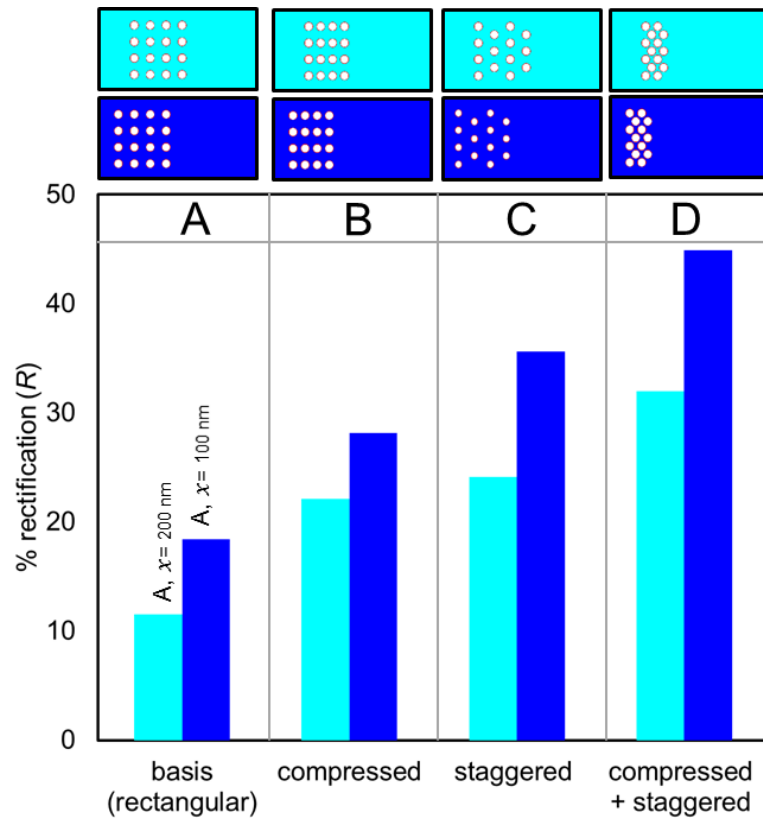


**Figure 6.3:** Monte Carlo simulations showing the effect of pore position, inter-pore distance compression and pore staggering on rectification ( $R$ ) on left axis. Geometries simulated are given in the panel above the figure. These are i) the basis (rectangular) arrangement of pores (‘A’) with pore diameter  $D = 50$  nm; ii) compressed arrangement (‘B’) which has the same configuration as ‘A’, but with halved inter-pore separation; iii) staggered arrangement (‘C’) given by shifting pore positions of ‘A’ by 50 nm in the y-direction; iv) compressed + staggered arrangement of pores (‘D’) by reducing inter-pore distance to 12.5 nm in (iii). Pores are placed at 200 nm from the domain edge in the first (light-blue,  $x = 200$  nm) cases in all four arrangements ‘A’ – ‘D’. They placed 100 nm from the domain edge in the second (dark-blue,  $x = 100$  nm) cases in all four arrangements. Adopted from Chakraborty *et al.* [62].

Next, in the second (dark-blue,  $x = 100$  nm) cases, we shift the entire pore geometry by 100 nm and place it at 100 nm from the domain edge ( $\sim 1$  MFP). We observe that just by moving the pores closer to the channel edge, the thermal rectification increases from the initial 11% to 18% (left-most structures, arrangement ‘A’). This shift of the porous region brings a substantial increase, and we can explain it as follows: The placement of the pores in different regions in the channel, with different temperatures, interacts with phonons of different MFPs. In the dark-blue,  $x = 100$  nm case, for example, in the ‘Forward’ direction the phonons encountering the pores have MFPs  $\lambda_H = 120$  nm ( $> \lambda_{pp} = 135$  nm since  $T = 308$  K), while in the ‘Reverse’ direction, they have MFP  $\lambda_C = 147$  nm (since  $T = 292$  K).

On the other hand, in the light-blue,  $x = 200$  nm case, the numbers are slightly closer together, i.e.  $\lambda_H = 124$  nm ( $T = 306$  K) in the ‘Forward’ direction and  $\lambda_C = 143$  nm ( $T = 294$  K) in the reverse direction. (Note that here we have considered the temperature of the beginning of the pore region that is closer to the corresponding contact to report the MFPs). The larger the differences in the MFPs of the phonons when they encounter the pores in the ‘Forward and ‘Reverse’ directions, the larger the rectification, and that is why the systems which place the pores closer to the device edge have larger rectification. The simple reason is that the longer the phonon MFPs, the more phonons are affected by nanostructuring (within the Matthiessen’s rule picture), and the larger the difference between the MFPs of the phonons when they encounter the porous regions in the two configurations, the larger the rectification. Please note, these MFP values have been extracted from the system and then checked against existing literature [83]. Near 300 K they appear to scale *almost linearly* with temperature, but this is no longer the case when the device temperature changes significantly. This has been examined closer in Fig. A13, in **Appendix A**, where we examine the effect of device temperature on rectification.

As a simple first order verification, inserting the above values in the model of Eqs. 6.5-6.6, provides values for  $R \sim 18\%$  for dark-blue,  $x = 100$  nm case and  $R \sim 13\%$  for the light-blue,  $x = 200$  nm case, very similar to the ones that result out of the simulation ( $R \sim 18\%$  and  $R \sim 11\%$ , respectively). It seems that the choice of picking the MFPs at the beginning of the porous regions closer to the contacts provides this very good match. Following the same geometrical arrangements, ‘A’ – ‘D’ in the dark-



blue cases (like in the light-blue, cases) we observe an increased rectification for the  $x = 100$  nm cases at all cases (compare the dark-blue bars to the light-blue bars). Bringing the pores closer together to  $d/2 = 25$  nm in the  $x$ -direction ('B' in Fig. 6.3) increases rectification to 28%, introducing staggering ('C') provides another increment to 35%, and combining the two geometries (and enforcing an even smaller separation) as in the 'D' arrangement, the overall rectification jumps as high as 44%.

#### 6.3.4 Influence of pore positions and density

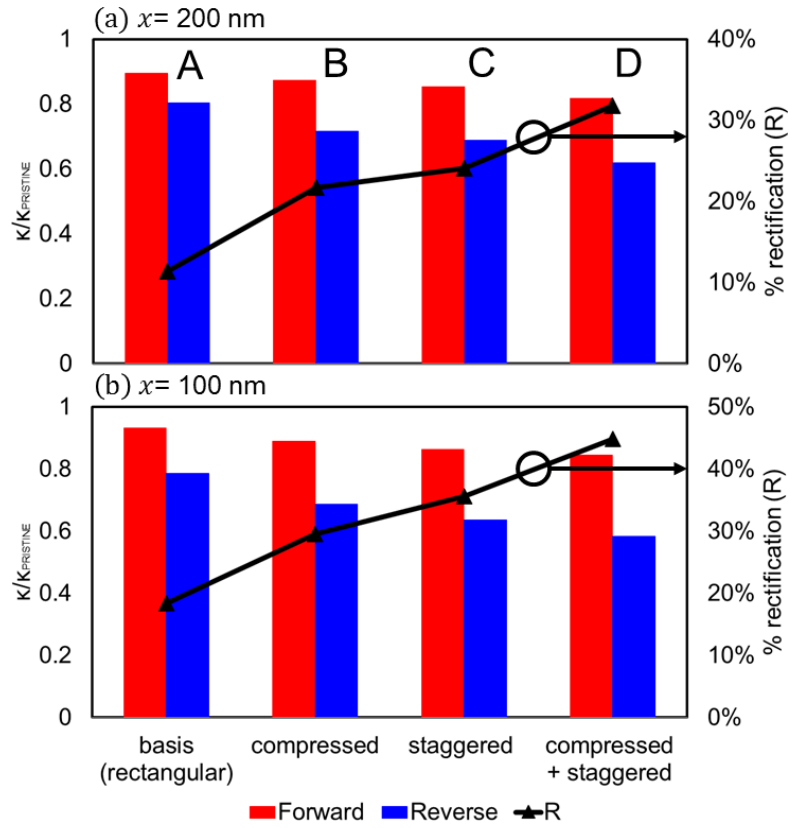


**Figure 6.4:** Normalized  $\kappa$  observed in the 'Forward' (red bars) and the 'Reverse' (blue bars) direction for each structures 'A'– 'D' of Fig. 3 (left axis). The rectification is shown by the black line in the right axis. (a) The pores are placed at 200 nm from the domain edge ( $x = 200$  nm). (b) The pores are shifted by 100 nm and placed 100 nm from the domain edge ( $x = 100$  nm). In each graph the  $\kappa$  is normalized to the bulk silicon value,  $\kappa_{\text{PRISTINE}}$  (i.e.  $148 \text{ Wm}^{-1} \text{ K}^{-1}$ ). Adopted from Chakraborty *et al.* [62].

In order to better understand the increase in rectification as we move pores closer to the device edge, we compare the contributions of  $\kappa_{\text{F}}$  and  $\kappa_{\text{R}}$  to rectification of the same structures in Fig. 6.3. In Fig. 6.4 we show the corresponding  $\kappa_{\text{F}}$  and  $\kappa_{\text{R}}$  by the red and blue bars, respectively.

Figure 6.4 shows that, as expected, both  $\kappa_F$  and  $\kappa_R$  drop as the structure becomes more resistive, but the reduction in  $\kappa_R$  (blue bars) is larger for all cases, and this is the primary reason behind the rectification improvements. For instance, the  $\kappa_R$  observed in the light-blue,  $x = 200$  nm case drops by  $\sim 29\%$  when comparing the basis left-most structure ('A') to the right-most one ('D'). On the other hand, the corresponding  $\kappa_R$  drop in the dark-blue,  $x = 100$  nm case is  $\sim 36\%$ . We can draw a couple of conclusions from these observations: i) the larger drop in  $\kappa_R$  compared to that of  $\kappa_F$  is what increases rectification in these structures, and ii) that  $\kappa_R$  reduces more as pores are brought closer to the cold domain edge. That is again in agreement with the simple Matthiessen's rule, which states that it is the long MFP colder phonons that are affected more when encountering the porous regions. Thus, the greatest rectification is seen for the most asymmetric case, where the temperature-dependent MFPs of phonons differ as much as possible between the 'Forward' and 'Reverse' directions. As placing the pores closer to the edge enhances rectification, from here on we consider the  $x = 100$  nm basis case to examine further geometrical configurations.

### 6.3.5 Effect of surface area and grading

From the simple model presented in Eqs. 6.5-6.6, rectification is determined by the asymmetry in the different interaction of the hot/cold MFPs in the porous regions, which of course will have a certain length. An interesting point to examine here, is the interplay between the effect of increasing asymmetry along the transport direction in a gradual (graded) way, versus having sharp junctions with a given interface length to separate the porous and pristine regions (length in our case of 2D simulations – in 3D it would be interface area). In the first (graded) case the rectification region will increase throughout the material, but its local influence will be smaller, whereas in the second case, the rectification region is small, essentially rectification is dominated by the junction between the porous/pristine regions, but its strength is larger. In the simulation results shown in Fig. 6.5 below, we begin again with the basis 'A' structure of 8% porosity. In order to examine the effect of increasing the interface area that separates the two regions, we rearrange the pores in an oblique configuration ('E') seen in the panel above Fig. 6.5.

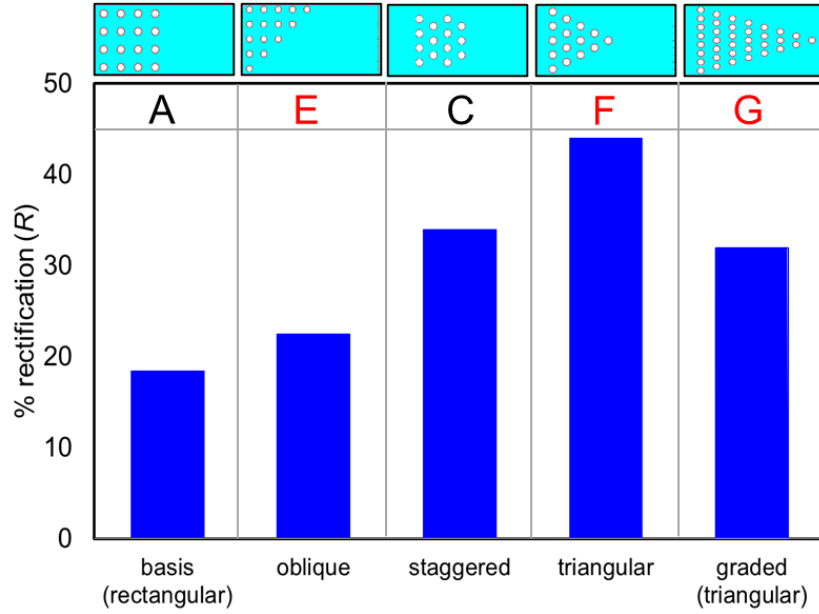


**Figure 6.5:** The dependence of thermal rectification on the exposed junction surface area and pore grading. Five cases are examined, and the geometries simulated are given above the bar chart. These are: i) the basis (rectangular) arrangement of pores (‘A’) with pore diameter  $D = 50$  nm; ii) oblique arrangement (‘E’) where pores are arranged in a right-triangular fashion to give increased exposed surface area; iii) staggered arrangement (‘C’); iv) triangular arrangement (‘F’); v) graded (triangular) arrangement (‘G’) of pores by uniformly decreasing pore density in the  $x$  direction. Adopted from Chakraborty *et al.* [62].

We find that increasing the interface area, i.e. increasing the surface area where rectification happens, increases  $R$  to  $\sim 22\%$  overall (comparing the ‘A’ with ‘E’ case bars in Fig. 6.5). By following the same logic for staggered pores (‘C’) and exposing both sides we consider a triangular arrangement of pores (arrangement ‘F’) we reach an amplified  $R = 45\%$  (as compared to  $R = 34\%$  of the simple staggered arrangement ‘C’). However, by extending this structure to get a graded geometry throughout the domain (graded-triangular) arrangement ‘G’ in Fig. 6.5), does not lead to any more rectification improvements. In fact,  $R$  drops to  $\sim 31\%$  from  $45\%$  that is achieved by the triangular structure (case ‘F’), which is more asymmetric and divides the domain into two discrete porous and non-porous segments. In the fully graded ‘G’ case phonons interact with the pores throughout the domain. It could be argued that that a graded porous structure would provide a small degree of rectification locally, but that would extend to the entire channel, and the aggregated effect could be significant. Our simulations show, however, the reverse, namely that that discontinuous regions (junctions) provide a greater rectification than graded geometries in our Si structures,

as also indicated in other materials [36, 99, 155, 234], as the differences between the phonon MFPs in the ‘Reverse’ and ‘Forward’ directions in each segment of the structure are now smaller.

### 6.3.6 Triangular arrangements and hierarchical nanopores

Here onwards we use the triangular geometry configurations with pores placed  $x = 100$  nm from the edge (green bars and green geometries in Fig. 6.6) which provide the maximum rectification, and compare them to our basis rectangular structures (dark-blue bars and dark-blue geometries in Fig. 6.6). The rectification for the basis (rectangular) structure ‘A’ is 18% and this increases to 45% for the triangular case, as we have already seen. We then explore the effects of: i) decreasing inter-pore spacing as before, and ii) introducing smaller pores in a hierarchical fashion to the previously considered geometries. In both cases we aim to increase the resistance of the porous region, a strategy that increases rectification, as we have observed earlier. The structures can be seen in the geometry panel above Fig. 6.6 (dark-blue for the rectangular and green for the triangular cases, respectively). In the second structure column (‘H’) in Fig. 6.6, by introducing smaller nanopores of with pore diameter  $D = 10$  nm to the existing base structures in a hierarchical fashion we increase the effective pore density. This gives  $R = 51\%$  for the triangular case compared to 24% in the rectangular case (green versus blue bars for structures ‘H’ of Fig. 6.6). We then reduce the inter-pore distance from  $d = 50$  nm to  $d/2 = 25$  nm in the  $x$ -direction (column ‘C’ in Fig. 6.6), thus making the structures more ‘compressed’ with increased thermal resistance. Structure ‘C’ in the triangular arrangement causes an increase to  $R = 57\%$ , compared to 28% in the rectangular ‘C’ case.

Finally, by combining the effects of density and hierarchical nanopores we get a maximum rectification of  $R = 61\%$  in the combined hierarchical structure (arrangement ‘I’) for the triangular case in Fig. 6.6. Compared to the arrangement ‘D’, the compressed rectangular case given by the white bar with blue-dashed outline in Fig. 6.6, the triangular configuration provides a 35% increase in heat rectification. This further stresses the importance of the larger rectifying junction length/area, as well as the high thermal resistance of the porous region, rather than the graded porous configurations in the structures we have investigated.

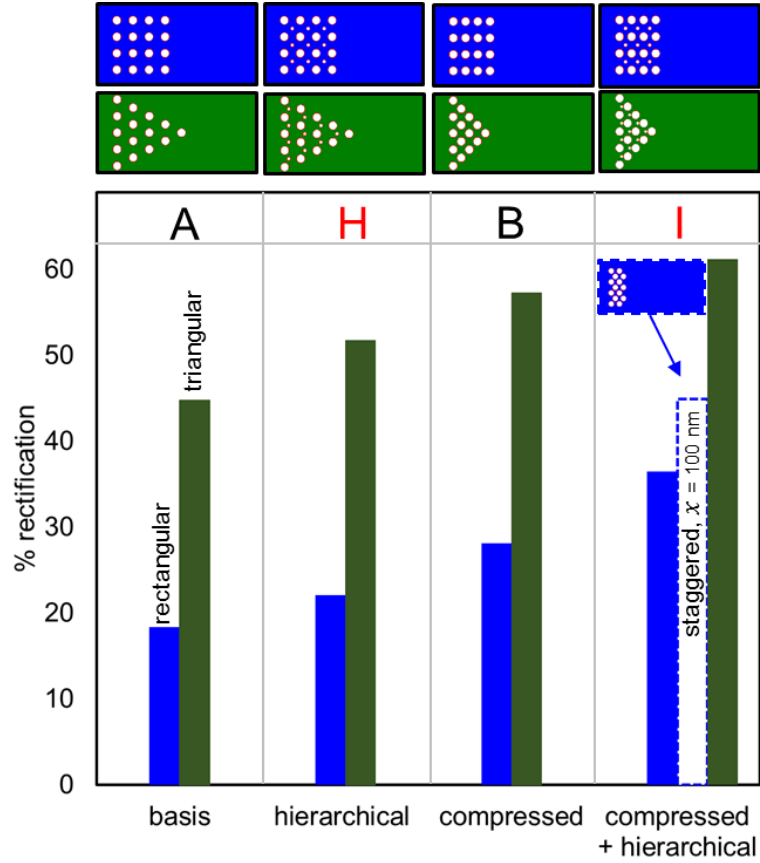


**Figure 6.6:** The rectification dependence on the construction of the triangular regions, and the hierarchical incorporation of smaller nanopores ( $D = 10$  nm) in between the bigger ones ( $D = 50$  nm). Four cases are examined, each for both rectangular geometries (dark-blue bars) and triangular geometries (green bars). The geometries simulated are shown in the panel above the figure. These are: i) the basis arrangement of pores ('A') for both rectangular and triangular configurations given by dark-blue bars or green bars, respectively. For all pores  $D = 50$  nm, and inter pore distance  $d = 50$  nm; ii) hierarchical arrangement ('H') by adding smaller pores in-between 'A'; iii) compressed arrangement ('B') with halved inter-pore separation  $d = 25$  nm; iv) compressed + hierarchical arrangement of pores ('I') by reducing halving the original inter-pore distance. The result for arrangement 'C' from Fig. 6.3 is also included for comparison. All structures are placed  $x = 100$  nm from the device edge. Adopted from Chakraborty *et al.* [62].

Although not the focus of this study, we also carried out simulations for rectification at higher and lower temperatures (see Fig. A13, **Appendix A**). It was found that increasing the temperature has a detrimental effect on rectification. This can be understood since, for a given geometry, higher temperatures reduce the phonon  $\lambda_{pp}$  due to larger phonon-phonon scattering and increase their influence in determining thermal resistance over the pore scattering, reducing rectification. Decreasing temperature causes an increased rectification effect – since a lower temperature

reduces phonon-phonon scattering so that the pore influence increases. This effect has also been noted in some other works [232, 236, 245, 248]. Yet, in the case of Gluchko *et al.* (the Nomura group) while the rectification effect observed did increase for lower temperatures, it was still within the margin of error [232]. This may be due to a few reasons i) the large radius of the pores used, which reduces rectification (Gluchko *et al.* surmise this is why rectification is observed when phonon MFPs are longer at low temperatures). ii) pores were arranged uniformly throughout the device – which we know from our study causes minimum rectification. No asymmetric geometrical junction/graded arrangements were used. iii) the Eucken model (Eq. 4.5) [205] was used to correct their  $\kappa$ , which only accounts for the reduction in the material volume ( $\phi$ ) in the first order, and does not give accurate results for nanoscopic pores [58, 59, 173, 182, 204]. Rectification was primarily created using asymmetry in pore shape – a method which gives varying results [155, 227, 232]. Apart from nanopores, it is also possible to create rectification effects using materials mismatch and nanocrystalline grain boundaries – methods which are subject to detailed prior study covered extensively in the literature [227, 230, 231, 233, 236, 246].

## 6.4 Conclusions

In this chapter we examined the effect of pore density, position, junction surface area, and hierarchical nanostructuring on thermal rectification in nanoporous Si using Monte Carlo simulations. Rectification requires asymmetry in geometry. We show that rectification is optimized: i) when the temperature-dependent phonon-phonon scattering limited MFPs of phonons encountering the porous regions are as different as possible in the ‘Forward’ compared to the ‘Reverse’ directions, ii) when the porous regions are as resistive as possible, and iii) when the rectifying junction that separates the porous and pristine regions is as large as possible. Practically, we have shown that these conditions are achieved: i) by placing the porous region as near to the contact as possible, ii) by making the porous region as resistive as possible (denser, compressed, staggered, hierarchically placed pores), and iii) by using triangular rather than rectangular pore region configurations. By combining these effects, we showed that rectification values of greater than 60 % can be reached. These results have been published in Chakraborty *et al.* [62].

## 7. Wave versus particle phonon nature in thermal transport in nanostructures

### 7.1 Introduction: wave and particle phonon treatment

Nanostructuring has magnified our ability to understand and control phonon transport in nanomaterials, giving rise to novel applications. Phonon waveguides, which can be used for nanoelectromechanical systems (NEMS) [251], phonovoltaics, which uses high energy phonons to generate power, similar to photovoltaics [252, 253], heat management, and primarily improved thermoelectrics are a few emerging technologies that depend on heat flow at the nanoscale. Nanostructuring of materials has demonstratively yielded extremely low thermal conductivity ( $\kappa$ ), even below the amorphous limit of materials, resulting in enhanced thermoelectric efficiency [5, 33]. Particularly for porous silicon materials, novel single-crystalline membranes with nanoscopic pores give reproducibly low  $\kappa$  around 1-2 Wm<sup>-1</sup> K<sup>-1</sup> [41, 53, 43].

Optimizing and controlling heat flow prerequisites a theoretical understanding of phonon transport in these materials. This requires methods that bridge through various length scales which are dictated by different physics related to the wave versus particle treatment of phonons. Yet, conventional computational methods consider these approaches (i.e., waves vs particles) independently, and whether and under what circumstances wave effects and coherence have significant influence in phonon transport is still an open question [196, 202, 254, 255].

Classical methods based on the Boltzmann Transport Equation (BTE) treat phonons as incoherent particles [196] and have been used very successfully to describe thermal transport properties in silicon across various nanostructures such as nanowires [16, 82, 149], thin films [150, 151, 256], nanoporous materials [58-62, 152-155], polycrystalline materials [58, 60, 95, 97, 156-158], nanocomposites [87, 159], corrugated structures [160-163], and silicon-on-insulator devices [164]. These methods scale very well computationally and allow flexibility in the treatment of scattering and geometrical features (Monte Carlo for example), and are commonly employed to simulate thermal transport in nanostructures.

However, these classical methods do not consider phonon wave effects that could be important at the nanoscale. For example, adding periodic pores in a thin film system to create a nanomesh [33, 41, 53, 152, 257] introduces a secondary artificial periodicity to the original lattice, potentially modifying the phonon dispersion relations to form a “phononic crystal”, analogous to the better-known photonic crystals [258]. Changes in phonon group velocities, band gaps, the density of states, and thermal conductivity that arise due to wave interactions are referred to as *coherent effects*. It is also suggested that such effects can lead to Anderson localization, mode conversion, or Rayleigh waves and drastically reduce  $\kappa$  [259, 260].

However, experimental results are still inconclusive on the relative importance of (wave-based) coherence effects versus (particle-based) boundary scattering effects [196, 202] at length scales below 100 nm [33, 41, 53, 43, 88, 98, 99, 201, 254, 255]. Theoretical investigations can help improve the understanding of phonon transport at these length scales, but investigations which include both wave-based and also particle-based methods are scarce. Fully understanding the qualitative and quantitative effects of such geometries on thermal transport and phonon transmission functions would allow the design of more efficient materials and devices for thermoelectric, heat management, and other phononic applications.

In this work, we attempt to shed some light on the difference in phonon transport through structures with nanoscale feature sizes when phonons are purely waves, versus being purely particles. We compare phonon transport in a simple porous silicon geometry using a full wave approach based on the atomistic Non-Equilibrium Green's Function (NEGF) method, and a particle-based approach using the ray-tracing Monte Carlo (MC) method, and quantify how much of the wave effects MC captures.

Our motivation resides in the fact that MC is a truly valuable tool, that allows one to simulate hierarchically disordered systems, such as the ones which are used for the new generation thermoelectric materials. It has been proved successful in interpreting experiments [10, 16, 81, 89, 151, 202, 224, 254, 255, 261], despite the fact that waves can only be approximated by particles only in the short wavelength limit, and despite the fact that long wavelength acoustic phonons carry a large portion of the heat.



Thus, our aim is to quantify the margin of validity (or error) of the simple ray-tracing (which we know fails under certain conditions) compared to wave-based physics. Using the same simple geometries for both methods, we find that phonon transmission through the pores agrees very well for both wave-based and particle-based methods, with an error margin of  $\pm 15\%$ , across phonon wavelengths even for features with sizes down to 3-4 nm. Only for smaller feature sizes, the wave-based NEGF shows that long wavelength phonons can transmit easily, whereas we find that comparatively MC underestimates their transmission. In addition, particle-based simulation methods appear more sensitive to nanoscale structural variations compared to the wave-based NEGF method. Insights and knowledge gleaned from comparing wave and particle methods can be used to provide a better and more complete understanding of phonon transport in nanomaterials.

The chapter is organized as follows: In Section 7.2 we describe the theoretical background and computational methods. In Section 7.3 we present our results, comparing wave-based Non-Equilibrium Green's Function (NEGF) and particle-based Monte Carlo ray-tracing simulations for simple geometries considering a single pore. In Section 7.4 we discuss the import of these results and examine geometries with more than one pore. Finally, in Section 7.5 we present our conclusions.

## **7.2 Approach: theoretical background and methods**

The wave nature of phonons can be approximated by particles when they have wavelengths smaller than the characteristic length scales of the static disorder in the material under consideration (in our case pore size, pore distance, neck – see Fig. 7.1a). In materials with boundaries such as nanowires and thin films, when the boundary roughness amplitude in the structure is small, phonon reflection is primarily specular across wavevectors and correlation lengths [192].

For large roughness amplitudes, phonon reflections are diffusive, multiple scattering events at boundaries arise, and the thermal conductivity reduces significantly [202, 224, 255]. On the other side of the spectrum, long-wavelength phonons, much longer than the characteristic disorder in the nanostructure, cannot be effectively treated as particles, as at this point diffraction and interference effects become important. For example, Maurer *et al.* showed that such modes can be thought

of as elastic-waves, which in the case of a large boundary roughness amplitude can experience a degree of localization, and Rayleigh waves can also appear in the material [192, 260].

Despite the limitation of Monte Carlo and ray-tracing when it comes to long wavelength phonons, the acoustic phonons that carry a significant portion of the heat are routinely treated as particles within Monte Carlo to describe thermal transport in nanostructures. Measured data has been successfully described in a large number of instances and materials with characteristic sizes smaller than the dominant phonon wavelengths [10, 16, 80, 81, 89, 151, 202, 254, 255, 261]. There is a growing interest in understanding thermal transport in hierarchically nanostructured materials, in which nanoscale features of various scales are embedded within a matrix material.

In this case, Monte Carlo simulations are highly applicable, as they allow flexibility in the simulation domain geometry and size and provide relatively good accuracy with reasonable computational cost. While large domains, larger than all important phonon wavelengths and mean-free-paths, can justify the treatment of the wave-phonons in terms of particles, still, in the vicinity of the smaller, nanoscale features, wave effects could persist. The influence of these features on the thermal conductivity under the wave versus particle phonon description is unknown.

The basis porous geometry we begin with is shown in Fig. 7.1a. The structure is defined by the pore diameter  $D$  and the neck size  $n$ , which is the minimum distance between the pore boundary and the upper/lower boundaries. For computational efficiency we consider a basis two-dimensional (2D) simulation domain of length  $L_x = 100$  nm ( $x$ -direction) and width  $L_y = 10$  nm ( $y$ -direction). For all geometries we considered, we calculate the transmission of phonons from one side to the other for both methods: the wave-based NEGF method and the particle-based MC method.

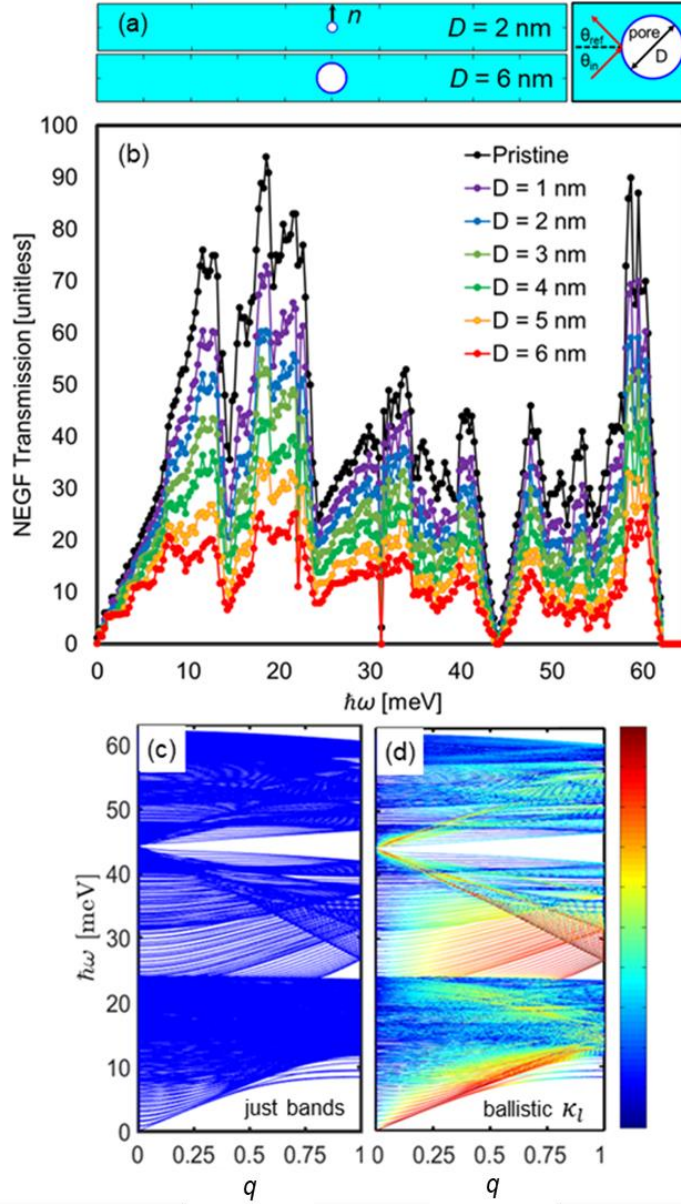


**Figure 7.1:** Nanostructures examined with NEGF wave approach. (a) Schematics of typical geometries studied with length of 100 nm, width 10 nm and thickness 1 nm for two pore diameters of  $D = 2$  nm and  $D = 6$  nm. The neck,  $n$ , is measured, as indicated, as the widest distance between the edge of the pore and the nearest geometry boundary. (b) The NEGF transmission [unitless] vs the energy,  $\hbar\omega$ . Transmission for the pristine case ( $T_{P, \text{NEGF}}$ ) is given by the black line. Transmission for nanostructured porous cases ( $T_{N, \text{NEGF}}$ ) are given for  $D = 1$  nm (purple line),  $D = 2$  nm (blue line),  $D = 3$  nm (dark-green line),  $D = 4$  nm (light-green line),  $D = 5$  nm (orange line),  $D = 6$  nm (red dots), respectively. (c) The typical phonon spectrum for a [100] Si nanowire of 10 nm width and 1 nm thickness calculated by applying periodic boundary conditions on the unit cell in the transport direction. The transmission of the pristine channel (black line in Fig. 7.1b) is essentially a count of the number of modes at each energy of Fig. 1c. (d) The contribution of each phonon state to the total ballistic thermal conductance at room temperature calculated using Eq. 7.8 (without Umklapp scattering). Red and blue colors indicate the largest contribution and the smallest contribution, respectively (colormap). Adopted from Chakraborty *et al.* [61].

### 7.2.1 Non-Equilibrium Green's Function method (NEGF)

The wave-based NEGF is a well-established, fully quantum mechanical method which can take into account the exact nanostructure geometry without any underlying assumptions. Thus, coherent effects are naturally captured. The work on NEGF was done in collaboration with our co-author H. Karamitaheri [61]. The method has been used primarily for electronic transport [134], but also for phonon transport in low-dimensional materials [126-132], yielding results in agreement with experimental measurements [126, 129]. It involves building the Dynamical matrix, which in our case, is built atomistically using force constants [123]. A first nearest-neighbour force constant method is used to set up the dynamical matrix component between the  $i^{th}$  and the  $j^{th}$  silicon atoms, which are the first nearest-neighbours of each other. The force constant tensor describing the coupling between the  $i^{th}$  and the  $j^{th}$  atom is given by:

$$K_0^{(ij)} = \begin{bmatrix} \phi_r & 0 & 0 \\ 0 & \phi_{ti} & 0 \\ 0 & 0 & \phi_{to} \end{bmatrix} \quad (7.1)$$

where we use  $\phi_r = 15.1319$  N/m,  $\phi_{ti} = 127.4988$  N/m, and  $\phi_{to} = 15.1319$  N/m, as the force constant fitting parameters for the radial, the in-plane transverse, and the out-of-plane transverse components of the force constant tensor, respectively [61, 125, 126]. Using these values the phononic bandstructure of bulk silicon is obtained to be in a relatively good agreement with the ones calculated using the more complete, but more computationally expensive modified valence force field method [126, 136]. The 3x3 dynamical matrix components are then calculated as:

$$D_{ij} = U_2^{-1} U_1^{-1} K_0^{(ij)} U_1 U_2 \quad (7.2)$$

where  $U_{1,2}$  are two unitary rotation matrices defined as:

$$U_1 = \begin{bmatrix} 1 & 0 & 0 \\ 0 & \cos \theta_{ij} & \sin \theta_{ij} \\ 0 & -\sin \theta_{ij} & \cos \theta_{ij} \end{bmatrix} \quad (7.3)$$

$$U_2 = \begin{bmatrix} \cos \phi_{ij} & \sin \phi_{ij} & 0 \\ -\sin \phi_{ij} & \cos \phi_{ij} & 0 \\ 0 & 0 & 1 \end{bmatrix} \quad (7.4)$$

where  $q_{ij}$  and  $\phi_{ij}$  represents, respectively, the polar and azimuthal angles of the bond between the  $i^{th}$  and the  $j^{th}$  silicon atoms. The dynamical matrix is then described as:

$$D = [D_{3 \times 3}^{(ij)}] = \left[ \frac{1}{M} \begin{cases} D_{ij} & i \neq j \\ -\sum_{l \neq i} D_{il} & i = j \end{cases} \right] \quad (7.5)$$

where  $M$  is the silicon atomic mass. Using the device dynamical matrix, the Green's function is given by [134]:

$$G(E) = \left[ (\hbar\omega)^2 I - D - \Sigma_1 - \Sigma_2 \right]^{-1} \quad (7.6)$$

here, the energy at the contacts is given by the self-energy matrices,  $\Sigma_1$  and  $\Sigma_2$ , which are calculated using the Sancho-Rubio iterative scheme [262]. Afterwards, the ballistic transmission function can be computed using the relation:

$$T_{ph}(\omega) = Trace \left[ \Gamma_1 G \Gamma_2 G^+ \right] \quad (7.7)$$

where,  $\Gamma$  are the broadening functions that describe the interaction between the contacts and the central region, defined at each contact as  $\Gamma = \Sigma^{in} + \Sigma^{out}$  [34]. The thermal conductance can then be obtained using the Landauer formula:

$$K_1 = \frac{1}{2\pi\hbar} \int_0^\infty T_{ph}(\omega) \hbar\omega \left( \frac{\partial n(\omega)}{\partial T} \right) d(\hbar\omega) \quad (7.8)$$

where  $n(\omega)$  is the Bose-Einstein distribution and  $T$  is the temperature. Figure 7.1a shows typical channels we simulate, with one pore located in the middle. The channels we simulate with NEGF have length  $L_x = 100$  nm, width  $L_y = 10$  nm, but also a small thickness of 1 nm, as the Dynamical matrix is built on atomistic lattice. The simulation domain contains 73,000 atoms. Figure 7.1b depicts the phonon transmissions obtained with NEGF ( $T_{NEGF}$ ) vs the energy ( $\hbar\omega$ ) for the different geometries simulated. Transmission for the pristine case is given by the black line, followed by transmission for the different porous cases. On average, we observe that the transmission is reduced from the pristine channel as the pore size increases - in the figure we show the geometry with  $D = 1$  nm (purple line),  $D = 2$  nm (blue line),  $D = 3$  nm (dark-green line),  $D = 4$  nm (light-green line),  $D = 5$  nm (orange line), and  $D = 6$  nm (red line).

The typical phonon spectrum for a [100] Si nanowire of 10 nm width and 1 nm thickness is also calculated by applying periodic boundary conditions on its unit cell in the transport direction and shown in Fig. 7.1c, where the quantized phonon sub-bands are evident. The transmission of the pristine channel (black line in Fig. 7.1b) is essentially a count of the number of modes at each energy of Fig. 7.1c. For reference, in Fig. 7.1d we show the contribution of each phonon state to the total ballistic thermal conductance at room temperature calculated as:

$$K_l = \frac{k_B}{A} \sum_{i,q} v_{g,i}(q) \left[ \frac{\hbar \omega_i(q)}{k_B T} \right]^2 \frac{e^{\hbar \omega_i(q)/k_B T}}{(e^{\hbar \omega_i(q)/k_B T} - 1)^2} \quad (7.9)$$

where  $v_{g,i}(q)$  is the group velocity of phonon with wavevector ‘ $q$ ’ in the ‘ $i^{th}$ ’ band and  $A$  is the cross section area. Red and blue colors indicate the largest contribution and the smallest contribution, respectively (colormap). As seen, in addition to the low frequencies, the high frequency phonons have some contribution to the ballistic conduction as well. In practice, however, Umklapp scattering is what limits the intrinsic conductivity, which also results in the high frequency phonons contributing only little to heat conduction. The largest contribution is attributed to the low frequency acoustic modes. Recently, approaches based on the quantum mechanical NEGF method, using atomistic meshes and including anharmonic phonon-phonon scattering have been developed [121, 196, 257], however, these are computationally costly, and thus bound to much smaller systems. Here, however, we seek something simpler: to isolate the coherent wave effects versus particle ray-tracing effects.

### 7.2.2 Monte Carlo ray-tracing method (MC)

For the particle-based simulations, we employ the ray-tracing Monte Carlo (MC) method to trace the phonon transmission in the nanostructures under consideration. Typically, Monte Carlo can accurately capture geometry details within micro–mesoscale domains and is therefore widely employed to understand phonon transport in nanostructures [16, 58-62, 82, 89, 95, 149-164]. However, as we are only interested in the (ballistic) transmission here, (where scattering happens only at the static pores), and in this case all phonons move in straight lines independent of their frequency, we follow a simple version of what is usually employed in advanced MC

simulations. In our MC (ray-tracing) method, phonons are now initialized one at a time at the left contact with only a random initial angle, (as in the single-phonon incident-flux method [83]). We do not use a specific dispersion relation, or Bose Einstein distribution to initialize the population as all phonons across the dispersion are treated in the same way. Phonons are initialized on the left contact and allowed to travel through the simulation domain where they are either transmitted to the right or backscattered to the left. Once the phonon exits, the next phonon is then initialized. Thus, we only trace the phonon paths, and compute the transmission probability by taking a large number of phonon counts – ten million phonons are initialized on the left contact for each structure. The transmission from MC, unlike the one from NEGF, it is frequency independent, and essentially only depends on geometry. Hence for every structure considered, a single value of phonon transmission is determined for the MC cases. The domain discretization is 0.1 nm, and scattering on pores and boundaries is considered specular (the angle of incidence is the same as the angle of reflection).

Thus, for a pristine system, the MC transmission,  $T_{P, MC}$  is 100%, i.e., all phonons that enter the system from the left contact leave from the right. When nanostructures are introduced in the domain, phonons backscatter, and the transmission,  $T_{N, MC}$ , is reduced from 100% depending on the pore diameter,  $D$ , and neck size  $n$  (Fig. 7.1a). This transmission is normalized by the pristine value to get a “fractional transmission from pristine” value for the MC. This is given by:

$$F_{MC} = \frac{T_{N, MC}}{T_{P, MC}} \quad (7.10)$$

In the pristine case  $F_{MC}$  is 1. Since scattering in MC is completely specular there is no wavevector (or frequency) dependence in the  $F_{MC}$  (these are shown as solid lines in all figures from Fig. 7.2 onwards). To directly compare the MC transmissions to the NEGF transmissions, the latter are also converted into a normalized, fractional transmission in the same way:

$$F_{NEGF}(\omega) = \frac{T_{N, NEGF}(\omega)}{T_{P, NEGF}(\omega)} \quad (7.11)$$

However, since the transmissions in NEGF have frequency dependence  $F_{NEGF}$  also varies when plotted versus energies,  $\hbar\omega$  because different energies behave differently

in the presence of nanostructuring. Note that although MC (ray-tracing) is completely particle-based, boundary scattering can be wavevector dependent and can be described using a boundary scattering treatment derived from diffraction theory [58, 192, 224, 263] (see Fig. A7 in **Appendix A**). In all these cases, however, the scattering behaviour at a boundary depends on the boundary roughness strength, but here we consider the pore and the domain boundaries in both NEGF and MC to be completely smooth. Although scattering by the nanopore boundary is wavevector dependent within the NEGF formalism, we have no way to include this in ray-tracing without the need to assume the surface roughness amplitude. This would then lead to a situation of not being able to compare the two approaches on the same structure. Since we do not include the coherence-breaking [263-265] phonon-phonon scattering in NEGF (that would be computationally extremely demanding), we do not include it in MC either for one-to-one comparison. Thus, we investigate the purely coherent wave effects extracted from NEGF, to the ray-tracing MC in which case particles travel ballistically in the simulation domain, and the only source of scattering is the static disorder from the pores.

### 7.3 Results: wave vs particle phonon behaviour

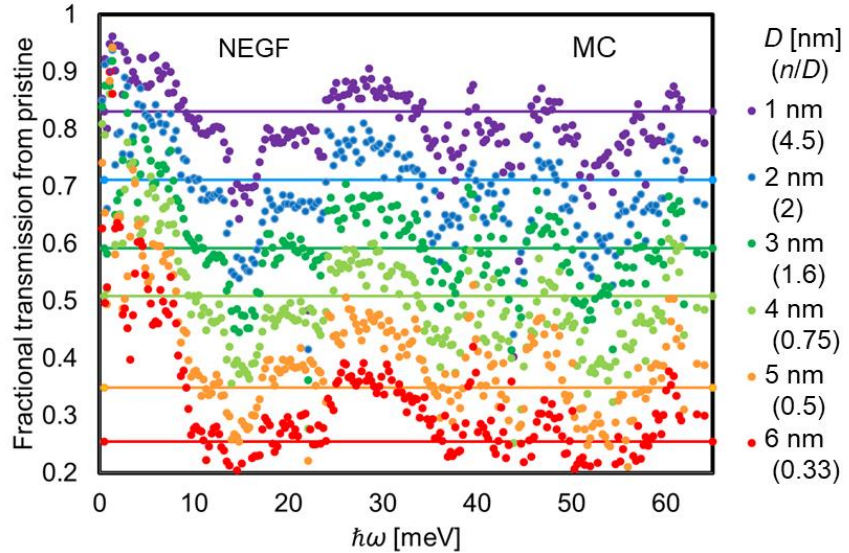


**Figure 7.2:** NEGF fractional transmission  $F_{\text{NEGF}}$  versus energy  $\hbar\omega$  given by Eq. 7.11, for  $D = 1$  nm (purple dots),  $D = 2$  nm (blue dots),  $D = 3$  nm (dark-green dots),  $D = 4$  nm (light-green dots),  $D = 5$  nm (orange dots),  $D = 6$  nm (red dots), respectively. Monte Carlo fractional transmission  $F_{\text{MC}}$  given by Eq. 7.10 (lines, same color scheme), for the same structures. The pore diameters ( $D$ ) and the corresponding neck to diameter ( $n/D$ ) ratios are given on the right axis. Adopted from Chakraborty *et al.* [61].



In order to evaluate the effect that each pore size (and corresponding neck) exert on the transmission, in Fig. 7.2 we consider the fractional transmissions, i.e., the ratios between each of the porous geometries to the pristine one. For this, the transmissions in all the porous structures (colored lines in Fig. 7.1b) are divided by the transmission of the pristine case (black line in Fig. 7.1b). For the case of NEGF transmissions, this is given by Eq. 7.11, and is plotted in Fig. 7.2 versus energy,  $\hbar\omega$  (the color scheme is the same as in Fig. 7.1b). For every pore size the neck to diameter ratio ( $n/D$ ) is also denoted on the right-side axis. The neck size characterizes the region available for phonon propagation, in addition to information about the scattering surface area which is implicit in the pore diameter. As we show later on, the  $n/D$  ratio is a more accurate measure of the scattering strength compared to the diameter, or the neck alone. In Fig. 7.2, the average fractional transmission (i.e., the average of all the dots for each geometry), which we label  $\langle T_{\text{NEGF}} \rangle$ , decreases from  $\sim 0.79$  for the smallest pore size ( $D = 1$  nm,  $n/D = 4.5$ , purple dots) to  $\sim 0.3$  for the largest pore size ( $D = 6$  nm,  $n/D = 0.33$ , red dots), a reduction of  $\sim 63\%$ . Interestingly, if we consider only very the low frequency (long wavelength) acoustic phonons with energies under 3 meV, we see that the corresponding reduction is only  $\sim 10\%$ . The high transmissions obtained with NEGF at low frequencies can be interpreted based on the wave-nature of phonons. Even for small neck sizes, low frequency, long wavelength phonons are more likely not to “see” the pores and propagate through them.

### 7.3.1 MC transmissions versus geometry

The exact same structures used for the NEGF calculations were also simulated with Monte Carlo. In Fig. 7.2, the solid straight lines indicate the MC fractional transmissions, given by Eq. 7.10, following the same coloring scheme for each corresponding structure. The average fractional transmission decreases from  $\sim 0.83$  for the smallest pore size (purple line) to  $\sim 0.26$  for the largest pore size (red line) a reduction of  $\sim 70\%$  as in the case of NEGF. Comparing the flat MC lines with the NEGF dots, we can clearly see that MC provides a good approximation of the wave-based NEGF results for: i) all structures for energies above 10 meV (within an error margin to be discussed later in this section), and ii) for some of the smaller diameter structures with neck sizes above  $n > 2$  nm for all frequencies. This observation is quite interesting, as it quantifies the validity of particle-based methods for the case of long

wavelength phonons, which is assumed to be problematic. It essentially shows that particle-based methods fail to describe the phonon transmission only when phonons are forced into extremely narrow constrictions of a few nanometres thick. In all other cases they seem to perform adequately.

### 7.3.2 Influence of neck size $n$ and $n/D$ ratio

To identify which structural feature size – neck or diameter or  $n/D$  – most affects the MC results, in Fig. 7.3 we compare the MC results in terms of the neck size, diameter, and  $n/D$  ratios.

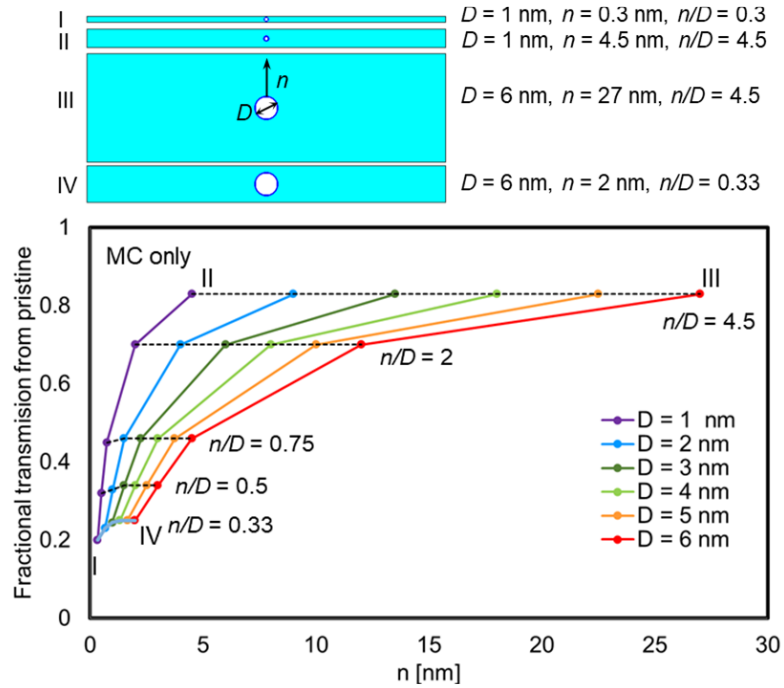


**Figure 7.3:** MC fractional transmission  $F_{MC}$  given by Eq. 7.10, for  $D = 1$  nm (purple line),  $D = 2$  nm (blue line),  $D = 3$  nm (dark-green line),  $D = 4$  nm (light-green line),  $D = 5$  nm (orange line),  $D = 6$  nm (red line), respectively, versus neck size,  $n$ . Typical geometries simulated are depicted in the panel above (I – IV). The common  $n/D$  values across structures are indicated by dashed lines. Adopted from Chakraborty *et al.* [61].

Here, each line plots the fractional transmissions for each porous structure of a given pore diameter using the same coloring as earlier. For each pore size the neck is increased by increasing the width of the simulation domain  $L_y$ . Typical geometries simulated are given in geometry panel above Fig. 7.3 (I – IV). Uniform  $n/D$  values are indicated by the dashed black lines. For a fixed diameter, the transmission increases as the neck size increases, as expected. In the case of  $D = 6$  nm (red line) the smallest neck size,  $n = 2$  nm (geometry IV in panel above), yields the smallest transmission,

and increasing the neck size for the same pore size (moving up the red line) increases fractional transmission to  $\sim 0.83$  (geometry III in panel above). The last point of the red line corresponds to  $n/D = 4.5$ . Interestingly, all other structures of different diameters, but of the same  $n/D$ , have the same fractional transmission (dashed lines for constant  $n/D$  ratios across Fig. 7.3). At the same neck size, on the other hand, as the diameter increases (moving vertically downwards from line to line), the fractional transmission decreases. Thus, the  $n/D$  ratio is better correlated to the MC fractional transmissions in these structures, than either  $D$  or  $n$  alone, indicating a better metric for identifying the influence of porosity and constrictions together. We have verified the strong correlation between  $n/D$  and thermal transport in molecular dynamics (MD) simulations as well (work done by other members of the group, as noted in Ref. [61]). We will discuss the effect of geometry based on this metric from here on.

### 7.3.3 Comparing NEGF and MC variations

We now quantify the variation between the fractional transmissions given by the two methods. In Fig. 7.4 we plot their variation as a percentage of the MC value ( $F_{\text{NEGF}}/F_{\text{MC}} - 1$ ). For the MC this quantity is flat at zero for all structures, i.e.,  $F_{\text{MC}}/F_{\text{MC}} - 1$ , and allows to extract a global variation measure between NEGF and MC across geometries and frequencies.

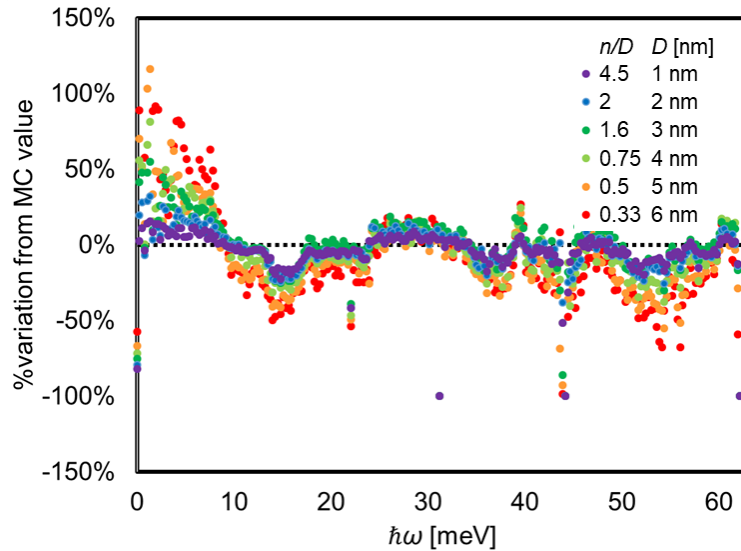


**Figure 7.4:** Percentage variation of the  $F_{\text{NEGF}}$  from the  $F_{\text{MC}}$  values for  $D = 1$  nm (purple dots),  $D = 2$  nm (blue dots),  $D = 3$  nm (dark-green dots),  $D = 4$  nm (light-green dots),  $D = 5$  nm (orange dots),  $D = 6$  nm (red dots), respectively, versus energy  $\hbar\omega$ . Adopted from Chakraborty *et al.* [61].

The data in Fig. 7.4 uses the same coloring scheme as in Fig. 7.2. The  $n/D$  values indicated in each case range from  $n/D = 4.5$  (purple dots) to  $n/D = 0.33$  (red dots). Overall, the NEGF fractional transmissions oscillate around the MC fractional transmissions (at 0). The variation increases with decreasing feature sizes, i.e., with a decreasing  $n/D$  ratio (compare red vs purple dots for the smaller/larger  $n/D$ , respectively). Again, the variation is highest for low frequency (long wavelength) acoustic phonons with energies under 3 meV, where variation in excess of  $\sim 100\%$  can be seen for  $n/D < 0.5$ , i.e., the fractional transmission from MC is half the value from NEGF at these energies. However, for phonons with energies greater than 8 meV, the MC method is able to approximate the NEGF phonon transmission within a 15% error margin especially for the smaller diameters/large neck sizes.

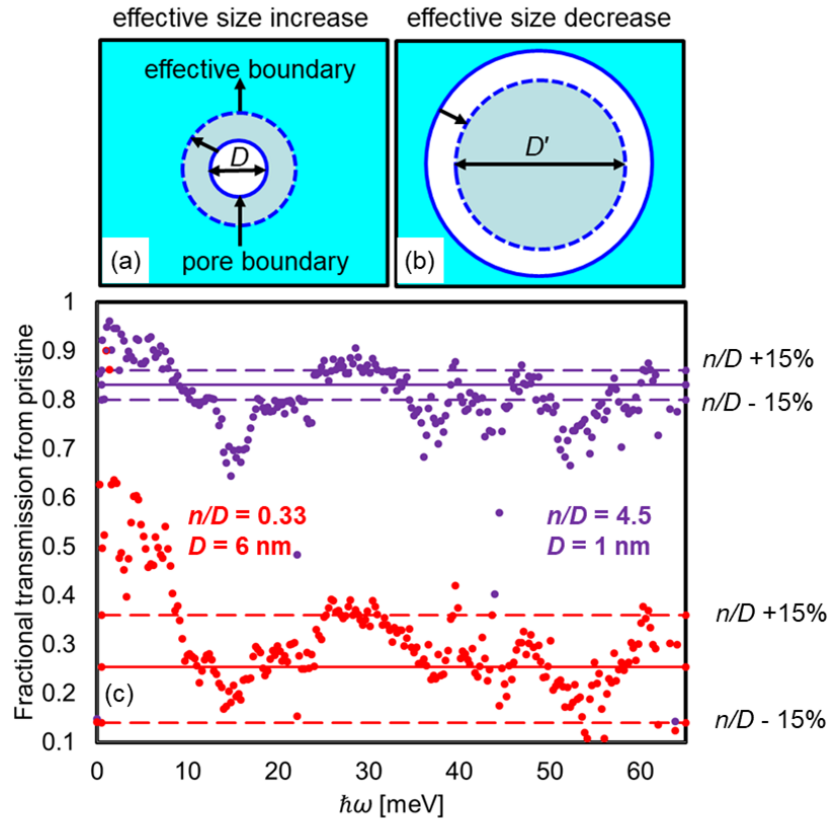


**Figure 7.5:** Comparing wave and particle approaches. (a) Schematic of effective increase in  $D$  and (b) effective decrease in  $D$ . (c) NEGF fractional transmission for structures with  $n/D = 4.5$ ,  $D = 1$  nm (purple dots), and  $n/D = 0.33$ ,  $D = 6$  nm (red dots), respectively, versus energy  $\hbar\omega$ . MC fractional transmission for the same structures are plotted by the solid lines. The dashed lines represent MC ray-tracing for structures with a  $\pm 15\%$  variation on their  $n/D$  ratio. Adopted from Chakraborty *et al.* [61].

The 15% margin within which the MC is able to approximate the NEGF is a consequence of the frequency dependence of the NEGF transmissions. This results in

variations around a mean value that is in any case adequately captured by the MC ray-tracing transmissions. In fact, this margin can also be captured in simple geometrical variations. We have simulated using MC structures in which we have altered the size of the pores, as seen in Fig. 7.5a and Fig. 7.5b such that  $n/D$  is varied by  $\pm 15\%$  for the smaller and the larger diameter structures. Smaller/larger pores will allow larger/smaller transmissions. The dashed lines in Fig. 7.5c indicate the change in the MC transmission as the  $n/D$  changes. Effectively this encompasses a larger proportion of the frequency dependent NEGF transmissions, but still not for the low frequency, long wavelength phonons, especially in the larger diameter structure.

#### 7.4 Discussion: limits of MC and NEGF

In the results above we see variations between the NEGF and the MC of 25% to 100% for frequencies below 8 meV, at low feature sizes, i.e., below  $n/D = 0.5$ ,  $n = 2$  nm. This quantifies the region of validity of particle-based approaches for this specific nanostructure (at least). However, looking at the global average of the NEGF transmissions (dots) we find that the error is less than 15% for most of the spectrum.

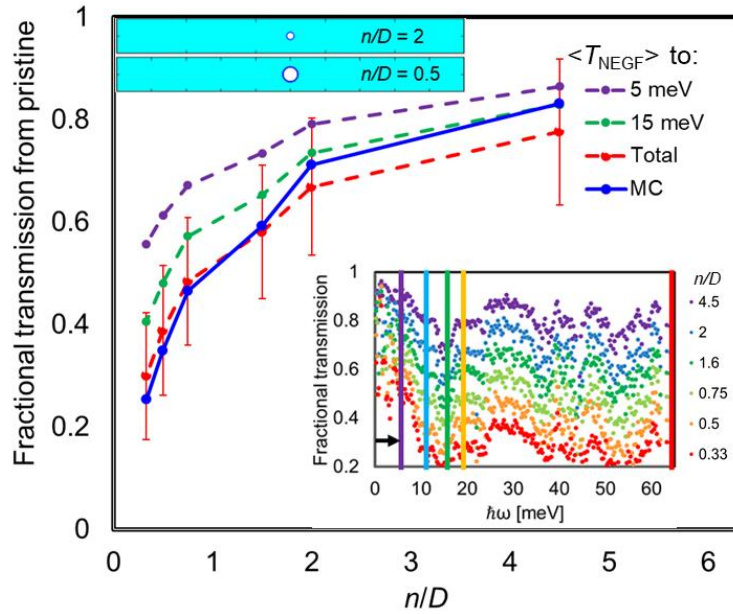


**Figure 7.6:** NEGF results averaged  $\langle T_{\text{NEGF}} \rangle$  over energy in a part of the spectrum up to 5 meV (purple-dashed line), up to 15 meV (green-dashed line) and for the whole spectrum (red-dashed line) vs  $n/D$ . These limits are depicted in the bottom inset with lines of corresponding colors. Error bars give the standard deviation of  $T_{\text{NEGF}}$  data. MC fractional transmission vs  $n/D$  (blue-solid line) is given for comparison. Schematics of some geometries simulated are depicted at the top left corner. Adopted from Chakraborty *et al.* [61].

This is shown in Fig. 7.6, which plots the global average transmission of the NEGF results for all frequencies,  $\langle T_{\text{NEGF}} \rangle$ , at a given  $n/D$  ratio (red-dashed line), and compares them to the values of MC for those same structures (blue line). The error margin for all  $n/D$  is less than 15%. MC slightly overestimates the transmission for structures with large necks and small pore sizes (when  $n/D > 2$ ) where  $D$  is the limiting variable. It slightly underestimates the transmission for structures with small neck sizes and large pore sizes ( $n/D < 2$ ), where  $n$  is the limiting variable. Thus, particle-based MC captures average wave-based thermal transmission effects largely within 15% down to constriction feature sizes of 2 nm. This knowledge could be very useful in quantifying the accuracy of simulations of thermal transport in nanostructured materials under different simulation methods.

While the dominant phonon wavelength is  $\sim 1$  nm at 300 K, we must note that a major component of the heat in Si is carried by long wavelength acoustic phonons with frequencies below 20 meV [16, 80, 81, 84, 125]. Furthermore, if we look at low temperature systems, the dominant wavelengths are much larger than at room temperature. This can result in the error in MC being larger in narrow constrictions, as it cannot capture the transmission of these long wavelength phonons accurately. On the other hand, in the presence of nanostructuring, where the phonon mean-free-paths are limited by the geometrical feature sizes, the relative contribution of phonons from the rest of the spectrum would increase [65, 266-268]. This can be intuitively seen from Matthiessen's rule, in which the overall mean-free-path of a phonon is dominated by the stronger of the scattering processes. Thus, a long mean-free-path will suffer relatively more in the presence of nanostructuring compared to shorter MFP phonons, which reduces the gap between their relative contributions to heat current. In fact, it is pointed out that optical phonons and the rest of the spectrum can also carry a significant portion of the heat at the nanoscale because longer (acoustic) mean-free-path phonons are scattered more strongly leading to a proportionally larger contribution to transport from (optical) mean-free-paths [83]. In order to further quantify the upper limit of the error that could be expected in MC, in Fig. 7.6 we also look at  $\langle T_{\text{NEGF}} \rangle$  in a part of the spectrum up to 5 meV (purple-dashed line) and 15 meV (green-dashed line). The deviation from the MC blue line, and thus the potential error, is at a maximum for the small  $n/D$  cases. At  $n/D = 0.33$ , the error is 120% when we consider  $\langle T_{\text{NEGF}} \rangle$  up to 5 meV. Conversely, the error is at its lowest (below 3%)

for high  $n/D$  structures (see  $n/D = 4.5$ ). In this case, thermal transport properties predicted by MC would be very applicable from nanostructures with  $n/D$  of 2 (or neck size 2 nm) and above. On the other hand, we find that the global average error (variation from MC value) for  $\langle T_{\text{NEGF}} \rangle$  up to 5 meV (purple-dashed line) is 46% while, if frequencies up to 15 meV are considered this reduces to 12%.

## 7.5 Multi-pore cases

Our results repeatedly show that MC underestimates transmissions for long wavelength phonons, compared to NEGF. This is due to the particle-nature of the method, in which by definition phonons always scatter when they hit pores. From a structural examination point of view, this also means the MC method is more sensitive to structural changes in the device. To study this more closely we examine structures with more than one pore. In Fig. 7.7 we take a system with two pores and measure the effect of pore separation on both the NEGF and the MC fractional transmissions.

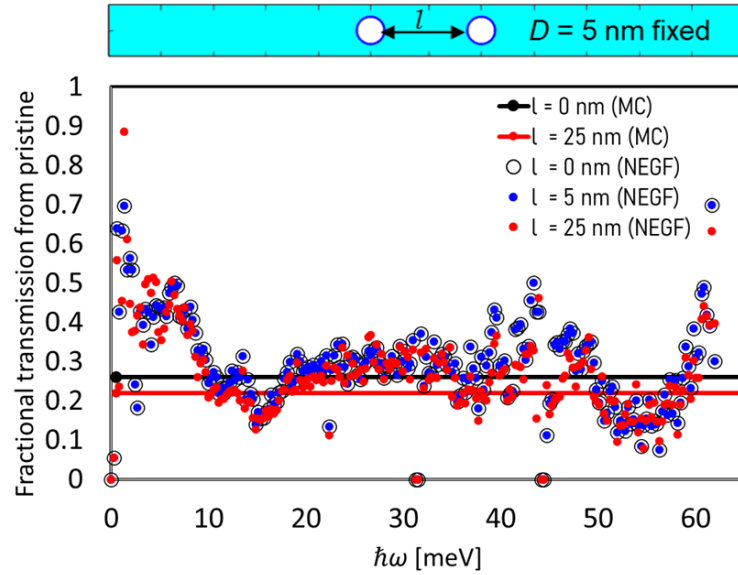


**Figure 7.7:** NEGF fractional transmission for two-pore structure with pore separation  $l = 0$  nm (black circles),  $l = 5$  nm (blue dots),  $l = 25$  nm (red dots) versus energy. MC fractional transmission for the same structures is shown by the solid lines. Schematic of a typical structure simulated with  $D = 5$  nm is given in the panel above. Updated and adopted from Chakraborty *et al.* [61].

The pore diameter is kept constant at  $D = 5$  nm and the pores are positioned equidistantly from the central point, with changing horizontal pore separation length,

$l$ , along the  $x$ -axis. Taking the average  $\langle T_{\text{NEGF}} \rangle$  for all energies at each given  $l$  we observe that the fractional transmission is reduced from an average of 0.27 in the  $l = 0$  nm case (black circles) in Fig. 7.7, where the pore boundaries are just touching, to 0.25, where the pores are separated by  $l = 25$  nm (red dots), . This is a difference of  $\sim 8\%$ . In the case of MC, we see a larger change in fractional transmissions for the same structures from 0.27 in the  $l = 0$  nm case (black line) to 0.22 when the pores are separated by  $l = 25$  nm (red line). This is a difference of 20%, as seen by comparing the two straight lines, more than double of what the NEGF experiences. The case of a vertical separation along the  $y$ -axis, is explored in Fig. 7.8, with pore sizes fixed at  $D = 2$  nm. The pores are placed at the mid-point of the structure along the  $x$ -axis and equidistantly from the middle of the  $y$ -axis, with changing pore separation distance,  $d$ .

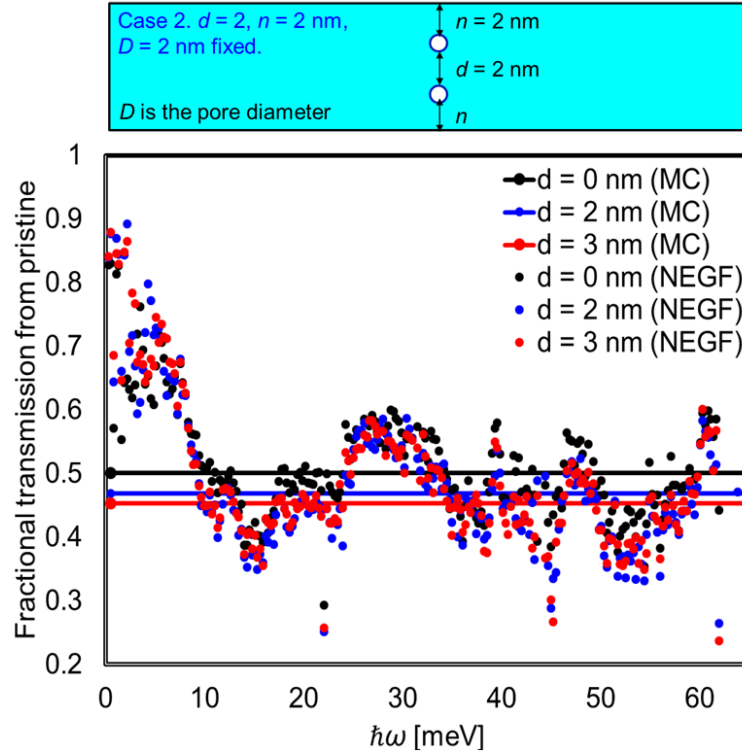


**Figure 7.8:** NEGF fractional transmission for two-pore structures with vertical separation  $d = 0$  nm (black dots),  $d = 2$  nm (blue dots),  $d = 3$  nm (red dots) versus energy. MC fractional transmissions for the same structures are shown by the solid lines. A schematic of a typical structure simulated with  $D = 2$  nm is given in the panel above. Adopted from Chakraborty *et al.* [61].

Taking the average  $\langle T_{\text{NEGF}} \rangle$  for all energies for each  $d$ , we observe that the fractional transmission reduces from an average of 0.49 in the  $d = 0$  nm case (black dots) to 0.47 in the  $d = 3$  nm case (red dots). This is a difference of only 4%. In the case of MC, we see a larger change in fractional transmissions for the same structures



from 0.5 in the  $d = 0$  nm case (black line) to 0.45 in the  $d = 3$  nm case (red line). This is a difference of 10%, again more than double compared to that observed in the NEGF case. Thus, we can conclude that the particle-based MC is more sensitive to geometrical details in the material structure than the wave-based NEGF at these feature sizes between 1 to 10 nm. Again, this is attributed to long wavelength phonons transmitting through or around the pores, being less affected by their structural details in NEGF. It is, however, possible to approximate the NEGF results by changing the effective size of the features simulated in MC, as we see in Fig. 7.5. For low feature sizes an effective decrease in pore size would increase transmission in MC to reduce the deviation from NEGF.

## 7.6 Conclusions

In this work, we investigated the effect of the wave versus particle nature of phonons in their flow through nanostructured porous Si with small pores and constrictions. We used a full wave approach based on the atomistic Non-Equilibrium Green's Function (NEGF) method, and a particle-based approach using ray-tracing Monte Carlo (MC). Using the same simple geometries for both methods, we showed that phonon transmission through the pores agrees well for both methods, with an error margin of  $\pm 15\%$  across phonon wavelengths even for constriction sizes as small as 2 nm and pore diameters as small as 1 nm as well. We also show that the neck to diameter ratio,  $n/D$  is a better measure of the effect of geometry, rather than the neck, or the diameter alone. We find that MC significantly underestimates the transmission of long wavelength phonons only in structures with  $n/D < 2$  compared to NEGF. Long wavelength phonons are shown to propagate more easily through small constrictions, compared to what a particle treatment would suggest. We also found that the particle-based MC is more sensitive to structural details compared to the wave-based NEGF method. Overall, this work suggests that in spite of the different assumptions made by each method, it is possible to use the MC even at the nanoscale and obtain results in agreement (within 15%) with NEGF, even down to very small features. Insights and features extracted from our comparison of wave versus particle methods can be useful in providing a better and more complete understanding of phonon transport in nanomaterials. These results have been published in Chakraborty *et al.* [61].

## 8. Effects of conductive nanoinclusions in resistive matrix

### 8.1 Introduction: conductive nanoinclusions (NI) in resistive matrix

There is a vast amount of study in the literature on the incorporation of nanoinclusions in inorganic crystalline materials in order to produce desirable thermoelectric properties. This can include enhanced thermoelectric efficiency by the reduction of thermal conductivity ( $\kappa$ ) [5, 33, 40-45, 100] or by an increase in power factor ( $PF$ ) [54-56]. The reduction in  $\kappa$  is generally accomplished due to phonon scattering at the matrix-NI interface and depends on the thermal boundary resistance of the interface and the dimensions of the NIs [269]. In their investigation of germanium nanoinclusions (lower  $\kappa = 58 \text{ Wm}^{-1} \text{ K}^{-1}$ ) in a silicon matrix (higher  $\kappa = 148 \text{ Wm}^{-1} \text{ K}^{-1}$ ) Jean *et al.* [260] report an 80% maximum reduction in thermal conductivity. Similarly works with other nanocomposite materials we have  $\kappa$  reductions using amorphous Si [220], Cu-Si [270], Si-Ge [270-272]. Furthermore, using hierarchical inclusions at the atomic scale, the nanoscale, and the mesoscale in the PbTe–SrTe system, Biswas *et al.* reported a  $\kappa$  of  $0.9 \text{ Wm}^{-1} \text{ K}^{-1}$  at 915 K and a  $ZT$  of 2.2 [5]. More recently, using this method for the p-type  $\text{Pb}_{0.98}\text{Na}_{0.02}\text{Te}$ -SrTe system, Tan *et al.* reported an even lower lattice  $\kappa$  of  $0.5 \text{ W K}^{-1}\text{m}^{-1}$  and a higher  $ZT$  of 2.5 at 923K [100]. Reports also show that hierarchical inclusions can improve the thermoelectric power factor as well [54-56].

On the opposite scenario, a common method to increase the thermal (or electrical) conductivity of resistive matrix media is to incorporate highly conductive nanoinclusions (NIs) [38, 273-276]. Important examples of these are organic materials, which are used for flexible electronics and thermoelectrics, but in their pristine form they conduct electricity and heat very poorly. In the case of organic materials the matrix thermal conductivity is very low, usually in the range of  $0.1 - 0.3 \text{ Wm}^{-1} \text{ K}^{-1}$  [38, 277-279], and conductive NIs are inserted in order to increase their  $PF$  [38, 276] and thus enhance their  $ZT$ .  $PF$ s of  $390 \mu \text{ Wm}^{-1} \text{ K}^{-1}$  and  $432 \mu \text{ Wm}^{-1} \text{ K}^{-1}$  for NIs of SnSe and  $\text{Bi}_2\text{Te}_3$  respectively, in PEDOT:PSS organic matrix ( $PF$  of  $143 \mu \text{ Wm}^{-1} \text{ K}^{-1}$ ) [274, 275, 280] have been attained using inorganic-organic hybrid nanocomposites. Including more hierarchical and layered structures, such as alternate

layers of materials (e.g. PANi/graphene-PEDOT:PSS/PANi/DWNT-PEDOT:PSS PEDOT:PSS) can raise  $PF$ s to  $2710 \mu\text{Wm}^{-1} \text{K}^{-1}$  [273]. However, including NIs leads to a change in the thermal properties as well, and particularly an increase in the  $\kappa$  of the given nanocomposite should be expected. However, the thermal conductivity trend is not monotonic, in general both an increase and a decrease can be observed with NI density [38, 276, 281]. This trend in  $\kappa$  is achieved due to two competing mechanisms – the increased intrinsic  $\kappa$  of the NI material which tends to increase the overall  $\kappa$ , and the increased boundary scattering at the matrix-NI interface as the NI density increases, which ends to decrease the overall  $\kappa$ . To-date, however, the specifics that determine this increase in  $\kappa$ , as well as the details which would explain the overall  $\kappa$  behavior, are not well understood. Here, we attempt to shed light on thermal transport in a low thermal conductivity medium in the presence of a network of nanoinclusions of higher thermal conductivity.

For this, we employ the Monte Carlo simulator described in **Chapter 3** and the simulation method specifics for this particular geometry are outlined in Section 8.2. In Section 8.3 we present the simulation results and compare them to experimental observations in real organic materials before drawing our conclusions in Section 8.4.

## 8.2 Approach: simulations of systems with NIs

The Monte Carlo (MC) approach has been adopted for a semi-classical particle-based description of phonon transport. For computational efficiency we consider a 2D simulation domain of length  $L_x = 1000 \text{ nm}$  and width  $L_y = 500 \text{ nm}$ . The domain is populated with nanoinclusions (NIs) of diameters  $D$ . The MC simulation method is described adequately in previous chapters (and our previous published works [58, 59]). Here we additionally incorporate nanoinclusions. The matrix-NI interface was described by a well-established lattice mismatch model – the diffusive mismatch model (DMM) which is, extensively described in the literature [282-286].

The DMM assumes perfectly diffusive phonon transport at interfaces. Phonons encountering an interface scatter in a diffuse fashion and are reinitialized in a random direction. Probability of transmission is proportional to the phonon density of states [116]. It is well established and is considered to be more suited to approximations at room temperature and higher than some other models [101, 116, 284-286]. We also utilize this model, as opposed to other models like the Acoustic Mismatch Model

(AMM) primarily because phonon scattering in organic materials, although not fully understood, is largely assumed to be diffusive in nature [38, 276]. Although, some works point out that no experiment has yet been able to distinguish between the AMM and DMM for energy transport between solids near room temperature. [286-288].

### 8.3 Results

Now we use the modified simulator to see how thermal conductivity changes for an artificial material. We take a bulk silicon channel and increase the scattering rate  $\tau$  to create an artificial material with thermal conductivity that is 10x lower than bulk silicon. Into this channel we then place NIs which have an intrinsic thermal conductivity of Si (10 times larger compared to the matrix material) to see the effects of NI density and size.

#### 8.3.1 Influence of NI density (%NI fraction)

NIs are added as filled circles with diameter  $D = 80$  nm (purple) as seen in the inset of Fig. 8.1. This process initially improves the overall  $\kappa$  of the nanocomposite as NI density increases. In the first no DMM case (blue line in Fig. 8.1c), the lattice mismatch is ignored and there is a steady increase in the thermal conductivity of the system as NI density increases. This is easily understood since the  $\kappa$  of the NIs is 10x larger as compared to the matrix material. This means that there is reduced intrinsic phonon scattering in the NI area (purple circles in inset of Fig. 8.1) which leads to an increase in  $\kappa$  proportional to the increase in NI area. However, when the lattice mismatch (DMM) is included phonons scatter at the NI boundaries (schematic Fig. 8.1b) and we see a different picture (purple line in Fig. 8.1c). Initially for a small number of NIs, as the NI density increases there is an improvement in the thermal conductivity. However, this reaches a peak normalized  $\kappa_n$  value of  $\sim 4.5$  at 20% NI density.  $\kappa_n$  is obtained by dividing the composite system  $\kappa_c$  by the matrix  $\kappa_M = 15 \text{ Wm}^{-1} \text{ K}^{-1}$ .

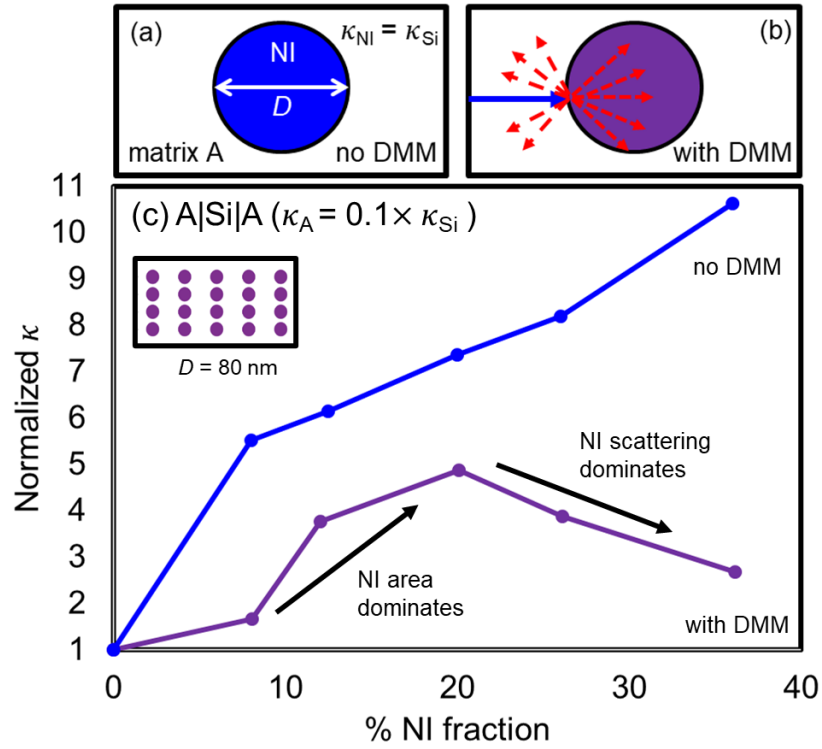


**Figure 8.1.** Effect of adding high  $\kappa$  nanoinclusions in low  $\kappa$  matrix. (a) Schematic of a nanoinclusion, with diameter,  $D$ . (b) Schematic of the DMM phonon scattering interaction with a nanoinclusion boundary. (c) NI density vs Normalized  $\kappa_n = \kappa_c/\kappa_M$  for NIs with no DMM (blue line) and with DMM (purple line) for the case of an artificial matrix  $\kappa_M = 0.1 \times \kappa_{Si}$ , and NIs with  $\kappa_{NI} = \kappa_{Si}$ , and  $D = 80$  nm. A typical geometry with configuration ‘C’ of NI density is seen as inset, with  $D = 80$  nm (purple NIs).

Increasing the NI density any more actually reduces  $\kappa_n$  as seen in Fig. 8.1c. We can interpret this as follows: The change in  $\kappa_n$  is achieved due to two competing mechanisms – the increased intrinsic  $\kappa$  of the NI material and NI-matrix interface scattering (Fig. 8.1b). The  $\kappa$  of the NI is 10x larger as compared to the matrix material which means reduced intrinsic phonon scattering in the NI area (purple circles in inset of Fig. 8.1). This process initially improves the overall  $\kappa_n$  of the nanocomposite as NI density increases, while it is dominant. However, the boundary scattering at the matrix-NI interface causes a reduction in thermal conductivity. As the number of NIs increase with increasing NI density the matrix-NI interface length increases and the boundary scattering becomes more dominant. This leads to a decrease in the overall  $\kappa$  of the nanocomposite system as NI density increases. To see how the strength of each process compares we change the diameters,  $D$  of the NIs.

### 8.3.2 Influence of NI Diameter ( $D$ )

As the positive effect of NI high thermal conductivity area competes with negative effect of NI boundary scattering, a peak is formed as the NI density increases, at the point where the strength of both is equally dominant. Here, in Fig. 8.2 by changing the NI size ( $D$ ) we observe multiple effects. The  $\kappa_{\text{NI}}/\kappa_{\text{M}}$  ratio is kept fixed at 10, with  $\kappa_{\text{M}} = 0.1 \times \kappa_{\text{Si}}$ , and NIs with  $\kappa_{\text{NI}} = \kappa_{\text{Si}}$ . We simulate different structures with increasing NI density (% NI fraction) for different NI sizes, i.e. changing  $D$ . Examples of the different NI sizes and configurations considered are given in the geometry panel above Fig. 8.2. Each line represents the change in normalized  $\kappa_{\text{n}}$ , for a fixed  $D$ , as NI density increases. We examine NIs with  $D = 80$  nm (purple line),  $D = 72$  nm (light-blue line),  $D = 60$  nm (green line),  $D = 44$  nm (orange line) and  $D = 30$  nm (red line). All NI boundaries are taken to be fully diffusive (DMM case).

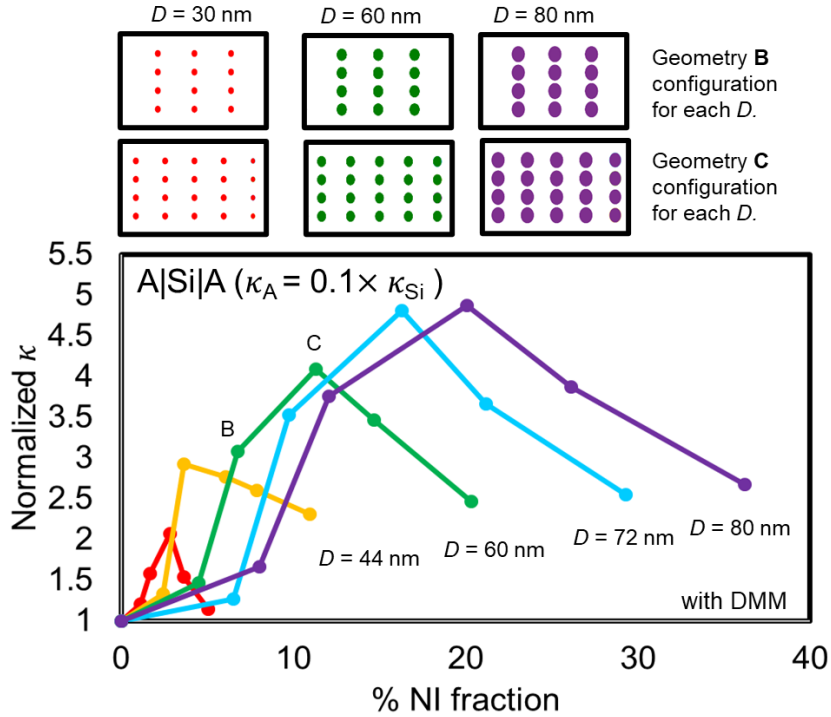


**Figure 8.2.** NI density vs Normalized  $\kappa_{\text{n}} = \kappa_{\text{C}}/\kappa_{\text{M}}$  for the case of an artificial matrix  $\kappa_{\text{matrix}} = 0.1 \times \kappa_{\text{Si}}$ , and NIs with  $\kappa_{\text{NI}} = \kappa_{\text{Si}}$ .  $\kappa_{\text{n}}$  for  $D = 30$  nm (red line),  $D = 44$  nm (orange line),  $D = 60$  nm (green line),  $D = 72$  nm (light-blue line) and  $D = 80$  nm (purple line) are given for the DMM case. Typical geometries simulated are seen in the geometry panel above for  $D = 30$  nm (red NIs),  $D = 60$  nm (green NIs),  $D = 80$  nm (purple NIs) cases, respectively.

Firstly, as  $D$  is reduced there is a marked reduction in the size of the peak formed. In the case of the  $D = 80$  nm (purple line) the peak normalized  $\kappa_n \sim 4.5$ . For a reduced  $D = 30$  nm (red line) the peak reduces to a normalized  $\kappa_n \sim 2$ . Simply put, smaller NI sizes have a smaller NI area/boundary ratio ( $A/b$  ratio) and hence at a given NI area the boundary scattering becomes dominant, causing a reduction in the thermal conductivity peak. In other words, this means that boundary scattering processes become more dominant at smaller NI densities for smaller NI sizes – which is also seen in Fig. 8.2. As NI size increases, the peaks in their  $\kappa_n$  shift to the right. For  $D = 80$  nm (purple line) the peak is formed at 20% NI density, for  $D = 44$  nm (green line) the peak is formed at 12% NI density, and for  $D = 30$  nm (red line) the peak forms at formed at 5% NI density.

As the non-monotonic trend is a consequence of the NI area and boundary length, in Fig. 8.3 we study the changes in total NI boundary length (sum of the boundaries of all NIs present in the system) and total NI area (sum of all NI areas in the domain) as NI size changes. For all configurations A – E (shown in the geometry panel above Fig. 8.3) the NI Area versus NI boundary is given for all NI sizes considered, starting from the largest  $D = 80$  nm (purple line), to the smallest  $D = 30$  nm (red line). For systems with smaller NI sizes the boundary length is much higher at the same NI Area. This can be seen in Fig. 8.3, where the NI boundary length for the  $D = 30$  nm case (red line) is always much longer than the NI boundary length for larger NI sizes, for the same NI area. Longer NI boundary translates to more phonon scattering and hence we get a reduced peak size for the  $D = 30$  nm case. In fact, the  $D = 80$  nm case (purple line in Fig. 8.3) has the lowest NI boundary length per unit area, and this translates to the highest peak as seen in Fig. 8.2 (purple line).

Looking at it in another way, the  $\kappa$  reduction due to boundary scattering is dependent on boundary length and thus proportional to  $D$ . The  $\kappa$  increase due to higher  $\kappa_{NI}$  is due to the NI area and is proportional to  $D^2$ . For small values of  $D$  there is less area per NI for the same number of NIs. However, as  $D$  increases the effect of  $\kappa_{NI}$  increases by  $D^2$  while the effect of boundary scattering increases by  $D$  – leading to larger peaks at higher NI densities for larger NI sizes. Hence the two competing effects seem largely dependent on the NI area to boundary length ( $A/b$ ) ratio. Our simulations are 2D, but similarly in 3D this should be Volume/Surface Area.

We closely examine the  $A/b$  ratio for the peak/maximum  $\kappa_n$  observed for each NI diameter in the inset of Fig. 8.3. Here we can clearly see that the peak  $\kappa_n$  occurs for a higher  $A/b$  ratio as NI size,  $D$ , increases, signifying a clear positive correlation. We can surmise that an increased in  $A/b$  ratio gives an increased peak  $\kappa_n$ .

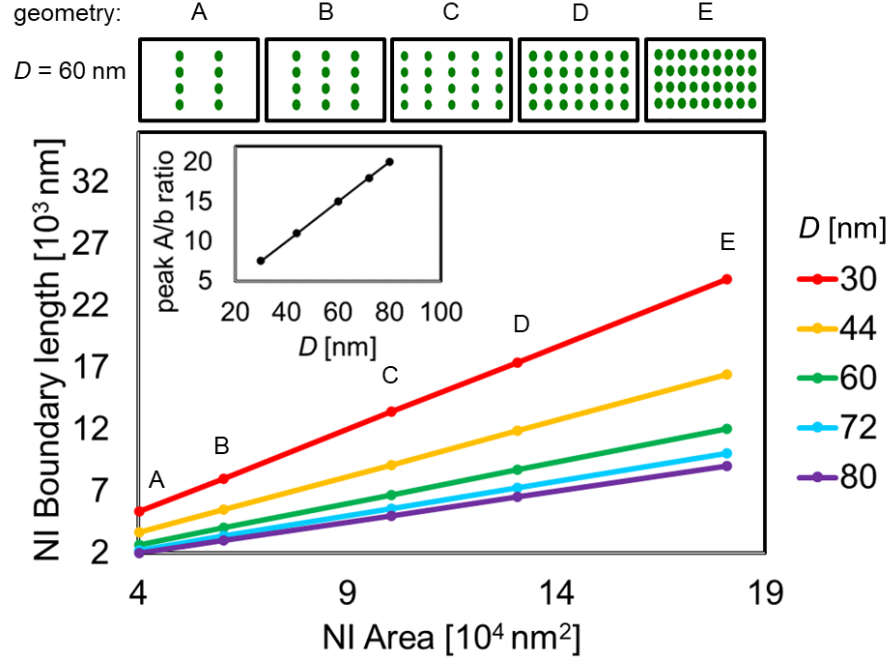


**Figure 8.3.** NI Area vs NI Boundary length for the case of an artificial matrix  $\kappa_M = 0.1 \times \kappa_{Si}$ , and NIs with  $\kappa_{NI} = \kappa_{Si}$  are given for all NI diameters and configurations. Typical geometries simulated with configurations A – E are seen in the geometry panel above for  $D = 60 \text{ nm}$  (green NIs). Inset gives the value of  $A/b$  ratio for the peak value of thermal conductivity observed as diameter ( $D$ ) changes.

Hence, introducing higher thermal conductivity NIs ( $\kappa_{NI}$ ) to resistive media can increase the overall thermal conductivity of the composite,  $\kappa_c$ . This can be done in a controlled fashion by modulating the NI size or the  $A/b$  ratio of the NIs. This is particularly important in organic electronics and thermoelectrics, where a flexible matrix can prove useful for numerous applications such as wearable electronics and thermoelectric devices, but the conductivity of the matrix needs to be improved. This is contrary to the usual motivation in thermoelectric devices where one wants to decrease thermal conductivity as much as possible to improve the ZT. Here the effort is to increase the electrical conductivity at the expense of the thermal conductivity. Next, compare how our work compares to some real-world examples. We have only identified systems of organic matrix with inorganic NIs, and although thermal



transport in organic materials is of very different nature compared to the organic crystalline materials that we treat within MC, still we compare these systems as similar trends are also observed.

### 8.3.3 Comparison to experiments

In order to mimic real world applications and materials we take the same artificial material channel with thermal conductivity that is 10 times lower than bulk silicon and place NIs which have an intrinsic thermal conductivity  $\frac{1}{2}$  of Si (5 times larger compared to the matrix material). In Fig. 8.4 we see how our results compare to some real-world examples of nanocomposites with an organic matrix with inorganic NIs.

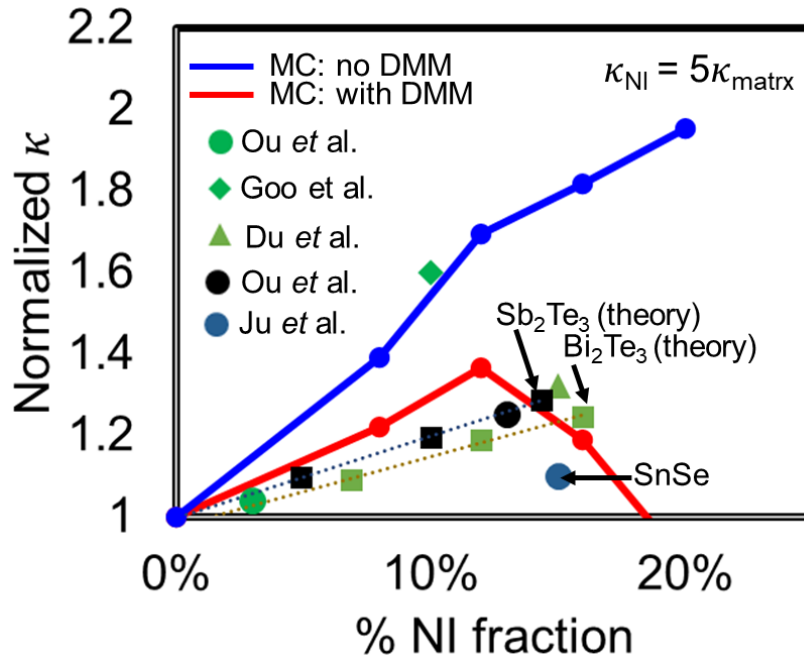


**Figure 8.4.** NI density vs Normalized  $\kappa_n = \kappa_C/\kappa_M$  for the case of an artificial matrix  $\kappa_M = 0.1 \times \kappa_{Si}$ , and NIs with  $\kappa_{NI} = 0.5 \times \kappa_{Si}$  are given for the MC with no DMM (blue line) and MC with DMM (red line) cases. Real-world experimental (and theory) results from the literature are given for similar  $\kappa_{NI}/\kappa_M$  ratios.

We maintain the same  $\kappa_{NI} \sim 5 \times \kappa_M$  for each case and compare the normalized  $\kappa_n$  values for each experimentally observed material with our predictions (red line in Fig. 8.4). The green data points in Fig. 8.4 are for experimental devices that use PEDOT:PSS as the organic matrix material with Bi<sub>2</sub>Te<sub>3</sub> nanoinclusions [279, 289, 275] and the green-dashed line gives the theoretical predictions for the same material

[279]. The black data points in Fig. 8.4 incorporate  $\text{Sb}_2\text{Te}_3$  nanoinclusions in the same organic matrix, (theoretical predictions given by dashed-black line) [279, 276]. We see some initial overall match between our results and these experimental observations. For a lower  $\kappa_{\text{NI}}$  we expect lower  $\kappa_{\text{n}}$  values. Indeed, looking at a  $\kappa_{\text{NI}} \sim 3 \times \kappa_{\text{M}}$  case with SnSe nanoinclusions [274] (dark-blue data point in Fig. 8.4, again with PEDOT:PSS as the organic matrix material) we see that the  $\kappa_{\text{n}}$  is lower than the predicted  $\kappa_{\text{NI}} \sim 5 \times \kappa_{\text{M}}$ , as expected. The characteristic peak that we observed here has been reported in other hybrid materials recently [290-295] and further experimental match with our simulation is anticipated as research into this area evolves.

## 8.4 Conclusions

In this work we have attempted to shed light on thermal transport in a low thermal conductivity medium in the presence of a network of nanoinclusions of higher thermal conductivity. We take a bulk silicon channel and increase the scattering rate within a Monte Carlo simulator to create an artificial material with thermal conductivity that is 10x lower than bulk silicon. Into this channel we then place NIs which have an intrinsic thermal conductivity 5x and 10x larger compared to the matrix material. We show that the thermal conductivity follows a non-linear trend with the density of NIs. Incorporation of low densities of NIs does improve the thermal conductivity, but as the NI density increases and phonons encounter more boundary scattering, thermal conductivity tends to decrease again. In fact, we show that as the NI boundary length to NI area ratio (surface to volume ratio in 3D) increases (i.e. several smaller NIs rather than a few larger ones), the reduction in thermal conductivity is encountered at lower NI densities, resulting in smaller overall increase in the thermal conductivity due to NIs. Insights extracted from this work can be used to provide a better understanding of phonon transport in nanocomposite materials with intrinsically low matrix thermal conductivities, where its beneficial to incorporate NIs of higher thermal conductivity, such as flexible organic thermoelectrics.

## 9. Conclusions and future work

### 9.1 Conclusions

In this thesis we investigated thermal transport in hierarchically nanostructured and highly disordered geometries through theory and large-scale simulations. The thesis developed and employed a ‘single-phonon’ Monte Carlo phonon transport simulator to solve the Boltzmann Transport Equation for phonons in hierarchical and disordered Si nanostructures. We have presented a thorough investigation into the impact of nanostructures on the thermal properties of these materials.

The main results of the work are as follows:

- 1) In nanocrystalline geometries the effect of grain size on thermal conductivity ( $\kappa$ ) is more pronounced at grain sizes  $\langle d \rangle$  smaller than the average phonon mean free path of the system ( $\lambda_{pp}$ ). In that case, boundary scattering dominates over internal three-phonon scattering. Further, effect of changing grain size and porosity ( $\phi$ ) on thermal conductivity is much larger than effect of boundary roughness and specularity ( $p$ ) in reducing  $\kappa$ . Combining defects to create hierarchical nanostructuring reduces thermal conductivity significantly.
- 2) Randomization or highly disordered porous geometry, which is often overlooked, can play an important effect, reducing thermal conduction by even up to 60% compared to the ordered pore geometry. Thus, non-uniformity can be as important, if not more important in reducing  $\kappa$  compared to boundary roughness and specularity ( $p$ ) and needs to be considered at a similar level in interpreting experimental data. We constructed new accurate analytical models for randomized porous structures, based on existing models for ordered structures, with excellent agreement with the full-scale Monte Carlo simulations.
- 3) Nanocrystalline grain boundaries are more effective at reducing thermal conductivity at higher temperatures. Up to  $\sim 40\%$  further reduction in thermal conductivity at high temperatures (800 K) can be attributed to the  $q$ -dependence of boundary scattering. Incorporating hierarchically disordered nanopores magnifies this effect by an additional  $\sim 15\%$  at 800 K.

This suggests that nanostructuring at high temperatures can be more effective than previously thought.

- 4) Thermal rectification was observed in silicon for small temperature differences. Rectification was defined in terms of system mean-free-paths rather than non-linearity in temperature – as conventionally done. It was shown that it is possible to enhance thermal rectification  $R$  in porous materials by using denser pores nearer the device edge. Triangular pore arrangements are more effective at thermal rectification than rectangular arrangements. Total of over 60% rectification was observed for an optimized geometry and nanostructure density.
- 5) Wave-based NEGF method and particle-based MC method were compared. Phonon transmission through the pores (for the same geometry) agree well for both methods, with an error margin of  $\pm 15\%$  across phonon wavelengths even for constriction sizes as small as 2 nm and pore diameters as small as 1 nm as well. Neck to diameter ratio,  $n/D$  is shown to be a better measure of the effect of geometry, rather than the neck, or the diameter alone. MC underestimates the transmission of long wavelength phonons in structures with  $n/D < 2$  compared to NEGF. Long wavelength phonons propagate more easily through small constrictions, compared to what a particle treatment would suggest. MC is more sensitive to structural details compared to the wave-based NEGF method. Overall, in spite of the different assumptions made by each method, it is possible to use the MC even at nanoscale and obtain results in agreement (within 15%) with NEGF, even down to very small features.
- 6) Incorporating nanoinclusions (NIs) consisting of a material of higher thermal conductivity compared to the matrix thermal conductivity, results in a peak value for thermal conductivity with NI surface fraction (volume in 3D). This is a consequence of the interplay of the high thermal conductivity regions that increase phonon transport, and the increased boundaries which impede phonon transport. Its amplitude is determined by the surface/area to boundary line ratio. These insights would be greatly helpful for understanding studies with a large difference on thermal conductivity between the matrix and NIs, for example organics or hybrid nanocomposites.

## 9.2 Future work

There are a few potentially interesting lines of inquiry that could follow from this work:

- 1) All through **Chapters 4** and **5** of this Thesis we discuss how thermal conductivity of certain systems change – it would be great to see how the electronic conductivity and Seebeck coefficient change for the same system to get an idea of the ZT. We already know from concurrent work in the group, however, that as long as the density of nanoinclusions/pores was kept within a certain margin there would be minimal negative impact due to the addition of these nanostructures. Although this was briefly discussed in **Chapters 1, 4** and **5** there could be more work done on this, specifically for the geometries we employ here.
- 2) Throughout **Chapters 4** to **Chapter 6** in this thesis, we use silicon as the base material to examine our hypotheses. While we do take into account germanium (in **Appendix A**) and some other artificial base materials in **Chapter 8** there could be further work done on this using different materials.
- 3) In **Chapter 6** we look at the thermal rectification offered by rearranging circular shaped pores into different geometrical shapes. In other very recent work, it was observed that using triangular pores arranged in specific geometric shapes enhanced thermal rectification in some materials. It would be interesting to see the changes in the rectification if other pore shapes are used.
- 4) Novel thermal materials such as phononic crystals and waveguides (analogous to photonic materials), thermal cloaks, heat channels (analogous to optical metamaterials) and other novel applications could be further examined.
- 5) In **Chapter 8** we describe thermal transport in dissimilar materials. Recently, there has been great interest in research on transport in heterogenous materials and layered hybrid (inorganic-organic) systems. There is scope for further investigation in this direction.

## Appendix A

In this **Appendix A** we include background information and sensitivity studies related to the simulation parameters and the various model choices we employ in the Thesis. The purpose is to demonstrate that the conclusions, and the analytical models we propose, are robust with respect to model assumptions and parameter choice.

### 1. Thermoelectric power generation efficiency:

Thermoelectric power generation efficiency of thermoelectric materials is compared to other methods of power generation. This is given in Fig. A1 below [9].

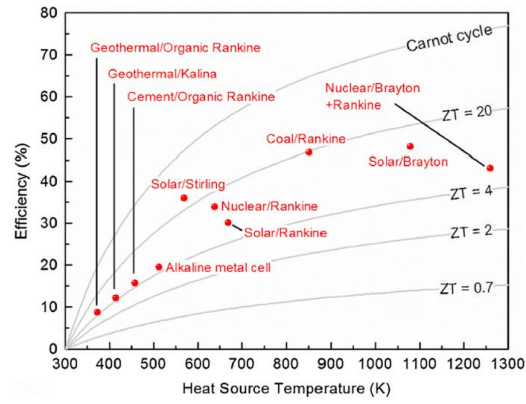


**Figure A1:** Comparison between the efficiency of conventional engines and the efficiency of thermoelectric generators reported as a function of  $ZT$  [9].

### 2. Simple dispersion relation:

Eq. 2.40 has been used to plot a simplified dispersion relation with one optical mode and one acoustic mode in Fig. A2 below. The first Brillouin zone is shown with an acoustic branch (blue line) and an optical branch (green line) for  $M_1 = 0.3M_2$ .

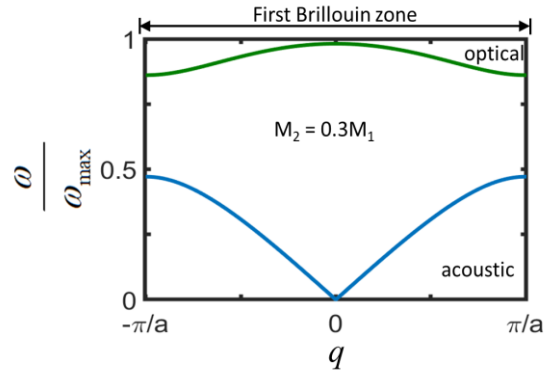


**Figure A2:** A simplified dispersion relation for a material with  $M_1 = 0.3M_2$ . The normalized frequencies are given for the first Brillouin zone with an acoustic branch (blue line) and an optical branch (green line).

### 3. Change in dispersion relation with Mass (M):

Eq. 2.40 has been used to plot a simplified dispersion relation in Fig. A3 below. Here the effect of mass on the dispersion relation is examined by comparing the cases where  $M_1 = 0.3M_2$  (Fig. A3a) and  $M_1 = M_2$  (Fig. A3b) below.

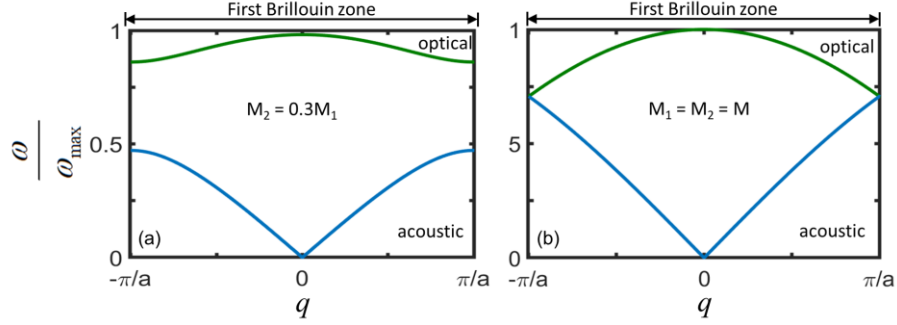


**Figure A3:** A simplified dispersion relation for a material with (a)  $M_1 = 0.3M_2$  and (b)  $M_1 = M_2$ . The normalized frequencies are given for the first Brillouin zone with an acoustic branch (blue line) and an optical branch (green line).

### 4. Time-of-flight <TOF> variation:

The variation of <TOF> for different phonon frequencies ( $\omega$ ) and specularities ( $p$ ) is given below.

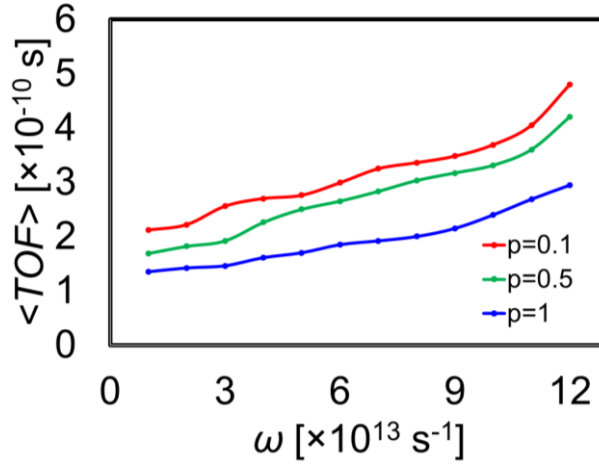


**Figure A4:** Variation of <TOF> with phonon frequency ( $\omega$ ) for cases were  $p = 1$  (blue line),  $p = 0.5$  (green line) and  $p = 0.1$  (red line).

### 5. Phonon-phonon mean-free-path (MFP) value:

The influence of a different choice for the phonon-phonon scattering mean-free-path (MFP)  $\lambda_{pp}$ . In the literature  $\lambda_{pp}$  varies from 100 nm to 300 nm, thus, here, we recreate Fig. 4.5 as Fig. A5 for  $\lambda_{pp} = 135$  nm – solid lines (as in the main text) and  $\lambda_{pp} = 300$  nm – dashed lines. Figure A5 shows the thermal conductivity versus

nanocrystalline domain size for porous materials with porosities  $\phi = 0\%$  and  $15\%$ , in both ordered and randomized pore conditions. Doubling the MFP has at most  $\sim 15\%$  qualitative difference in our results in the pristine material with no crystallinity and no porosity (compare the dashed to solid blue lines at  $\langle d \rangle = 1000$  nm), which drops to  $\sim 6\%$  in the case where high and randomized disorder is introduced (dashed versus solid purple lines at  $\langle d \rangle = 1000$  nm). At smaller  $\langle d \rangle$  the dependence on MFP is insignificant, indicating that boundary scattering dominates transport. Thus, the assumption of MFP choice does not change any of our quantitative or qualitative trends.

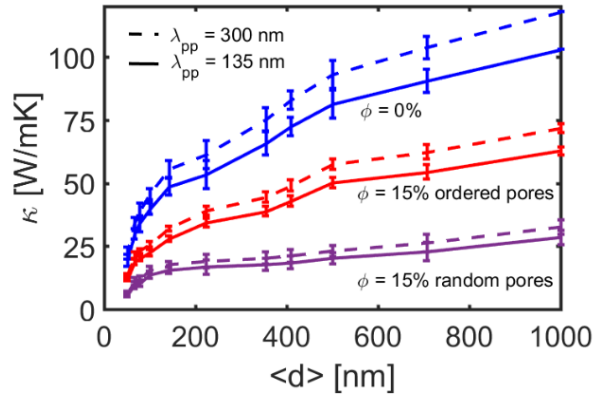


**Figure A5:** Monte Carlo simulations showing the effect of different phonon-phonon scattering MFPs on the combined effects of grain size  $\langle d \rangle$  and porosity ( $\phi$ ). The blue lines show the thermal conductivity in the presence of nanocrystallinity only (no pores). Ordered pores case (red lines) and random pores case (purple lines) versus grain size  $\langle d \rangle$  are also shown. Porosity  $\phi = 15\%$  is considered. The dashed lines indicate the simulations where  $\lambda_{pp} = 300$  nm [11, 171]. The solid lines are for  $\lambda_{pp} = 135$  nm as in the main text [83, 88]. Adopted from Chakraborty *et al.* [58].

## 6. Channel length dependence:

Throughout the paper, we have fixed the channel length at  $L_x = 1000$  nm, which is indeed shorter than some of the phonon mean-free-paths in Si, and used a scaling to adjust for this short channel described by Eq. 3.12. Here we performed Monte Carlo simulations in nanoporous materials of channel length twice as much, at  $L_x = 2000$  nm and compare the thermal conductivity results for the two cases. Figure A6a shows the comparison of the thermal conductivity versus porosity in channels with the different lengths,  $L_x = 1000$  nm (blue line), and  $L_x = 2000$  nm (red line). Indeed, due to the scaling performed, the boundary scattering on the upper/lower surfaces, as well as scattering on the pores, the channel we consider ( $L_x = 1000$  nm) is already diffusive,



and changing the length does not alter the thermal conductivity, either for the pristine channel (for  $\phi = 0$ ) or for the porous cases at any porosity.

In order to have a clear picture on the transport regime at which the channel operates (ballistic versus diffusive), we calculate the average phonon path length in our polycrystalline structures from the moment the phonons enter the domain after initialization, to the moment they are extracted from the domain. This is shown below in Fig. A6b versus the nanocrystalline size  $\langle d \rangle$ . The average phonon path length in the pristine channel is only twice the length of the domain (at  $\langle d \rangle = 1000$  nm), which is the reason for the phonon mean-free-path scaling we employ by Eq. 3.12. As the nanocrystallites are reduced in size, the path increases (since total distance a phonon travels increases due to scattering), especially when their size becomes smaller compared to  $\lambda_{pp}$  (135 nm). The path of the phonons is then more than an order of magnitude compared to the channel length, indicating complete channel diffusion, and large reductions in the thermal conductivity.

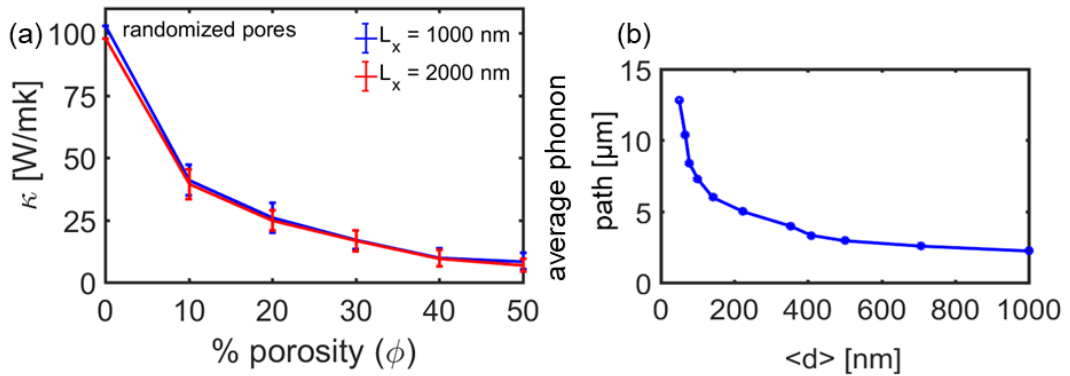


**Figure A6:** (a) Thermal conductivity versus porosity for randomized nanoporous geometries in the nominal domain length  $L_x = 1000$  nm (blue line) and doubled domain length  $L_x = 2000$  nm (black line). Pore boundary specularity is  $p = 0.1$ . (b) Average phonon path vs  $\langle d \rangle$  for nanocrystalline geometry cases.  $\langle d \rangle$  is varied from  $\langle d \rangle = 1000$  nm to  $\langle d \rangle = 50$  nm. Updated and adopted from Chakraborty *et al.* [58].

### **7. Constant roughness $\Delta_{rms}$ versus constant specularity $p$ :**

Instead of a constant specularity  $p$ , in Monte Carlo it is also customary to determine the actual specularity for each phonon using the expression  $p(q) = \exp(-4q^2 \Delta_{rms}^2)$ , which also allows wavevector dependence reflections. In that case, what is constant is the surface roughness ( $\Delta_{rms}$ ). Below, we recreate Fig. 4.3 for the ordered pore cases only, as Fig. A7, but include simulation results for constant  $\Delta_{rms} = 0.3$  nm treatment of pore boundary scattering (i.e. note there is  $q$ -dependent

scattering), a value which corresponds well to rough silicon surfaces [197, 198]. This specific  $p = 0.1$  (red line in Fig. A7) we employ throughout, seems to correspond to this  $\Delta_{\text{rms}} \sim 0.3$  nm over the entire range of porosity values we consider (black-dashed line in Fig. A7).

However, we must qualify that, while there is a good quantitative understanding of the phonon reflection process using roughness or specularity, detailed understanding of how phonons of specific wavelengths reflect from atomically rough surfaces remains unclear – primarily due to limited control over high frequency phonon generation and detection [296]. For instance, while it is established and widely accepted that the increase in roughness of pore boundaries reduces the thermal conductivity observed, in one of his works Maldovan argues that it is possible to get the lowest thermal conductivity using specular reflections on pore boundaries [297]. This is a field where research continues to evolve.

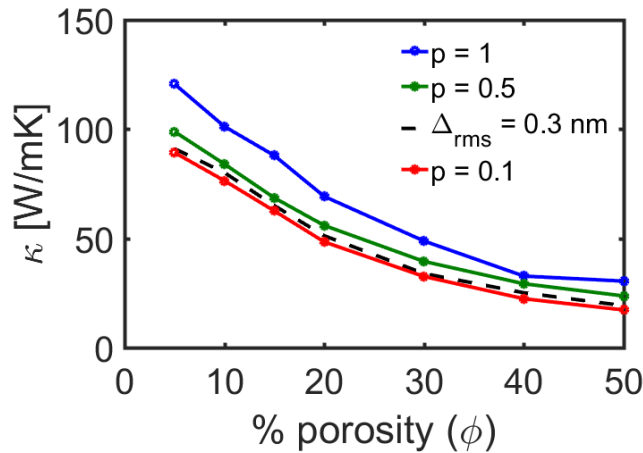


**Figure A7:** Comparison of fixed specularity values vs fixed  $\Delta_{\text{rms}}$  (black line) for ordered porous geometry cases. Three different values for fixed boundary specularity are considered:  $p = 1$ , totally specular boundary scattering (blue line);  $p = 0.5$  (green line); and  $p = 0.1$ , almost diffusive boundary scattering (red line). The results for the fixed  $\Delta_{\text{rms}} = 0.3$  nm (black-dashed line) most closely correspond to  $p = 0.1$ . Adopted from Chakraborty *et al.* [58].

### **8. Pore scattering surface area dependence:**

In order to examine the effect of pore scattering surface on thermal conductivity,  $\kappa$ , we look at both the ordered and the disordered porous case – where both pore size and position is randomly distributed. Both the specular case ( $p = 1$ , blue lines) and the diffusive case ( $p = 0.1$ , red lines) are examined in ordered (solid lines) and polydispersed (dashed lines) pore combinations in Fig. A8 below. For lower pore scattering surface (percentage porosities)  $\kappa$  is much greater in the ordered case than

the disordered case for both cases (comparing solid and dashed lines respectively). This would indicate that the reduction in  $\kappa$  is not just the effect of increased surface area, but also greatly dependent pore position for lower pore scattering surface (percentage porosities). At higher pore scattering surface (above  $\sim 13,000$  nm) the effect of pore position reduces and reduction in  $\kappa$  is due to surface area in polydispersed cases increases.

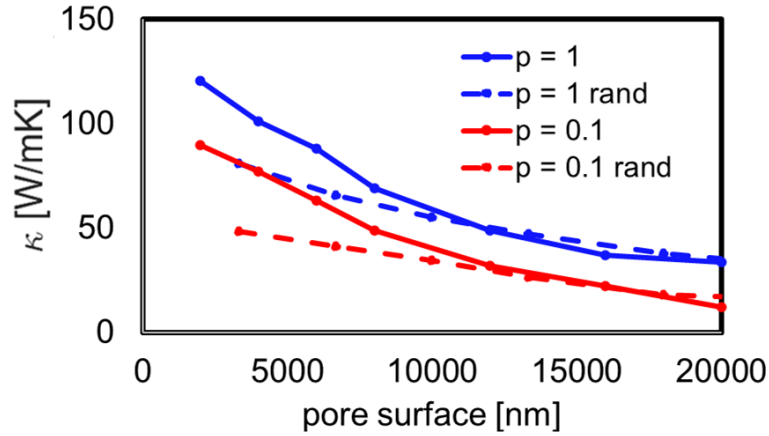


**Figure A8:** Thermal conductivity versus pore scattering surface for specular pore boundaries with  $p = 1$  (blue lines) and the diffusive pore boundaries with  $p = 0.1$  (red lines). Both ordered cases (solid lines) and polydispersed cases (dashed lines) are examined.

### **9. Kapitza resistance variation:**

In the analytical models for nanocrystalline materials described by Eqs. 4.1-4.3 the value of the Kapitza resistance appears. There is a slight variation in the values of the Kapitza resistance in the literature, from  $R_K = 1$  to  $1.16 \cdot 10^9 \text{ Km}^2\text{W}^{-1}$ . Here we vary the value of  $R_K$  in that range to examine the amplitude of this variation in the thermal conductivity. Indeed, the effect of this variation, as shown in Fig. A10 is minor, both qualitatively and quantitatively.

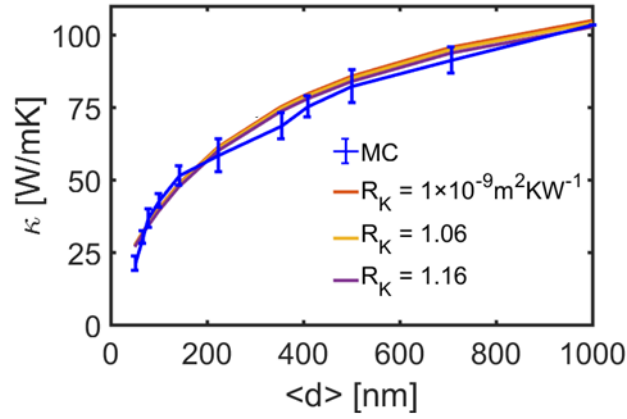


**Figure A9:** Thermal conductivity versus grain size from the commonly employed Yang model [203] analytical model for nanocrystalline geometries compared to the Monte Carlo results (blue line). We assume  $\Delta_{\text{rms}} = 1$  nm. The Kapitza resistance value is varied from  $1 \times 10^9 \text{ Km}^2\text{W}^{-1}$  (red line), to  $1.06 \times 10^9 \text{ Km}^2\text{W}^{-1}$  (yellow line) to  $1.16 \times 10^9 \text{ Km}^2\text{W}^{-1}$  (purple line). Adopted from Chakraborty *et al.* [58].

#### **10. Choice of domain splitting $l_s$ for the randomized analytical models:**

Randomization causes additional reduction in thermal conductivity as seen in theory and experimental works [58, 60, 298]. In the extension of the analytical models in order to capture the effect of randomized porosity (Eqs. 4.11, 4.13), we split the simulation domain in lengths of  $l_s = \delta$ , where  $\delta$  is the scattering length introduced by the pores, and determine the deviation in porosity across the length of the channel based on that  $l_s$  region separation. Although  $\delta$  is determined by the underlying geometry,  $l_s$  is a choice we make based on the fact that the effect of porosity will be correlated to the scattering distance it causes. However, here we investigate the sensitivity of the proposed models on the choice of  $l_s$ . We separated the domain in  $l_s = \delta$ ,  $l_s = 2\delta$  and  $l_s = \delta/2$ , and extracted the deviations in porosity based on those separation. We then included them in the analytical model given by Eq. 4.13. Figure A10 below is a recreation of Fig. 4.8 of the main text, which shows that: i) independent of the choice of  $l_s$ , the model that included deviations provides better fit to the Monte Carlo data compared to the simple, non-randomized model (dashed-purple line), ii) large  $l_s$  compared to  $\delta$  still gives accurate results, iii) smaller  $l_s$  compared to  $\delta$  overestimates the effect of disorder variability, especially at lower porosities. However, at higher porosities the inaccuracy decreases independent of the choice of  $l_s$ .

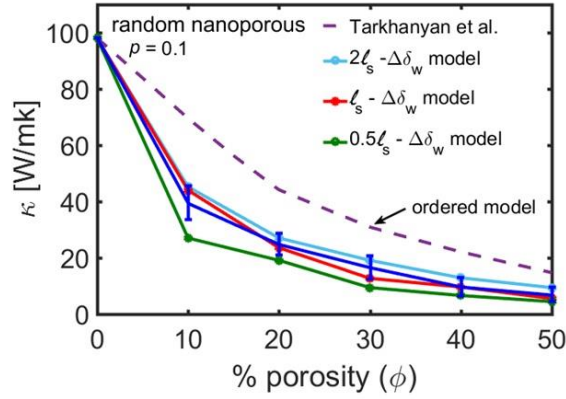


**Figure A10:** The sensitivity of the randomized models in the  $l_s$  distance that we choose to split the channel into for the calculation of the porosity variation along the transport direction. Results for  $2l_s$ , and  $l_s/2$ , where  $l_s = \delta$  are shown and compared to the Monte Carlo results and the simpler non-randomized model of Eq. 4.8. Adopted from Chakraborty *et al.* [58].

### 11. Germanium thermal conductivity:

In order to verify our simulator for a different material we used the bulk case of germanium (Ge). Optical modes are neglected from the dispersion relations, as in previous works, for both Si [16, 58, 59, 80, 81, 89] and Ge, [153, 299]. For simplicity, we use the quadratic fit for the dispersion for the acoustic branches as described by Eq. 2.50 in **Chapter 2** as [85]:

$$\omega(q) = v_s q + c q^2 \quad (2.50)$$

Above, the fitting parameters  $v_s$  and  $c$  for both silicon and germanium materials are parameters as indicated in Table A1 and plotted in Fig. A11.

Parameter	Longitudinal acoustic (LA) branch	Transverse acoustic (TA) branch	Material
$v_s$ [ms <sup>-1</sup> ]	$9.01 \times 10^3$	$5.23 \times 10^3$	Si
$c$ [m <sup>2</sup> s <sup>-1</sup> ]	$-2 \times 10^{-7}$	$-2.26 \times 10^{-7}$	Si
$v_s$ [ms <sup>-1</sup> ]	$5.63 \times 10^3$	$2.60 \times 10^3$	Ge
$c$ [m <sup>2</sup> s <sup>-1</sup> ]	$-1.5 \times 10^{-7}$	$-1.13 \times 10^{-7}$	Ge

**Table. A1.** Fitting parameters that are used to produce the Si and Ge acoustic phonon branches, respectively [85, 153].

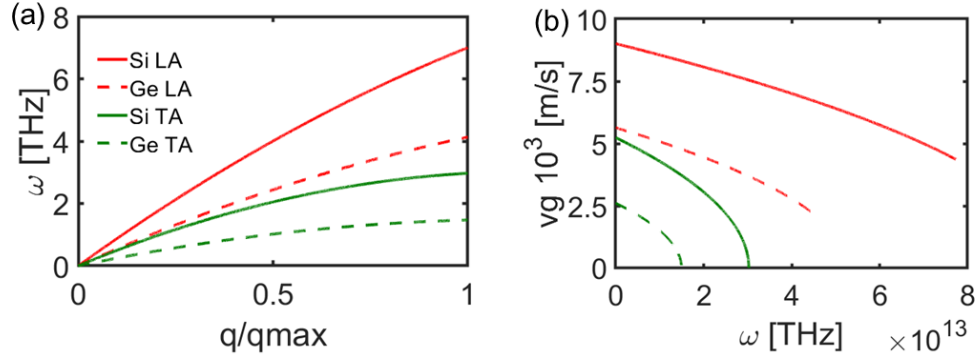


**Figure A11:** (a) The fit for the dispersion relation  $\omega$  obtained as in Refs. [85, 153] and (b) the group velocities for longitudinal acoustic (LA, red lines) and transverse acoustic waves (TA, green lines) for the cases of silicon (solid lines) and germanium (dashed lines), respectively.

All validation of the simulator was carried out using a fixed simulation domain of length  $L_x = 1000$  nm and width  $L_y = 500$  nm. Good agreement is found between our simulated results and literature values of silicon thermal conductivity ( $\kappa = 148 \text{ Wm}^{-1} \text{ K}^{-1}$ ) and germanium thermal conductivity ( $\kappa = 55 \text{ Wm}^{-1} \text{ K}^{-1}$ ) [153, 300].

## **12. Phonon Transport GUI - The GUIDE app:**

This project was aimed to optimise the design of nanostructured thermoelectric (TE) materials that convert heat directly into electricity. During the course of this project we developed a fully functional Monte Carlo phonon transport code. To make this simulator more accessible to users across the spectrum, the more complex and computationally expensive MC code was simplified into the phonon transport simulator app “Guided User Interface Developed for Experimentalists” (GUIDE) created by myself within the duration of my PhD course at Warwick (over the last 3 years from November 2016). The Phonon Transport GUIDE app is a simple graphic guided user interface with interactive inputs that allows the user to generate geometric structures with thermal properties. It has been created entirely in Matlab, with simple intuitive inputs and a user friendly interface. It was validated by myself against established literature sources [41, 86, 89, 96, 152, 1898, 190, 191] for porous silicon material specific applications. Subsequently, it was given to students for their project work (whereupon they validated it independently) for simple porous structures based on silicon. The GUIDE app, is designed to predict thermal properties of given materials and can be used to maximize  $\kappa$  reduction as well as explore thermal

rectification. The GUI input does not allow for significant parallelization (although this was attempted by a project student). It takes certain approximations (e.g. linear thermal gradient is pre-assumed, increased domain discretization, etc.) in order to significantly reduce computation time. For instance, this allowed us to quickly study a range of different geometry configurations for their rectification values before investigating the best ones in-depth using the full MC Monte Carlo phonon transport simulator. Our results from these studies were subsequently published as Chakraborty *et al.* [62]. The code is currently being integrated into a unified electro-thermal computational platform for predicting nanomaterial properties – which should be available shortly. Screenshots of its two currently operational versions of the GUIDE app v1.1 and v1.3 are given below.

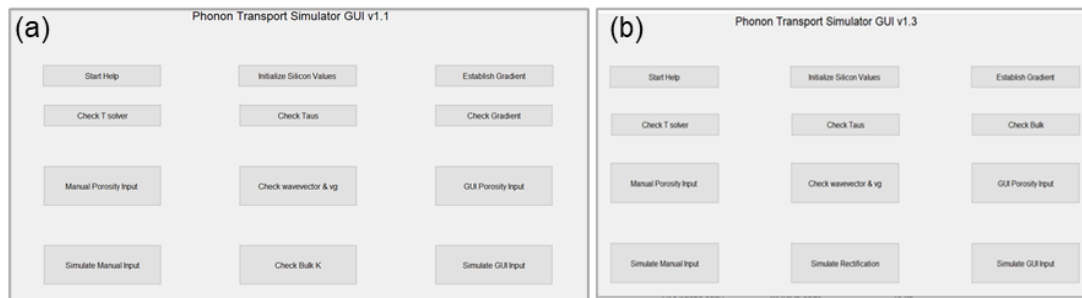


**Figure A12:** Screenshots of GUIDE’s two operational versions (a) v1.1 and (b) v1.3.

This ties into our overall aim to integrate the MC code, wave based NEGF codes etc. developed by our group into a unified electro-thermal computational platform for predicting nanomaterial properties. The latest updates on this (including codes when made available) are given on our University website, which I helped design and maintain until May 2020.

More details given on our website:

[https://warwick.ac.uk/fac/sci/eng/research/grouplist/sensorsanddevices/computational\\_nanotechnology\\_lab/erc\\_nanothermma/](https://warwick.ac.uk/fac/sci/eng/research/grouplist/sensorsanddevices/computational_nanotechnology_lab/erc_nanothermma/)

### 13. Effect of device temperature on thermal rectification:

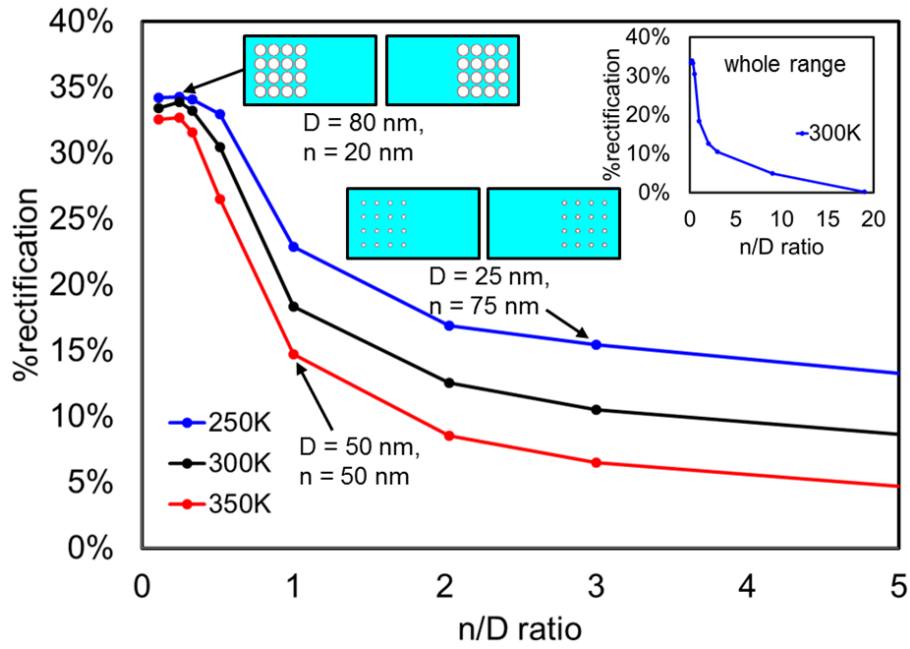


**Figure A13:** The rectification dependence on the pore and neck sizes – given by the neck/diameter ( $n/D$ ) ratio, and the mean temperature of the simulation domain. Three temperature ranges are examined  $T_{\text{avg}} = 350$  K (light-blue line) for  $T_H = 360$  K to  $T_C = 340$  K,  $T_{\text{avg}} = 300$  K (blue line) with  $T_H = 310$  K to  $T_C = 290$  K and  $T_{\text{avg}} = 250$  K (purple line) with  $T_H = 260$  K to  $T_C = 240$  K. The rectification for whole range of  $n/D$  values simulated for the  $T_{\text{avg}} = 300$  K (blue line) case is given as an inset on the top right corner. Typical geometries simulated are also indicated in the insets. Adopted from Chakraborty *et al.* [62].

In Fig. A13 we show the effect of temperature. We have performed simulations for different geometries at two different temperatures, one higher ( $T_H = 350$  K), and one lower ( $T_H = 250$  K). For a given geometry, higher temperatures reduce the phonon  $\lambda_{\text{pp}}$  due to larger phonon-phonon scattering ( $\lambda_{\text{pp}} = 100$  nm for  $T_H = 350$  K), and increase their influence in determining thermal resistance over the pore scattering, which reduces rectification. In contrast, lower temperatures increase the phonon MFPs ( $\lambda_{\text{pp}} = 220$  nm for  $T_H = 250$  K), which reduce their influence on determining thermal resistance over the pore scattering (or the pore influence becomes bigger), which increases rectification.



## Appendix B

### **1. Journal Publications:**

This work has led to journal publications in the following peer-reviewed journals:

1. D. Chakraborty, S. Foster, and N. Neophytou, Monte Carlo phonon transport simulations in hierarchically disordered silicon nanostructures, *Physical Review B*, **98**, 115435 (2018). [Chapter 3 and Chapter 4]
2. D. Chakraborty, S. Foster, and N. Neophytou. Monte Carlo simulations for phonon transport in silicon nanomaterials. *Materials Today: Proceedings*, **8**, 652 (2019). [Chapter 3]
3. D. Chakraborty, L. de Sousa Oliveira, and N. Neophytou. Enhanced Phonon Boundary Scattering at High Temperatures in Hierarchically Disordered Nanostructures. *Journal of Electronic Materials*, **48**, 4, 1909-1916, (2019). [Chapter 5]
4. D. Chakraborty, J. Brooke, N. C. S. Hulse and N. Neophytou. Thermal rectification optimization in nanoporous Si using Monte Carlo simulations. *Journal of Applied Physics* **126**, 184303 (2019). [Chapter 6]
5. D. Chakraborty, H. Karamitaheri, L. de Sousa Oliveira, and N. Neophytou. Effect of wave versus particle phonon nature in thermal transport through nanostructures. *Computational Materials Science*, **180**, 109712 (2020). [Chapter 7]
6. D. Chakraborty and N. Neophytou. Effects of boundary interfaces on dissimilar materials. *APL Materials*, *in process*. [Chapter 8]

Further details about these publications is available on my google scholar or the university webpage. Links given below:

Google Scholar page:

<https://scholar.google.co.uk/citations?hl=en&user=jvni1XwAAAAJ>

University webpage:

[https://warwick.ac.uk/fac/sci/eng/research/grouplist/sensorsanddevices/computational\\_nanotechnology\\_lab/dhritimanc](https://warwick.ac.uk/fac/sci/eng/research/grouplist/sensorsanddevices/computational_nanotechnology_lab/dhritimanc)

## **2. Conference Presentations:**

Certain segments of the research presented in this thesis have been presented at multiple high impact national and international conferences, receiving certain awards. A selected list of (oral and poster) presentations is given below (\* denotes lead presenter):

1. Dhritiman Chakraborty\*, Samuel Foster, Neophytos Neophytou.  
Oral presentation: ‘Multi-Scale Phonon Transport Monte Carlo Simulations in Hierarchically Disordered Nanomaterials,’ European Conference on Thermoelectrics, ECT, Padova, Italy, September 2017. ([link to pdf](#))
2. S. Foster\*, D. Chakraborty, M. Thesberg, H. Kosina, N. Neophytou.  
Oral presentation: Monte Carlo simulations for extracting the power factor in 1D systems”, EPSRC Thermoelectric Network Meeting, Manchester UK, Feb. 14-15, 2017.
3. Dhritiman Chakraborty\*, Samuel Foster, Laura Oliveira, Neophytos Neophytou.  
Poster presentation: ‘Phonon transport in hierarchically disordered silicon nanostructures,’ UK Thermoelectric Network Meeting, Edinburgh, UK, February 2018. (**Best poster award**). ([link to pdf](#))
4. Dhritiman Chakraborty\*, Samuel Foster, Laura de Sousa Oliveira, Neophytos Neophytou.  
Poster presentation: ‘Phonon transport in hierarchically disordered silicon nanostructures’, IET Midlands Power Group Annual Prize Award Evening, 7th March, 2018, Aston University, Birmingham. (**Exceptional poster presentation certificate**).
5. Laura de Sousa Oliveira\*, Dhritiman Chakraborty, Chathurangi Kumarasinghe, Samuel Foster, Vassilios Vargiamidis, and Neophytos Neophytou.  
Poster presentation: ‘Phonon and electronic transport in nanostructures and complex materials’, School on Electron-Phonon Physics from First Principles, 20th March, 2018, ICTP, Trieste, Italy.
6. Dhritiman Chakraborty\* and Neophytos Neophytou.  
Poster presentation: ‘Phonon transport in hierarchically disordered silicon nanostructures’, University of Warwick Engineering Symposium, 20th April, 2018, University of Warwick, Coventry, UK. ([link to pdf](#))
7. Neophytos Neophytou\*, Dhritiman Chakraborty, Laura de Sousa Oliveira.  
Oral presentation: ‘Phonon transport simulations in large scale hierarchically disordered nanostructures’, EMRS Spring Meeting, Strasbourg, France, June 18-22, 2018.

8. Dhritiman Chakraborty\*, Laura de Sousa Oliveira, Samuel Foster, and Neophytos Neophytou.  
Poster presentation: ‘Phonon Transport in hierarchically disordered nanostructures: From Monte Carlo simulations to simple analytical models’, 37th International Conference on Thermoelectrics and 16th European Conference on Thermoelectrics, Caen, France, 2nd July, 2018. ([link to pdf](#))
9. Laura de Sousa Oliveira\*, Dhritiman Chakraborty, and Neophytos Neophytou,  
Oral presentation: ‘Molecular dynamics simulations to understand phonon transport in nanoporous materials’, International Conference on Thermoelectrics / European Conference on Thermoelectrics, ICT/ECT 2018, Caen, France, July, 2018.
10. N. Neophytou\*, S. Foster, V. Vargiamidis, D. Chakraborty, L. Oliveira, C. Kumarasinghe, and M. Thesberg,  
Invited talk: ‘Simulation studies of nanostructured thermoelectric materials,’ IEEE NANO 2018, Cork, Ireland, July 24-26, 2018.
11. Laura de Sousa Oliveira\*, Dhritiman Chakraborty, Vassilios Vargiamidis, Samuel Foster, and Neophytos Neophytou.  
Oral presentation: “Transport simulations in hierarchically disordered nanostructures for thermoelectric materials design”, IEEE Nanotechnology Materials and Devices Conference, October 15th–17th 2018, Portland, Oregon, USA.
12. Laura de Sousa Oliveira, Dhritiman Chakraborty, and Neophytos Neophytou.  
Oral presentation: “Molecular dynamics simulations in disordered nanoporous materials”, CNRS Groupement de Recherche Européen, October 11th–12th 2018, Lyon, France.
13. Dhritiman Chakraborty\*, Laura de Sousa Oliveira, H. Karamitaheri, and Neophytos Neophytou.  
Poster presentation: ‘Phonon transport simulations in nanostructured silicon: Merging information from Monte Carlo, NEGF and MD’, Nanoscale and Microscale Heat Transfer VI, Eurotherm seminar No. 111, 2 – 7 December, 2018, Levi, Lapland, Finland. ([Book of Abstracts](#))
14. Dhritiman Chakraborty\*, Laura de Sousa Oliveira, Samuel Foster, and Neophytos Neophytou.  
Oral + Poster presentation: ‘Phonon Transport in hierarchically disordered nanostructures: Monte Carlo simulations to analytical models’, IET Midlands Power Group Annual Prize Award Evening, 27th March, 2019, University of Birmingham, Birmingham. (**Exceptional presentation award + Valued poster certificate**).
15. Dhritiman Chakraborty\*, Samuel Foster, Neophytos Neophytou  
Poster presentation: ‘Analytical models for thermal conductivity in highly disordered nanostructures’ UK Thermoelectric Network Meeting, Kings College London, UK, May 2019. ([link to pdf](#))

16. Dhritiman Chakraborty\*, Neophytos Neophytou,  
 Oral presentation: ‘Phonon transport in hierarchically disordered silicon nanostructures.’, Engineering Postgraduate Symposium, 23rd April, 2019, University of Warwick, Coventry, UK. ([link to pdf](#))
17. Dhritiman Chakraborty\*, H. Karamitaheri, Neophytos Neophytou,  
 Oral presentation: ‘Phonon transport in hierarchically disordered silicon nanostructures: Monte Carlo to wave-informed Monte Carlo using multi-physics.’, International School of Physics ‘Enrico Fermi’, Varenna, Italy, July 2019. ([link to pdf](#))
18. Laura de Sousa Oliveira\*, Dhritiman Chakraborty, Vassilios Vargiamidis, Neophytos Neophytou,  
 Oral presentation: ‘The effect of geometry on thermal transport in nanoporous Si from large-scale MD’, International School of Physics ‘Enrico Fermi’, Varenna, Italy, July 2019.
19. Neophytos Neophytou, Vassilios Vargiamidis, Samuel Foster, Laura de Sousa Oliveira, Dhritiman Chakraborty, Chathurangi Kumarasinghe, Patrizio Graziosi, and Mischa Thesberg,  
 Oral presentation: ‘Advanced thermoelectric transport simulations in complex bandstructure and nanostructured materials,’ 17th European Conference on Thermoelectrics, Limassol, Cyprus, 2019. ([link to pdf](#))

Extended abstracts printed or published as a part of conference contributions:

1. D. Chakraborty\*, N. Neophytou. ‘Phonon transport simulations in hierarchically disordered silicon-based nanostructures,’ PGR Engineering Symposium, University of Warwick, Coventry, UK, April 23, 2019 (**oral presentation**). ([link to pdf](#))
2. D. Chakraborty\*, S. Foster, L. Oliveira, N. Neophytou. ‘Phonon transport in hierarchically disordered Silicon nanostructures’ PGR Engineering Symposium, University of Warwick, Coventry, UK, April 20, 2018 (**poster presentation**). ([link to pdf](#))
3. Neophytou, N. Neophytou\*, S. Foster, V. Vargiamidis, D. Chakraborty, L. Oliveira, C. Kumarasinghe, and M. Thesberg, ‘Simulation studies of nanostructured thermoelectric materials,’ IEEE NANO 2018, Cork, Ireland, July 24-26, 2018 (**invited talk**). ([link to pdf](#))

Further details about these presentations available on our webpages online. Links given below:

[https://warwick.ac.uk/fac/sci/eng/research/grouplist/sensorsanddevices/computational\\_nanotechnology\\_lab/dhritimanc](https://warwick.ac.uk/fac/sci/eng/research/grouplist/sensorsanddevices/computational_nanotechnology_lab/dhritimanc) (including extended abstracts)

[http://nneophytou.com/?page\\_id=12](http://nneophytou.com/?page_id=12) (detailed list on supervisor’s webpage)

### **3. Public engagement activities:**

During the course of this PhD, I participated in various public engagement activities designed to disseminate information and raise awareness about our project to members of the general public. We applied for fiscal support from and were awarded the Warwick Public Engagement Fund, on the basis of which we participated at the Cheltenham Science Festival (June 2019) and the British Science Festival (Sept. 2019), apart from my participation at the yearly Warwick Engineering and Open days.

*Cheltenham Science Festival: 4 - 9 June 2019, Imperial Square, Cheltenham*



Topic: Energy crisis: Nanomaterials for green energy generation

Brief Background: The Cheltenham Science Festival took place at the Imperial Square in Cheltenham from 4 - 9 June 2019. We, (the members of the Computational Nanotechnology Lab, School of Engineering) from the University of Warwick interacted with children and adults alike to share their knowledge and expertise in the field of thermoelectric power generation and green energy. Our collaborators from the University of Exeter also participated in the presentations by displaying graphene based flexible LEDs, smart fabrics.

Exhibit description: Energy harvesting is a very relevant subject, potentially able to promote energy sustainability and reduction in the use of fossil fuels, with huge environmental and societal benefits. Two thirds of the energy used in power generation ends up as wasted heat. An incredibly large amount of heat is available basically everywhere from our bodies to our natural environment. Thermoelectric materials can convert this waste heat into useful electrical energy, and vastly contribute to energy sustainability, fighting against energy scarcity and global warming. Our exhibit captured the essence of thermoelectric power conversion and generation, with an assortment of modules and devices that took heat from common sources to power electronic appliances of everyday use, thereby converting heat to examples of useful work. e.g. charging of a phone, lighting a lamp, and powering a fan.

British Science Festival (Family Day): 14 Sept. 2019, University of Warwick



Topic: Energy crisis: Nanomaterials for green energy

Brief Background: The British Science Festival took place at the University of Warwick in Coventry from 11 - 14 September 2019. We, (the members of the Computational Nanotechnology Lab, School of Engineering) interacted with children and adults alike on Family Day to share their knowledge and expertise in the field of thermoelectric power generation and green energy. Our collaborators from the University of Exeter also participated in the presentations at the British Science Festival (Family Day).

Exhibit description: At this event we presented modules to show how thermoelectric power generation can help solve the current energy crisis, to kids and adults alike. With roughly two thirds of all energy we use wasted as heat, new generation devices and nanomaterials can efficiently harvest this heat, convert it back to electricity and inject it back into our power supply. Our exhibit captured the essence of thermoelectric power conversion and generation, with an assortment of modules and devices that took heat from common sources to power electronic appliances of everyday use, thereby converting heat to examples of useful work. e.g. charging of a phone, lighting a lamp, and turning a fan.

Further details about these activities available on our webpage. Link given below:

[https://warwick.ac.uk/fac/sci/eng/research/grouplist/sensorsanddevices/computational\\_nanotechnology\\_lab/publicengagement/](https://warwick.ac.uk/fac/sci/eng/research/grouplist/sensorsanddevices/computational_nanotechnology_lab/publicengagement/)



## References

- [1] S. Pandya, G. Velarde, L. Zhang, J. D. Wilbur, A. Smith, B. Hanrahan, C. Dames, and L. W. Martin. New approach to waste-heat energy harvesting: pyroelectric energy conversion. *Nature Asia Materials* 11(1), 1-5 (2019). <https://doi.org/10.1038/s41427-019-0125-y>
- [2] X. Wang, Y. Huang, C. Liu, K. Mu, K. H. Li, S. Wang, Y. Yang, L. Wang, Chia-Hung Su, and Shien-Ping Feng. Direct thermal charging cell for converting low-grade heat to electricity. *Nature Comm.* 10(1), 1-8 (2019). <https://doi.org/10.1038/s41467-019-12144-2>
- [3] Livermore Lawrence National Laboratory and Department of Energy. Estimated U.S. Energy Consumption, (2020) at <https://flowcharts.llnl.gov/>.
- [4] Bo Zhao, P. Santhanam, K. Chen, S. Buddhiraju, and S. Fan. Near-field thermophotonic systems for low-grade waste-heat recovery. *Nano Lett.* 18(8), 5224-5230 (2018). <https://doi.org/10.1021/acs.nanolett.8b02184>
- [5] K. Biswas, J. He, I. D. Blum, C.-I. Wu, T. P. Hogan, D. N. Seidman, V. P. Dravid, and M. G. Kanatzidis. High- performance bulk thermoelectrics with all-scale hierarchical architectures. *Nature* 489, 414 (2012). <https://doi.org/10.1038/nature11439>
- [6] C. Forman, I. K. Muritala, R. Pardemann, and B. Meyer. Estimating the global waste heat potential. *Renewable and Sustainable Energy Reviews* 57, 1568-1579 (2016). <https://doi.org/10.1016/j.rser.2015.12.192>
- [7] S. H. Park, S. Jo, B. Kwon, F. Kim, H. W. Ban, J. E. Lee, D. H. Gu, S. H. Lee, Y. Hwang, J. S. Kim, and D. B. Hyun. High-performance shape-engineerable thermoelectric painting. *Nature Comm.* 7(1), 1-10, (2016). <https://doi.org/10.1038/ncomms13403>
- [8] C. J. An, Y. H. Kang, A. Lee, K. Jang, Y. Jeong, and S. Y. Cho. Foldable thermoelectric materials: improvement of the thermoelectric performance of directly spun CNT webs by individual control of electrical and thermal conductivity. *ACS applied materials & interfaces* 8(34), 22150, (2016). <https://doi.org/10.1021/acsami.6b04485>
- [9] D. Beretta, N. Neophytou, J. M. Hodges, M. G. Kanatzidis, D. Narducci, M. Martin-Gonzalez, M. Beekman, B. Balke, G. Cerretti, W. Tremel, and A. Zevalkink, A. I. Hofmann, C. Müller, B. Döring, M. Campoy-Quiles, M. Caironia. Thermoelectrics: From history, a window to the future. *Materials Science and Engineering: R: Reports*, 138, 100501, (2019). <https://doi.org/10.1016/j.mser.2018.09.001>
- [10] S. Mei, L. N. Maurer, Z. Aksamija, and I. Knezevic. Full-dispersion Monte Carlo simulation of phonon transport in micron-sized graphene nanoribbons. *J. Appl. Phys.* 116(16), 164307, (2014). <https://doi.org/10.1063/1.4899235>

- [11] E. Pop, S. Sinha, and K. E. Goodson, Thermal phenomena in nanoscale transistors, *J. Electron. Packag.* 128, 102 (2006). <https://doi.org/10.1115/1.2188950>
- [12] T. Ould Ely, D. Kamzabek, D. Chakraborty, and M. E. Doherty. Lithium–Sulfur Batteries: State of the Art and Future Directions. *ACS Applied Energy Materials* 1(5), 1783–1814 (2018). <https://doi.org/10.1021/acsaem.7b00153>
- [13] T. Ould Ely, D. Kamzabek, and D. Chakraborty, D. (2019). Batteries Safety: Recent Progress and Current Challenges. *Front. in Ener, Res.* 7, 71 (2019). <http://nur.nu.edu.kz/handle/123456789/4407>
- [14] J. Jaguemont, L. Boulon, and Y. Dubé. A comprehensive review of lithium-ion batteries used in hybrid and electric vehicles at cold temperatures. *Appl. Energy* 164, 99-114 (2016). <https://doi.org/10.1016/j.apenergy.2015.11.034>
- [15] S. Abada, G. Marlair, A. Lecocq, M. Petit, V. Sauvant-Moynot, and F. Huet. Safety focused modeling of lithium-ion batteries. *J. Power Sources* 306, 178-192 (2016). <https://doi.org/10.1016/j.jpowsour.2015.11.100>
- [16] D. Lacroix, K. Joulain, and D. Lemonnier, Monte Carlo transient phonon transport in silicon and germanium at nanoscales, *Phys. Rev. B* 72, 064305 (2005). <https://doi.org/10.1103/PhysRevB.72.064305>
- [17] A.F. Ioffe, *Semiconductor Thermoelements, and Thermoelectric Cooling*, Infosearch, London, (1957).
- [18] M. Telkes. The Efficiency of Thermoelectric Generators. *J. Appl. Phys.* 18, 1116 (1947). <https://doi.org/10.1063/1.1697593>
- [19] A. Sharma, J. H. Lee, K. H. Kim, and J. P. Jung. Recent Advances in Thermoelectric Power Generation Technology. *J. Microelectron. Packag. Soc.* 24 (1), 9, (2017). <https://doi.org/10.6117/kmeps.2017.24.1.009>
- [20] B. C. Blanke, J. H. Birden, K. C. Jordan, and E. L. Murphy. Nuclear battery-thermocouple type summary report. No. MLM-1127. Mound Lab., Miamisburg, Ohio, 1960. <https://doi.org/10.2172/4807049>
- [21] V. Parsonnet, A.D. Bernstein, G.Y. Perry. The nuclear pacemaker: Is renewed interest warranted. *Am. J. Cardiol.*, 66, 837 (1990). [https://doi.org/10.1016/0002-9149\(90\)90361-4](https://doi.org/10.1016/0002-9149(90)90361-4)
- [22] N. Neophytou, S. Foster, V. Vargiamaidis, D. Chakraborty, L. Oliveira, C. Kumarasinghe, and M. Thesberg. Simulation studies of nanostructured thermoelectric materials. *IEEE 18th International Conference on Nanotechnology (IEEE-NANO)*, pp. 420-425. IEEE, 2018. <https://doi.org/10.1109/NANO.2018.8626378>
- [23] T. Ould Ely, D. Kamzabek, and D. Chakraborty. "Batteries Safety: State of the Art and Current Challenges." *Frontiers in Energy Research* (2019). <https://doi.org/10.3389/fenrg.2019.00071>



- [24] C. Singhal, A. Ingle, D. Chakraborty, A. Krishna, C. S. Pundir, and J. Narang. Impedimetric genosensor for detection of hepatitis C virus (HCV1) DNA using viral probe on methylene blue doped silica nanoparticles. *Int. J. Bio. Macromole.* 98, 84 (2017). <https://doi.org/10.1016/j.ijbiomac.2017.01.093>
- [25] J. Narang, N. Malhotra, C. Singhal, A. Mathur, D. Chakraborty, A. Anil, A. Ingle, and C. S. Pundir. Point of care with micro fluidic paper based device integrated with nano zeolite–graphene oxide nanoflakes for electrochemical sensing of ketamine. *Biosensors and Bioelectronics* 88, 249 (2017). <https://doi.org/10.1016/j.bios.2016.08.043>
- [26] D. Chakraborty, G. Rajan, and R. Isaac. A splendid blend of nanotechnology and forensic science. *J. Nano. (Engineering and Medicine)* 6(1), 010801 (2015). <https://doi.org/10.1115/1.4030421>
- [27] J. Narang, N. Malhotra, C. Singhal, A. Mathur, D. Chakraborty, A. Ingle, and C. S. Pundir. Point of care with micro fluidic paper based device incorporated with nanocrys of Zeolite–GO. *Procedia Tech.* 27, 91 (2017). <https://doi.org/10.1016/j.protcy.2017.04.039>
- [28] M. Fazal-ur-Rehman. Novel applications of nanomaterials and nanotechnology in medical sciences-a review. *J. Basic Appl. Sci. Res.*, 8(4), 1 (2018). <https://doi.org/10.1063/1.1697593>
- [29] K. Zhao, P. Qiu, X. Shi, and L. Chen. Recent advances in liquid-like thermoelectric materials. *Adv. Func. Mater.* 1903867 (2019). <https://doi.org/10.1002/adfm.201903867>
- [30] B. Hinterleitner, I. Knapp, M. Poneder, Y. Shi, H. Müller, G. Eguchi, C. Eisenmenger-Sittner, M. Stöger-Pollach, Y. Kakefuda, N. Kawamoto, and Q. Guo. Thermoelectric performance of a metastable thin-film Heusler alloy. *Nature* 576 (7785), 85 (2019). <https://doi.org/10.1038/s41586-019-1751-9>
- [31] M. Maldovan. Sound and heat revolutions in phononics. *Nature* 503(7475), 209–217, (2013). <https://doi.org/10.1038/nature12608>
- [32] N. Neophytou, ‘The heat goes up on thermoelectric materials,’ *EU Research*, p. 34-36, Spring 2020  
[https://issuu.com/euresearcher/docs/nanothermma\\_eur22\\_h\\_res](https://issuu.com/euresearcher/docs/nanothermma_eur22_h_res)
- [33] J. A. P. Taborda, M. M. Rojo, J. Maiz, N. Neophytou, M. M. González. Ultra-low thermal conductivities in large-area Si-Ge nanomeshes for thermoelectric applications. *Nat. Sci. Rep.* 6, 32778 (2016). <https://doi.org/10.1038/srep32778>
- [34] N. Neophytou, *Theory and Simulation Methods for Electronic and Phononic Transport in Thermoelectric Materials*. Springer Nature, 2020. <https://doi.org/10.1007/978-3-030-38681-8>

- [35] H. Mamur, M. R. A. Bhuiyan, F. Korkmaz, M. Nil. A review on bismuth telluride (Bi<sub>2</sub>Te<sub>3</sub>) nanostructure for thermoelectric applications. *Renewable Sustainable Energy Rev.* 82, 4159–69, 2018. <https://doi.org/10.1016/j.rser.2017.10.112>
- [36] W. T. Chiu, C. L. Chen, Y. Y. Chen. A strategy to optimize the thermoelectric performance in a spark plasma sintering process. *Sci. Rep.* 6. 23143, (2016). <https://doi.org/10.1038/srep23143>
- [37] A. Nozariasbmarz, J. S. Krasinski, D. Vashaee. N-Type bismuth telluride nano- composite materials optimization for thermoelectric generators in wearable applications. *Mater.* 12(9), 1529, (2019). <https://doi.org/10.3390/ma12091529>
- [38] Z. Soleimani, S. Zoras, B. Ceranic, S. Shahzad, and Y. Cui. A review on recent developments of thermoelectric materials for room-temperature applications. *Sustainable Ener. Tech. and Assess.* 37, 100604, (2020). <https://doi.org/10.1016/j.seta.2019.100604>
- [39] Y. Zhang, Y. J. Heo, M. Park, S. J. Park. Recent advances in organic thermoelectric materials: principle mechanisms and emerging carbon-based green energy materials. *Polym* 11(1), 167 (2019). <https://doi.org/10.3390/polym11010167>
- [40] K. Biswas, J. He, Q. Zhang, G. Wang, C. Uher, V. P. Dravid, and M. G. Kanatzidis. Strained endotaxial nanostructures with high thermoelectric figure of merit. *Nat. Chem.* 3 (2), 160–166, (2011). <https://doi.org/10.1038/nchem.955>
- [41] J. Tang, H. T. Wang, D. H. Lee, M. Fardy, Z. Huo, T. P. Russell, & P. Yang. Holey silicon as an efficient thermoelectric material. *Nano Lett.* 10, 4279 (2010). <https://doi.org/10.1021/nl102931z>
- [42] I. D. Noyan, M. Dolcet, M. Salleras, A. Stranz, C. Calaza, G. Gadea, M. Pacios, A. Morata, A. Tarancon, and L. Fonseca. All-silicon thermoelectric micro/nanogenerator including a heat exchanger for harvesting applications. *J. Power Sources* 413, 125 (2019). <https://doi.org/10.1016/j.jpowsour.2018.12.029>
- [43] J. Lee, J. Lim & P. Yang. Ballistic phonon transport in holey silicon. *Nano Lett.* 15, 3273 (2015). <https://doi.org/10.1021/acs.nanolett.5b00495>
- [44] S. Tanusilp, and K. Kurosaki. Si-Based Materials for Thermoelectric Applications. *Mater.* 12 (12), 1943 (2019). <https://doi.org/10.3390/ma12121943>
- [45] B. Lorenzi, D. Narducci, R. Tonini, S. Frabboni, G. C. Gazzadi, G. Ottaviani, N. Neophytou & X. Zianni. Paradoxical enhancement of the power factor of polycrystalline silicon as a result of the formation of nanovoids. *J. Electron. Mater.* 43, 3812 (2014). <https://doi.org/10.1007/s11664-014-3170-x>

- [46] X. Wang, H. Wang, B. Xiang, H. Shang, B. Zhu, Y. Yu, H. Jin, R. H. Zhao, Z. Y. Huang, L. J. Liu, and F. Q. Zu. Attaining reduced lattice thermal conductivity and enhanced electrical conductivity in as-sintered pure n- type Bi<sub>2</sub>Te<sub>3</sub> alloy. *J. Mater. Sci.* 54 (5), 4788–97, (2019). <https://doi.org/10.1007/s10853-018-3172-9>
- [47] Y. Kang, Q. Zhang, C. Fan, W. Hu, C. Chen, L. Zhang, Y. Fengrong T. Yongjun, and Bo Xu. High pressure synthesis and thermoelectric properties of polycrystalline Bi<sub>2</sub>Se<sub>3</sub>. *J. Alloys Comp.* 700, 223–7, (2017). <https://doi.org/10.1016/j.jallcom.2017.01.062>
- [48] E. K. Lee, L. Yin, Y. Lee, J. W. Lee, S. J. Lee, J. Lee, S.N. Cha, D. Whang, G.S. Hwang, K. Hippalgaonkar and A. Majumdar. Large thermoelectric figure-of-merits from SiGe nanowires by simultaneously measuring electrical and thermal transport properties. *Nano Lett.* 12, 2918 (2012). <https://doi.org/10.1021/nl300587u>
- [49] C. Chiritescu, C. Mortensen, D. G. Cahill, D. Johnson, and P. Zschack. Lower limit to the lattice thermal conductivity of nanostructured Bi<sub>2</sub>Te<sub>3</sub>-based materials. *J. Appl. Phys.* 106, 073503 (2009). <https://doi.org/10.1063/1.3226884>
- [50] J. Park, Z. Aksamija, H. C. Shin, H. Kim, R. H. Blick RH. Phonon-assisted field emission in silicon nanomembranes for time-of-flight mass spectrometry of proteins. *Nano Lett.* 13, 2698 (2013). <https://doi.org/10.1021/nl400873m>
- [51] Y. Nakamura, M. Isogawa, T. Ueda, S. Yamasaka, H. Matsui, J. Kikkawa, S. Ikeuchi, T. Oyake, T. Hori, J. Shiomi, and A. Sakai. Anomalous reduction of thermal conductivity in coherent nanocrystal architecture for silicon thermoelectric material. *Nano Energy* 12, 845–851 (2015). <https://doi.org/10.1016/j.nanoen.2014.11.029>
- [52] T. Oyake, L. Feng, T. Shiga, M. Isogawa, Y. Nakamura, and J. Shiomi. Ultimate Confinement of Phonon Propagation in Silicon Nanocrystalline Structure. *arXiv preprint arXiv:1801.04376*, (2018). <https://doi.org/10.1103/PhysRevLett.120.045901>
- [53] J. Lim, H. T. Wang, J. Tang, S. C. Andrews, H. So, J. Lee & P. Yang. Simultaneous thermoelectric property measurement and incoherent phonon transport in holey silicon. *ACS Nano* 10, 124 (2015). <https://doi.org/10.1021/acsnano.5b05385>
- [54] N. Neophytou, X. Zianni, H. Kosina, S. Frabboni, B. Lorenzi, and D. Narducci. Simultaneous increase in electrical conductivity and Seebeck coefficient in highly boron-doped nanocrystalline Si. *Nanotechnology* 24, 205402 (2013). <https://doi.org/10.1088/0957-4484/24/20/205402>
- [55] N. Neophytou, X. Zianni, H. Kosina, S. Frabboni, B. Lorenzi, and D. Narducci. Power factor enhancement by inhomogeneous distribution of dopants in two-phase nanocrystalline systems. *J. Electron. Mater.* 43, 1896 (2014). <https://doi.org/10.1007/s11664-013-2898-z>

- [56] N. Neophytou, S. Foster, V. Vargiamidis, G. Pennelli, and D. Narducci. Nanostructured potential well/barrier engineering for realizing unprecedentedly large thermoelectric power factors. *Mater. Tod. Phys.* 11, 100159 (2019). <https://doi.org/10.1016/j.mtphys.2019.100159>
- [57] S. Foster, M. Thesberg, and N. Neophytou. Thermoelectric power factor of nanocomposite materials from two-dimensional quantum transport simulations. *Phys. Rev. B* 96, 195425 (2017). <https://doi.org/10.1103/PhysRevB.96.195425>
- [58] D. Chakraborty, S. Foster, and N. Neophytou, Monte Carlo phonon transport simulations in hierarchically disordered silicon nanostructures. *Phys. Rev. B* 98, 115435 (2018). <https://doi.org/10.1103/PhysRevB.98.115435>
- [59] D. Chakraborty, S. Foster, and N. Neophytou. Monte Carlo simulations for phonon transport in silicon nanomaterials. *Mater. Tod. Proc.* 8, 652 (2019). <https://doi.org/10.1016/j.matpr.2019.02.065>
- [60] D. Chakraborty, L. de Sousa Oliveira, and N. Neophytou. Enhanced Phonon Boundary Scattering at High Temperatures in Hierarchically Disordered Nanostructures. *J. Elec. Mater.* 48, 4, 1909-1916, (2019). <https://doi.org/10.1007/s11664-019-06959-4>
- [61] D. Chakraborty, H. Karamitaheri, L. de Sousa Oliveira, and N. Neophytou. Effect of wave versus particle phonon nature in thermal transport through nanostructures. *Comp. Mater. Sci.* 180, 109712 (2020). <https://doi.org/10.1016/j.commatsci.2020.109712>
- [62] D. Chakraborty, J. Brooke, N. C. S. Hulse and N. Neophytou. Thermal rectification optimization in nanoporous Si using Monte Carlo simulations. *J. Appl. Physics* 126, 184303 (2019). <https://doi.org/10.1063/1.5119806>
- [63] C. Kittel. *Introduction to solid state physics*. Vol. 8. New York: Wiley, (1976). (8<sup>th</sup> edition 1986). <https://doi.org/10.1063/1.3061720>
- [64] P. G. Klemens. Thermal conductivity and lattice vibrational modes. *Solid state physics*. Vol. 7. Academic Press, 1-98, (1958). [https://doi.org/10.1016/S0081-1947\(08\)60551-2](https://doi.org/10.1016/S0081-1947(08)60551-2)
- [65] M. Maldovan. Thermal energy transport model for macro-to- nanograin polycrystalline semiconductors. *J. Appl. Phys.* 110, 114310 (2011). <https://doi.org/10.1063/1.3665211>
- [66] R. Winter. *Condensed Matter Physics*. Aberystwyth Uni. <https://users.aber.ac.uk/ruw/teach/>.
- [67] R. Tubino, L. Piseri, G. Zerbi. Lattice dynamics and spectroscopic properties by a valence force potential of diamondlike crystals: C, Si, Ge, and Sn. *J. Chem. Phys.* 56, 1022 (1972). <https://doi.org/10.1063/1.1677264>
- [68] L. E. Black. *New Perspectives on Surface Passivation: Understanding the Si-Al<sub>2</sub>O<sub>3</sub> Interface*. Springer, 17, (2016). <https://doi.org/10.1007/978-3-319-32521-7>

- [69] L. C. Feldman. Fundamental Aspects of Silicon Oxidation. Springer Science & Business Media, 1, (2001). <https://doi.org/10.1007/978-3-642-56711-7>
- [70] J. Dabrowski, J-H, Müssig. Silicon Surfaces and Formation of Interfaces: Basic Science in the Industrial World. World Scientific, 3–13, (2000). <https://doi.org/10.1142/3615>
- [71] P. Siffert, E. Krimmel. Silicon: Evolution and Future of a Technology. Springer Sci. & Bus. Med., (2013). <https://doi.org/10.1007/978-3-662-09897-4>
- [72] W. Heywang, K. H. Zaininger. Silicon: Evolution and Future of a Technology. Springer Sci. & Bus. Med., 26-29, (2013). <https://doi.org/10.1007/978-3-662-09897-4>
- [73] R. He, W. Heyn, F. Thiel, N. Pérez, C. Damm, D. Pohl, B. Rellinghaus, C. Reimann, M. Beier, J. Friedrich, and H. Zhu. Thermoelectric properties of silicon and recycled silicon sawing waste. J. Materiomics, 5(1), 15-33 2019. <https://doi.org/10.1016/j.jmat.2018.11.004>
- [74] G.H. Zhu, H. Lee, Y. C. Lan, X. W. Wang, G. Joshi, D. Z. Wang, J. Yang., D. Vashaee, H. Guilbert, A. Pillitteri, and M. S. Dresselhaus. Increased phonon scattering by nanograins and point defects in nanostructured silicon with a low concentration of germanium. Phys Rev Lett, 102(19), (2009). <https://doi.org/10.1103/PhysRevLett.102.196803>
- [75] A. Yusufu, K. Kurosaki, Y. Miyazaki, M. Ishimaru, A. Kosuga, Y. Ohishi, H. Muta, and S. Yamanaka. Bottom-up nanostructured bulk silicon: a practical high-efficiency thermoelectric material. Nanoscale 6(22), 13921-13927 (2014). <https://doi.org/10.1039/C4NR04470C>
- [76] R. He, G. Schierning, and K. Nielsch. Thermoelectric devices: a review of devices, architectures, and contact optimization. Adv. Mater. Tech. 3, 1700256 (2018). <https://doi.org/10.1002/admt.201700256>
- [77] M. Lee. Silicon: a Revenant Thermoelectric Material?. J. Superconduc. Nov. Magne. 33(1), 253-257 (2020). <https://doi.org/10.1007/s10948-019-05268-5>
- [78] C. B. Vining. A model for the high-temperature transport properties of heavily doped n-type silicon-germanium alloys. J. Appl. Phys. 69 (1), 331 (1991). <https://doi.org/10.1063/1.347717>
- [79] G. Chen. Nanoscale Energy Transport and Conversion: A Parallel Treatment of Electrons, Molecules, Phonons, and Photons. Oxford University Press, New York, (2005). <https://searchworks.stanford.edu/view/5792603>
- [80] Q. Hao, G. Chen, and M.-S. Jeng. Frequency-dependent Monte Carlo simulations of phonon transport in two-dimensional porous silicon with aligned pores. J. Appl. Phys. 106, 114321 (2009). <https://doi.org/10.1063/1.3266169>

- [81] S. Mazumder and A. Majumdar. Monte Carlo study of phonon transport in solid thin films including dispersion and polarization, *J. Heat Transfer* 123, 749 (2001). <https://doi.org/10.1115/1.1377018>
- [82] D. Lacroix, K. Joulain, D. Terris, and D. Lemonnier. Monte Carlo simulation of phonon confinement in silicon nanostructures: Application to the determination of the thermal conductivity of silicon nanowires. *Appl. Phys. Lett.* 89, 103104 (2006). <https://doi.org/10.1063/1.2345598>
- [83] C. Jeong, S. Datta, and M. Lundstrom. Thermal conductivity of bulk and thin-film silicon: A Landauer approach. *J. Appl. Phys.* 111, 093708 (2012). <https://doi.org/10.1063/1.4710993>
- [84] A. Mittal, and S. Mazumder. Monte Carlo study of phonon heat conduction in silicon thin films including contributions of optical phonons. *J. Heat Transfer* 132, 052402 (2010). <https://doi.org/10.1115/1.4000447>
- [85] E. Pop, R. W. Dutton, and K. E. Goodson. Analytic band Monte Carlo model for electron transport in Si including acoustic and optical phonon dispersion. *J. Appl. Phys.* 96, 4998 (2004). <https://doi.org/10.1063/1.1788838>
- [86] S. Wolf, N. Neophytou, Z. Stanojevic, and H. Kosina. Monte Carlo simulations of thermal conductivity in nanoporous Si membranes. *J. Electron. Mater.* 43, 3870 (2014). <https://doi.org/10.1007/s11664-014-3324-x>
- [87] M. S. Jeng, R. Yang, D. Song, and G. Chen. Modeling the thermal conductivity and phonon transport in nanoparticle composites using Monte Carlo simulation. *J. Heat Trans.* 130(4), 042410 (2008). <https://doi.org/10.1115/1.2818765>
- [88] M. G. Holland. Analysis of lattice thermal conductivity. *Phys. Rev.* 132, 2461 (1963). <https://doi.org/10.1103/PhysRev.132.2461>
- [89] S. Wolf, N. Neophytou, and H. Kosina, Thermal conductivity of silicon nanomeshes: Effects of porosity and roughness, *J. Appl. Phys.* 115, 204306 (2014). <https://doi.org/10.1063/1.4879242>
- [90] C. Goupil, H. Ouerdane, K. Zabrocki, W. Seifert, N. F. Hinsche, E. Müller, Eckhard. *Thermodynamics and thermoelectricity: Continuum Theory and Modeling of Thermoelectric Elements*. New York, New York, USA: Wiley-VCH, 2–3, (2016). <https://doi.org/10.1002/9783527338405>
- [91] T.J. Seebeck. Magnetic polarization of metals and ores by temperature differences. *Ann. Phys.* 82, 253–286 (1826). <https://doi.org/10.1002/andp.18260820302>
- [92] A. I. Boukai, Y. Bunimovich, J. Tahir-Kheli, J. K. Yu, W. A. Goddard Iii, and J. R. Heath, Silicon nanowires as efficient thermoelectric materials, *Nature* 451, 168 (2008). [https://doi.org/10.1142/9789814317665\\_0018](https://doi.org/10.1142/9789814317665_0018)



- [93] A. I. Hochbaum, R. K. Chen, R. D. Delgado, W. J. Liang, E. C. Garnett, M. Najarian, A. Majumdar, and P. D. Yang. Thermal conductance of thin silicon nanowires. *Nature* (London) 451, 163 (2008). <https://doi.org/10.1103/PhysRevLett.101.105501>
- [94] D. G. Cahill, S. K. Watson, and R. O. Pohl. Lower limit to the thermal conductivity of disordered crystals. *Phys. Rev. B* 46, 6131 (1992). <https://doi.org/10.1103/PhysRevB.46.6131>
- [95] B. T. Kearney, B. Jugdersuren, D. R. Queen, T. H. Metcalf, J. C. Culbertson, P. A. Desario, R. M. Stroud, W. Nemeth, Q. Wang, and X. Liu. From amorphous to nanocrystalline: The effect of nanograins in an amorphous matrix on the thermal conductivity of hot-wire chemical-vapor deposited silicon films, *J. Phys.: Condens. Matter* 30, 085301 (2018). <https://doi.org/10.1088/1361-648X/aaa43f>
- [96] Z. Wang, J. E. Alaniz, W. Jang, J. E. Garay, and C. Dames. Thermal conductivity of nanocrystalline silicon: Importance of grain size and frequency-dependent mean free paths. *Nano Lett.* 11, 2206 (2011). <https://doi.org/10.1021/nl1045395>
- [97] B. Jugdersuren, B. T. Kearney, D. R. Queen, T. H. Metcalf, J. C. Culbertson, C. N. Chervin, R. M. Stroud, W. Nemeth, Q. Wang, and X. Liu. Thermal conductivity of amorphous and nanocrystalline silicon films prepared by hot-wire chemical-vapor deposition. *Phys. Rev. B* 96, 014206 (2017). <https://doi.org/10.1103/PhysRevB.96.014206>
- [98] M. T. Dunham, B. Lorenzi, S. C. Andrews, A. Sood, M. Asheghi, D. Narducci, and K. E. Goodson. Enhanced phonon scattering by nanovoids in high thermoelectric power factor polysilicon thin films. *Appl. Phys. Lett.* 109, 253104 (2016). <https://doi.org/10.1063/1.4972483>
- [99] S. Basu and M. Francoeur. Near-field radiative transfer based thermal rectification using doped silicon. *Appl. Phys. Lett.* 98, 113106 (2011). <https://doi.org/10.1063/1.3567026>
- [100] G. Tan, F. Shi, S. Hao, L.D. Zhao, H. Chi, X. Zhang, C. Uher, C. Wolverton, V. P. Dravid, & M. G. Kanatzidis. Non-equilibrium processing leads to record high thermoelectric figure of merit in PbTe–SrTe. *Nat. Comm.* 7, 12167, (2016). <https://doi.org/10.1038/ncomms12167>
- [101] A. Chernatynskiy, D. Clarke, and S. Phillpot. Thermal Transport in Nanostructured Materials. Chapter 19, 545–572, (2012). <https://doi.org/10.1201/b11930-24>
- [102] A. Chernatynskiy and S. R. Phillpot, Evaluation of computational techniques for solving the Boltzmann transport equation for lattice thermal conductivity calculations, *Phys. Rev. B*, 82(13), 134301 (2010). <https://doi.org/10.1103/PhysRevB.82.134301>
- [103] S. Sinha, and K. E. Goodson. Review: Multiscale Thermal Modeling in Nanoelectronics. *Int. J. Multiscale Computational Eng.* 3(1), 1–26 (2005). <https://doi.org/10.1615/IntJMultCompEng.v3.i1.80>

- [104] F. VanGessel, J. Peng, and P. W. Chung. A review of computational phononics: the bulk, interfaces, and surfaces. *J. Mater. Sci.* 53(8), 5641-5683 (2018). <https://doi.org/10.1007/s10853-017-1728-8>
- [105] X. Gu, and Y. Ronggui. Phonon transport and thermal conductivity in two-dimensional materials. *Ann. Rev. of Heat Trans.* 19 (2016). <https://doi.org/10.1615/AnnualRevHeatTransfer.2016015491>
- [106] D. G. Cahill, P. V. Braun, G. Chen, D. R. Clarke, S. Fan, K. E. Goodson, P. Keblinski, W. P. King, G. D. Mahan, A. Majumdar, H. J. Maris, S. R. Phillpot, E. Pop, and L. Shi. Nanoscale thermal transport. II. 2003-2012. *Appl. Phys. Reviews* 1(1), (2014). <https://doi.org/10.1063/1.4832615>
- [107] A. Chernatynskiy, J. Turner, A. J. McGaughey, C. Amon, and S. Phillpot. Phonon mediated thermal conductivity in ionic solids by lattice dynamics based methods. *J. Am. Ceram. Soc.* 94, 3523–3531 (2011). <https://doi.org/10.1111/j.1551-2916.2011.04743.x>
- [108] P. K. Schelling, S. R. Phillpot, and P. Keblinski. Comparison of atomic-level simulation methods for computing thermal conductivity. *Phys. Rev. B* 65(14), 1–12 (2002). <https://doi.org/10.1103/PhysRevB.65.144306>
- [109] M. S. Green. Markoff random processes and the statistical mechanics of time-dependent phenomena. II. Irreversible processes in fluids. *J. Chem. Phys.* 22(3), 398-413 (1954). <https://doi.org/10.1063/1.1740082>
- [110] R. Kubo, M. Yokota, and S. Nakajima. Statistical-mechanical theory of irreversible processes. II. Response to thermal disturbance. *J. Phys. Soc. of Japan* 12(11), 1203-1211, (1957). <https://doi.org/10.1143/JPSJ.12.1203>
- [111] A. Kinaci, J. B. Haskins, and T. Çağın. On calculation of thermal conductivity from Einstein relation in equilibrium molecular dynamics. *J. Chem. Phys.* 137(1), 014106 (2012). <https://doi.org/10.1063/1.4731450>
- [112] T. Ikeshoji, and B. Hafskjold. Non-equilibrium molecular dynamics calculation of heat conduction in liquid and through liquid-gas interface. *Mole. Phys.* 81(2), 251-261 (1994). <https://doi.org/10.1080/00268979400100171>
- [113] F. Müller-Plathe. A simple nonequilibrium molecular dynamics method for calculating the thermal conductivity. *J. Chem. Phys.* 106(14), 6082-6085 (1997). <https://doi.org/10.1063/1.473271>
- [114] J. Severin, and P. Jund. Thermal conductivity calculation in anisotropic crystals by molecular dynamics: Application to  $\alpha$ -Fe<sub>2</sub>O<sub>3</sub>. *J. Chem. Phys.* 146(5), 054505 (2017). <https://doi.org/10.1063/1.4974933>
- [115] D. P. Sellan, E. S. Landry, J. E. Turney, A. J. H. McGaughey, and C. H. Amon. Size effects in molecular dynamics thermal conductivity predictions, *Phys. Rev. B* 81, 214305 (2010). <https://doi.org/10.1103/PhysRevB.81.214305>



- [116] D. G. Cahill, W. K. Ford, Fan, K. E. Goodson, G. D. Mahan, A. Majumdar, H. J. Maris, R. Merlin, S. R. Phillpot. Nanoscale thermal transport. *Journal of Appl. Phys.* 93(2), 793–818 (2003). <https://doi.org/10.1063/1.1524305>
- [117] C. Kimmer, S. Aubry, A. Skye, and P. K. Schelling. Scattering of phonons from a high-energy grain boundary in silicon: Dependence on angle of incidence. *Phys. Rev. B* 75(14), 144105 (2007). <https://doi.org/10.1103/PhysRevB.75.144105>
- [118] P. K. Schelling, S. R. Phillpot, and P. Keblinski. Kapitza conductance and phonon scattering at grain boundaries by simulation. *J. Appl. Phys.* 95(11), 6082 (2004). <https://doi.org/10.1063/1.1702100>
- [119] M. Yao, T. Watanabe, P. K. Schelling, P. Keblinski, D. G. Cahill, and S. R. Phillpot. Phonon-defect scattering in doped silicon by molecular dynamics simulation. *J. Appl. Phys.* 104(2), 024905 (2008). <https://doi.org/10.1063/1.2959840>
- [120] V. Varshney, J. Lee, A. K. Roy, and B. L. Farmer. Modeling of interface thermal conductance in longitudinally connected carbon nanotube junctions. *J. Appl. Phys.* 109(8), 084913 (2011). <https://doi.org/10.1063/1.3560914>
- [121] A. J. C. Ladd, B. Moran, and W. G. Hoover. Lattice thermal conductivity: A comparison of molecular dynamics and anharmonic lattice dynamics. *Phys. Rev. B*, 34(8), 5058–5064 (1986). <https://doi.org/10.1103/PhysRevB.34.5058>
- [122] J. A. Thomas, J. E. Turney, R. M. Iutzi, C. H. Amon, and A. J. H. McGaughey, Predicting phonon dispersion relations and lifetimes from the spectral energy density, *Phys. Rev. B* 81(8), 081411 (2010). <https://doi.org/10.1103/PhysRevB.81.081411>
- [123] H. Karamitaheri, N. Neophytou, M. Pourfath, and H. Kosina. Study of thermal properties of graphene-based structures using the force constant method. *J. Comp. Elec.* 11(1), 15 (2012). <https://doi.org/10.1007/s10825-011-0380-9>
- [124] M. Pourfath. *The Non-Equilibrium Green's Function Method for Nanoscale Device Simulation*. Springer, Vienna, (2014). <https://doi.org/10.1007/978-3-7091-1800-9>
- [125] H. Karamitaheri, N. Neophytou, and H. Kosina, Anomalous diameter dependence of thermal transport in ultra-narrow Si nanowires, *J. Appl. Phys.* 115(2), 024302, (2014). <https://doi.org/10.1063/1.4858375>
- [126] H. Karamitaheri, M. Pourfath, H. Kosina, and N. Neophytou. Low-dimensional phonon transport effects in ultranarrow disordered graphene nanoribbons. *Phys. Rev. B* 91, 16 (2015). <https://doi.org/10.1103/PhysRevB.74.125402>
- [127] N. Mingo. Anharmonic phonon flow through molecular-sized junctions. *Phys. Rev. B* 74 12, 125402 (2006). <https://doi.org/10.1103/PhysRevB.74.125402>

- [128] T. Yamamoto, and K. Watanabe. Nonequilibrium Green's function approach to phonon transport in defective carbon nanotubes. *Phys. Rev. Lett.* 96(25), 255503, (2006). <https://doi.org/10.1103/PhysRevLett.96.255503>
- [129] H. Karamitaheri, N. Neophytou, M. Pourfath, R. Faez, and H. Kosina. Engineering enhanced thermoelectric properties in zigzag graphene nanoribbons. *J. Appl. Phys.* 111(5), 054501 (2012). <https://doi.org/10.1063/1.3688034>
- [130] Y. Xu, J-S.Wang, W. Duan, B-L Gu, and B. Li. Nonequilibrium Green's function method for phonon-phonon interactions and ballistic-diffusive thermal transport. *Phys. Rev. B* 78(22), 224303 (2008). <https://doi.org/10.1103/PhysRevB.78.224303>
- [131] Z. Huang, T. S. Fisher, and J. Y. Murthy. Simulation of thermal conductance across dimensionally mismatched graphene interfaces. *J. Appl. Phys.* 108(11), 114310 (2010). <https://doi.org/10.1063/1.3514119>
- [132] M. Luisier, Investigation of thermal transport degradation in rough Si nanowires. *J. Appl. Phys.* 110(7), 074510 (2011). <https://doi.org/10.1063/1.3644993>
- [133] Z. W. Tan, J.-S. Wang, and C. K. Gan. First-principles study of heat transport properties of graphene nanoribbons. *Nano Lett.* 11, 214–219 (2011). <https://doi.org/10.1021/nl103508m>
- [134] S. Datta. *Electronic Transport in Mesoscopic Systems*, Cambridge Univ. Press, Cambridge MA, (1997). <https://doi.org/10.1017/CBO9780511805776>
- [135] A. Chernatynskiy, R. W. Grimes, M. A. Zurbuchen, D. R. Clarke, and S. R. Phillpot, Crossover in thermal transport properties of natural, perovskite-structured superlattices, *Appl. Phys. Lett.* 95(16), 161906 (2009). <https://doi.org/10.1063/1.3253421>
- [136] N. Neophytou, H. Karamitaheri, and H. Kosina. Atomistic calculations of the electronic, thermal, and thermoelectric properties of ultra-thin Si layers. *J. Comp. Elec.* 12(4), 611–622 (2013). <https://doi.org/10.1007/s10825-013-0522-3>
- [137] K. Schwab, E. Henriksen, J. Worlock, and M. Roukes. Measurement of the quantum of thermal conductance. *Nature* 404(6781), 975 (2000). <https://doi.org/10.1038/35010065>
- [138] M. Kusunoki, and H. Suzuki. Lattice thermal conductivity of deformed copper–aluminum alloy crystals at low temperatures. *J. Phys. Soc. Japan.*, 26(4), 932–938 (1969). <https://doi.org/10.1143/JPSJ.26.932>
- [139] R. L. Sproull, M. Moss, and H. Weinstock. Effect of dislocations on the thermal conductivity of lithium fluoride, *J. Appl. Phys.* 30(3), 334 (1959).

- [140] T. Suzuki, and H. Suzuki. Effect of dislocations on the thermal conductivity of LiF. J. Phys. Soc. Japan., 32(1), 164 (1972). <https://doi.org/10.1063/1.1735163>
- [141] G. A. Kneze, and A. V. Granato. Effect of independent and coupled vibrations of dislocations on low-temperature thermal conductivity in alkali halides. Phys. Rev. B 25(4), 2851 (1982). <https://doi.org/10.1103/PhysRevB.25.2851>
- [142] A. C. Anderson, and M. E. Malinowski, Interaction between thermal phonons and dislocations in LiF, Phys. Rev. B 5(8), 3199–3210 (1972). <https://doi.org/10.1103/PhysRevB.5.3199>
- [143] M. Shur, and R. Davis eds., GaN Based Materials and Devices. World Scientific Publishing Co, New Jersey (2004). [https://doi.org/10.1142/9789812562364\\_fmatter](https://doi.org/10.1142/9789812562364_fmatter)
- [144] B. K. Singh, V. J. Menon, and K. C. Sood. Phonon conductivity of plastically deformed crystals: Role of stacking faults and dislocations. Phys. Rev. B, 74(18), 184302 (2006). <https://doi.org/10.1103/PhysRevB.74.184302>
- [145] A. Einstein. On the Motion of Small Particles Suspended in Liquids at Rest Required by the Molecular-Kinetic Theory of Heat. Ann. Phys. 17, 549-560 (1905). <https://guides.loc.gov/einstein-annus-mirabilis/1905-papers>
- [146] J. Ziman, Electrons and Phonons. Clarendon Press, Oxford, U.K. (1962). <https://doi.org/10.1093/acprof:oso/9780198507796.001.0001>
- [147] K. E. Goodson. Phonon Transport Theory. Dept. of Mech. Engineer. Stanford University <https://nanoheat.stanford.edu/tools/phonon-transport-theory>, March (2020).
- [148] Z. Aksamija. Full band Monte Carlo simulation of phonon transport in semiconductor nanostructures. 14th IEEE International Conference on Nanotechnology, 37–40, (2014). [10.1615/ICHMT.2015.IntSympAdvComputHeatTransf.1170](https://doi.org/10.1615/ICHMT.2015.IntSympAdvComputHeatTransf.1170)
- [149] C. Bera. Monte Carlo simulation of thermal conductivity of Si nanowire: An investigation on the phonon confinement effect on the thermal transport. J. Appl. Phys. 112, 074323 (2012). <https://doi.org/10.1063/1.4757633>
- [150] R. C MacKenzie, J. M. Frost, and J. A. Nelson. A numerical study of mobility in thin films of fullerene derivatives. J. Chem. Phys. 132, 064904 (2010). <https://doi.org/10.1063/1.3315872>
- [151] Z. Aksamija and I. Knezevic. Thermoelectric properties of silicon nanostructures. J. Comput. Electron. 9, 173 (2010). <https://doi.org/10.1007/s10825-010-0339-2>
- [152] J. K. Yu, S. Mitrovic, D. Tham, J. Varghese, and J. R. Heath. Reduction of thermal conductivity in phononic nanomesh structures. Nat. Nanotechnol. 5, 718 (2010). <https://doi.org/10.1038/nnano.2010.149>

- [153] V. Jean, S. Fumeron, K. Termentzidis, S. Tutashkonko, and D. Lacroix. Monte Carlo simulations of phonon transport in nanoporous silicon and germanium. *J. Appl. Phys.* 115, 024304 (2014). <https://doi.org/10.1063/1.4861410>
- [154] S. Mei, C. J. Foss, L. N. Maurer, O. Jonasson, Z. Aksamija, and I. Knezevic. Boundaries, interfaces, point defects, and strain as impediments to thermal transport in nanostructures. *Proceedings of IEEE International Reliability Physics Symposium (IEEE, Monterey, CA, 2017)*, pp. 6A1.1-6A1.10. <https://doi.org/10.1109/IRPS.2017.7936333>
- [155] Z. Yu, L. Ferrer-Argemi, and J. Lee. Investigation of thermal conduction in symmetric and asymmetric nanoporous structures. *J. Appl. Phys.* 122, 244305 (2017). <https://doi.org/10.1063/1.5006818>
- [156] Z. Aksamija and I. Knezevic. Lattice thermal transport in large area polycrystalline graphene. *Phys. Rev. B* 90, 035419 (2014). <https://doi.org/10.1103/PhysRevB.90.035419>
- [157] A. J. H. McGaughey and A. Jain. Nanostructure thermal conductivity prediction by Monte Carlo sampling of phonon free paths. *Appl. Phys. Lett.* 100, 061911 (2012). <https://doi.org/10.1063/1.3683539>
- [158] F. Hao and D. Fang. Mechanical deformation and fracture mode of polycrystalline graphene: Atomistic simulations. *Phys. Lett. A* 376, 1942 (2012). <https://doi.org/10.1016/j.physleta.2012.04.040>
- [159] Y. Huang, B. Zhao, J. Fang, R. Ang, and Y. Sun. Tuning of microstructure and thermoelectric properties of  $\text{Ca}_3\text{Co}_4\text{O}_9$  ceramics by high-magnetic-field sintering. *J. Appl. Phys.* 110, 123713 (2011). <https://doi.org/10.1063/1.3671403>
- [160] X. Zianni. Band structure engineering in geometry-modulated nanostructures for thermoelectric efficiency enhancement. *J. Electron. Mater.* 43, 3753 (2014). <https://doi.org/10.1007/s11664-014-3125-2>
- [161] K. H. Park, P. N. Martin, and U. Ravaioli. Electronic and thermal transport study of sinusoidally corrugated nanowires aiming to improve thermoelectric efficiency. *Nanotech.* 27, 035401 (2015). <https://doi.org/10.1088/0957-4484/27/3/035401>
- [162] Y. Nie, G. Xia, and T. Pacey. Simulations of an energy dechirper based on dielectric lined waveguides. *Nucl. Instrum. Methods Phys. Res. A* 875, 1 (2017). <https://doi.org/10.1016/j.nima.2017.11.050>
- [163] K. Termentzidis, M. Verdier, and D. Lacroix. Effect of amorphisation on the thermal properties of nanostructured membranes. *Z. Naturforsch. A* 72, 189 (2017). <https://doi.org/10.1515/zna-2016-0384>
- [164] D. Vasileska, K. Raleva, S. M. Goodnick, Z. Aksamija, and I. Knezevic. Thermal modeling of nanodevices. *14th International Workshop on Computational Electronics, Pisa (IEEE, Pisa, 2010)*, Vol. 355, pp. 1–5. [10.1109/IWCE.2010.5677916](https://doi.org/10.1109/IWCE.2010.5677916)

- [165] S. V. J. Narumanchi, J. Y. Murthy, and C. H. Amon, Comparison of different phonon transport models for predicting heat conduction, *J. Heat Transfer* 127, 713 (2005). <https://doi.org/10.1115/1.1924571>
- [166] B. Davier, J. Larroque, P. Dollfus, L. Chaput, S. Volz, D. Lacroix, and J. Saint-Martin. Heat transfer in rough nanofilms and nanowires using full band ab initio Monte Carlo simulation. *J. Phys.: Cond. Mat.* 30(49), 495902 (2018). <https://doi.org/10.1088/1361-648X/aaea4f>
- [167] Y.-J. Han, and P. G. Klemens. Anharmonic thermal resistivity of dielectric crystals at low temperatures. *Phys. Rev. B* 48, 6033 (1993). <https://doi.org/10.1103/PhysRevB.48.6033>
- [168] G. Srivastava. *The Physics of Phonons*, Adam Hilger, Bristol, UK, (1990). <https://doi.org/10.1002/adma.19920040706>
- [169] E. B. Ramayya, L. N. Maurer, A. H. Davoody, and I. Knezevic, I.: thermoelectric properties of ultrathin silicon nanowires. *Phys. Rev. B*, 86(11), 115328, (2012). <https://doi.org/10.1103/PhysRevB.86.115328>
- [170] L. Weber and E. Gmelin, Transport properties of silicon, *Appl. Phys. A* 53, 136 (1991). <https://doi.org/10.1007/BF00323873>
- [171] Y. S. Ju and K. E. Goodson, Phonon scattering in silicon films with thickness of order 100 nm, *Appl. Phys. Lett.* 74, 3005 (1999). <https://doi.org/10.1063/1.123994>
- [172] G. Chen. Thermal conductivity and ballistic phonon transport in cross-planedirection of superlattices. *Phys. Rev. B* 57, 14958 (1998). <https://doi.org/10.1103/PhysRevB.57.14958>
- [173] R. Dettori, C. Melis, X. Cartoixa, R. Rurali, and L. Colombo, Model for thermal conductivity in nanoporous silicon from atomistic simulations, *Phys. Rev. B* 91, 054305 (2015). <https://doi.org/10.1103/PhysRevB.91.054305>
- [174] J. S. Blakemore, *Solid State Physics*, 2 ed., Cambridge University Press, Cambridge, (1985). <https://doi.org/10.1107/S0108767386099646>
- [175] Q. Hao, Y. Xiao, and Q. Chen. Determining phonon mean free path spectrum by ballistic phonon resistance within a nanoslot-patterned thin film. *Mater. Tod. Phys.* 10, 100126 (2019). <https://doi.org/10.1016/j.mtphys.2019.100126>
- [176] D. Song, and G. Chen. Thermal conductivity of periodic microporous silicon films. *Appl. Phys. Lett.* 84(5), 688 (2004). <https://doi.org/10.1063/1.1642753>
- [177] Q. Hao, Y. Xiao, and H. Zhao. Characteristic length of phonon transport within periodic nanoporous thin films and two-dimensional materials *J. Appl. Phys.* 120(6), 065101 (2016). <https://doi.org/10.1063/1.4959984>
- [178] R. Anufriev, J. Ordonez-Miranda, and M. Nomura. Measurement of the phonon mean free path spectrum in silicon membranes at different temperatures using arrays of nanoslits. *Phys. Rev. B* 101(11), 115301 (2020). <https://doi.org/10.1103/PhysRevB.101.115301>

- [179] X. Gu and R. Yang, Phonon transport and thermal conductivity in two-dimensional materials, *Annu. Rev. Heat Transfer* 19, 1 (2016). <https://doi.org/10.1103/PhysRevB.96.134312>
- [180] C. M DaSilva, Predicting phonon transport in two dimensional materials, in *Proceedings IEEE Engineering in Medicine and Biology*, Vol. 5822 (IEEE, Piscataway, NJ, 2016), p. 357. <http://hdl.handle.net/1807/76383>
- [181] M. Maldovan. Phonon wave interference and thermal bandgap materials. *Nature materials*, 14(7), 667-674 (2015). <https://doi.org/10.1038/nmat4308>
- [182] M. Verdier, R. Vaillon, S. Merabia, D. Lacroix, and K. Termentzidis, *Nanostructured Semiconductors* (Pan Stanford, Singapore, 2017), Chap. 4. <https://doi.org/10.1088/1742-6596/785/1/012009>
- [183] S. Uma, A. D. McConnell, M. Asheghi, K. Kurabayashi, and K. E Goodson. Temperature-dependent thermal conductivity of undoped polycrystalline silicon layers. *Int. J. Thermophys.* 22, 605 (2001). <https://doi.org/10.1023/A:1010791302387>
- [184] H. Dong, B. Wen, and R. Melnik. Relative importance of grain boundaries and size effects in thermal conductivity of nanocrystalline materials. *Sci. Rep.* 4, 7037 (2014). <https://doi.org/10.1038/srep07037>
- [185] K. Valalaki, P. Benech, and A. G. Nassiopoulou. Significant enhancement of the thermoelectric figure of merit of polycrystalline Si films by reducing grain size. *Nanoscale Res. Lett.* 11, 201 (2016). <https://doi.org/10.1088/0022-3727/49/31/315104>
- [186] M. Von Arx, O. Paul, and H. Baltes. Process-dependent thin-film thermal conductivities for thermal CMOS MEMS. *J. Microelectromech. Syst.* 9, 136 (2000). <https://doi.org/10.1109/84.825788>.
- [187] M. T. Dunham, B. Lorenzi, S. C. Andrews, A. Sood, M. Asheghi, D. Narducci, and K. E. Goodson. Enhanced phonon scattering by nanovoids in high thermoelectric power factor polysilicon thin films. *Appl. Phys. Lett.* 109, 253104 (2016). <https://doi.org/10.1063/1.4972483>
- [188] G. Gesele, J. Linsmeier, V. Drach, J. Fricke, and R. Arens- Fischer. Temperature-dependent thermal conductivity of porous silicon. *J. Phys. D: Appl. Phys.* 30, 2911 (1997). <https://doi.org/10.1088/0022-3727/30/21/001>
- [189] A. D. McConnell, S. Uma, and K. E. Goodson, Thermal conductivity of doped polysilicon layers, *J. Microelectromech. Syst.* 10, 360 (2001). <https://doi.org/10.1109/84.946782>.
- [190] I. El-Kady, R. H. Olsson III, P. E. Hopkins, Z. C. Leseman, D. F. Goettler, B. Kim, C. M. Reinke, and M. F. Su. Phonon manipulation with phononic crystals. Sandia Labs, Albuquerque, NM, Report SAND2012-0127 (2012). <https://prod-ng.sandia.gov/techlib-noauth/access-Control.cgi/2012/120127.pdf>



- [191] J. Lim, H-T. Wang, J. Tang, S. C. Andrews, H. So, J. Lee, D. H. Lee, T. P. Russell, and P. Yang. Simultaneous thermoelectric property measurement and incoherent phonon transport in holey silicon. *ACS nano* 10(1), 124-132 (2016). <https://doi.org/10.1021/acsnano.5b05385>
- [192] A. A. Maznev. Boundary scattering of phonons: Specularity of a randomly rough surface in the small-perturbation limit. *Phys. Rev. B* 91(13), 134306 (2015). <https://doi.org/10.1103/PhysRevB.91.134306>
- [193] G. Romano, A. Di Carlo, and J. C. Grossman. Mesoscale modeling of phononic thermal conductivity of porous Si: Interplay between porosity, morphology and surface roughness. *J. Comput. Electron.* 11, 8 (2012). <https://doi.org/10.1007/s10825-012-0390-2>
- [194] G. Chen. Size and interface effects on thermal conductivity of superlattices and periodic thin-film structures. *J. Heat Transfer* 119, 220 (1997). <https://doi.org/10.1115/1.2824212>
- [195] N. K. Ravichandran and A. J. Minnich. Coherent and incoherent thermal transport in nanomeshes. *Phys. Rev. B* 89, 205432 (2014). <https://doi.org/10.1103/PhysRevB.89.205432>
- [196] J. Lee, W. Lee, G. Wehmeyer, S. Dhuey, D. L. Olynick, S. Cabrini, C. Dames, J. J. Urban, and P. Yang. Investigation of phonon coherence and backscattering using silicon nanomeshes. *Nat. Commun.* 8, 14054 (2017). <https://doi.org/10.1038/ncomms14054>
- [197] S. Essig, O. Moutanabbir, A. Wekkeli, H. Nahme, E. Oliva, A. W. Bett, and F. Dimroth. Fast atom beam-activated n-Si/n-GaAs wafer bonding with high interfacial transparency and electrical conductivity. *J. Appl. Phys.* 113, 203512 (2013). <https://doi.org/10.1063/1.4807905>
- [198] Y. Muramatsu, M. Tsuji, and N. Aoto. Control of Si surface characteristics by a new etching solution BHF/H/sub 2/O/sub 2/ in Proceedings of International Symposium on Semiconductor Manufacturing (IEEE, Austin TX, 1995), pp. 47–50. <https://doi.org/10.1109/ISSM.1995.524356>.
- [199] C. Hua and A. J. Minnich. Importance of frequency-dependent grain boundary scattering in nanocrystalline silicon and silicon-germanium thermoelectrics. *Semicond. Sci. Technol.* 29, 124004 (2014). <https://doi.org/10.1088/0268-1242/29/12/124004>
- [200] C. W. Nan, R. Birringer, D. R. Clarke, and H. Gleiter. Effective thermal conductivity of particulate composites with interfacial thermal resistance. *J. Appl. Phys.* 81, 6692 (1997). <https://doi.org/10.1063/1.365209>
- [201] J. H. Lee, J. C. Grossman, J. Reed, and G. Galli. Lattice thermal conductivity of nanoporous Si: Molecular dynamics study. *Appl. Phys. Lett.*, 91(22), (2007). <https://doi.org/10.1063/1.2817739>

- [202] G. Xie, Z. Ju, K. Zhou, X. Wei, Z. Guo, Y. Cai, and G. Zhang. Ultra-low thermal conductivity of two-dimensional phononic crystals in the incoherent regime. *Npj Comp. Mater.*, 4(1), 1–7 (2018). <https://doi.org/10.1038/s41524-018-0076-9>
- [203] H. S. Yang, G. R. Bai, L. J. Thompson, and J. A. Eastman. Interfacial thermal resistance in nanocrystalline yttria-stabilized zirconia. *Acta Mater.* 50, 2309 (2002). [https://doi.org/10.1016/S1359-6454\(02\)00057-5](https://doi.org/10.1016/S1359-6454(02)00057-5)
- [204] R. H. Tarkhanyan and D. G. Niarchos. Reduction in lattice thermal conductivity of porous materials due to inhomogeneous porosity. *Int. J. Thermal Sci.* 67, 107 (2013). <https://doi.org/10.1016/j.ijthermalsci.2012.12.008>
- [205] A. Eucken, *Forschung auf dem Gebiete des Ingenieurwesens* (Ausgabe B, Band 3, 3/4 VDI Forschungsheft 353, 1932).
- [206] S. Aubry, C. J. Kimmer, A. Skye, and P. K. Schelling. Comparison of theoretical and simulation-based predictions of grain- boundary Kapitza conductance in silicon. *Phys. Rev. B* 78, 064112 (2008). <https://doi.org/10.1103/PhysRevB.78.064112>
- [207] G. L. Pollack. Kapitza resistance. *Rev. Mod. Phys.* 41, 48 (1969). <https://doi.org/10.1103/RevModPhys.41.48>
- [208] S. Ju and X. Liang. Thermal conductivity of nanocrystalline silicon by direct molecular dynamics simulation. *J. Appl. Phys.* 112, 064305 (2012). <https://doi.org/10.1063/1.4752266>
- [209] J. Chen, G. Zhang, and B. Li. Thermal contact resistance across nanoscale silicon dioxide and silicon interface. *J. Appl. Phys.* 112, 064319 (2012). <https://doi.org/10.1063/1.4754513>
- [210] J. K. Bohrer, K. Schroer, L. Brendel, and D. E. Wolf. Thermal resistance of twist boundaries in silicon nanowires by nonequilibrium molecular dynamics. *AIP Adv.* 7, 045105 (2017). <https://doi.org/10.1063/1.4979982>
- [211] H. Looyenga. Dielectric constants of heterogeneous mixtures. *Physica* 31, 401 (1965). [https://doi.org/10.1016/0031-8914\(65\)90045-5](https://doi.org/10.1016/0031-8914(65)90045-5)
- [212] B. Lorenzi, R. Dettori, M. T. Dunham, C. Melis, R. Tonini, L. Colombo, A. Sood, K. E. Goodson, and D. Narducci. Phonon scattering in silicon by multiple morphological defects: A multiscale analysis. *J. Electron. Mater.* 47, 5148 (2018). <https://doi.org/10.1007/s11664-018-6337-z>
- [213] G. Romano and J. C. Grossman. Phonon bottleneck identification in disordered nanoporous materials. *Phys. Rev. B* 96, 115425 (2017). <https://doi.org/10.1103/PhysRevB.96.115425>
- [214] K. D. Parrish, J. R. Abel, A. Jain, J. A. Malen, and A. J. H. McGaughey. Phonon-boundary scattering in nanoporous silicon films: Comparison of Monte Carlo techniques. *J. Appl. Phys.* 122, 125101 (2017). <https://doi.org/10.1063/1.4993601>



- [215] W. Park, G. Romano, E. C. Ahn, T. Kodama, J. Park, M. T. Barako, J. Sohn, S. J. Kim, J. Cho, A. M. Marconnet, and M. Asheghi. Phonon conduction in silicon nanobeam labyrinths. *Sci. Rep.* 7, 1 (2017). <https://doi.org/10.1038/s41598-017-06479-3>
- [216] V. Vargiamidis, S. Foster, and N. Neophytou. Thermoelectric power factor in nanostructured materials with randomized nanoinclusions. *Phys. Status Solidi A* 215, 1700997 (2018). <https://doi.org/10.1002/pssa.201700997>
- [217] A. D. Caplin and C. Rizzuto. Systematics of Matthessens rule breakdown at low temperatures. *Aust. J. Phys.* 24, 309 (1971). <https://doi.org/10.1071/PH710309>
- [218] J. Bass. Deviations from Matthiessen's rule. *Phys. Lett. A* 41, 303 (1972). <https://doi.org/10.1080/00018737200101308>
- [219] M. Aldegunde, A. Martinez, and J. R. Barker. Study of individual phonon scattering mechanisms and the validity of Matthiessen's rule in a gate-all-around silicon nanowire transistor. *J. Appl. Phys.* 113, 014501 (2013). <https://doi.org/10.1063/1.4772720>
- [220] M. Verdier, K. Termentzidis, and D. Lacroix. Crystalline-amorphous silicon nano-composites: Nano-pores and nano-inclusions impact on the thermal conductivity. *J. Appl. Phys.* 119(17), 175104 (2016). <https://doi.org/10.1063/1.4948337>
- [221] F. Stern, Calculated Temperature Dependence of Mobility in Silicon Inversion Layers, *Phys. Rev. Lett.* 44, 1469 (1980). <https://doi.org/10.1103/PhysRevLett.44.1469>
- [222] M. Verdier, K. Termentzidis, and D. Lacroix. Effect of the amorphization around spherical nano-pores on the thermal conductivity of nano-porous Silicon. *J. Phys.: IOP Conf. Ser.* 785, 012009 (2017). <https://doi.org/10.1088/1742-6596/785/1/012009>
- [223] K. Kukita, and Y. Kamakura. Monte Carlo simulation of phonon transport in silicon including a realistic dispersion relation. *J. of Appl. Phys.* 114, 154312 (2013). <https://doi.org/10.1063/1.4826367>
- [224] L. N. Maurer, Z. Aksamija, E. B. Ramayya, A. H. Davoody, and I. Knezevic, *Appl. Phys. Lett.* 106, 133108 (2015). <https://doi.org/10.1063/1.4916962>
- [225] D. Chakraborty, S. Foster, L. Oliveira, N. Neophytou. Phonon transport in hierarchically disordered Silicon nanostructures. PGR Engineering Symposium, University of Warwick, Coventry, UK (2018). <https://doi.org/10.1103/PhysRevB.98.115435>
- [226] D. Chakraborty, N. Neophytou. Phonon transport simulations in hierarchically disordered silicon-based nanostructures. PGR Engineering Symposium, University of Warwick, Coventry, UK, (2019). <https://doi.org/10.1103/PhysRevB.98.115435>

- [227] J. Lee, V. Varshney, A. K. Roy, J. B. Ferguson, and B. L. Farmer. Thermal rectification in three-dimensional asymmetric nanostructure. *Nano lett.* 12(7), 3491-3496 (2012). <https://doi.org/10.1021/nl301006y>
- [228] M. Verdier, D. Lacroix, and K. Termentzidis. Thermal transport in two-and three-dimensional nanowire networks. *Phys. Rev. B* 94, 1 (2018). <https://doi.org/10.1103/PhysRevB.98.155434>
- [229] M. Ohnishi and J. Shiomi. Towards ultimate impedance of phonon transport by nanostructure interface. *APL Mater.* 7, (2019). <https://doi.org/10.1063/1.5055570@apm.2019.IEM2019.issue-1>
- [230] Z. Cheng, B. M. Foley, T. Bougher, L. Yates, B. A. Cola, and S. Graham. Thermal rectification in thin films driven by gradient grain microstructure. *J. Appl. Phys.* 123(9), 095114 (2018). <https://doi.org/10.1063/1.5021681>
- [231] A. Rajabpour, S. M. Vaez Allaei, and F. Kowsary. Interface thermal resistance and thermal rectification in hybrid graphene-graphane nanoribbons: a nonequilibrium molecular dynamics study. *Appl. Phys. Lett.* 99(5), 051917 (2011). <https://doi.org/10.1063/1.3622480>
- [232] Sergei Gluchko , Roman Anufriev , Ryoto Yanagisawa , Sebastian Volz , and Masahiro Nomura. On the reduction and rectification of thermal conduction using phononic crystals with pacman-shaped holes. *Appl. Phys. Lett.* 114, 023102 (2019). <https://doi.org/10.1063/1.5079931>
- [233] Nuo Yang, Gang Zhang, and Baowen Li. Thermal rectification in asymmetric graphene ribbons. *Appl. Phys. Lett.* 95, 033107 (2009). <https://doi.org/10.1063/1.3183587>
- [234] C. Starr. The copper oxide rectifier. *J. Appl. Phys.* 7, 15 (1936). <https://doi.org/10.1063/1.1745338>
- [235] J. J. Martinez-Flores, Dinesh Varshney, and J. Alvarez-Quintana. Thermal rectification via sequential deactivation of magnons. *Appl. Phys. Lett.* 113, 264102 (2018). <https://doi.org/10.1063/1.5063479>
- [236] Z. Cheng, B. M. Foley, T. Bougher, L. Yates, B. A. Cola, and S. Graham. Thermal Rectification in CVD Diamond Membranes Driven by Gradient Grain Structure. *arXiv preprint arXiv:1712.07025* (2017). <https://doi.org/10.1063/1.5021681>
- [237] X. Yang, D. Yu, B. Cao, and A. C. To. Giant Thermal Rectification from Single-Carbon Nanotube–Graphene Junction. *ACS Appl. Mater. Interfaces* 9, 24078 (2017). <https://doi.org/10.1021/acsami.7b04464>
- [238] H. Machrafi, G. Lebon, and D. Jou. Thermal rectifier efficiency of various bulk–nanoporous silicon devices. *Int. J. Heat Mass Transf.* 97, 603 (2016). <https://doi.org/10.1016/j.ijheatmasstransfer.2016.02.048>
- [239] R. Dettori, C. Melis, R. Rurali, and L. Colombo. Thermal rectification in silicon by a graded distribution of defects. *J. Appl. Phys.* 119, (2016). <https://doi.org/10.1063/1.4953142>

- [240] D. Sawaki, W. Kobayashi, Y. Moritomo, and I. Terasaki. Thermal rectification in bulk materials with asymmetric shape. *Appl. Phys. Lett.* 98, 081915 (2011). <https://doi.org/10.1063/1.3559615>
- [241] Y. Wang, S. Chen, and X. Ruan. Tunable thermal rectification in graphene nanoribbons through defect engineering: A molecular dynamics study. *Appl. Phys. Lett.* 100, 163101 (2012). <https://doi.org/10.1063/1.3703756>
- [242] C. L. Chiu, C. H. Wu, B. W. Huang, C. Y. Chien, and C. W. Chang. Detecting thermal rectification. *AIP Adv.* 6, (2016). <https://doi.org/10.1063/1.4968613>
- [243] Yue-Yang Liu, Wu-Xing Zhou, Li-Ming Tang, and Ke-Qiu Chen. An important mechanism for thermal rectification in graded nanowires. *Appl. Phys. Lett.* 105, 203111 (2014). <https://doi.org/10.1063/1.4902427>
- [244] M. Terraneo, M. Peyrard, G. Casati. Controlling the energy flow in nonlinear lattices: a model for a thermal rectifier. *Phys. Rev. Lett.* 88 (9), 4302 (2002). <https://doi.org/10.1103/PhysRevLett.88.094302>
- [245] M. Criado-Sancho, F. X. Alvarez, and D. Jou. Thermal rectification in inhomogeneous nanoporous Si devices. *J. Appl. Phys.* 114, (2013). <https://doi.org/10.1063/1.4816685>
- [246] A. Malhotra, K. Kothari, and M. Maldovan. Cross-plane thermal conduction in superlattices: Impact of multiple length scales on phonon transport. *J. Appl. Phys.* 125, (2019). <https://doi.org/10.1063/1.5065904>
- [247] A. Yousefzadi Nobakht, Y. A. Gandomi, J. Wang, M. H. Bowman, D. C. Marable, B. E. Garrison, D. Kim, and S. Shin. Thermal rectification via asymmetric structural defects in graphene. *Carbon N. Y.* (2018). <https://doi.org/10.1016/j.carbon.2018.02.087>
- [248] N. A. Roberts and D. G. Walker. A review of thermal rectification observations and models in solid materials. *Int. J. Therm. Sci.* 50, 648 (2011). <https://doi.org/10.1016/j.ijthermalsci.2010.12.004>
- [249] M. Schmotz, J. Maier, E. Scheer and P. Leiderer. A thermal diode using phonon rectification. *New J. Phys.* 13 113027 (2011). <https://doi.org/10.1088/1367-2630/13/11/113027>
- [250] H. Tian, D. Xie, Y. Yang, T.-L. Ren, G. Zhang, Y.-F. Wang, C.-J. Zhou, P.-G. Peng, L.-G. Wang, and L.-T. Liu. A novel solid-state thermal rectifier based on reduced graphene oxide. *Sci. Rep.* 2, 523 (2012). <https://doi.org/10.1038/srep00523>
- [251] D. Hatanaka, I. Mahboob, K. Onomitsu, and H. Yamaguchi. Phonon waveguides for electromechanical circuits. *Nat. Nano.* 9(7), 520 (2014). <https://doi.org/10.1038/nnano.2014.107>
- [252] C. Melnick, and M. Kaviani. Phonovoltaic. I. Harvesting hot optical phonons in a nanoscale p– n junction. *Phys. Rev. B* 93(9), 094302 (2016). <https://doi.org/10.1103/PhysRevB.93.094302>

- [253] C. Melnick, and M. Kaviany. From thermoelectricity to phonoelectricity. *Appl. Phys. Rev.* 6(2), 021305 (2019). <https://doi.org/10.1063/1.5031425>
- [254] A. Jain, Y.-J. Yu, and A.J.H. McGaughey. Phonon transport in periodic silicon nano- porous films with feature sizes greater than 100 nm. *Phys. Rev. B* 87, (2013) 195301. <https://doi.org/10.1103/PhysRevB.87.195301>
- [255] N.K. Ravichandran, and A.J. Minnich. Coherent and incoherent thermal transport in nanomeshes, *Phys. Rev. B* 89, (2014) 205432. <https://doi.org/10.1103/PhysRevB.89.205432>
- [256] M. Asheghi, Y. K. Leung, S. S. Wong and K. E. Goodson. Phonon-boundary scattering in thin silicon layers. *Appl. Phys. Lett.* 71, 1798 (1997). <https://doi.org/10.1063/1.119402>
- [257] P. E. Hopkins, C. M. Reinke, M. F. Su, R. H. Olsson, E. A. Shaner, Z. C. Leseman, J. R. Serrano, L. M. Phinney, and I. El-Kady. Reduction in the Thermal Conductivity of Single Crystalline Silicon by Phononic Crystal Patterning. *Nano Lett.* 11(1), 107-112, (2011). <https://doi.org/10.1021/nl102918q>
- [258] E. Yablonovitch. Inhibited spontaneous emission in solid-state physics and electronics. *Phys. Rev. Lett.*, 58(20), 2059 (1987). <https://doi.org/10.1103/PhysRevLett.58.2059>
- [259] T. Juntunen, O. Vänskä, and I. Tittonen. Anderson Localization Quenches Thermal Transport in Aperiodic Superlattices. *Phys. Rev. Lett.*, 122(10), (2019). <https://doi.org/10.1103/PhysRevLett.122.105901>
- [260] V. Jean, S. Fumeron, K. Termentzidis, S. Tutashkonko, and D. Lacroix. Monte Carlo simulations of phonon transport in nanoporous silicon and germanium. *J. Appl. Phys.*, 115(2) (2014). <https://doi.org/10.1063/1.4861410>
- [261] L.N. Maurer, S. Mei, and I. Knezevic. Rayleigh waves, surface disorder, and phonon localization in nanostructures *Phys. Rev. B* 94(4), 045312 (2016). <https://doi.org/10.1103/PhysRevB.94.045312>
- [262] M. L. Sancho, J. L. Sancho, and J. Rubio. Quick iterative scheme for the calculation of transfer matrices: application to Mo (100). *J. Phys. F* 14(5), 1205 (1984). <https://doi.org/10.1088/0305-4608/14/5/016>
- [263] J. Sadhu, and S. Sinha. Room-temperature phonon boundary scattering below the Casimir limit, *Phys. Rev. B* 84 (11), 115450 (2011). <https://doi.org/10.1103/PhysRevB.84.115450>
- [264] J. Ma, J. S. Sadhu, D. Ganta, H. Tian, S. Sinha. Thermal transport in 2-and 3-dimensional periodic “holey” nanostructures. *AIP Adv.* 4 (12), 124502 (2014). <https://doi.org/10.1063/1.4904073>
- [265] P.G. Sverdrup, S. Sinha, M. Asheghi, S. Uma, K.E. Goodson. Measurement of ballistic phonon conduction near hotspots in silicon. *Appl. Phys. Lett.* 78 (21), 3331–3333 (2001). <https://doi.org/10.1063/1.1371536>

- [266] D. Donadio, and G. Galli. Temperature dependence of the thermal conductivity of thin silicon nanowires. *Nano Lett.* 10(3), 847 (2010). <https://doi.org/10.1021/nl903268y>
- [267] J. Lee, W. Lee, J. Lim, Y. Yu, Q. Kong, J. J. Urban, and P. Yang. Thermal transport in silicon nanowires at high temperature up to 700 K. *Nano letters* 16 (7), 4133-4140 (2016). <https://doi.org/10.1021/acs.nanolett.6b00956>
- [268] A. Malhotra, and M. Maldovan. Impact of Phonon Surface Scattering on Thermal Energy Distribution of Si and SiGe Nanowires. *Sci. Rep.* 6, 25818 (2016). <https://doi.org/10.1038/srep25818>
- [269] G. Chen. Phonon heat conduction in nanostructures. *Int. J. Therm. Sci.* 39, 471 (2000). [https://doi.org/10.1016/S1290-0729\(00\)00202-7](https://doi.org/10.1016/S1290-0729(00)00202-7)
- [270] H. Machrafi, and G. Lebon. Effective thermal conductivity of spherical particulate nanocomposites: Comparison with theoretical models, Monte Carlo simulations and experiments. *Inter. J. Nanosci.* 13(3), 1-8 (2014). <https://doi.org/10.1142/S0219581X14500227>
- [271] A. Minnich, and G. Chen. Modified effective medium formulation for the thermal conductivity of nanocomposites. *Appl. Phys. Lett.* 91(7), 073105 (2007). <https://doi.org/10.1063/1.2771040>
- [272] A. Behrang, M. Grmela, C. Dubois, S. Turenne, P.G. Lafleur, *J. Appl. Phys.* 114, 014305 (2014). <https://doi.org/10.1063/1.4812734>
- [273] C. Cho, K. L. Wallace, P. Tzeng, J. Hsu, C. Yu, J. C. Grunlan. Outstanding low temperature thermoelectric power factor from completely organic thin films enabled by multidimensional conjugated nanomaterials. *Adv. Energy. Mater.* 6(7), 1502168 (2016). <https://doi.org/10.1002/aenm.201502168>
- [274] H. Ju, and J. Kim. Fabrication of conductive polymer/inorganic nanoparticles composite films: PEDOT:PSS with exfoliated tin selenide nanosheets for polymer-based thermoelectric devices. *Chem Eng J.* 297, 66–73 (2016). <https://doi.org/10.1016/j.cej.2016.03.137>
- [275] G. Goo, Anoop G, Unithrattil S, Kim WS, Lee HJ, Kim HB, et al. Proton-irradiation effects on the thermoelectric properties of flexible Bi<sub>2</sub>Te<sub>3</sub>/PEDOT:PSS composite films. *Adv Elec. Mater.* 5(4), 1–10 (2019). <https://doi.org/10.1002/aelm.201800786>
- [276] C. Ou, Z. Lu, Q. Jing, V. Narayan, and S. Kar-Narayan. Compositionally Graded Organic–Inorganic Nanocomposites for Enhanced Thermoelectric Performance. *Advanced Electronic Materials* 6(1), 1900720 (2020). <https://doi.org/10.1002/aelm.201900720>
- [277] A. Kausar. Thermally conducting polymer/nanocarbon and polymer/inorganic nanoparticle nanocomposite: a review. *Polymer-Plastics Technology and Materials*, 1-15 (2020). <https://doi.org/10.1080/25740881.2019.1708103>

- [278] X. Hu, K. Zhang, J. Zhang, S. Wang, and Y. Qiu. Thermoelectric properties of conducting polymer nanowire–tellurium nanowire composites. *ACS Appl. Energy Mater.* 1(9), 4883 (2018). <https://doi.org/10.1021/acsaem.8b00909>
- [279] C. Ou, Canlin, A. L. Sangle, T. Chalklen, Q. Jing, V. Narayan, and S. Kar-Narayan. Enhanced thermoelectric properties of flexible aerosol-jet printed carbon nanotube-based nanocomposites. *APL Materials* 6 (9), 096101 (2018). <https://doi.org/10.1063/1.5043547@apm.2019.FLEX2019.issue-1>
- [280] X. Wang, A. K. K. Kyaw, C. Yin, F. Wang, Q. Zhu, T. Tang, et al. Enhancement of thermoelectric performance of PEDOT:PSS films by post-treatment with a superacid. *RSC Adv* 8, 18334 (2018). <https://doi.org/10.1039/C8RA02058B>
- [281] K. Zhang, Y. Zhang, and S. Wang. Enhancing thermoelectric properties of organic composites through hierarchical nanostructures. *Sci Rep* 3, 3448 (2013). <https://doi.org/10.1038/srep03448>
- [282] Z. Aksamija, and I. Knezevic. Thermal conductivity of Si<sub>1-x</sub>Gex/Si<sub>1-y</sub>Gey superlattices: Competition between interfacial and internal scattering. *Phys. Rev. B* 88(15), 1–11 (2013). <https://doi.org/10.1103/PhysRevB.88.155318>
- [283] J. Larroque, P. Dollfus, and J. Saint-Martin. Phonon transmission at Si/Ge and polytypic Ge interfaces using full-band mismatch based models. *J. Appl. Phys.* 123(10), 25702 (2018). <https://doi.org/10.1063/1.5007034>
- [284] E. T. Swartz, and R. O. Pohl. Thermal Boundary Resistance. *Rev. Mod. Phys.* 61, 605–668 (1989). <https://doi.org/10.1103/RevModPhys.61.605>
- [285] W. S. Capinski, H. J. Maris, T. Ruf, M. Cardona, K. Ploog, and D. S. Katzer. Thermal-Conductivity Measurements of GaAs/AlAs SLs Using a Picosecond Optical Pump-and-Probe Technnique. *Phys. Rev. B* 59, 8105 (1999). <https://doi.org/10.1103/PhysRevB.59.8105>
- [286] D. G. Cahill. Heat transport in dielectric thin films and at solid-solid interfaces. *Micro. Therm. Engin.* 1, 85 (1997). [10.1080/108939597200296](https://doi.org/10.1080/108939597200296)
- [287] D. G. Cahill, A. Bullen, and L. Seung-Min. Interface thermal conductance and the thermal conductivity of multilayer thin films. *High Temperatures High Pressures* 32.2, 135-142 (2000). <https://doi.org/10.1068/htwi9>
- [288] R. S. Prasher, and P. E. Phelan. A scattering-mediated acoustic mismatch model for the prediction of thermal boundary resistance. *J. Heat Transfer* 123 (1), 105-112 (2001). <https://doi.org/10.1115/1.1338138>
- [289] Du Y, Liu X, Xu J, Shen SZ. Flexible Bi-Te-based alloy nanosheet/PEDOT:PSS thermoelectric power generators. *Mater Chem Front* 3, 1328 (2019). <https://doi.org/10.1039/C9QM00087A>
- [290] Z. Liu, Z. Chen, and F. Yu. Enhanced thermal conductivity of microencapsulated phase change materials based on graphene oxide and carbon nanotube hybrid filler. *Solar Energy Materials and Solar Cells* 192, 72–80 (2019). <https://doi.org/10.1016/j.solmat.2018.12.014>



- [291] C. Fu, Q. Li, J. Lu, S. Mateti, Q. Cai, X. Zeng, G. Du, R. Sun, Y. Chen, J. Xu, C. P. Wong. Improving thermal conductivity of polymer composites by reducing interfacial thermal resistance between boron nitride nanotubes. *Composites Science and Technology*, 165, 322–330 (2018). <https://doi.org/10.1016/j.compscitech.2018.07.010>
- [292] L. Ren, Q. Li, J. Lu, X. Zeng, R. Sun, J. Wu, J. Xu, C. P. Wong. Enhanced thermal conductivity for Ag-deposited alumina sphere/epoxy resin composites through manipulating interfacial thermal resistance. *Composites Part A: Applied Science and Manufacturing*, 107, 561–569 (2018). <https://doi.org/10.1016/j.compositesa.2018.02.010>
- [293] J. Huang, Y. Zhu, L. Xu, J. Chen, W. Jiang, and X. Nie. Massive enhancement in the thermal conductivity of polymer composites by trapping graphene at the interface of a polymer blend. *Comp. Science and Technology* 129, 160–165 (2016). <https://doi.org/10.1016/j.compscitech.2016.04.029>
- [294] B. Lee, and G. Dai. Influence of interfacial modification on the thermal conductivity of polymer composites. *J. of Mater. Sci.* 44(18), 4848–4855 (2009). <https://doi.org/10.1007/s10853-009-3739-6>
- [295] L. Wang, Z. Zhang, Y. Liu. Exceptional thermoelectric properties of flexible organic–inorganic hybrids with monodispersed and periodic nanophase. *Nat Commun* 9, 3817 (2018). <https://doi.org/10.1038/s41467-018-06251-9>
- [296] N. K. Ravichandran, H. Zhang, and A. J. Minnich. Spectrally resolved specular reflections of thermal phonons from atomically rough surfaces. *Phys. Rev. X* 8(4), 041004 (2018). <https://doi.org/10.1103/PhysRevX.8.041004>
- [297] M. Maldovan. Specular Reflection Leads to Maximum Reduction in Thermal Conductivity. *arXiv preprint arXiv:1810.07383* (2018). <https://doi.org/10.1063/1.5092341>
- [298] Y. He, D. Donadio, J-H. Lee, J. C. Grossman, and G. Galli. Thermal transport in nanoporous silicon: interplay between disorder at mesoscopic and atomic scales. *ACS Nano* 5(3), 1839-1844 (2011). <https://doi.org/10.1021/nn2003184>
- [299] W. Tian, and R. Yang. Thermal conductivity modeling of compacted nanowire composites. *J. Appl. Phys.* 101(5), 054320 (2007). <https://doi.org/10.1063/1.2653777>
- [300] M-J. Huang, and T-Y. Kang. A Monte-Carlo study of the phonon transport in nanowire-embedded composites. *Inter. J. Thermal Sci.* 50, 1156 (2011). <https://doi.org/10.1016/j.ijthermalsci.2011.02.011>

\*\*\*